

This file is part of the following work:

Van Ryt, Matthew (2019) *The mineralisation, alteration paragenesis and hydrothermal fluids at the Geita Hill gold deposits, NW Tanzania*. PhD Thesis, James Cook University.

Access to this file is available from:

<https://doi.org/10.25903/5ef146396bcce>

Copyright © 2019 Matthew Van Ryt.

The author has certified to JCU that they have made a reasonable effort to gain permission and acknowledge the owners of any third party copyright material included in this document. If you believe that this is not the case, please email

researchonline@jcu.edu.au

**The mineralisation, alteration paragenesis and
hydrothermal fluids at the Geita Hill gold deposits, NW
Tanzania**

Thesis submitted by

Matthew Van Ryt

February 2019

For the Degree of Doctor of Philosophy

College of Science and Engineering

James Cook University

Statement of access

I, the undersigned author of this thesis, understand that James Cook University will make this thesis available for use within the university library and allow access in other approved libraries after its submission. All users consulting this thesis will have to sign the following statement:

In consulting this thesis, I agree not to copy or closely paraphrase it in whole or in part without the written consent of the author; and to make proper public written acknowledgement for any assistance that I have obtained from it.

Beyond this statement, I do not wish any restrictions placed on access to this thesis.

Matthew Van Ryt

February 2019

Every reasonable effort has been made to gain permission and acknowledge the owners of copyright material. I would be pleased to hear from any copyright owner who has been omitted or incorrectly acknowledged.

Declaration

I declare this thesis to be the product of my own work, and that it has not been submitted in any form for another degree of diploma at any university or other institute for tertiary education. Information derived from the published or unpublished work of others has been acknowledged in the text and references given.

Matthew Van Ryt

February 2019

List of publications

This thesis is based on the following publications.

- | <i>Chapter</i> | <i>Publication on which the chapter is based</i> |
|----------------|---|
| 2 | van Ryt, M. R. , Sanislav, I. V., Dirks, P. H. G. M., Huizenga, J. M., Mturi, M. I., & Kolling, S. L. (2017). Alteration paragenesis and the timing of mineralised quartz veins at the world-class Geita Hill gold deposit, Geita Greenstone Belt, Tanzania. <i>Ore Geology Reviews</i> , 91, 765-779. |
| 3 | van Ryt, M. R. , Sanislav, I. V., Dirks, P. H. G. M., Huizenga, J., Mturi, M. I., & Kolling, S. L. (2019). Biotite chemistry and the role of halogens in Archaean greenstone hosted gold deposits: a case study from Geita Gold Mine, Tanzania. <i>Ore Geology Reviews</i> , 111, 102982. |
| 4 | van Ryt, M. R. , Sanislav, I. V., Dirks, P. H. G. M., Huizenga, J. Trace element associations in hydrothermal pyrite at the Geita Hill gold deposit, Tanzania, revealed through LA-ICP-MS mapping. <i>Journal of Geochemical Exploration</i> , (in press). |
| 5 | van Ryt, M. R. , Huizenga, J., Dirks, P. H. G. M., Sanislav, I. V. Evolution of fluids associated with Archean gold mineralisation at Geita Hill (Tanzania): a fluid inclusion study. |

Additionally, research presented in this thesis forms a component of a review article.

Dirks, P. H. G. M, Sanislav, I. V. **van Ryt, M. R.**, Huizenga, J. M., Blenkinsop, S. L., Kolling, S. D., Kelwa, The Geita Gold deposit, Tanzania: a late Archaean, Te-enriched, intrusion related gold system. *Economic Geology*, (in press)

Statement of Contribution of Others

<i>Nature of assistance</i>	<i>Name and affiliation of contributor</i>
Advisory Panel	Dr Ioan Sanislav (Primary advisor) ^a Dr Jan Marten Huizenga ^a Prof. Paul Dirks ^a
External advisor	Prof. Nick Oliver ^a
Proposal writing	Prof. Paul Dirks ^a Dr Ioan Sanislav ^a Dr Carl Spandler ^a
Mine visits and fieldwork	Marwa Mturi ^b Sergio Kolling ^b
Data collection and analysis	Dr Jan Marten Huizenga ^a Dr Ioan Sanislav ^a Prof Paul Dirks ^a Marwa Mturi ^b Sergio Kolling ^b Dr. Kevin Blake ^c Dr Yi Hu ^c Dr James Daniell ^a Alexander Parker ^a

<i>Nature of assistance</i>	<i>Name and affiliation of contributor</i>
Editorial assistance	Prof Paul Dirks ^a Dr Ioan Sanislav ^a Dr Jan Marten Huizenga ^a Dr. Kevin Blake ^c Dr Yi Hu ^c
Financial support	Geita Gold Mine and AngloGold Ashanti Economic Geology Research Centre College of Science and Engineering, JCU
Scholarship	James Cook University Australian Federal Government

Affiliations

a: James Cook University

b: Geita Gold Mine

c: Advanced Analytical Centre at James Cook University

Acknowledgements

I would first like to thank my primary advisor Ioan Sanislav for his tireless support throughout this PhD project. The skills and knowledge you have imparted to me are greatly appreciated, as was your patience and good humour throughout.

I would like to sincerely thank my advisor Jan Huizenga, whom I have had the good fortune to know and to learn from since being an undergraduate. If not for you, I would not be on this path.

Well-deserved thanks are also owed to my advisor Paul Dirks, for all the robust and enlightening discussions we have had on the topic of Geita Hill and geology in general.

This thesis would not have been possible without the support of Marwa Mturi and Sergio Kolling of AngloGold Ashanti, thank you for this opportunity, and I wish you every success in your future ventures.

I would also like to mention the wider faculty at James Cook University; James Daniell, Christa Placzek, Carl Spandler, Eric Roberts, Judy Botting, Rebecca Steele, Tom Blenkinsop, Mike Rubenach and Zhaoshan Chang. This marks the end of a long journey with you all, thank you for the time you have invested in me.

To my friends and colleges; Refilwe, Alex, Robbie, Jelle, Paul, Christopher Todd, Tegan, Christopher Yule, Jaime, Leigh, Caleb, Michal, Kelly and Ashish, my time with you was always enjoyable, thank you for all the laughs.

Lastly, I must mention my partner and best friend Samantha. Your support has kept me motivated, and when I wasn't motivated, at least moving in the right direction. I can't express how grateful I am.

Thesis abstract

Archean greenstones represent a large percentage of worlds total gold endowment and are actively mined on every continent barring Antarctica. Greenstone-hosted gold deposits often have complex deformation and alteration histories, and a general deposit model remains controversial. The aim of this thesis is to improve our understanding of gold mineralisation in Archean greenstone belts, based on a comprehensive case study of the world-class Geita Hill deposit in Tanzania. Geita Hill is one of the largest gold deposits within the Geita Greenstone Belt in north-western Tanzania and has been mined as an open pit since 2002. The deposit is hosted within a greenschist facies metamorphosed and complexly deformed sedimentary package dominated by ironstone and intruded by diorite dykes. The gold mineralisation is spatially associated with the Geita Hill Shear Zone which, is a NE-trending, moderately west dipping deformation zone of discontinuous shear fractures. Detailed structural studies have defined a deformation history for the deposit, providing an opportunity for an in-depth study of the hydrothermal alteration and fluids associated with gold mineralisation.

The first component of this thesis builds a paragenetic framework for the Geita Hill deposit. The regional metamorphism is characterised by biotite + chlorite + actinolite + K-feldspar + magnetite ± pyrrhotite ± pyrite indicating upper greenschist facies metamorphism. The gold-related alteration overprints the regional metamorphism and is characterised by silicification and sulfidation fronts that end within one meter of the mineralised zone. Locally, the silicification and sulfidation of the wall rock occurs along a series of mineralised quartz veins which have a sub-vertical dip and tend E-W. Paleostress analysis of the mineralised shear fractures of the Geita Hill Shear Zone suggests vertical maximum compressive stress (σ_1) and northerly extensional stress (σ_3) consistent with the orientation of the mineralised quartz veins and indicating N-S extension. The composition of the mineralised quartz veins is characterised by quartz + biotite + K-feldspar + pyrite, which also overprints the metamorphic mineral assemblage. Gold is closely associated with secondary pyrite and occurs as free gold and gold tellurides (sylvanite, calaverite and nagyagite). It occurs mainly as inclusions in pyrite and as invisible gold in pyrite but gold inclusions in biotite and along quartz grain boundaries are also present. The gold-bearing pyrite is associated with secondary biotite and K-feldspar. Two distinct textural styles of auriferous pyrite can be distinguished: inclusion rich subhedral pyrite and inclusion free euhedral pyrite. It is common for the inclusion rich pyrite to have

thick rims of inclusion free pyrite. The mineralising alteration is overprinted by barren, multi-phase quartz-carbonate, and carbonate-chlorite veins. This alteration is characterised by the assemblage calcite + siderite + chlorite \pm quartz \pm pyrite \pm barite.

The thesis then builds on the paragenetic framework through silicate and sulfide geochemistry. Biotite was identified as a primary mineral both in the metamorphic assemblage and gold-related hydrothermal alteration assemblage. The study of silicates was conducted through detailed core logging, petrography, SEM mineral identification of alteration assemblages, SWIR measurements and microprobe analyses of biotite in order to identify the nature of the mineralising fluid and its spatial effect across the Geita Hill deposit. Results show that the mineralised assemblage is slightly more oxidized (pyrite + magnetite) compared to the metamorphic background (pyrrhotite + magnetite). The intense sulfidation within the ore zone resulted in the formation of Mg-rich biotite, which grades into more Fe-rich biotite away from the ore zone. This change in biotite composition can be detected using short wavelength infrared spectra, though a shift in the Fe-OH 2250 nm absorption feature to lower wavelengths. This shift is also correlated with an increase in gold grade within the mineralised zone. Halogen chemistry of the biotite implied the presence of multiple hydrothermal fluids during mineralisation, suggesting that within the ore zone a metamorphic fluid in equilibrium with the host rock was overprinted by and mixed with an infiltrating fluid that was enriched in fluorine.

Study of the sulfides in the deposit was conducted through laser ablation inductively coupled plasma mass spectrometry (LA-ICP-MS) analysis of pyrite and magnetite grains. The gold distribution correlates well with Te, Ag, Bi and Pb consistent with its occurrence as micro- and nano-inclusions of gold bearing telluride minerals. As, Co and Ni distribution in pyrite grains hosted in quartz veins is patchy, whereas in pyrite grains from ironstone and diorite these elements show zoning characteristic of growth pattern. Elements including As, Ni, Co, Cu and Zn appear to be dominantly locally derived, and remobilised into the pyrite during sulfidation. The concentrations of these elements are highly lithologically controlled, and they are not consistently incorporated into the pyrite after initial stages of growth. Au, Ag, Te, Sn, Bi and Pb appear to be dominantly externally derived, and closely correlate in all varieties of pyrite. The Se content is typical of pyrite from

Archean gold deposits (~30ppm) and reflects to an average temperature of ~340°C for the mineralising fluid on the basis of temperature dependent incorporation into pyrite.

Lastly, the gold-bearing hydrothermal fluids were studied directly through detailed microthermometry and raman microspectroscopy, and three principle fluids were identified: (1) A low salinity, carbonic-rich ($X_{CO_2} > 0.8$) fluid with minor N_2 ($X_{N_2}/(X_{CO_2} + X_{N_2}) < 0.15$) that was interpreted to be metamorphic in origin; (2) A high salinity ($NaCl+CaCl_2 > 20$ wt.%; $NaCl/(NaCl+CaCl_2)$ mass ratio > 0.45), aqueous brine that was interpreted to be magmatic in origin; and (3) A low salinity ($NaCl < 5$ wt.%) aqueous fluid that was interpreted to be meteoric in origin. Preserved fluid assemblages imply mineralisation occurred at pressures of less than 2 kbar, likely from 1.4 to 1.7 kbar, at temperatures of approximately 350 °C. C-O-H fluid modelling of the carbonic-rich fluid has constrained $f_{O_2}^{fluid}$ to 1.5-1.8 \log_{10} units above $f_{O_2}^{FMQ}$ corresponding to absolute values of $10^{30.5}$ bar. The gold was likely transported in the high salinity brine as Au-bisulfide complexes with tellurium, potentially introduced as a vapour. Deposition of Au was triggered via interaction of gold-bearing fluids with the relatively reduced Fe-rich host rocks and the low salinity CO_2 -rich fluid.

Appendices

Additional material to supplement the research presented in this thesis is included as appendices. With the exception of appendix 1 and 2, which are journal articles in publication format, all appendices are digital, and not included in the text of this thesis. A contents document is also included in the digital appendix folder, which contains a description of each appendix and how to open them if specific software is required.

Appendix 1.....	166
van Ryt, M. R., Sanislav, I. V., Dirks, P. H. G. M., Huizenga, J. M., Mturi, M. I., & Kolling, S. L. (2017). Alteration paragenesis and the timing of mineralised quartz veins at the world-class Geita Hill gold deposit, Geita Greenstone Belt, Tanzania. <i>Ore Geology Reviews</i> , 91, 765-779.	
Appendix 2.....	182
Dirks, P. H. G. M, Sanislav, I. V. van Ryt, M. R., Huizenga, J. M., Blenkinsop, S. L., Kolling, S. D., Kelwa, The Geita Gold deposit, Tanzania: a late Archaean, Te-enriched, intrusion related gold system. <i>Economic Geology</i> , (in press).	
Appendix 3.....	Digital
Sample list and core logging summary	
Appendix 4.....	Digital
Alteration paragenesis report and section descriptions	
Appendix 5.....	Digital
Data pursuant to chapter 3: Biotite Chemistry and the Role of Halogens in Archaean Greenstone Hosted Gold Deposits: A Case Study from Geita Gold Mine, Tanzania	
Appendix 6.....	Digital
Data pursuant to chapter 4: Trace element associations in hydrothermal pyrite at the Geita Hill gold deposit, Tanzania, revealed through LA-ICP-MS mapping	
Appendix 7.....	Digital
Data pursuant to chapter 5: Evolution of fluids associated with Archean gold mineralisation at Geita Hill (Tanzania): a fluid inclusion study.	

Table of Contents

Statement of Access.....	I
Declaration.....	II
List of Papers.....	III
Statement of Contribution of Others.....	IV
Acknowledgements.....	VI
Thesis Abstract.....	VII
Appendices.....	X
Introduction to the Thesis.....	1
Chapter 1.....	7
Regional and Local Geology of the Geita Hill Gold Deposit	
Chapter 2.....	14
Alteration Paragenesis and the Timing of Mineralised Quartz Veins at the World-Class Geita Hill Gold Deposit, Geita Greenstone Belt, Tanzania	
Chapter 3.....	37
Biotite Chemistry and the Role of Halogens in Archaean Greenstone Hosted Gold Deposits: A Case Study from Geita Gold Mine, Tanzania	
Chapter 4.....	66
Trace element associations in hydrothermal pyrite at the Geita Hill gold deposit, Tanzania, revealed through LA-ICP-MS mapping	
Chapter 5.....	102
Evolution of fluids associated with Archean gold mineralisation at Geita Hill (Tanzania): a fluid inclusion study.	
Chapter 6.....	138
Thesis summary	

Introduction to the thesis

Archean greenstone hosted gold deposits

Archean greenstone belts are elongated supracrustal packages accreted between and intruded by multi-staged plutons with tonalite-trondhjemite-granodiorite (TTG) and potassic affinities. These granite-greenstone terranes are well-exposed on every continent; e.g. the Yilgarn and Pilbara Cratons in Western Australia, the Superior Province in Canada, the North Atlantic Craton in West Greenland, the Kaapvaal and Zimbabwe Cratons in southern Africa and the Tanzania Craton in eastern Africa (Condie, 1981; de Wit and Ashwal, 1995; 1997; Condie, 2007; Anhaeusser, 2014; Sanislav et al., 2014b). The supracrustal packages that comprise greenstone belts are dominated by mafic to intermediate volcanics, interbedded and intercalated with clastic sediments ranging from shales to sandstones and rare conglomerates.

Most greenstone belts are partly bounded by steeply dipping, brittle-ductile shear zones that separate them from granite-gneiss complexes (e.g., Ridley et al., 1997; Hickman, 2004; 2009; 2012; Sanislav et al., 2018b). Geophysical modelling indicates that these shear zones flatten with depth (Ridley et al., 1997; de Wit, 1998). A defining feature of greenstone belts themselves is their ubiquitous and multistage deformation, the tectonic significance of which remains the object of debate. One school of thought advocates modern style collisional tectonics and subduction to explain greenstone belt formation. In this model early collisional accretion caused thin-skinned, compressional thrusting and stratigraphic duplication, giving way to late transpression and extension (de Wit and Ashwal, 1995; 1997; Jelsma and Dirks, 2002; Hickman, 2004; Kabete et al., 2012a). An alternate model for the formation of greenstones calls for density driven vertical tectonics, with the diapiric emplacement of melt generated in the mid to lower crust as the principle cause of deformation (Collins et al., 1998; Bleeker, 2002; van Kranendonk, 2011). Whether modern-style subduction tectonics was active during the Archean remains debated. Recent geophysical modelling suggests it is possible (Hynes, 2013), and may have occurred intermittently (van Hunen and Moyen, 2012). However, geodynamic modelling of metamorphic processes in granite greenstone terrains (e.g., Sizova et al., 2018) shows that observed geothermal gradients in greenstones can also be generated without subduction.

Archean greenstone belts host a large number of world-class gold deposits, with most of these deposits classified as orogenic gold systems (e.g., Groves and Foster, 1991; Goldfarb et al., 2001; Pitcairn et al., 2006; Morey et al., 2007; Holwell et al., 2013; Dirks et al., 2013; Steadman et al., 2014; Sanislav et al., 2015; 2017; de Souza Martins et al., 2016; Groves and Santosh, 2016; Mishra et al., 2018). The orogenic model argues for subduction-related tectonic accretion and crustal thickening, followed by metamorphic devolatilisation and concentration of the resulting fluids along crustal scale structures. Mineralising fluids in this model are thought to be mostly metamorphically derived, i.e. they are low salinity carbonic-aqueous fluids with near neutral pH (Mikucki and Ridley, 1993; Goldfarb and Groves, 2015).

The timing of gold deposition in orogenic systems has been linked to a shift in the regional stress regime from compression to transpression or even extension, which generally occurs tectonically late in the history of the greenstone belt (Groves et al., 1998; 2003; 2018; Goldfarb et al., 2001; 2005; Phillips and Powell, 2010). Many studies of world-class Archaean gold deposits suggest that mineralisation involved multiple stages of gold enrichment (e.g., Bateman and Hagemann, 2004; Robert et al., 2005; Blewett et al., 2010; Baker et al., 2010; Helt et al., 2014). In contrast, Groves et al. (2018) argue that all orogenic gold deposits, including Archean deposits, formed during a single, late-stage event in a subduction-related tectonic setting.

By classifying Archean gold deposits as orogenic it is implicit that gold mineralisation formed in a uniformitarian plate-tectonic setting; a contention that remains strongly contested (e.g., Bédard et al., 2003; Bédard, 2006; Hamilton, 2011; van Kranendonk, 2011; Dirks et al., 2013). For example, Sanislav et al. (2018) demonstrate that the geochemistry of the greenstone sequence in the Geita Greenstone Belt that hosts the world-class Geita deposit, the subject of this thesis, is best explained through vertical melt accretion in an oceanic plateau-like environment, away from any horizontal accretionary margins.

The Geita Greenstone Belt (GGB) in the N part of the Tanzania Craton (Fig. 1.1) hosts world-class gold deposits spread along a 35 km long corridor in the central parts of the greenstone belt. These deposits, include (from W to E) the Star and Comet, Nyangkanga, Lone Cone, Geita Hill, Matandani and Kukuluma deposits (Fig. 1.1), and are commonly referred to collectively as Geita mine (Bierlein et al., 2006). All these deposits are largely hosted in silicified, magnetite-rich

metasedimentary units (referred to in the mine as meta-ironstones) near the intrusive contacts of monzonitic to dioritic bodies that intruded internal to the greenstone belt (Borg, 1994; Sanislav et al., 2015; 2017; Kwelwa et al., 2018a)

To date, detailed structural and geochemical studies have been published for the Nyankanga, Geita Hill, Matandani and Kukuluma deposits (Sanislav et al., 2015; 2017; Kwelwa et al., 2018b; 2018a; 2018c). However, no detailed textural and geochemical work has been published on the mineralisation and alteration assemblages that characterise the deposits, apart from work presented in this thesis (van Ryt et al., 2017). This thesis will address this point for the Geita Hill deposit, and provides detailed descriptions of the sulfide and telluride mineralogy that characterises mineralisation, together with studies of the alteration assemblage and mineralising fluids. Additionally, SWIR (short-wavelength infrared) reflectance spectra of biotite has been studied to determine if this technique can be applied to assess the footprint of gold mineralisation. Collectively, this new information provides additional constraints on the tectonic history of the Geita Greenstone Belt and gold mineralisation within it.

Research objectives

In this PhD thesis I present a hydrothermal alteration study of the Geita Hill gold deposit, with the aim of building a detailed deposit model, and improving the understanding of how greenstone-hosted gold deposits form more broadly. Towards this end, the following research objectives were set out, which form the basis of the four chapters in this thesis. These objectives are:

- Provide a detailed mineralogical and petrological description of the Geita Hill gold deposit, including descriptions of the protolith, metamorphic and hydrothermal mineral assemblages. Place each hydrothermal mineral assemblage into a structural context and construct a mineral and alteration paragenesis for the deposit (this objective has been addressed in chapter 2).
- Link the gold-related hydrothermal alteration at the deposit to a specific deformation event, and place it into a wider structural context for the greenstone belt as a whole (this objective has been addressed in chapter 2).

-
- Using the mineral paragenesis as a starting point, investigate changes in mineral chemistry associated with the gold-related hydrothermal alteration, with reference to sources of hydrothermal fluids, and identify feasible tools to track these changes (this objective has been addressed in chapter 3).
 - Develop techniques to allow the mapping of mineralisation and associated alteration assemblages on the basis of trace element content at the μm scale using laser ablation (this objective has been addressed in chapter 4).
 - Use these trace element maps and other LA-ICPMS techniques to investigate the element associations within sulfides and oxides in the Geita Hill deposit, with the aim of ascertaining which elements were hydrothermally derived, and which were locally remobilised during gold deposition (this objective has been addressed in chapter 4).
 - Use microthermometry and Raman spectroscopy to describe and model the hydrothermal fluids at the deposit, with the aim of constraining the conditions of mineralisation and the source of gold-bearing hydrothermal fluids (this objective has been addressed in chapter 5).

The structure of this thesis and authorship

The thesis consists of 6 chapters, including the geological setting (Chapter 1), and general conclusions (Chapter 6) chapters. The main body of work in this thesis is contained in chapters 2 to 5, each chapter representing a stand-alone piece of research intended to be published in a peer reviewed, internationally recognised academic journal. At the time of submission of this thesis, Chapter 2 has been published in the journal *Ore Geology Reviews* (a preprint has been included in appendix 1). Chapter 3 has been submitted for peer review, also in *Ore Geology reviews*, and Chapter 4 has been submitted for peer review in the journal *Mineralium Deposita*. Chapter 5 is in preparation for submission in early 2019. Additionally, I have contributed to several additional papers on gold mineralisation in the Geita Greenstone Belt, the first of which is included as Appendix 2.

As the four main chapters are presented in the format of a published manuscript, some repetition exists in the structure of the thesis, specifically with regard to sections pertaining to the regional and local geology of the deposit. In an effort to rectify this, the regional geology sections of

each manuscript have been cut from the chapters, and a single version is presented in Chapter 1. Additionally, the references for each chapter have been merged into a single reference list presented at the end of this thesis.

Chapter 2

Chapter 2 is titled “Alteration paragenesis and the timing of mineralised quartz veins at the world-class Geita Hill gold deposit, Geita Greenstone Belt, Tanzania” and was published in the journal *Ore Geology Reviews* in 2017. The first author of this paper Matthew Van Ryt (myself), with co-authors Ioan Sanislav, Paul Dirks, Jan Marten Huizenga, Marwa Mturi and Sergio Kolling. I was the principle scientific investigator. Sanislav was fundamentally involved with co-ordinating with the Geita Mine for fieldwork and core logging, use of the FaultKinWin program and manuscript redaction. Dirks was critically involved in interpretation, final manuscript editing and participated in fieldwork. Huizenga was critically involved with optical techniques and manuscript redaction. Mturi and Kolling represented industry contacts and facilitated the collection and transport of samples back to Australia and were central to the organisation of fieldwork.

Chapter 3

Chapter 3 is titled “Biotite chemistry and the role of halogens in Archaean greenstone hosted gold deposits: a case study from Geita Gold Mine, Tanzania”, and has been submitted for publication in the journal *Ore Geology Reviews*. The first author of this paper is Matthew Van Ryt, with co-authors Ioan Sanislav, Paul Dirks, Jan Marten Huizenga, Marwa Mturi and Sergio Kolling. I was the principal scientific investigator. Sanislav was critically involved with interpretation and manuscript redaction. Dirks and Huizenga both contributed to data interpretation and manuscript redaction. Mturi and Kolling facilitated sampling, travel and participated in fieldwork.

Chapter 4

Chapter 4 is titled “Trace element associations in magnetite and hydrothermal pyrite from the Geita Hill gold deposit, Tanzania” and has been submitted for publication in the *Journal of Geochemical Exploration*. The first author of this paper is Matthew Van Ryt, with co-authors Ioan Sanislav, Paul Dirks, and Jan Marten Huizenga. I was the principle scientific investigator. Sanislav was critically involved with analytical techniques, interpretation and manuscript redaction. Huizenga assisted with

data analysis and manuscript redaction. Dirks was central to interpretation and manuscript redaction.

Chapter 5

Chapter 5 is titled “Evolution of fluids associated with Archean gold mineralisation at Geita Hill (Tanzania): a fluid inclusion study” and is in preparation for submission to an academic journal in early 2019. The first author of this paper is Matthew Van Ryt, with co-authors Jan Marten Huizenga, Paul Dirks and Ioan Sanislav. I was the principle scientific investigator. Huizenga was fundamental to analytical techniques, interpretation and manuscript redaction. Dirks and Sanislav were both critically involved with interpretation and manuscript redaction.

Chapter 6

Chapter 6 contains a summary of research outcomes and general conclusions for the project. It outlines the mineral and alteration paragenesis for the Geita Hill deposit, and describes the changes in the silicate and sulfide assemblages with proximity to gold mineralisation. I also characterise the principle hydrothermal fluids active during gold mineralisation, identify the sources for each and summarise the mechanisms behind gold transport and deposition.

Chapter 1

Regional and local geology of the Geita Hill gold deposit

1.1. Regional Geology

The Archean Tanzania Craton is exposed across most of central and northern Tanzania, southeast Uganda, western Kenya and likely extends north under Lake Victoria. The craton is bounded to the east, south and west by a series of mostly Proterozoic high-grade mobile belts and transitions under poor exposure into the Paleo-Mesoarchean Uganda Basement to the north (Ikingura et al., 1992; Lenoir et al., 1994; Möller et al., 1995; Deblond et al., 2001). The northern part of the Tanzania Craton (Fig. 1.1) comprises a suit of Neoproterozoic granitoids and associated gneissic terranes, which intrude and separate a series of regional-scale greenstone belts (Manya and Maboko, 2008; Kabete et al., 2012a; 2012b).

Historically the stratigraphy of the Tanzania Craton has been subdivided into the Dodoman, Nyanzian and Kavirondian Supergroups (Bath, 1990; Borg et al., 1990; Kuehn et al., 1990; Borg, 1992; Borg and Shackleton, 1997; Borg and Krogh, 1999). Based on geophysical and remote sensing interpretations Kabete et al. (2012a) proposed a sub-division of the Tanzania Craton into a series of shear-zone bounded NW trending accretionary terranes; the East Lake Victoria, Mwanza-Lake Eyasi, Lake Nyanza, Moyowosi–Manyoni, Dodoma Schist and Dodoma Basement terranes.

The Dodoman Supergroup has been interpreted to represent the lowermost stratigraphic unit. It is dominated by granitoids and migmatites with slivers of narrow, WNW-ESE trending granulite- to greenschist-facies metamorphic belts (Kabete et al., 2012a). The Dodoman Supergroup is overlain by the Nyanzian Supergroup which in turn is unconformably overlain by the Kavirondian Supergroup (e.g., Quenell et al., 1956; Borg and Shackleton, 1997). The Nyanzian Supergroup is further subdivided into the Lower and Upper Nyanzian. The Lower Nyanzian is dominated by amphibolite facies metamorphosed mafic volcanics including gabbro and pillow basalt (Manya and Maboko, 2003; 2008; Cook et al., 2016). The Upper Nyanzian is dominated by felsic volcanics and pyroclastics interbedded with volcanoclastic, turbiditic and chemical sediments such as chert, ironstone, black-shale, mudstone and sandstone (Borg, 1992; Borg and Krogh, 1999; Krapez, 2008). The Kavirondian Supergroup unconformably overlies the Nyanzian, and is dominated by detrital sediments including conglomerate, arkosic and feldspathic grit and quartzite, with minor sandstone, siltstone, shale, tuff and phyllite (Gabert, 1990).

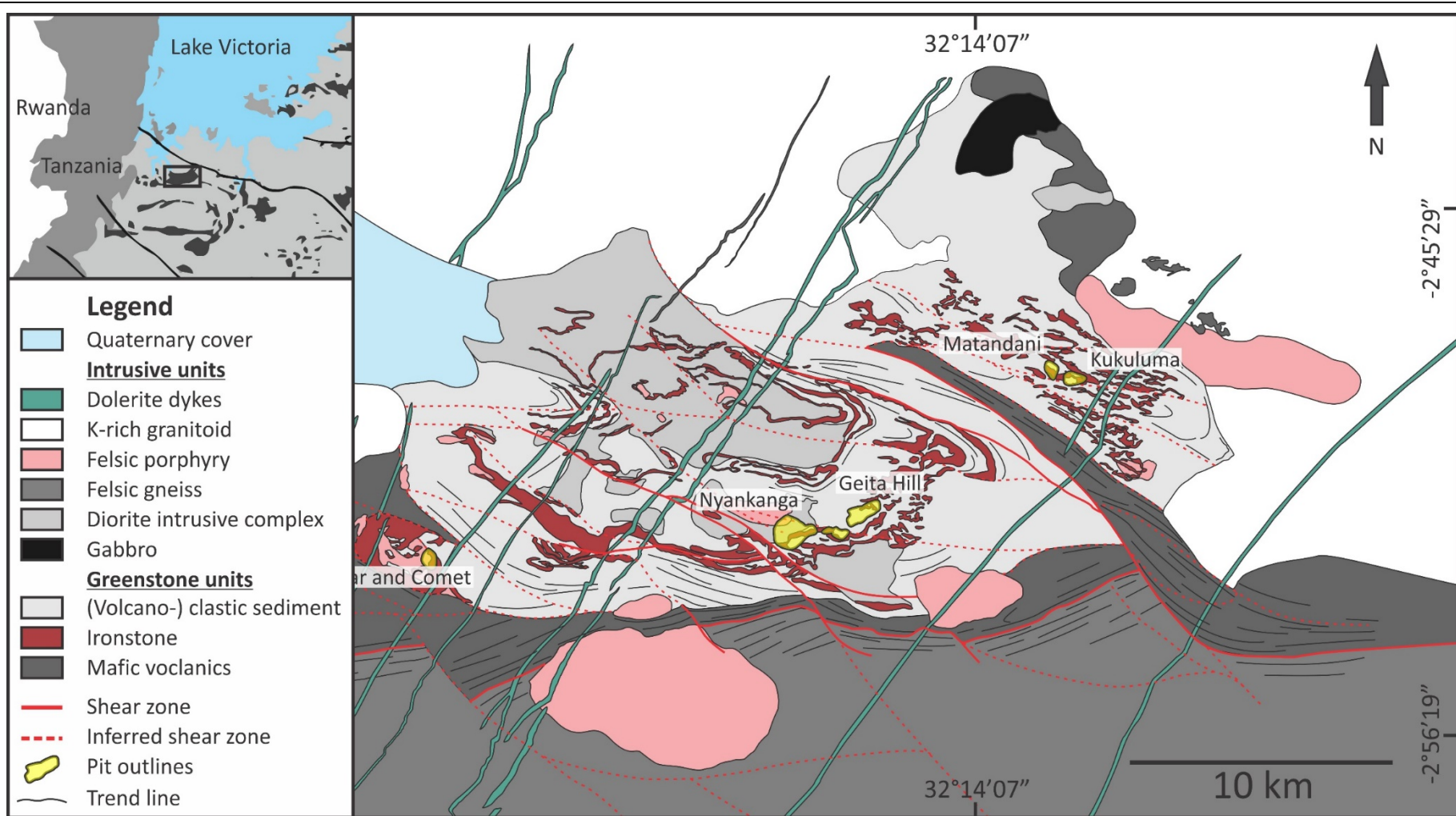


Figure 1.1. Geological map of the Geita Greenstone Belt showing the main geological units (modified after Sanislav et al., 2015). Inset shows the location of the Geita Greenstone Belt south of Lake Victoria.

Six roughly E-W trending, regional-scale greenstone provinces have been identified within the Nyanzian and Kavirondian supergroups (Borg and Shackleton, 1997). These are: the Sukumaland Greenstone Belt (SGB), Shinyanga–Malita Greenstone Belt, Musoma–Mara Greenstone Belt, Kilimafedha Greenstone Belt, Nzega Greenstone Belt and Iramba–Sekenke Greenstone Belt (Borg and Krogh, 1999; Sanislav et al., 2014b). The greenstone belts exhibit complex, multistage deformation histories, generally under greenschist facies conditions, except near to syn- to post-tectonic granite intrusions, where amphibolite facies metamorphism has been recorded.

The Geita Greenstone Belt (GGB, see Fig. 1.1) comprises an E-W trending, (50 × 25 km) greenstone sequence, and forms the northern part of the larger SGB (Borg et al., 1990; Borg and Krogh, 1999). The GGB is bounded to the north, east and west by undeformed high-K granites and to the south by TTG gneisses along a steeply dipping, E-W trending shear zone (Sanislav et al., 2014b).

The southern part of the GGB is dominated by ~2820 Ma mafic metavolcanic rocks, including pillow basalt and minor gabbro of the Kiziba Formation (Manya and Maboko, 2008; Cook et al., 2016). The remainder of the GGB consists of cherts and ironstones, intercalated and overlain by turbiditic sediments (mudstone, siltstone and sandstone with rare conglomerate), volcanoclastics, and intruded by diorite and granitoid dykes and sills (Sanislav et al., 2015). A diorite sill that intruded the ironstone sequence at the Geita Hill deposits has been dated at 2699±9 Ma (Borg and Krogh, 1999), while a diorite from the Nyankanga Intrusive Complex was dated to 2698±14 Ma (Chamberlain and Tosdal, 2007). These ages mark the end of sedimentation in the region.

1.2. Local Geology and Gold Mineralisation

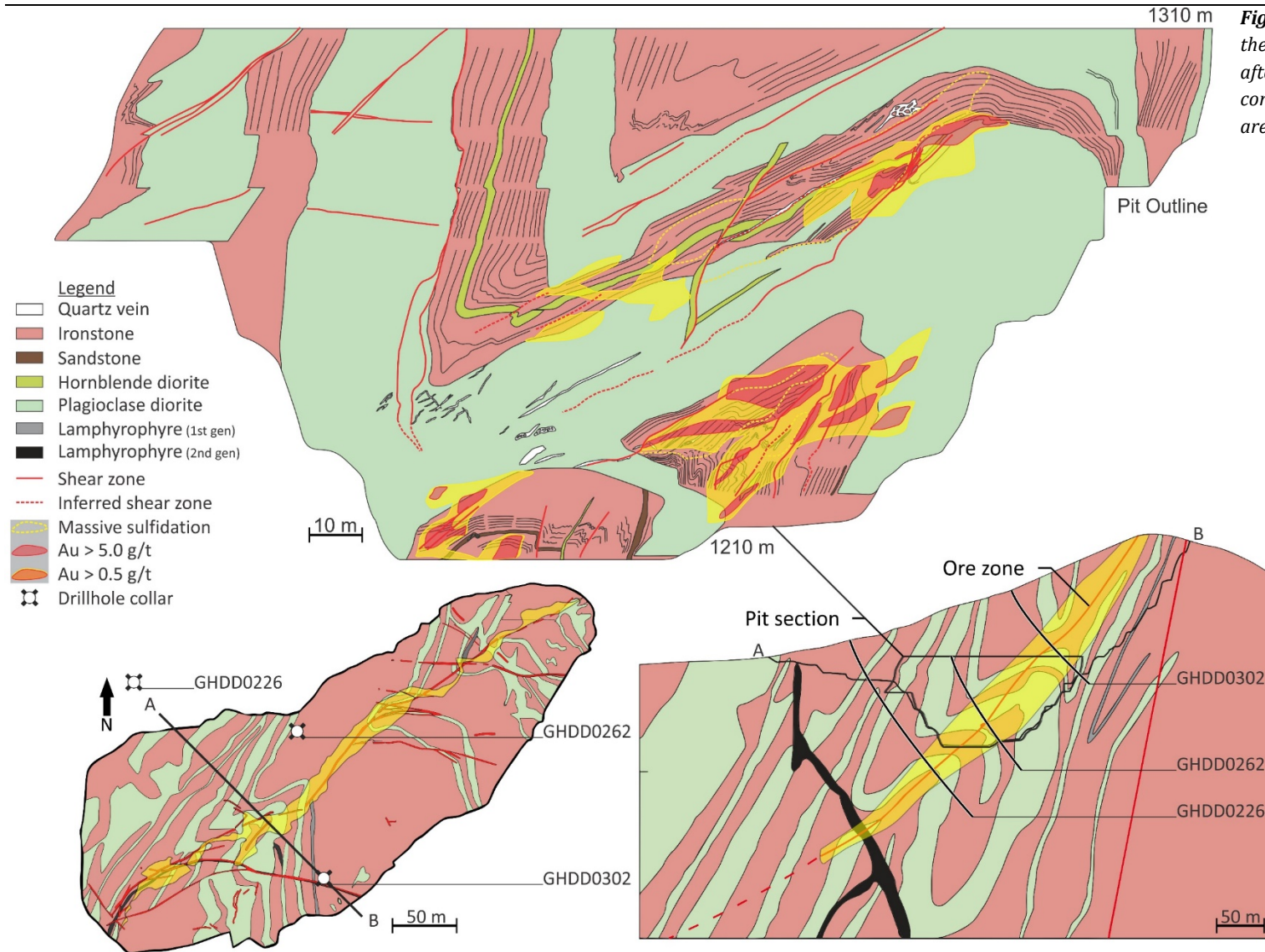
The Geita Hill gold deposit and the nearby Nyankanga and Lone Cone gold deposits, are hosted within a thick unit of ironstone and chert, locally intercalated with laminated shale, siltstone and sandstone beds, deposited around 2700 Ma (Borg and Krogh, 1999), interpreted as turbidites (Sanislav et al., 2017), deposited in a prograding submarine deltaic or fan environment. The turbidite beds broadly consist of immature, chlorite and plagioclase-rich, probably andesite-derived sediments (Borg, 1994). The sedimentary sequence was intruded by a series of diorite dykes and sills, felsic porphyries

and late-tectonic lamprophyres. They contain small amounts of intercalated conglomeratic beds with angular chert clasts.

The region was affected by at least five folding events and three brittle-ductile shearing events (Sanislav et al., 2015; 2017). In the Geita Hill and the Nyankanga area D_1 is preserved as compositional banding overprinting sedimentary bedding. The earliest folding event, D_2 , produced tight and isoclinal folds. The large-scale folding geometry in both deposits is controlled by the D_2 - D_3 fold interference patterns. The D_3 folds are dominant on outcrop-scale and plunge moderately to the NW. The D_3 axial surfaces were refolded along NW-plunging axis during D_4 and along sub-horizontal axis during D_5 . The D_6 deformation produced reverse-sinistral brittle-ductile shear zones, in which the Geita Hill deposit occurs more-or-less parallel to the D_3 axial planar surfaces of several 50m scale D_3 folds ((Sanislav et al., 2017).

These steeply dipping and NE trending D_6 shear zones have affected the entire greenstone belt, and show evidence of dextral and normal reactivation by D_7 and D_8 deformation. The D_7 reactivation structures in Geita Hill are steeply dipping, and bear similarities to the D_7 movement and deformation described in the Nyankanga gold deposit (Sanislav et al., 2014b). Normal (D_8) reactivation affects thrusts in the Geita Hill and Nyankanga deposits, with ~ E-W trending shear fractures recording meter-scale normal displacement (Sanislav et al., 2017).

The deformed sedimentary pile at Geita Hill has been intruded multiple times by variably deformed diorite dykes and sills, which merge southwest into the Nyankanga Intrusive Complex (Fig. 1.1; Sanislav et al., 2015). Diorite dykes and sills originating from the Nyankanga Intrusive Complex have been dated in the Nyankanga pit at 2698 ± 14 Ma (Chamberlain and Tosdal, 2007), and in the Geita Hill at 2699 ± 9 Ma (Borg and Krogh, 1999) suggesting that the Nyankanga Intrusive Complex intruded soon after the sedimentation ceased. The diorite dikes and sills are folded by and intrude into the D_2 and D_3 structures suggesting that the Nyankanga Intrusive Complex was active at least since late D_2 . Two generations of lamprophyre dykes that intrude the Geita Hill deposit have been recognised. The first generation intruded pre- D_3 folding, it is metamorphosed, foliated, and highly altered. The second generation is relatively unaltered, shows localised brittle-ductile shearing and has intruded the D_6 - D_7 structures (Sanislav et al., 2017), but were overprinted by D_8 normal faults



and mineralisation. Borg and Krogh (Borg and Krogh, 1999) dated these second generation lamprophyres at 2644 ± 3 Ma.

The gold mineralisation at Geita Hill is trending NE, dips moderately NW and is spatially associated with the D₆ Geita Hill Shear Zone (GHSZ) and D₃ fold hinge zones (Fig. 1.2). However, the mineralisation appears to overprint the D₆ GHSZ and the D₆₋₇ late-tectonic lamprophyres, suggesting that the mineralising event is of D₇ or D₈ in origin (Sanislav et al., 2015; 2017). Based on the occurrence of actinolite and biotite with auriferous pyrite, a temperature range of 350 – 480 °C has been assumed for the mineralising fluids (Borg, 1994).

Chapter 2

Alteration paragenesis and the timing of mineralised quartz
veins at the world-class Geita Hill gold deposit, Geita
Greenstone Belt, Tanzania

Published in Ore Geology Reviews (van Ryt et al., 2017)

Abstract

The world-class Geita Hill deposit is one of the largest gold deposits located within the Geita Greenstone Belt in north-western Tanzania. The deposit is hosted within a greenschist facies metamorphosed and complexly deformed sedimentary package dominated by ironstone and intruded by diorite dykes. The gold mineralisation is spatially associated with the Geita Hill Shear Zone which, is a NE-trending, moderately dipping W deformation zone of discontinuous shear fractures. The regional metamorphism is characterised by $Bt + Chl + Act + Kfs + Mt \pm Po \pm Py$ indicating upper greenschist facies metamorphism. The gold-related alteration overprints the regional metamorphism and is characterised by silicification and sulfidation fronts that end within one meter of the mineralised zone. Locally, the silicification and sulfidation of the wall rock occurs along a series of mineralised quartz veins with sub-vertical dip and trending ~E-W. Paleostress analysis of the mineralised shear fractures of the Geita Hill Shear Zone gives vertical σ_1 and northerly σ_3 consistent with the orientation of the mineralised quartz veins and indicating N-S extension. The composition of the mineralised quartz veins is characterised by $Qtz+Bt+Kfs+Py$ which, also overprints the metamorphic background. Gold is closely associated with secondary pyrite and occurs as free gold and gold tellurides (sylvanite, calaverite and nagyagite). It occurs mainly as inclusions in pyrite and as invisible gold in pyrite but gold inclusions in biotite and along quartz grain boundaries are also present. The gold-bearing pyrite is associated with secondary biotite and K-feldspar. Two distinct textural styles of auriferous pyrite can be distinguished: inclusion rich subhedral pyrite and inclusion free euhedral pyrite. It is common for the inclusion rich pyrite to have thick rims of inclusion free pyrite. The mineralising alteration is overprinted by barren, multi-phase quartz-carbonate, and carbonate-chlorite veins. This alteration is characterised by the assemblage $Ca + Sd + Chl \pm Qtz \pm Py \pm Ba$.

2.1. Introduction

Archean gold deposits are commonly referred to in the literature as lode-gold deposits, because of the common presence of gold-bearing, quartz-carbonate veins (e.g., Robert and Brown, 1986b; Robert and Brown, 1986a; Groves et al., 1998; Goldfarb et al., 2005) with many good examples in the Kalgoorlie Terrane in the Yilgarn Craton of Australia (e.g., Groves et al., 1995; Cassidy et al., 1998; Witt and Vanderhor, 1998) or the Abitibi gold deposits from the Superior Province in Canada (e.g., Kitney et al., 2011). However, there are many Archean gold deposits where gold mineralisation is not directly hosted by veins, e.g. BIF hosted gold deposits (e.g., Vielreicher et al., 1994; Geusebroek and Duke, 2004; Ribeiro-Rodrigues et al., 2007; Steadman et al., 2014; Sanislav et al., 2015; 2017) in which sulfidation of the chemically reactive wall rock resulted in the replacement of magnetite by disseminated gold-bearing sulfides. In the case of vein hosted gold deposits, a link can be made between the timing of the veins, the deposition of the gold mineralisation and the regional deformation (e.g., Robert and Brown, 1986a; Ridley and Mengler, 2000; Morey et al., 2007; Weinberg and Van Der Borgh, 2008). In general, it is accepted that the mineralised veins formed as extensional veins late during regional deformation (e.g., Dirks et al., 2013). The gold may be hosted by extensional veins that crosscut major structures (Ridley and Mengler, 2000) or, as is often the case, by veins that are hosted within and/or directly related to the structures (e.g., Weinberg et al., 2004; Doublier et al., 2014; Vielreicher et al., 2015).

However, some authors argue that the gold mineralisation is introduced into the system throughout the entire tectonic history of a region (e.g., Bateman et al., 2001; Davis and Maidens, 2003) and in the case of sediment (BIF, black shales) hosted deposits recent research suggests that the gold may be syngenetic and just locally redistributed and enriched through multiple events to form a deposit (e.g., Large et al., 2009; 2011; Thomas et al., 2011; Steadman et al., 2014). For replacement type deposits the timing of gold deposition becomes even less clear since early to late structures can be affected to various degrees by the hydrothermal alteration, i.e. a multistage gold deposition process cannot be excluded (e.g., Michel et al., 1994; Sung et al., 2009; Meffre et al., 2015). For example, the gold mineralisation at the Geita Hill deposit was initially considered syngenetic due to its close spatial relationship with the ironstones but, later studies (Borg, 1994) demonstrated the epigenetic origin of the gold mineralisation. More recent studies (Sanislav et al., 2017) used

structural evidence to suggest that the gold mineralisation is very late and postdates the main period of deformation and metamorphism. However, a direct link between the gold related alteration and the structural framework is missing at the Geita Hill deposit.

Geita Greenstone Belt is a relatively small greenstone belt in the northern Tanzania craton, which contains at least 15 ironstone-hosted gold deposits over a strike length of 40 km (Sanislav et al., 2014a), making this a giant gold mineralised system. In the early 1990's it was suggested that the Geita gold deposits are not syngenetic, but that they are structurally controlled and formed late during regional deformation (Borg et al., 1990; Borg, 1994). More recent studies investigated in detail the geological and structural controls on two of the largest deposits, the Nyankanga (Sanislav et al., 2015) and the Geita Hill (Sanislav et al., 2017) gold deposits. These studies presented structural evidence indicating that the deposits have experienced a prolonged deformation history including ductile (D₁ to D₅) deformation followed by a series of brittle (D₆ to D₈) deformation events. The gold mineralisation is of replacement type and overprints the wall rock damage zone associated with the D₆, moderately, W to N dipping and multiply reactivated brittle-ductile shear structures, and the D₇, steep and mainly NW trending strike-slip structures. This implies that while the damage zones hosting the gold were formed as a result of D₂ to D₆ events, mineralising fluids were introduced during a later D₈, N-S extensional event. In the early 20th century underground mining at Geita Hill focused on mineralised shear zones (the Geita shear) as well as associated quartz veins and breccia zones. This, in combination with bulk open pit mining over the last thirteen years resulted in very few mineralised quartz veins to be preserved. In this contribution I present detailed microstructural and mineralogical data from mineralised host rock and rare mineralised quartz veins found in the Geita Hill deposit and I discuss their significance for the timing and processes that lead to gold deposition.

2.2. Methodology

2.2.1. Sampling Strategy

Representative samples were collected from the floor and walls and from drill cores in the Geita Hill west deposit (Fig. 1.1). Three drill holes representing a sectional view of the Geita Hill deposit (Fig.

2.1), were logged in detail and sampled for petrography and alteration analysis. The relationship between quartz veins and gold mineralisation was investigated through systematic recording of vein orientations, mineralogy, gold content (where possible) and relationships with the structures.

2.2.2. *Microscopy and electron probe micro analysis*

Covered and polished thin sections (n = 34) representing the various protolith and alteration styles found at the Geita Hill deposit were examined in detail using transmitted and reflective microscopy. The thin sections of all mineralised lithologies were mapped on the microscopic scale to provide insight into the overprinting relationships between alteration assemblages. Several relevant thin section descriptions, photomicrographs and schematic alteration maps are included in Appendix 4. A Jeol JXA8200 “Superprobe” housed at the Advanced Analytical Centre at James Cook University was used to supplement mineral identification through semi-quantitative energy dispersive spectroscopy (EDS) and to locate sub-microscopic gold grains.

2.3. Regional metamorphism, alteration and mineral paragenesis

Gold mineralisation at the Geita Hill gold deposit is distributed along a NE – SW trending ore envelope (≥ 0.5 g/t) and dips approximately $40\text{--}45^\circ$ NW (Sanislav et al., 2017). Although the ore envelope (Fig. 1.2) shows a homogenous distribution for the mineralisation, the higher-grade gold values are highly variable, and influenced by the proximity of shear zones, fractures and diorite-ironstone contacts (Fig. 2.1). That is, the gold values are high (≥ 1 g/t) near shear and fracture zones, and sheared ironstone-diorite contacts and drop to background values (≤ 0.05 g/t) when moving away from these structures within a meter or less (Fig. 2.1). The alteration associated with the gold mineralisation shows a similar behaviour and heavily altered rock passes into largely non-altered rock within a meter or less (Fig. 2.1). The mineral assemblages preserved within the rocks that host the Geita Hill deposit can be subdivided into three types: 1. the regional metamorphic assemblage which formed during $D_2\text{--}D_3$ events and acts as the background assemblage which later, more localised alteration of lower metamorphic grade overprints; 2. minerals associated with gold mineralisation which is interpreted to have occurred during D_8 (Sanislav et al., 2015; 2017); and 3. post-mineralisation alteration (Table. 2.1/Fig. 2.2).

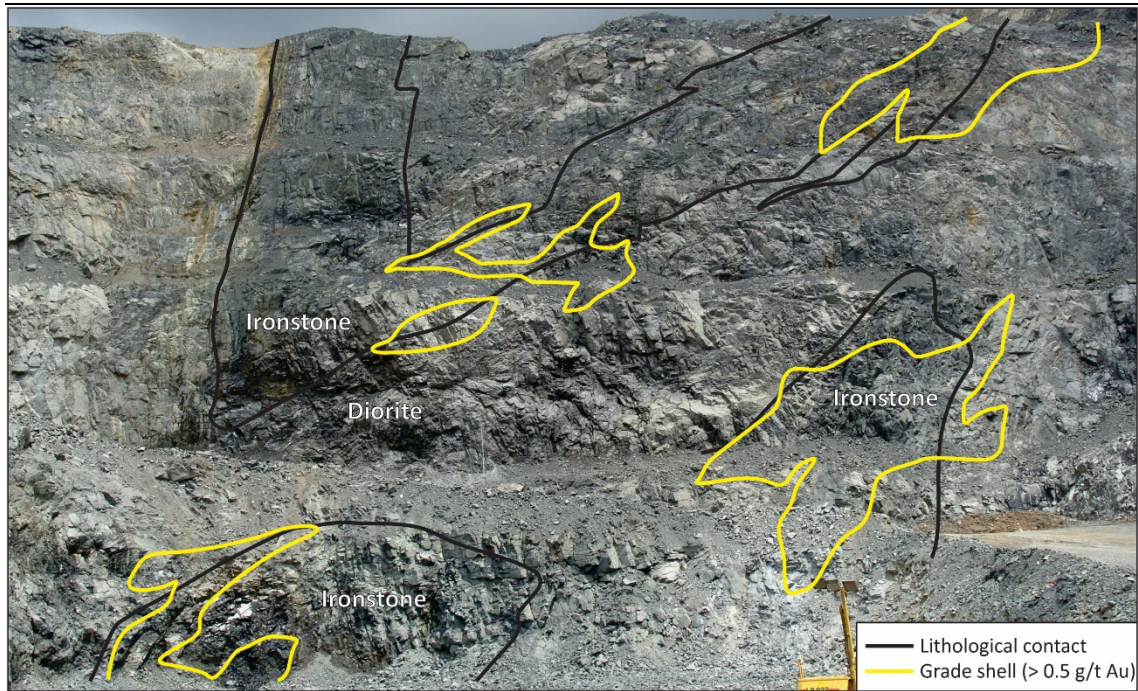


Figure 2.1. Photograph, looking NE, showing an exposed section from the middle of the Geita Hill pit. The (darker) folded ironstone layer was intruded by syn-D3 diorite (Sanislav et al., 2017). The mineralisation envelope shown in Fig. 1.2 appears to follow the D3 folds and the D6 GHSZ. However, as seen in this example the mineralisation is not continuous and occurs as localised sulfidation fronts where steeply-dipping and ~ E-W trending quartz veins and/or fracture zones intersect the folded ironstone and diorite. The width of the picture is ~ 150 m.

Table 2.1

Schematic representation of different textural types of pyrite found in the Geita Hill deposit

Lithology	Textural Type	Description	Schematic sketch
<i>Pre-mineralisation</i>			
Ironstone	Pyrite-1a	Very fine anhedral grains hosted as randomly oriented inclusions within magnetite, and disseminated within magnetite-rich units	
Diorite	Pyrite-1b	Fine subhedral grains disseminated throughout metamorphosed diorite, preferentially hosted within retrograded mafic phenocrysts	
<i>Syn-mineralisation</i>			
Ironstone	Pyrite-2a	Fine to intermediate subhedral grains abundant oxide inclusions, minor silicate and sulfide inclusions generally without preferential orientation, hosts gold as either solid solution or ultra-fine inclusions	
Ironstone and diorite	Pyrite-2b	Fine to intermediate euhedral grains occurring independently or as pyrite-2a overgrowth, characterised by absence of oxide, silicate and sulfide inclusions and by presence of gold and gold telluride inclusions	
<i>Post-mineralisation</i>			
Ironstone and diorite	Pyrite-3a	Very fine hosted within late-stage carbonate chlorite veining, overprints mineralised pyrite-2a and pyrite-2b.	
Ironstone and diorite	Pyrite-3b	Coarse euhedral grains associated with late-stage quartz-carbonate veining, overprints pyrite-2a and pyrite-2b, no direct relationship observed with pyrite-3a.	

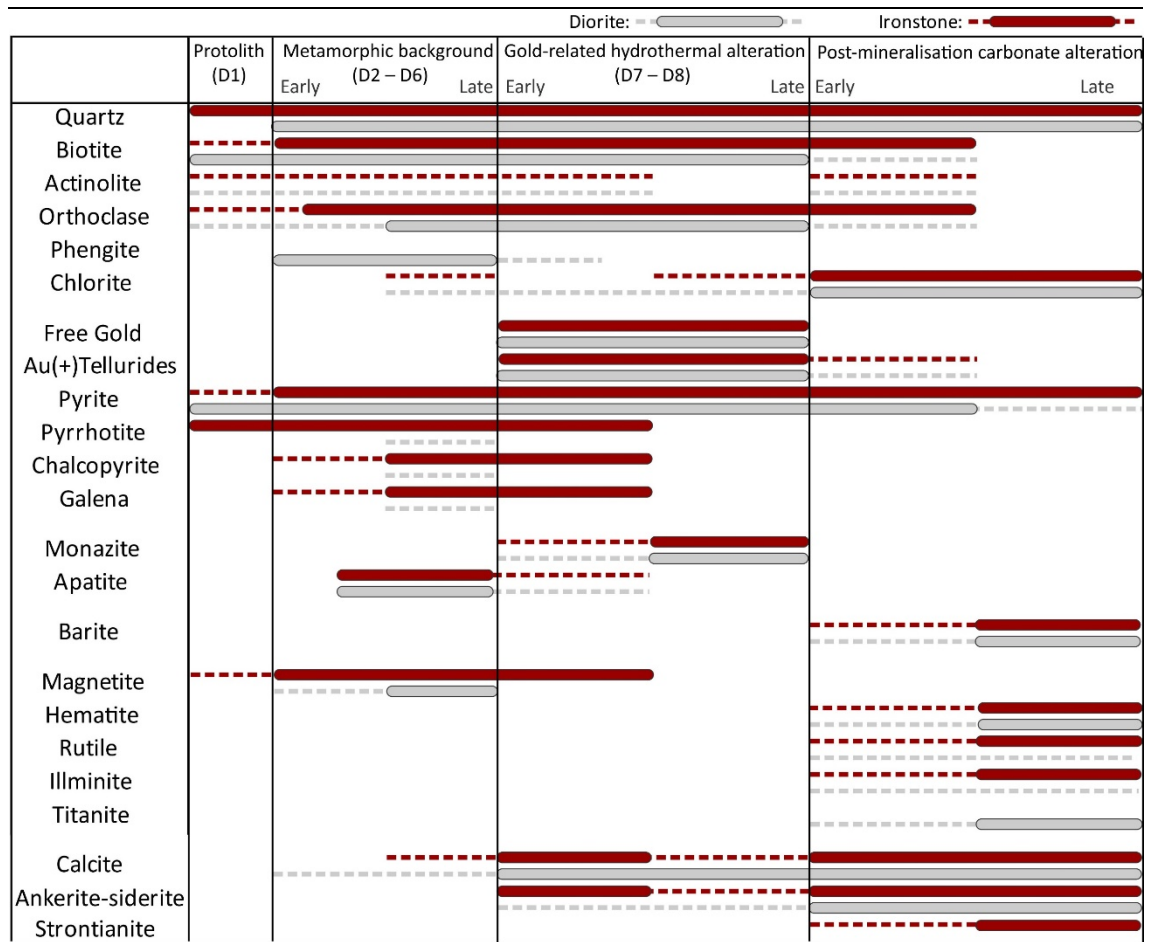


Figure 2.2. Schematic alteration paragenesis of the Geita Hill deposit

2.3.1. The regional metamorphic assemblage

Banded ironstones, pelitic to psammitic sediment and the diorite dykes and sills form the principal host lithologies to the Geita Hill deposit, and have been metamorphosed to upper-greenschist facies during D₂ and D₃ folding and shearing events. The mineral paragenesis associated with regional metamorphism includes biotite + chlorite + K-feldspar + actinolite ± magnetite ± pyrrhotite ± pyrite-1a (Table. 2.1). The ironstone units are characterized by intercalations of chert layers and magnetite-rich shale layers that are locally overprinted by pyrrhotite which formed during D₁. Fine-grained biotite and K-feldspar is well developed within the magnetite-rich shale layers (Fig. 2.3a, b). Along the contact between these magnetite-rich bands and the chert layers, fine-grained, fibrous actinolite is present (Fig. 2.3c). The magnetite-rich layers contain disseminated, micron-scale, anhedral grains of pyrite and rarer galena, which probably formed during pre- to syn- D₁ events. Larger magnetite grains may contain inclusions of pyrite and galena (Fig. 2.3b) up to 20 µm across. Pyrrhotite is

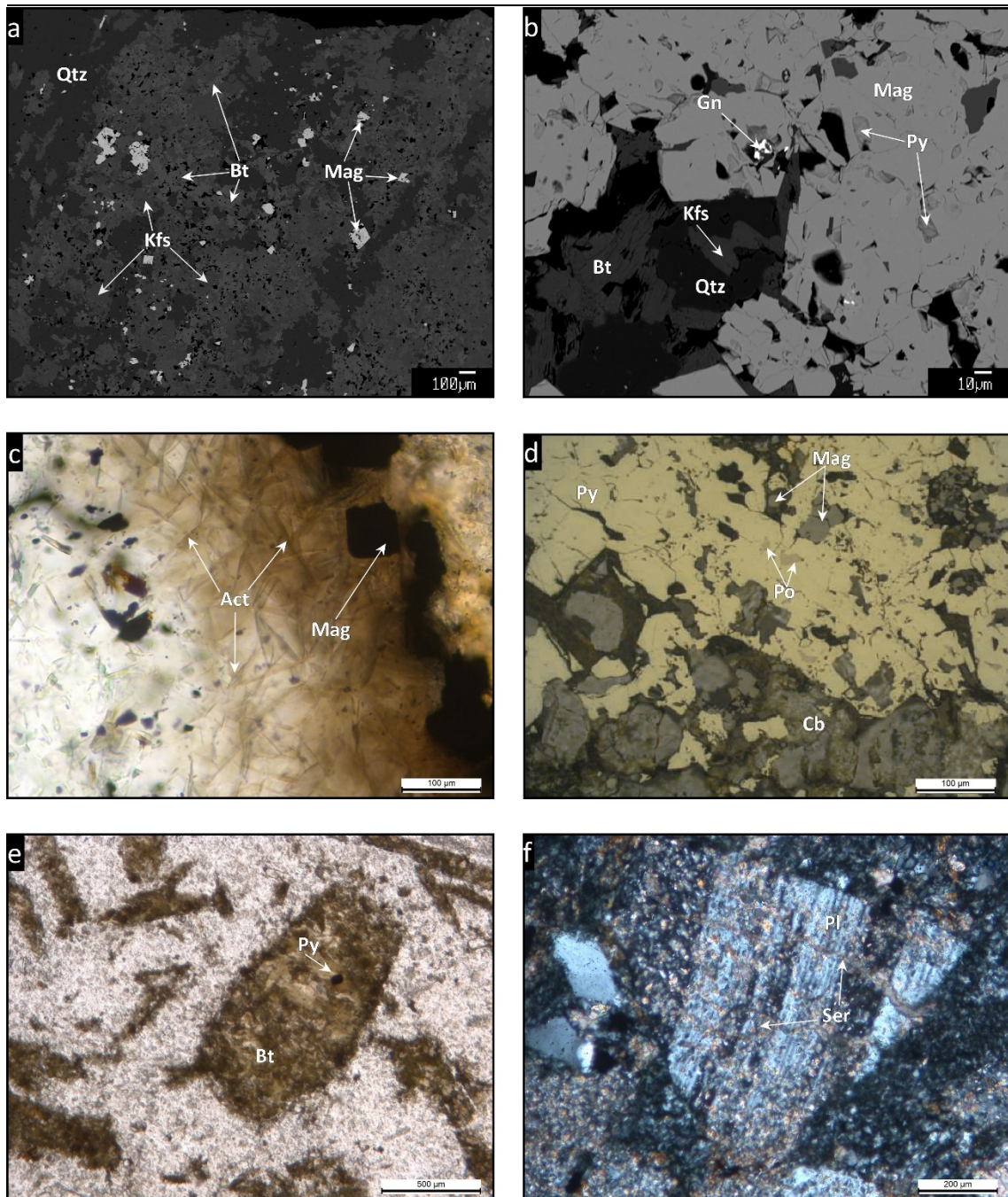


Figure 2.3. Photomicrographs showing examples of the pre-mineralisation, metamorphic assemblages at the Geita Hill. (a) backscatter electron (BSE) image showing the biotite+K-feldspar+magnetite association typical in the shale-rich ironstone units; (b) BSE image showing the same mineral assemblage in the magnetite-rich ironstones. Note that the magnetite grains contain inclusions of pyrite and galena of possible sedimentary origin; (c) transmitted plane-polarised light image of fibrous actinolite growth at the contact between magnetite and chert laminae; (d) reflected light image showing syn-mineralisation pyrite overgrowing pyrrhotite and magnetite. The pyrrhotite pre-dates the syn-mineralisation pyrite and is interpreted to be syn-metamorphic. The carbonate grains in the image are post-mineralisation overprint; (e) transmitted plane-polarised light image of a biotite-altered hornblende phenocrysts within diorite. Altered phenocrysts can also contain pyrite and minor calcite, larger grains frequently show an Fe-oxide rim; (f) transmitted cross-polarised image of sericite altered plagioclase feldspar within diorite.

relatively common and spatially related to cm- to dm- scale, syn-sedimentary extensional fracture systems which are well visible in drill core, and were probably related to syn-sedimentary sulfidation events either preceding or contemporaneous with D1 events. Pyrrhotite commonly forms alteration fronts replacing magnetite, and to a lesser extent as fracture-infill within early quartz veins. It is also present as inclusions in syn-mineralisation pyrite (Fig. 2.3d) but only where the pyrite is replacing magnetite layers.

In diorite, hornblende and clinopyroxene phenocrysts are partly replaced by biotite (Fig. 2.3e) and the plagioclase is partly sericitized (Fig. 2.3f). Disseminated pyrite grains (pyrite-1b) are common throughout varieties of diorite. This pyrite is fine-grained and subhedral, with a close spatial relationship to biotite-altered mafic phenocrysts.

The sediments and the diorite contain early quartz veins that are folded with the sedimentary layers and in the diorite are crosscut by later, mineralised quartz veins.

2.3.2. *Gold-related alteration*

Gold-related alteration in the Geita Hill deposit manifests itself in three distinct textural styles: 1. sulfide alteration fronts; 2. gold-bearing quartz veins; and 3. gold-bearing micro-fractures. Sulfide alteration fronts refer to zones of intense sulfidation that typically occur along diorite-ironstone contacts (Fig. 2.4a), along contacts between chert layers and magnetite-rich layers (Fig. 2.4b) and where quartz veins intersect magnetite-rich layers (Figs. 2.4c and d). Macroscopically they appear as silicified zones, rich in disseminated, coarse- to fine-grained pyrite. All types of sulfide alteration fronts are associated with secondary hydrothermal biotite and K-feldspar alteration.

Gold-bearing quartz veins and veinlets in the Geita Hill deposit along the Geita shear zone were the focus of past underground mining (Carter, 1959). Currently, gold-bearing quartz veins are rare and most mineralisation is associated with sulfide alteration fronts. However, where present, the quartz veins provide important insights into the mineralising process. The veins contain minor amounts of pyrite, but at the contact between quartz veins and the ironstone or diorite, zones of intense sulfidation can be present (Fig. 2.4e). Around larger quartz veins a zone of intense microfracturing has usually developed. Where a quartz vein crosscuts the ironstone layering, sulphide-rich zones develop parallel to layering (preferentially in the magnetite-rich layers) and in

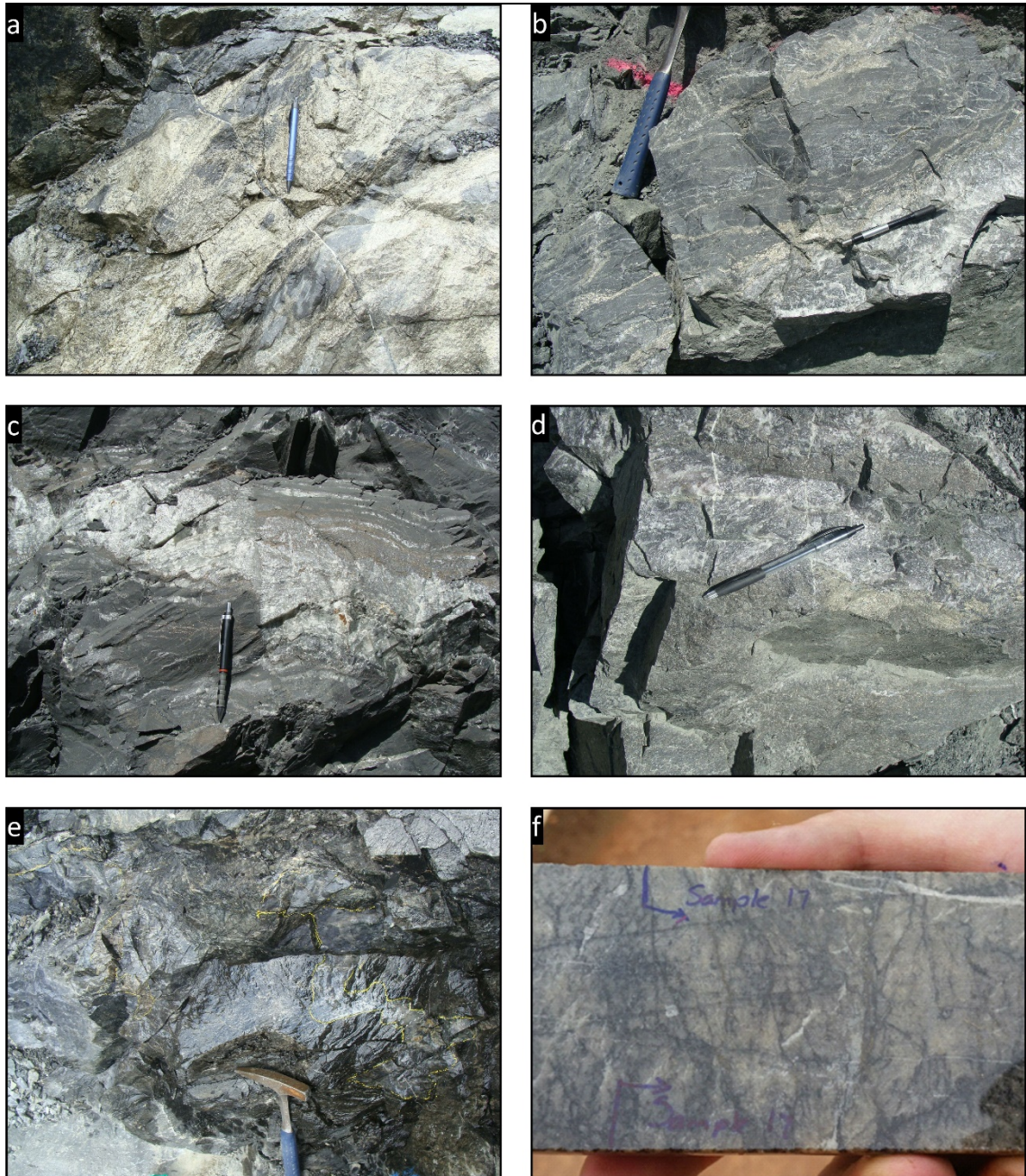


Figure 2.4. Photographs showing the typical macroscopic aspect of syn-mineralisation alteration at the Geita Hill deposit. (a) Example of silicification and massive sulfidation front of coarse grained pyrite developed at the contact between ironstone and diorite; (b) Example of pyrite microveins and sulfidation front formed around a feeder quartz-vein; (c) Feeder quartz-vein crosscutting the ironstones. From the quartz vein a network of pyrite rich veinlets irradiate into the ironstone and pyrite growth also occurs along the contact between the magnetite and chert bands. Half a meter away from the quartz vein the pyrite disappeared almost completely. (d) Example of mineralised quartz vein in the diorite. Note the sulfidation near the vein-diorite contact, while away from the quartz vein the pyrite is disseminated and soon is not visible anymore. (e) Example of a quartz vein in the diorite with a silicification halo developed around it. The silicified is rich in disseminated pyrite grains. (f) photograph of a high-grade core sample of diorite. The igneous texture was completely destroyed by silicification. A network of biotite-rich veinlets overprints the silicification and contains numerous small pyrite grains.

three quartz veins vein (Fig. 2.4d). In diorite, the alteration halo around quartz veins includes silicification of the host rock and an increase in the amount of disseminated pyrite grains (Fig. 2.4f). In general, the quartz veins crosscutting the ironstones returned between 3 and 4 g/t gold, while the nearby sulfidised ironstone returned gold values > 15 g/t). The mineralogy of the mineralised quartz veins is relatively simple and consists mainly of quartz with minor pyrite, biotite and K-feldspar.

Gold-bearing micro-fractures appear as along zones of intense microfracturing generally overprinting previously silicified ironstone or diorite (Figs. 2.4f and 2.5a). The disseminated gold-bearing pyrite in ironstone and diorite is related to the development of this microfracturing. This is evidenced by the alignment of pyrite grains along networks of micro-fractures visible on μm to mm scale. Alteration minerals that have been deposited along these micro-fracture networks include pyrite and/or biotite with minor quartz and K-feldspar. Minor amounts of gold-bearing, sphalerite-chalcopyrite-galena micro-veins are also present in the silicified zones (Fig. 2.5b).

Gold occurs as free gold, gold tellurides and invisible gold in pyrite. Both the free gold and the gold tellurides can be found as inclusions in pyrite and biotite (minor), or along grain boundaries between pyrite, biotite and quartz (Figs. 2.5c and d). The free gold contains appreciable silver. Gold-bearing tellurides include sylvanite $[(\text{Au},\text{Ag})_2\text{Te}_4]$, calaverite $[\text{AuTe}_2]$ and nagyagite $[\text{Pb}_3(\text{Pb},\text{Sb})_2\text{S}_6(\text{Au},\text{Te})_2]$. Associated with the gold tellurides occurs the silver telluride hessite $[\text{Ag}_2\text{Te}]$ and lead telluride altaite $[\text{PbTe}]$.

Two textural styles of gold-bearing pyrite are present in the Geita Hill deposit (Fig. 2.5f). These are inclusion-rich, euhedral to anhedral pyrite grains (pyrite-2a) and largely inclusion free, mostly euhedral pyrite grains (pyrite-2b). The inclusions in pyrite-2a (Table. 1) are comprised mostly of magnetite, quartz, chalcopyrite, galena, sphalerite, pyrrhotite and K-feldspar (in order of abundance). These mineral inclusions are absent in pyrite-2b (Table. 1). The inclusion-rich pyrite-2a commonly contains a rim of inclusion-free pyrite-2b, suggesting that the former predates the latter. However, it is unclear at the moment if this zonation is due to the gradual evolution of mineralising fluids or resulted from two separate mineralising events involving two different fluids percolating at different times.

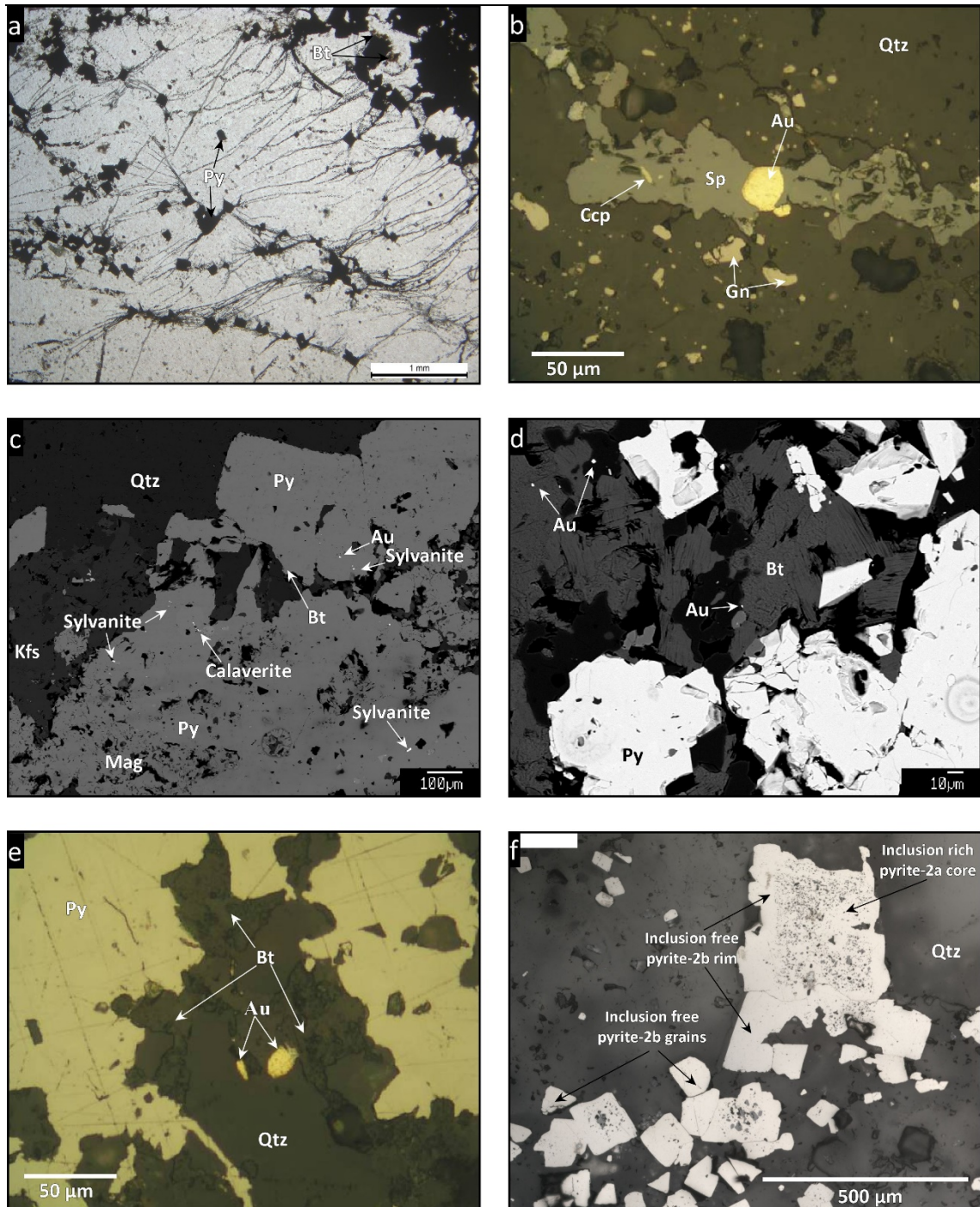


Figure 2.5. Photomicrographs showing the syn-mineralisation alteration at the Geita Hill deposit; (a) transmitted plane-polarised light image showing the development of a network of pyrite-rich micro-fracture in the chert layers. These micro-fracture also contain minor amounts of biotite and K-feldspar. (b) BSE image showing pyrite sulfide front replacing magnetite along the contact between magnetite and chert bands. The majority of the bright specs seen in the pyrite grains are Au-bearing tellurides or free Au. (c) BSE image showing pyrite-biotite alteration and native gold (bright specs) in biotite and along quartz micro-fractures. (d) reflected light image showing two large gold grains along the contact between quartz and biotite; (e) reflected light image showing large gold grain associated with a sphalerite micro-vein in a larger quartz vein. Note the association of sphalerite with chalcopyrite and galena; (f) reflected light image showing the textural relationships between the two types of auriferous pyrite – the inclusion rich pyrite-2a and the inclusion free pyrite-2b. Note that the inclusion free pyrite-2b occurs as rims to pyrite-2a or as individual crystals.

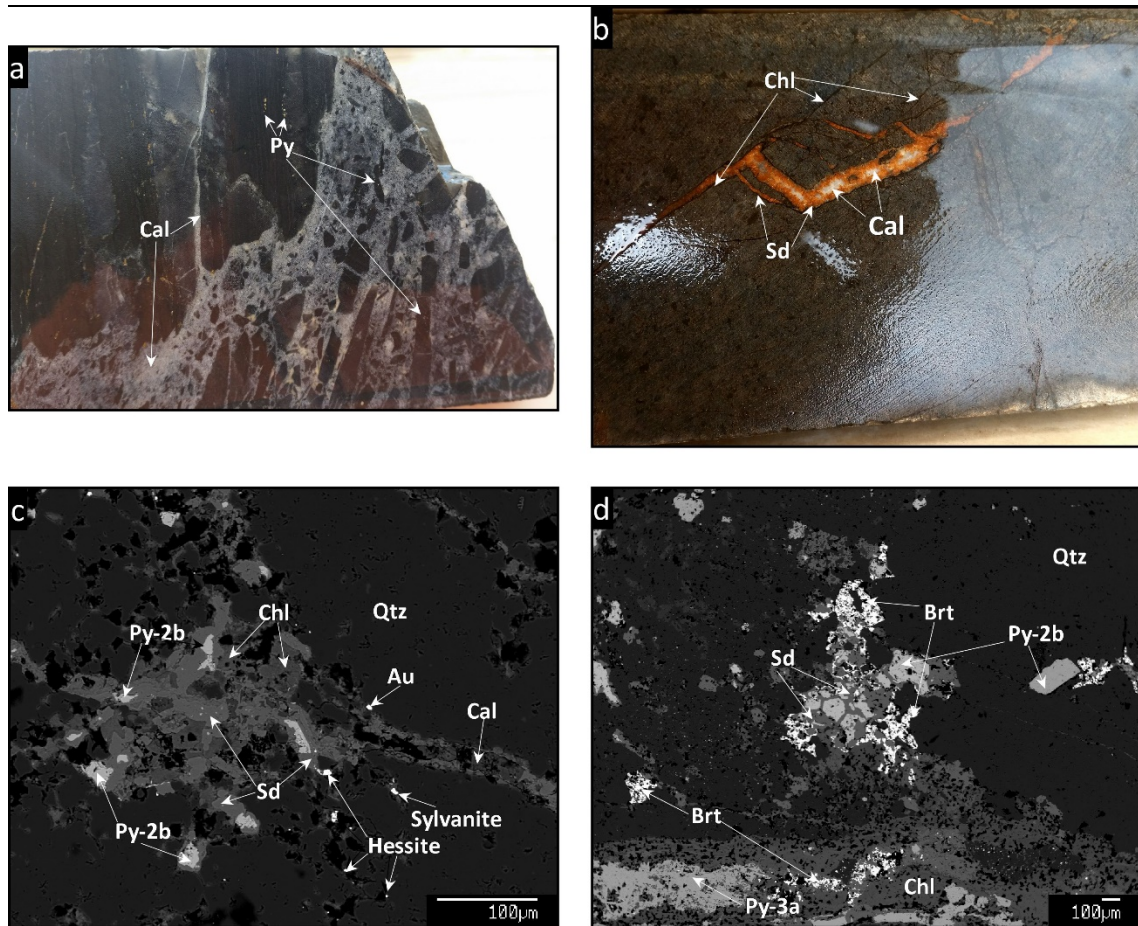


Figure 2.6. Photographs showing the post-mineralisation alteration assemblages present at Geita Hill; (a) brecciated mineralised-ironstone with carbonate (calcite) infill. Note the coarse euhedral pyrite along the magnetite-chert contact. The broken ironstone clasts contain same type of pyrite while the carbonate infill contains no pyrite indicating that the pyrite predates the brecciation. (b) Late-stage carbonate vein in diorite. The margin of the vein is siderite while the centre of the veins is calcite. Note the chlorite associated with the carbonates. (c) BSE image showing carbonate overprinting of mineralised potassic alteration. The pyrite grains are partly replaced by siderite and the biotite grains are altered to chlorite. Away from the pyrite-biotite association the carbonate is calcite. (d) BSE image showing a late carbonate vein cutting across an earlier quartz vein. Near the carbonate vein, earlier pyrite has been partly replaced by siderite. Along the carbonate vein a new generation of fine-grained pyrite is deposited. Note the abundance of barite and chlorite associated with the carbonate alteration.

2.3.3. Post-mineralisation alteration

Zones with gold mineralisation are commonly overprinted by barren quartz-carbonate and carbonate-chlorite veins and veinlets (Fig. 2.6). This is a multistage event and the characteristic mineral association is calcite + siderite + chlorite \pm pyrite (pyrite-3a or pyrite-3b) \pm quartz \pm barite. Carbonate alteration manifests itself as veins, breccia infill and disseminated carbonates (Fig. 2.6a). Calcite and siderite are the main carbonate phases, but trace amounts of strontianite were observed in some samples. Textural relationships suggest that the CO₂-bearing fluid precipitated siderite first, followed by calcite (Fig. 2.6b). The carbonate rich-fluid reacted with the iron-rich minerals to form

siderite while the remaining carbonated precipitated mainly as calcite. This is well illustrated where carbonate veins crosscut earlier pyrite-biotite-bearing micro-fractures and the CO₂ reacts with the pyrite and biotite to form siderite and chlorite (Fig. 2.6c). Barite is present as an accessory mineral within carbonate veins and veinlets, but is generally lacking in carbonate overprint of mineralised alteration assemblages. Associated with this post-mineralisation alteration are two types of barren pyrite; the first type (pyrite-3a; Table. 1) comprises fine, sub-micron-scale grains, and is associated with carbonate and chlorite veins (Fig. 2.6d), the second type (pyrite-3b; Table. 1) is relatively coarse, with mm- to cm-scale grains which are generally subhedral and is associated with late quartz-carbonate veins.

2.4. Vein Orientation

The relationship between veins and gold mineralisation was investigated by systematically recording the orientation, mineralogy and gold content (where possible) for veins exposed in the pit and in drill cores. Three main types of veins occur in Geita Hill pit: quartz-rich veins, sulfide-rich veins and quartz-carbonate veins. The quartz-rich veins can be translucent and grey in colour or milky white (Fig. 2.4c). The translucent-grey quartz veins commonly contain small amounts of euhedral to subhedral, medium to coarse grained and disseminated sulfides with minor amounts of biotite and K-feldspar. It is common for these veins to be surrounded by a sulfide-rich alteration halo (Fig. 2.4). In most situation these alteration halo returns high gold grades, and have been the focus of past mining operations (Horne, 1959). Because in general the gold grade of these quartz veins is much lower than the surrounding alteration halo they were considered barren in the past, or to post-date the mineralisation (Carter, 1959; Horne, 1959). I observed a few translucent-grey quartz veins, 10-30 cm wide and up to 30 m long but in general they are much smaller. However, old underground mining reports describe similar types of quartz veins, as meters wide and tens of meters long (Carter, 1959; Horne, 1959). The milky-white quartz veins are relatively rare and no significant alteration accompanies them. The sulfide-rich veins (Fig. 2.4) can be pyrrhotite-rich (rare) or pyrite-rich, centimetre wide and up to a meter long. The pyrrhotite veins are restricted to the ironstone layers and are overprinted by all the other vein types. The pyrite-rich veins or stringers are spatially related

to the translucent-grey quartz veins and commonly irradiate away from the quartz veins (Fig. 2.4). The quartz-carbonate veins vary in composition between carbonate-rich (with only minor amounts of quartz) and quartz-rich (with only minor amounts of carbonate). They usually contain various amounts of pyrite, in general fine-grained and anhedral. The gold-bearing quartz-veins (Fig. 2.7a) are consistently steeply-dipping and trending ~ E-W. The quartz veins that have a mineralogical composition similar to the gold-related alteration (quartz + pyrite + biotite ± K-feldspar) have a similar, E-W trend, but their dip is moderate to steep (Fig. 2.7b). In contrast, all the other quartz-bearing veins (including carbonate-bearing veins) are either steeply dipping and NE-SW trending or shallowly dipping and E-W trending (Fig. 2.7c).

Two styles of mineralised quartz veins were observed in the drill cores. The first style consists of small, translucent and en-echelon quartz veins (Fig. 2.8a) surrounded by a silicified alteration halo. These veins occur together with a network of conjugate, pyrite-filled, fractures/microveins, also surrounded by small alteration halos. In the less altered wall rock the pyrite appears disseminated. These en-echelon veins dip moderately south, but their envelope dips steeply north (Fig. 2.8b). The second style of mineralised quartz veins consists of translucent veins that are up to several cm wide, with alteration that is similar to the alteration style of similar veins observed in the pit (Fig. 2.4). They are consistently dipping steeply north (Fig. 2.8c).

2.5. Paleo-stress inversion from fault-slip data (kinematic analyses)

Movement along fault planes commonly results in some sort of linear markers (striae, slicken-lines, etc.) which indicate the relative direction of movement along the fault plane. Measurements of the fault planes, the slicken-lines and the relative sense of movement can be used to calculate the kinematic axes. A number of 20 to 40 reliable measurements are sufficient to yield a statistically stable stress tensor solution (Arlegui-Crespo and Simon-Gomez, 1998). The method relies on the assumption that the slip direction coincides with the resolved shear stress on the fault plane, and that the set of faults used in the analysis, formed or were active in response to the same far field stress. Fault-slip data can be inverted to a reduced moment tensor with information on the direction

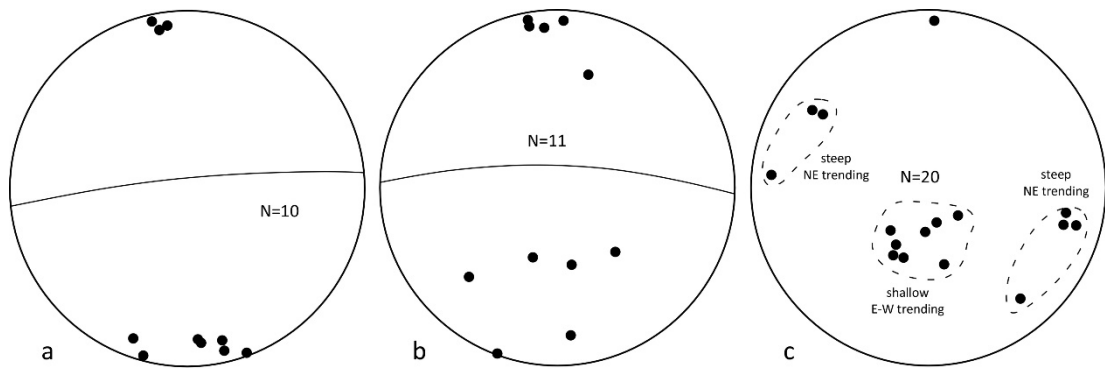


Figure 2.7. Stereonets of poles to planes showing the orientation of the measured quartz veins, from the Geita Hill pit. The great circle in (a) and (b) shows the average dip and dip-direction. (a) stereonet of gold-bearing quartz veins. (b) Stereonet of quartz veins having a similar mineralogy with the gold-bearing quartz veins. (c) stereonet of all other quartz veins.

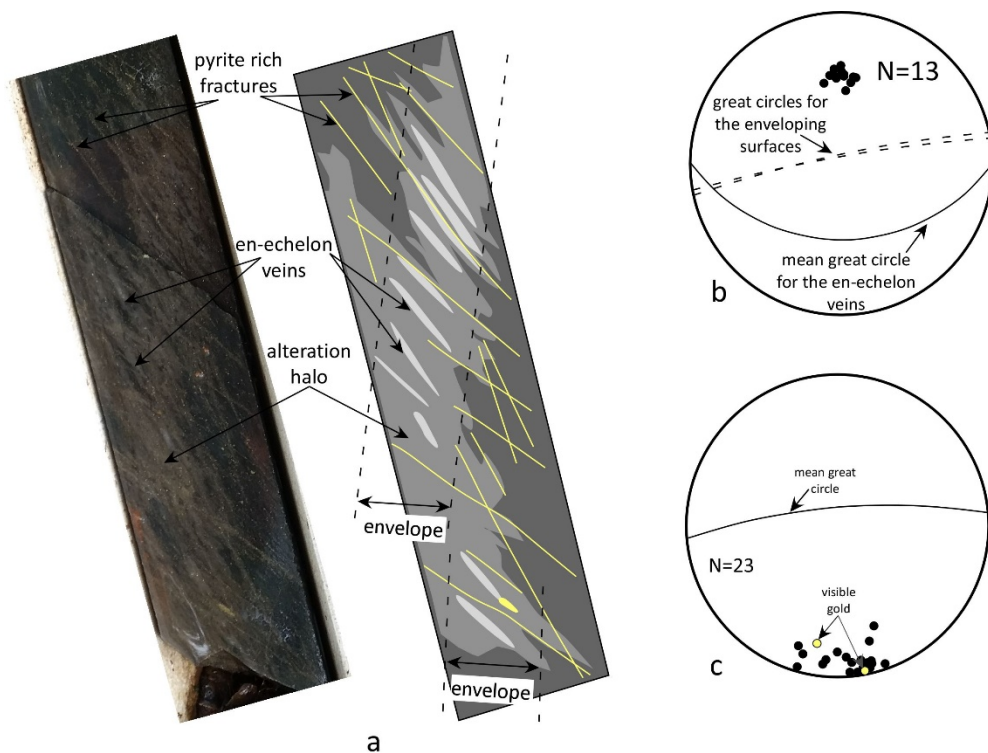


Figure 2.8. Photograph and interpretation of en-echelon quartz veins from a mineralised shale. Note the silicification around the quartz veins and conjugate set of fractures filled with pyrite grains. (b) stereonet of poles to planes for the en-echelon quartz veins and their average great circle. The enveloping surface of the en-echelon quartz veins is steeply dipping north. (c) stereonet of poles to plane for mineralised quartz veins measured from drill cores. The poles to two veins that contained visible gold are coloured yellow. All mineralised quartz veins dip steeply north and trend ~ E-W. This is almost identical to the mineralised quartz veins measured from the pit.

of the principal stress axes with their relative size expressed as a stress ratio (Delvaux and Sperner, 2003; Angelier, 1994). This reduced stress tensor can be calculated using the P (shortening) and T (extension) axes that bisect the fault plane and an auxiliary plane perpendicular to the fault, by using least-square minimization techniques of direction cosines (e.g., Marrett and Allmendinger, 1990) or iterative methods that test a variety of possible tensor solutions (e.g., Etchecopar et al., 1981). Stress axes can also be determined graphically using the right dihedral method (Delvaux and Sperner, 2003; Lisle, 1987), which constrains the orientation of principal stress axes by determining the area of maximum overlap of compressional and extensional quadrants for a suite of faults.

The orientation of the fault-slip data was analysed with the computer programmes Win-Tensor (Delvaux, 1993; Delvaux, 2012) and FaultKinWin (Allmendinger, 2001). The Win-Tensor programme follows the numerical approach outlined by Angelier (1994). Principal stress axes (σ_1 , σ_2 and σ_3) and the ratio of principal stress differences ($R = (\sigma_2 - \sigma_3) / (\sigma_1 - \sigma_3)$) are determined using an improved version of the method of Angelier and Mechler (1977), with optimization achieved by minimizing deviation angles (α) between observed and predicted slip vectors on fault planes, and by maximizing the shear stress magnitude (σ_t) on fault planes. In maximizing the shear stress, it is assumed that the dihedral angle between conjugate fault planes is 60° and bisected by σ_1 . Optimisation is achieved by using an iterative procedure that involves successive rotations on σ_1 , σ_2 and σ_3 axes until a best fit is found (Delvaux and Sperner, 2003). Misfits in the dataset (i.e. faults with large deviation angles) can be identified and excluded in an interactive manner. A quality assessment for the data is provided and follows quality ranking schemes developed in the World Stress Map Project (e.g., Sperner et al., 2003). This scheme combines assessment of the type and quality of data used, with quantitative assessment of the size of the data set, the distribution of slip and fault plane data and the average slip deviation between the observed and predicted slip vectors, to provide a quality ranking ranging from A (best) to E (worst) (Delvaux and Sperner, 2003). The nature of the calculated stress regime can be expressed as a stress ratio R , which varies from constrictional stress ($R=1$ with $\sigma_1 = \sigma_2$) via plane stress ($R = 0.5$ with $\sigma_2 = 0$) to flattening stress ($R = 0$ with $\sigma_2 = \sigma_3$), and varies with the orientation of the principal stress axes. Delvaux and Sperner (2003) define a parameter R' to express the stress regime numerically as a number between 0 and 3 with $R' = R$ when σ_1 is vertical (i.e. plunging steeper than 45° representing an extensional stress regime), $R' = 2 - R$

when σ_2 is vertical (strike-slip stress regime) and $R' = 2 + R$ when σ_3 is vertical (compressional stress regime). The programme output is a diagram displaying the fault-slip data, a histogram of α values, a diagram showing the direction of the maximum and minimum horizontal stress axes (σ_{hmin} and σ_{hmax}), the orientation of σ_1 , σ_2 and σ_3 , the R value and a quality ranking (Fig. 2.8a).

The FaultKinWin programme (Allmendinger, 2001) uses the distribution of P and T axes for a suite of faults (Angelier and Mechler, 1977) to calculate a Bingham axial distribution based on a least squares minimization technique for direction cosines. In this technique the dihedral angle between the fault plane and an auxiliary plane is 90° and bisected by P and T axes. The eigenvectors for the calculated Bingham axial distribution provide average orientations for the maximum, minimum and intermediate concentration direction of the P and T axes, and the eigenvalues provide a measure of the relative concentration, or distribution of P and T axes. These eigenvalues vary between -0.5 and +0.5, with maximum values reached when P and T axes are perfectly concentrated. Variations in the eigenvalues (ev) can be linked to the stress regime using the relative size of the normalised eigenvalues expressed in a ratio, R_{ev} , (with $R_{\text{ev}} = [\text{ev}_2 - \text{ev}_3] / [\text{ev}_1 - \text{ev}_3]$) in the same way as described for ratio R in Win-Tensor (constrictional stress: $R_{\text{ev}} = 1$ with $\text{ev}_1 = \text{ev}_2$; plane stress: $R_{\text{ev}} = 0.5$ with $\text{ev}_2 = 0$; flattening stress: $R_{\text{ev}} = 0$ with $\text{ev}_2 = \text{ev}_3$). Considering the orientation of the principal stress axes, the ratio R_{ev} can be adjusted to a ratio $R_{\text{ev}'}$ to provide an indication for the calculated stress regime, again following the method of calculating R' in Win-Tensor (Delvaux and Sperner, 2003). The FaultKinWin programme output is a plot of P and T axes and linked Bingham axes with eigenvalues and a related fault plane solution diagram displaying P and T quadrants in a manner similar to earthquake focal mechanisms (Fig. 2.8b).

2.5.1. *Fault-slip data and results*

The gold mineralisation is spatially associated with the Geita Hill Shear Zone (Fig. 1.2), which formed during D_6 as a reverse fault and was later reactivated as a strike slip fault (during D_7) and as a normal fault (during D_8 ; Sanislav et al., 2016). For any kinematic analyses to be meaningful it is important that only fault slip data belonging to the same slip event are used. For the purpose of this study I used only fault striations indicative of the last movement (i.e. not overprinted at the site of observation) and where the level of confidence was very high. However, it is not clear whether the lineations measured from different fault planes formed during the same event, formed as a result of separate

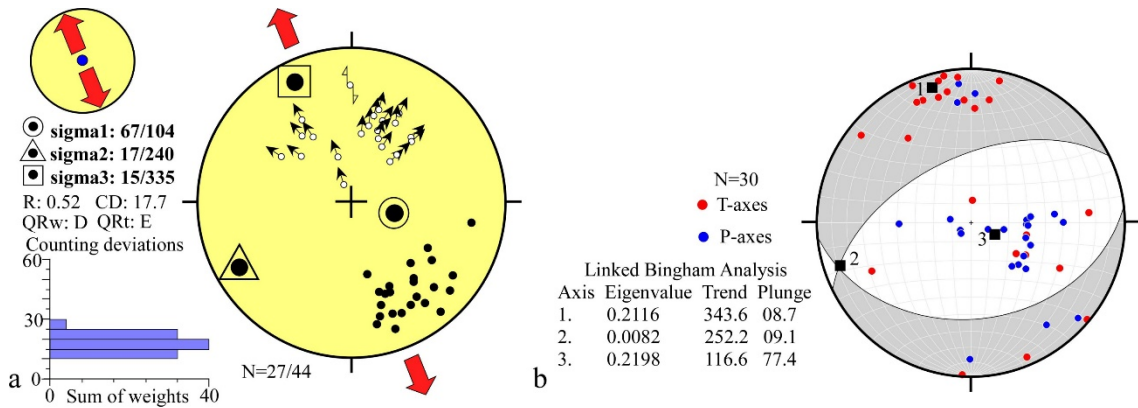


Figure 2.9. Stereoplots showing the result of the fault-slip data analyses. (a) The orientation of slickensided fracture planes and slip vector distributions as well as the results of stress inversion using Win-Tensor (Delvaux and Sperner, 2003) for the Geita Hill deposit. The orientation of the principal stress tensors (σ_1 – σ_3) is provided together with the principal horizontal stress directions (red arrow indicating pure extension) and a histogram of deviation angles. (b) the result of paleostress analyses using the computer program FaultKinWin (Allmendinger, 2001). The results obtained from both programs are almost identical and indicate ~ N-S extension.

events or indicate slip partitioning in a continuous event. With the Win-Tensor program the data that does not fit the overall population can be optimised in an iterative manner. The data are considered invalid on the basis of their Counting Deviations values. If they are higher than a threshold value, they are eliminated. The iteration is done until the counting value for σ_1 equals 0 and for σ_3 equals 100. In our case a subset of 27 fault-slip data have been extracted from the initial data set of 44 fault-slip data. The result of the analyses using the right dihedron method in Win-Tensor (Fig. 2.9a), is consistent with an extensional regime with σ_1 being steep (67°) and σ_3 being sub-horizontal (15°) and directed NW (335°). For the FaultKinWin calculations only the fault slip data associated with the last reactivation of the fault surfaces was used. The result of the FaultKinWin analyses (Fig. 2.9b) is similar with the result obtained by using the right dihedron method in Win-Tensor. The maximum concentration of T-axes is given by the eigenvector 1 ($9^\circ/344^\circ$) and the maximum concentration of P-axes is given by the eigenvector 3 ($77^\circ/117^\circ$). Assuming that the direction of the eigenvectors coincides with the direction of the principal stresses this indicates an extensional stress field with σ_1 being steep (77°) and σ_3 being sub-horizontal (9°) and directed NNW (344°).

2.6. Discussion

2.6.1. *The mineralising conditions*

The Geita Hill metasedimentary rocks show evidence of an early metamorphic event characterised by the appearance of biotite, K-feldspar and actinolite. Biotite and K-feldspar are stable over a wide range of metamorphic conditions, but the actinolite stability field during regional metamorphism has been constrained experimentally to a narrower P-T field (Ernst, 1966; Jenkins and Bozhilov, 2003). The first appearance of actinolite as a metamorphic mineral was experimentally constrained at 1 kbar to be above 375°C (Hellner and Schürmann, 1966) with an upper stability field of 570°C. However, these experiments did not take into account the oxygen fugacity, and experiments conducted using the iron-magnetite buffer (Ernst, 1966) showed that under constrained oxygen fugacity conditions, the upper thermal stability limit of actinolite is at 460°C. Jenkins and Bozhilov (2003) showed that the maximum thermal stability of actinolite under natural conditions is 480 °C at 2 kbars (Fig. 2.10). They showed that above 2 kbars grunerite will start nucleating and above 3 kbars grunerite becomes abundant. The lack of grunerite and other minerals (garnet, cordierite) indicative of higher metamorphic grade constrains the maximum PT conditions at Geita Hill to between 375 and 480 °C, at pressures that probably did not exceed 3 kbars. The auriferous alteration, overprints the metamorphic background and is characterised by quartz + biotite + K-feldspar + pyrite, indicating that the mineralising fluids were hot enough and of the right composition for these minerals to be stable. Borg (1994) proposed that at the Geita Hill deposit the mineralising fluids had a temperature range of 350-480°C, which is similar to the inferred peak metamorphic conditions. With the exception of actinolite, this mineral assemblage associated with gold mineralisation is almost identical to the peak metamorphic assemblage. The lack of actinolite from the gold-bearing alteration assemblage can be related to the lack of carbonate during the gold mineralising events. For example, intense Ca and CO₂ metasomatism would have resulted in the deposition of carbonates and at least some actinolite growth by reaction with magnetite. Instead, the reaction of the mineralising fluid with the host rock produced only K-feldspar, biotite and pyrite. Since, the bulk of the mineralisation is hosted by sulfidised alteration fronts formed in ironstone and diorite the dominant gold forming event must have involved the fluid-rock interaction. Thus, the destabilisation of Au(HS)₂⁻ complex by a reaction between reduced S-rich ore fluids and Fe-bearing host rocks

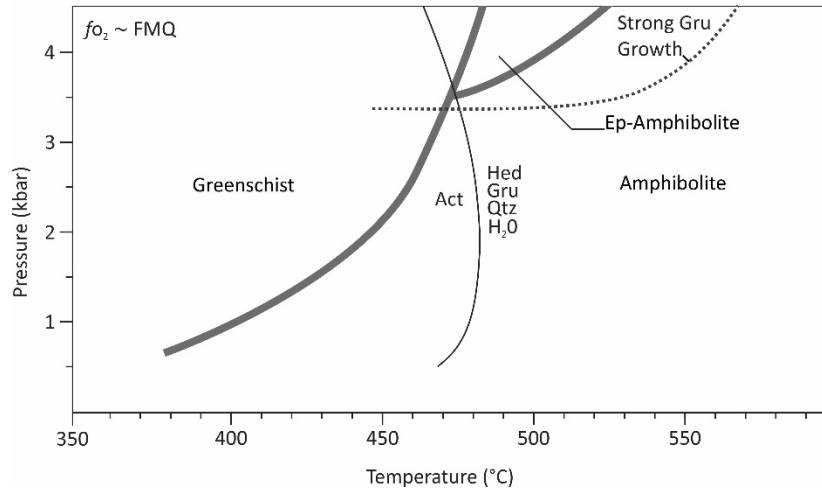


Figure 2.10. Pressure-temperature diagram showing the most likely peak metamorphic conditions. Peak metamorphism at the Geita Hill deposit is characterized by K-feldspar + biotite + actinolite. Biotite and K-feldspar are stable over a wide range of P-T conditions, but the thermal stability of actinolite was constrained to be between 350°C at 480°C (Jenkins and Bozhilov, 2003). Experiments have shown that above 2 kbars actinolite is replaced by grunerite. Thus, the lack of grunerite in the Geita Gill deposit constrains the maximum pressure at 2 kbars. With the exception of actinolite, the syn-mineralisation alteration assemblage is almost identical suggesting that the mineralising fluid was hot enough so that the K-feldspar and biotite were not affected.

(Phillips and Groves, 1983) produced steep-gradients in the activity of H_2S which can easily result in 10- to 100-fold decrease in gold solubility (Mikucki and Ridley, 1993). The first generation of mineralised pyrite, pyrite-2a, is inclusion-rich and contains rare, sub-microscopic gold grains suggesting rapid growth (Borg, 1994; Borg and Rittenauer, 2000) and possibly the onset of decreasing gold solubility. On the other hand, the inclusion free, pyrite 2b, contains frequent, large gold grains which may indicate slower growth and a significant decrease in gold solubility.

2.6.2. Timing of gold mineralisation

The close spatial relationship between the D₆ GHSZ and the gold mineralisation suggest a genetic link between the D₆ deformation and gold mineralisation. However, the D₆ GHSZ fault surfaces contain slickenlines with normal sense of movement that overprint earlier slickenlines indicating sinistral reverse movement (Sanislav et al., 2017). The kinematic analysis of the late slickenlines found on the GHSZ fault surfaces is consistent with N-S extensional reactivation of the GHSZ (Fig. 2.9), which was referred to as D₈ by Sanislav et al. (Sanislav et al., 2017) and linked to extensional events that took place after the emplacement of the second generation of the lamprophyre dykes at 2644 Ma (Borg, 1994). The steeply dipping, ~ E-W trending mineralised quartz veins are consistent with N-S extension. The high grade ore shoots occur as sulfidation fronts where these steeply dipping

mineralised quartz vein intersect ironstone and diorite suggesting that the mineralisation occurred during this N-S extensional event and post-date the D₆ reverse-sinistral structures. The orientation of the mineralised veins and the late-tectonic (D₈) normal movement along the D₆ shears is compatible with earlier observations in the Geita Hill and Nyankanga deposits (Sanislav et al., 2015; 2017). For example, the regional Iyoda Shear which is located just west of the GHSZ is a dextral transcurrent shear zone (Sanislav et al., 2015). Dextral shearing along the Iyoda shear zone will cause reverse movement along the NE-SW oriented GHSZ. Thus, the gold mineralisation at the Geita Hill deposit must postdate this movement and is related to the D₈ N-S extensional deformation. The second generation 2644±3 Ma old lamprophyres (Borg and Krogh, 1999) at the Geita Hill deposit intruded along D₇ structures (Sanislav et al., 2017) suggesting that the gold mineralisation is 2644 Ma or younger. In terms of regional geological history, this coincides with the emplacement of large volumes of late syn-tectonic high-K granites between 2660 and 2620 Ma (Sanislav et al., 2014b).

2.7. Conclusions

The Geita Hill gold deposit is hosted within a package of iron-rich shales, turbiditic sediments and dioritic intrusives, metamorphosed to greenschist facies during pre-mineralisation deformation. The regional metamorphic assemblage includes biotite + chlorite + K-feldspar + actinolite ± magnetite ± pyrrhotite ± pyrite_{1a}. Peak metamorphic conditions for the deposit are inferred to between 375° and 480 °C, and less than 3 kbars. The gold-related alteration is present as sulfide alteration fronts, gold-bearing quartz veins and gold-bearing micro-fractures. Mineralisation and sulfidation is usually associated with silicification of the host-rock, and is most prevalent within iron-rich lithologies, proximal to the diorite contact or steeply dipping shear structures. Pyrite is the dominant sulfide at the deposit, and is associated with secondary hydrothermal biotite and K-feldspar alteration in all mineralised lithologies. Two textural styles of gold-bearing pyrite are present at the Geita Hill deposit; pyrite-2a is generally subhedral, and contains abundant mineral inclusions; pyrite-2b is generally euhedral, and occurs both as a rim overgrowing pyrite-2a, and as independent grains. Textural relationships suggest that pyrite-2a precedes pyrite-2b, but it is currently unclear whether this zonation is due to the gradual evolution of mineralising fluids or the result of two separate mineralising events. The gold-related alteration is overprinted by multi-phase quartz-carbonate and carbonate-chlorite veins and veinlets. This alteration has a general mineral association of calcite +

siderite + chlorite ± quartz ± pyrite (pyrite-3a or pyrite -3b) ± barite, and is at least partly lithologically controlled.

Two styles of mineralised quartz veins were observed at the Geita Hill deposit. The first comprises networks of small, translucent, and en-echelon quartz veins. Individual veins dip moderately south, but their alteration envelope dips steeply to the north. The second style are larger, up to several cm wide, and are consistently dipping steeply north. The orientation of these veins is consistent with an extensional regime, with σ_1 being steeply dipping (77°) towards the NW, implying that mineralisation occurred during normal reactivation (D_8) of existing (D_6) reverse thrusts.

Chapter 3

Biotite chemistry and the role of halogens in Archaean
greenstone hosted gold deposits: a case study from Geita Gold
Mine, Tanzania

Published in Ore Geology Reviews (van Ryt et al., 2017)

Abstract

Geita Hill is one of the largest Tanzanian gold deposits, located southwest of Lake Victoria and ~ 2 km along strike from the giant Nyankanga deposit. The deposit is hosted by metasedimentary rocks dominated by ironstones and intruded by numerous diorite dykes. Textural, structural and geochronological estimates indicate that the gold mineralisation overprints all the ductile fabrics and the late orogenic D₆ reverse faulting event, suggesting that gold was introduced during later D₇ and D₈ events. The metamorphic background is characterized by biotite + K-feldspar + actinolite ± pyrrhotite, which is overprinted by the gold related alteration consisting of sulfidation fronts, veins and micro-fractures dominated by quartz + biotite + K-feldspar + pyrite. The similar mineralogy of the mineralised assemblage and the metamorphic background makes it difficult to identify the source, the effect and the spatial extent of the mineralising fluid. As part of this study detailed analyses of biotite were conducted in order to identify the nature of the mineralising fluid and its spatial effect across the Geita Hill deposit. Results show that the mineralised assemblage is slightly more oxidized (pyrite + magnetite) compared to the metamorphic background (pyrrhotite + magnetite). The intense sulfidation within the ore zone resulted in the formation of Mg-rich biotite, which grades into more Fe-rich biotite away from the ore zone. This change in biotite chemistry causes a shift in the SWIR Fe-OH 2250 nm absorption feature to lower wavelengths, which is also correlated with an increase in gold grade within the mineralised zone. The abundance of F in biotite significantly increases within the ore zone indicating the presence of relatively F-rich hydrothermal fluids during mineralisation. Late timing of mineralisation, synchronous with the emplacement of voluminous high-K granites, and the presence of K- and F-bearing fluids indicate a genetic connection between the mineralising fluids and the late granites. Biotite grains from different deposit types (porphyry, IOCG, lode-Au) appear to have distinct composition suggesting that the source of the fluids involved in the formation of each deposit type has a characteristic halogen chemistry.

3.1. Introduction

The Neoproterozoic gold deposits in the Lake Victoria Goldfield, Tanzania, include several world-class deposits such as the Geita and Bulyanhulu Gold camps, both of which contain over 15 Moz of gold (Henckel et al., 2016). These deposits are generally classified as orogenic (e.g. Goldfarb et al., 2001; Bierlein et al., 2006), thereby suggesting that they formed as a result of fluid flow along deep-tapping structures, with crustal scale metamorphic fluids providing the main metal source for mineralisation (e.g., Goldfarb and Groves, 2015). However, we know little about the large-scale flow systems and fluids that contributed to gold mineralisation in these deposits (Henckel et al., 2016), apart from the fact that gold deposition occurred late relative to deformation and involved extensive silicification and sulfidation (e.g., Chamberlain, 2003; van Ryt et al., 2017). In the Geita gold camp, mineralisation occurred during extensional reactivation of earlier formed structures synchronous with the emplacement of large volumes of high-K granites (Borg and Krogh, 1999; Sanislav et al., 2015; 2017), with highly focussed, potassic alteration and the deposition of Bi-Pb-bearing tellurides (van Ryt et al., 2017). Extensive sulfidation of Fe²⁺ rich lithologies (e.g., Borg and Rittenauer, 2000) indicate that redox gradients were important in precipitating gold from solution, and the presence of breccia zones along extensional faults (Sanislav et al., 2015; 2017) suggests that phase separation could also have played a role (e.g., Phillips and Powell, 2010). However, the extent and exact nature of the alteration systems and associated fluid pathways in the Geita deposits remain unstudied, and it is unclear how the alteration assemblages can be linked to the dynamic behaviour of fluids that contributed to the gold system.

In this context the geochemistry of biotite and in particular the halogen (i.e. F-Cl) content of the biotite can be of use in identifying alteration characteristics that can link high-grade gold mineralisation to a specific fluid source and possible fluid pathways (Boomeri et al., 2010; Bath et al., 2013). The composition of biotite is not just sensitive to host rock chemistry, P and T, but also varies with the activity of OH⁻, F⁻, Cl⁻, HS⁻ and O₂ of an altering hydrothermal fluid (e.g., Munoz, 1984; Cleverley, 2006; Boomeri et al., 2010). The biotite composition and especially variations in composition of texturally variable biotite (i.e. igneous, vs. metamorphic, vs hydrothermal biotite) can therefore be used to constrain the nature of hydrothermal fluid in a gold system, and the extent to which this fluid penetrated and interacted with the host rocks (Munoz, 1984; Zhu and Sverjensky, 1992; Sallet, 2000; Yavuz, 2003; Rasmussen and Mortensen, 2013; Afshooni et al., 2013; Bath et al., 2013). The F and Cl content of biotite has been studied in porphyry systems to constrain fluid

pathways and P-T conditions (Beane, 1974; Boomeri et al., 2009; Boomeri et al., 2010), but few studies have focussed on Neoproterozoic orogenic gold deposits (Bath et al., 2013). Geita mine offers a good opportunity to do so.

Considering that biotite is one of the characteristic alteration minerals in the Geita gold camp, where it occurs together with K-feldspar, pyrite and carbonates (van Ryt et al., 2017), this study will focus on a detailed geochemical analysis of texturally different biotite types at the Geita Hill gold deposit (i.e. the original mine in the Geita gold camp, Cowley, 2001). With the use of short wavelength infrared spectroscopy (SWIR), the extent of biotite alteration haloes around high-grade ore zones will be investigated. In determining the composition and distribution of hydrothermal biotite, the nature of the mineralising fluids and their role in the formation of the Geita Hill deposit will be constrained.

3.2. Gold mineralisation, alteration and metamorphism at Geita Hill

Gold mineralisation at the Geita Hill deposit is concentrated along a NE trending ore envelope approximately 1400 m long and 30 m wide. The ore zone dips moderately to the NW and coincides with a fractured zone that extends along D₃ fold hinges and D₆ shear zones, (Sanislav et al., 2015; van Ryt et al., 2017). Gold-related alteration overprints the second generation of (2644 Ma) lamprophyre dykes, and is closely associated with sub-vertical, E-W trending quartz veins. Field relationships indicate that mineralisation occurred during D₇ or D₈ deformation, and is related to transcurrent and extensional structures (Sanislav et al., 2015; 2017; van Ryt et al., 2017). The highest-grade mineralisation is concentrated within damage zones along the contacts between intrusive diorite and chert-magnetite-bearing metasedimentary rocks (ironstone).

The gold-related alteration at Geita Hill is associated with silicification, sulfidation and potassic alteration. It occurs in sulfide alteration fronts, gold-bearing quartz veins and gold-bearing micro-fracture networks (Fig. 3.1a, e, f). Pyrite is the dominant sulfide, followed by pyrrhotite with minor amounts of chalcopyrite, sphalerite and galena. The main alteration minerals are quartz,

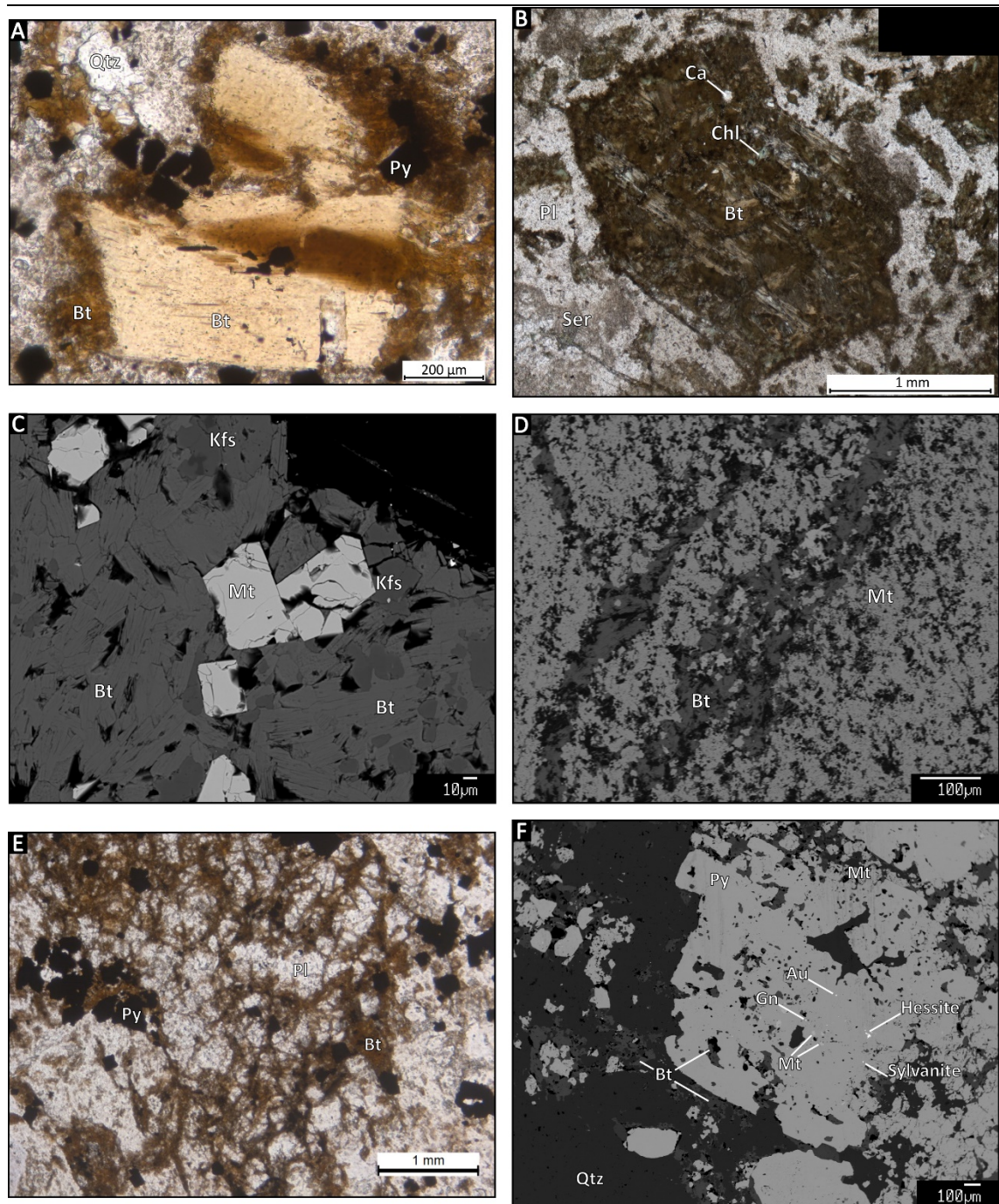


Figure 3.1. Photomicrographs and electron microprobe images of the regional metamorphic and mineralised assemblage at Geita Hill. A) PPL image of diorite, primary igneous biotite grains are overgrown by the mineralised assemblage of biotite, K-feldspar and opaque pyrite. B) PPL image of diorite, breakdown of igneous hornblende phenocryst into secondary biotite with minor accessory minerals during regional metamorphism. C) BSE-COMP image of Mt-poor ironstone. D) BSE-COMP image of Mt-rich ironstone. E) PPL image of mineralised microfracturing within diorite, the density of this microfracturing is directly correlated with grades. F) BSE-COMP image of sulfidation front within ironstone, occurring on the contact between ironstone and chert laminae.

biotite and K-feldspar, with minor calcite, apatite, monazite and tellurides. Gold is found as free gold and gold-telluride inclusions in pyrite, biotite, K-feldspar, between grain boundaries and within the crystal lattice of pyrite (van Ryt et al., 2017). Sulfidation fronts appear as silicified zones with abundant disseminated, fine- to coarse-grained pyrite, as well as secondary biotite and K-feldspar alteration. Gold-bearing quartz veins and associated breccia zones are present throughout the Geita Hill deposit, and were the target of past underground mining operations (Carter, 1959; Horne, 1959). The silicified and sulfidised alteration halos around these veins are highly mineralised, while the veins themselves are generally lower grade. The mineralogy of these veins is relatively simple and dominated by quartz with minor pyrite, biotite and K-feldspar. Disseminated gold-bearing pyrite in silicified diorite and ironstone is related to the development of networks of dense, (sub) mm-scale micro-fractures (e.g., van Ryt et al., 2017), that are not spatially related to shear zones, but rather form zones of intense fracturing without any visible displacement.

Multistage, barren quartz-carbonate and carbonate-chlorite alteration veins and veinlets overprint the mineralised assemblage at Geita Hill. These late stage alteration events are characterised by a calcite + siderite + chlorite ± pyrite ± quartz ± barite mineral association. Where carbonate veins cross-cut mineralised micro-fractures, the carbonate-rich fluid reacted with pyrite and biotite to form siderite and chlorite. This alteration also overprints the regional metamorphic assemblage, with biotite being replaced by chlorite.

The rocks of the Geita Hill deposit were metamorphosed to greenschist facies during D₂ and D₃ ductile deformation. The mineral paragenesis associated with this regional metamorphism includes biotite + chlorite + K-feldspar + actinolite ± magnetite ± pyrrhotite ± pyrite. Within diorite and monzonite units, hornblende and pyroxene phenocrysts are replaced by biotite with accessory K-feldspar, calcite, chlorite, epidote, apatite, pyrite and Fe-oxides (Fig. 3.1b). Plagioclase phenocrysts have been partly to completely replaced by sericite. Fine-grained biotite and K-feldspar is well developed in magnetite-shale laminae (Fig. 3.1c, d). Fine-grained, fibrous actinolite is disseminated in chert layers, and forms dense masses near the contact with the magnetic shale layers. Peak metamorphic conditions at Geita Hill have been estimated at 375-480 °C, based on co-existence of actinolite and biotite, at pressures that probably did not exceed 3 kbars (van Ryt et al., 2017).

Within the context of this study it is important to note that the peak metamorphic mineral assemblage in rocks at Geita Hill is similar to the hydrothermal assemblage that formed during gold mineralisation, making the recognition of alteration assemblages difficult. The characteristic alteration assemblage pyrite-biotite-K-feldspar is generally only recognisable based on its textural position and associated micro-fracture networks. Alteration fronts associated with mineralisation are relatively narrow (10's of meters in width), with the exception of silicification, which may extend for 100's of meters away from deposits.

3.3. Sampling and methodology

Three drill holes transecting the ore zone at the Geita Hill deposit (Fig. 1.2) were logged in detail (Appendix. 3) and representative samples containing alteration biotite as well as regional metamorphic and igneous biotite were collected for petrography, SWIR and geochemical analysis. The rocks sampled include ironstones, mudstones and multiple varieties of diorite. These samples were complemented with samples of mineralised and barren quartz veins collected from the pit walls and floor.

3.3.1. *Microscopy and electron probe micro analysis*

Normal and polished thin sections were prepared from 73 samples for petrography and mineral chemistry. A detailed alteration paragenesis for the Geita Hill deposit was established based on systematic logging of drill holes and on detailed transmitted and reflected light petrography for all 73 samples (van Ryt et al., 2017). Mineral chemistry analysis was conducted using the Jeol JXA8200 "Superprobe" housed at the Advanced Analytical Centre at James Cook University, under operating conditions of 15 KeV and 20 nÅ, with a beam diameter of 1 µm. Scanning electron microscopy (SEM) was used to supplement mineral identification through semi-quantitative energy dispersive spectroscopy (EDS) analysis. The major element composition of biotite was measured using quantitative wavelength dispersive spectroscopy (WDS) analysis with natural and synthetic standards.

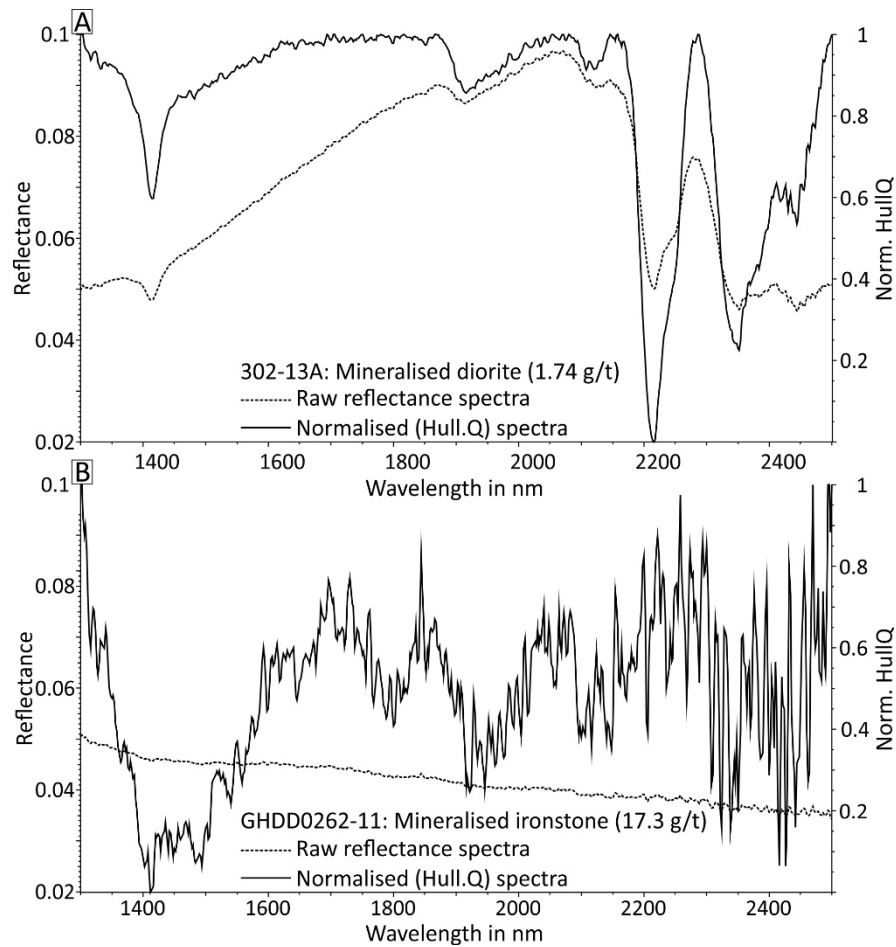


Figure 3.2. Reflectance spectra of diorite and ironstones, showing the effects of hull quotient normalisation. Diorite lithologies return good reflectance spectra, sedimentary rock, specifically ironstones, returns poor spectra.

3.3.2. Short wavelength infrared spectroscopy (SWIR)

A total of 297 SWIR spectra (Fig. 3.2a) were collected from intrusive units and analysed individually. SWIR analyses for ironstones did not return usable spectra due to low signal to noise ratios (Fig. 3.2b). All spectra were collected using a PIMA-SP field spectrometer with a spectral resolution of ~ 7 nm, sampling interval of 2 nm and a spectral range of 1300–2500 nm. The equipment scans a 2×10 mm area of sample, and a measurement time of 30 seconds per spectra was used. Data was collected using PimaAcq v2.3 software, and processed using The Spectral Geologist (TSG) v7.1 software. Mineral spectral libraries of the United States Geological Survey (Clark et al., 2007) and TSG v7.1 were used for mineral identification. Reflectance spectra were hull corrected to minimise background absorption (Clark, 1999), and the position of the Fe-OH absorption feature was estimated manually.

3.4. Biotite chemistry

Three types of biotite were identified in the ironstones and diorite in the Geita Hill deposit: igneous biotite, metamorphic biotite and hydrothermal biotite.

3.4.1. *Igneous biotite*

The igneous biotite (Fig. 3.1a) is found as large, euhedral crystals in both hornblende- and plagioclase-rich diorite. In general, biotite grains from hornblende-rich diorite are Fe and Al rich, while biotite grains from plagioclase-rich diorite are Mg and Si rich. Tetrahedral Si and Al^{iv} atoms per formulae unit (apfu) do not vary significantly between different biotite grains (Table 3.1.). Octahedral Al^{vi} ranges from 0.10 to 0.33 apfu in hornblende-rich diorite and from 0.45 to 0.55 apfu in plagioclase-rich diorite. Most octahedral sites are filled by Fe_{total} (1.97 to 2.20 apfu) and Mg (2.77 to 3.30 apfu), with corresponding Fe/(Fe+Mg) ratios from 0.39 to 0.66. The Fe-content of igneous biotite shows only small variations between lithological units, while the Mg content drops significantly in the hornblende-rich diorite compared to the plagioclase-rich diorite. An increased Al^{vi} content is positively correlated with a decrease in Mg. Ti content in igneous biotite varies from 0.16 to 0.43 apfu (average 0.24 apfu). Octahedral Mn is typically below 0.02 apfu. Interlayer sites are almost entirely filled by K (1.87 to 2.01 apfu), with only small amounts of Na (up to 0.01 apfu). Calcium is below detection limits in all analysed grains. The F content of igneous biotite is in general below detection limits but can be as high as 0.38 apfu near the ore zone.

3.4.2. *Metamorphic biotite*

3.4.2.1. *Ironstone units*

The metamorphic biotite (Fig. 3.1c) is common in the ironstone units and occurs as disseminated euhedral to subhedral grains and intergrown with magnetite. The Al and Si content varies systematically across different lithological units and between laminae of different composition. For example, the magnetite-rich laminae show an increase in Si with a corresponding decrease in the Al^{iv} content (Table 3.1). Al^{vi} occupies between 0.24 and 0.41 apfu of the octahedral sites in biotite grains from chert-rich laminae but does not occur in biotite grains from magnetite-rich laminae. The

Table 3.1.*Chemistry of representative biotite grains from ironstone and quartz vein units at Geita Hill*

Mineral association	Ironstone laminae		Chert laminae		Igneous	Hornblende replacement			Distal veining		Gold bearing micro-fractures		
SiO ₂	37.47	38.93	37.82	38.62	37.15	37.38	36.50	37.38	38.15	37.30	39.22	40.09	40.47
TiO ₂	0.59	0.58	1.18	1.09	1.61	1.65	1.27	1.65	1.11	1.94	1.65	2.24	1.59
Al ₂ O ₃	10.98	12.52	14.78	14.36	16.49	15.97	17.05	15.97	17.09	15.46	14.79	13.76	15.98
FeO	25.47	23.50	17.50	17.30	17.01	16.53	20.74	16.53	16.64	18.62	12.61	16.38	12.96
MnO	0.23	0.24	0.15	0.13	0.14	0.15	0.22	0.15	0.15	0.05	0.09	0.07	0.05
MgO	11.19	11.73	14.55	14.92	12.64	13.57	10.37	13.57	12.92	12.82	16.64	12.71	15.57
CaO	0.17	0.00	0.02	0.09	0.02	0.05	0.03	0.05	0.04	<LOD	<LOD	<LOD	0.03
Na ₂ O	0.06	0.06	0.06	0.06	0.11	0.11	0.08	0.11	0.72	0.05	0.00	0.10	0.04
K ₂ O	8.05	9.41	9.80	9.87	9.88	9.83	9.84	9.83	7.89	9.76	9.90	10.27	10.05
F	-	-	-	-	0.52	<LOD	<LOD	0.00	0.33	0.09	0.97	0.76	0.84
Cl	-	-	-	-	0.08	0.05	0.07	0.05	0.08	0.02	<LOD	0.02	0.05
Total	94.20	96.97	95.86	96.44	95.64	95.29	96.16	95.29	95.11	96.11	95.88	96.39	97.62
Stoichiometry based on 22 oxygen													
Si	5.94	5.93	5.69	5.76	5.55	5.63	5.56	5.63	5.65	5.61	5.68	5.89	5.75
Al	2.05	2.25	2.62	2.52	2.90	2.83	3.06	2.83	2.99	2.74	2.52	2.38	2.68
^{iv} Al	2.05	2.07	2.31	2.24	2.45	2.37	2.44	2.37	2.35	2.39	2.32	2.11	2.25
Σ(iv) (Z Sites)	7.99	8.00	8.00	8.00	8.00	8.00	8.00	8.00	8.00	8.00	8.00	8.00	8.00
viAl	<LOD	0.18	0.31	0.28	0.45	0.46	0.61	0.46	0.64	0.36	0.21	0.28	0.42
Ti	0.09	0.07	0.13	0.12	0.18	0.19	0.15	0.19	0.12	0.22	0.18	0.25	0.17
Fe	3.38	3.00	2.20	2.16	2.13	2.08	2.64	2.08	2.06	2.34	1.53	2.01	1.54
Mn	0.03	0.03	0.02	0.02	0.02	0.02	0.03	0.02	0.02	0.01	0.01	0.01	0.01
Mg	2.64	2.67	3.26	3.32	2.81	3.04	2.35	3.04	2.85	2.88	3.59	2.79	3.30
Σ(vi) (Y Sites)	6.14	5.76	5.92	5.90	5.59	5.79	5.78	5.79	5.70	5.80	5.52	5.33	5.44
Ca	0.03	<LOD	<LOD	0.01	<LOD	0.01	0.00	0.01	0.01	<LOD	<LOD	<LOD	<LOD
Na	0.02	0.02	0.02	0.02	0.03	0.03	0.02	0.03	0.21	0.01	0.00	0.03	0.01
K	1.63	1.83	1.88	1.88	1.88	1.89	1.91	1.89	1.49	1.87	1.83	1.93	1.82
Σ(xii) (X Sites)	1.67	1.85	1.90	1.91	1.92	1.93	1.94	1.93	1.70	1.89	1.83	1.95	1.84
F	-	-	-	-	0.24	<LOD	<LOD	0.00	0.15	0.04	0.45	0.35	0.38
Cl	-	-	-	-	0.02	0.01	0.02	0.01	0.02	<LOD	0.00	0.00	0.01
Total	15.80	15.60	15.82	15.81	15.77	15.73	15.74	15.73	15.58	15.74	15.79	15.64	15.66
Fe/(Fe + Mg)	0.56	0.53	0.40	0.39	0.43	0.41	0.53	0.41	0.42	0.45	0.30	0.42	0.32
Si/(Si + Al)	0.74	0.73	0.68	0.70	0.66	0.67	0.67	0.67	0.65	0.67	0.69	0.71	0.68

octahedral sites are dominated by Mg (3.10 to 3.43 apfu) and Fe_{total} (2.05 to 2.34 apfu) in biotite grains from chert and shale layers. Biotite grains from the magnetite-rich laminae show a sharp increase in Fe_{total} (up to 3.38 apfu). The Fe/(Fe+Mg) ratio in chert and shales varies from 0.37 to 0.43, while in magnetite-rich laminae this ratio increases to 0.56. The Ti content in most biotite grains ranges from 0.11 to 0.14 apfu, but decreases to 0.07 apfu in biotite grains from magnetite-rich laminae. The Mn content is generally below 0.02 apfu, but becomes slightly higher in biotite from magnetite-rich laminae (0.03 apfu). The interlayer sites are dominated by K (1.70 to 1.90 apfu) with minor amounts of Na (0.01 to 0.07 apfu) and Ca contents of up to 0.04 apfu. Interlayer-site vacancies range from 0.04 to 0.27 apfu, increasing slightly to 0.33 apfu in biotite from magnetite-rich laminae.

3.4.2.2. *Diorite*

In diorite, metamorphic biotite (Fig. 3.1b) occurs as fine-grained aggregates replacing igneous amphibole and pyroxene phenocrysts. There is a distinct compositional difference between biotite from plagioclase-rich and hornblende-rich diorite. The tetrahedral site occupancy in biotite grains from plagioclase-rich diorite (Si/Si+Al ratio of 0.65 to 0.73) is higher when compared to biotite grains from hornblende-rich diorite (Si/Si+Al ratio of 0.63 to 0.65). The Mg content of biotite grains in plagioclase-rich diorite ranges from 2.8 to 3.8 apfu while the Fe content ranges from 1.60 to 2.34 apfu. In hornblende-rich diorite, the Mg and Fe content range from 2.30 to 2.52 apfu, and 2.55 to 2.71 apfu respectively. The remaining octahedral sites are filled by Ti (0.09 to 0.28 apfu), and minor Mn (up to 0.03 apfu). The interlayer sites are filled mainly by K (1.66 to 2.00 apfu), with Ca and Na usually <0.05 apfu. Interlayer site vacancies average 0.10 apfu. The F content is variable, but close to the ore zone it can be as high as 0.27 apfu for biotite grains in plagioclase-rich diorite, and 0.14 apfu for biotite grains in hornblende-rich diorite. The Cl content is less than 0.04 apfu.

3.4.3. *Hydrothermal biotite*

Hydrothermal biotite grains can be found up to 150 meters away from the ore zone where it occurs as biotite selvages along micro-fractures and in barren quartz veins. The intensity of biotite alteration increases towards the ore zone, but their composition is host rock dependent.

3.4.3.1. *Ironstone*

In ironstone, the hydrothermal biotite (Fig. 3.1f) is associated with sulfide alteration fronts. Biotite grains are finer grained compared to metamorphic biotite, and in general the hydrothermal biotite is anhedral in shape (Fig. 3.1d). The biotite composition varies between chert and magnetite laminae.

3.4.3.2. *Chert laminae*

In chert-rich laminae in ironstone, the octahedral Al^{vi} values range from 0.21 to 0.33 apfu, with Mg (3.11 to 3.64 apfu), being the dominant cation in the octahedral sites. The Fe_{total} values vary from 1.92 to 2.32 apfu. The remaining sites are filled by Ti (0.12 to 0.18 apfu) and Mn (0.02 to 0.03 apfu). The interlayer sites are dominated by K (1.79 to 1.93 apfu), with Ca contents of up to 0.03 apfu. The Na content is generally less than 0.07 apfu. The interlayer-site vacancy rate varies from 0.03 to 0.2 apfu.

3.4.3.3. *Magnetite laminae*

In magnetite-rich laminae in ironstone, tetrahedral Si and Al^{iv} occupancy varies between grains, with some grains showing anomalously low Al^{iv} occupancy (< 2.10 apfu). Biotite from magnetite-rich laminae is on average more Si rich (6.00 apfu) compared to biotite from chert laminae (5.74 apfu). Some biotite grains (n=6) have no Al^{vi} in the octahedral sites and show vacancies in the tetrahedral sites ([Si^{iv} + Al^{iv}] < 8). For the remaining grains, the calculated octahedral Al^{vi} values range from 0.04 to 0.45 apfu. The Fe/(Fe+Mg) ratio is variable, ranging from 0.4 to 0.59. Mg ranges from 2.34 to 3.58 apfu, and Fe_{total} from 2.37 to 3.91 apfu. The Ti content is on average 0.04 apfu while the average Mn content is very low (0.025 apfu). There is a strong positive correlation between Fe_{total} and $\sum^{vi} > 6$, and a strong negative correlation between Fe_{total} and $\sum^{iv} < 8$. Thus, the octahedral sites are overfilled while the tetrahedral sites have increased vacancies. This may indicate substantial amounts of Fe³⁺ into the octahedral sites. The interlayer sites are filled mainly by K (1.33 to 1.91 apfu), with Na and Ca up to 0.04 apfu, while the number of vacancies is high, ranging from 0.04 to 0.61 apfu. There is a positive correlation between interlayer vacancies and increased Fe_{total}.

3.4.3.4. *Diorite*

In diorite, hydrothermal biotite occurs as fine grains along micro-fracture networks (Fig. 3.1e), and less commonly replaces igneous (Fig. 3.1a) and metamorphic biotite. In plagioclase-rich diorite, the tetrahedral Si^{iv} values vary from 5.50 to 6.31 apfu, whereas Al^{iv} varies from 1.69 to 2.51 apfu. Biotite grains in hornblende-rich diorite have Si^{iv} values that range from 5.53 to 5.58 apfu, and Al^{iv} values from 2.66 to 2.80 apfu. In general, the octahedral Al^{vi} is low with many grains having no Al in octahedral sites, but Al^{iv} can be as high as 1.28 apfu in some biotite grains in plagioclase-rich diorite. Octahedral sites are dominated by Mg (2.22 to 3.69 apfu) while the Fe content varies from 1.37 to 3.13 apfu. The interlayer sites are mainly occupied by K (1.57 to 2.12 apfu). Ca and Na are low with maximum values of 0.13 apfu and 0.05 apfu respectively. The F content of biotite is high (up to 0.54 apfu), while the maximum Cl content is 0.04 apfu.

3.4.3.5. *Quartz veins*

In mineralised quartz veins, biotite occurs as euhedral to subhedral grains in association with pyrite and K-feldspar. Tetrahedral Si varies between 5.48 and 5.93 apfu and Al^{iv} values range from 2.53 to 3.19 apfu, with the highest values consistently found in biotite grains from diorite-hosted veins. In general, biotite grains in quartz veins have a higher Al^{vi} content compared to biotite grains in the surrounding wall rock. Octahedral sites are dominated by Mg (2.40 to 3.40 apfu) and Fe (1.51 to 2.93 apfu). The remaining octahedral sites are filled by Ti (0.05 to 0.24 apfu) and Mn (0.01 to 0.03 apfu). The interlayer sites are occupied by K (1.42 to 1.93 apfu), with minor Ca (up to 0.03 apfu) and Na (up to 0.06 apfu). The F content is generally high with maximum values close to 0.6 apfu.

3.4.4. ***Local vs deposit scale compositional variations***

Because gold mineralisation is hosted mainly along micro-fracture networks, major compositional variations can occur within the same sample depending on the textural type and position of individual biotite grains. In the previous section a detailed account of biotite compositional variations was presented based on textural type and host rock lithology. Figure 3.3 shows examples of compositional variations as a function of textural position within a single thin section, for biotite grains from a mineralised diorite and ironstone. In ironstone (Fig. 3.3a), hydrothermal biotite grains in sulfidation fronts display a large variation in Fe/(Fe+Mg) ratios, whereas metamorphic matrix

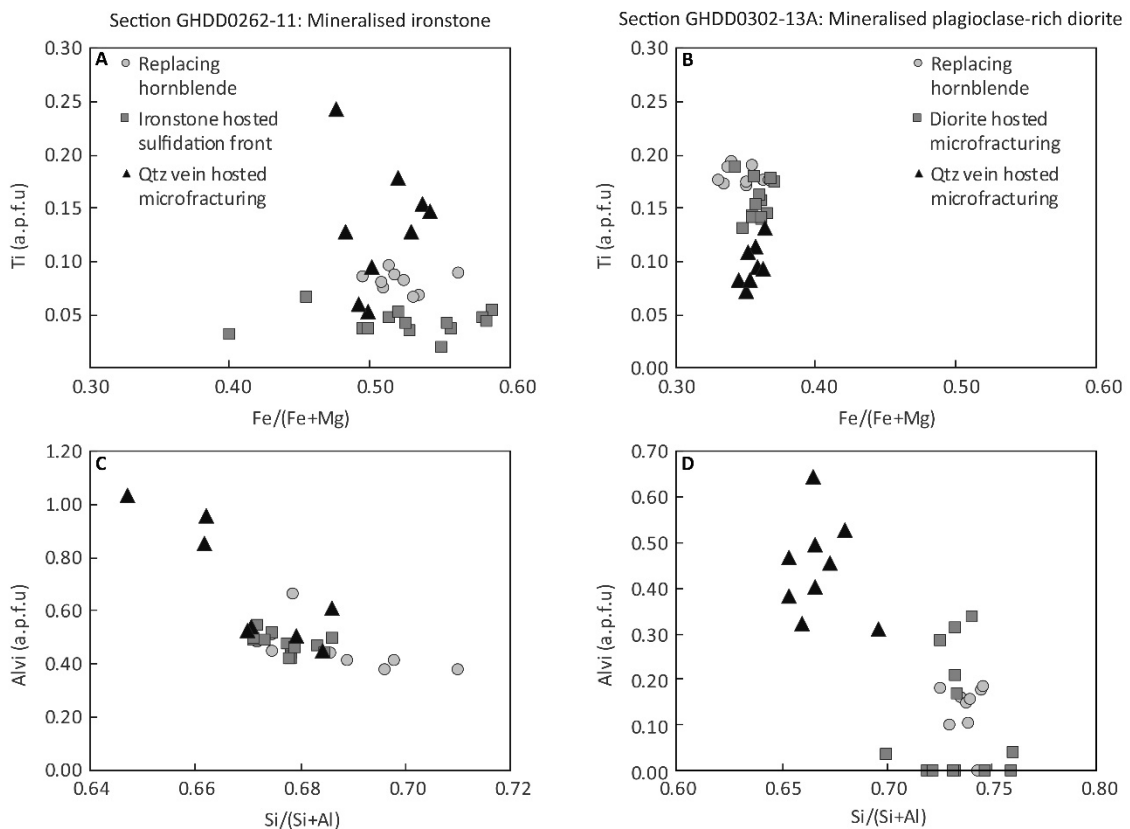


Figure 3.3. Biotite mineral chemistry on the thin section-scale, comparing the composition of texturally regional, mineralised and quartz-vein hosted biotite grains in plagioclase-rich diorite and Mt-rich ironstone. Figure shows Ti vs Fe/(Fe+Mg) and Al^{vi} vs Si/(Si+Al) stoichiometry plots for mineralised ironstone (A, C) and mineralised plagioclase-rich diorite (B, D) respectively. The chemistry of biotite in ironstones and other metasediments is more variable than similar grains in diorite, this variability is also present in grains of the same textural association (i.e., pre-mineralisation metamorphic, sulfidation-associated and micro-fracture hosted).

biotite displays smaller variations, and biotite grains in quartz veins have an almost constant ratio. This suggests that in ironstone, biotite grains in different textural positions did not completely equilibrate during the hydrothermal alteration process, and as a result preserve variable Fe/Fe+Mg ratios, which may or may not be related to their original composition. By comparison, the Fe/(Fe+Mg) ratio for biotite grains in diorite (Fig. 3.3b) is near-constant for grains in all textural positions. This indicates that all generations of biotite grains in diorite equilibrated during the hydrothermal overprint and achieved similar Fe/Fe+Mg ratios. The difference in equilibration behaviour of biotite in ironstone and diorite is probably due composition and textural effects. In diorite, biotite is the most common ferromagnesian phase (after hydrothermal alteration) and it is relatively homogeneously distributed. Therefore, it is likely that the hydrothermal alteration affected most biotite grains in a similar way. By contrast, laminated ironstone units contain multiple Fe- and

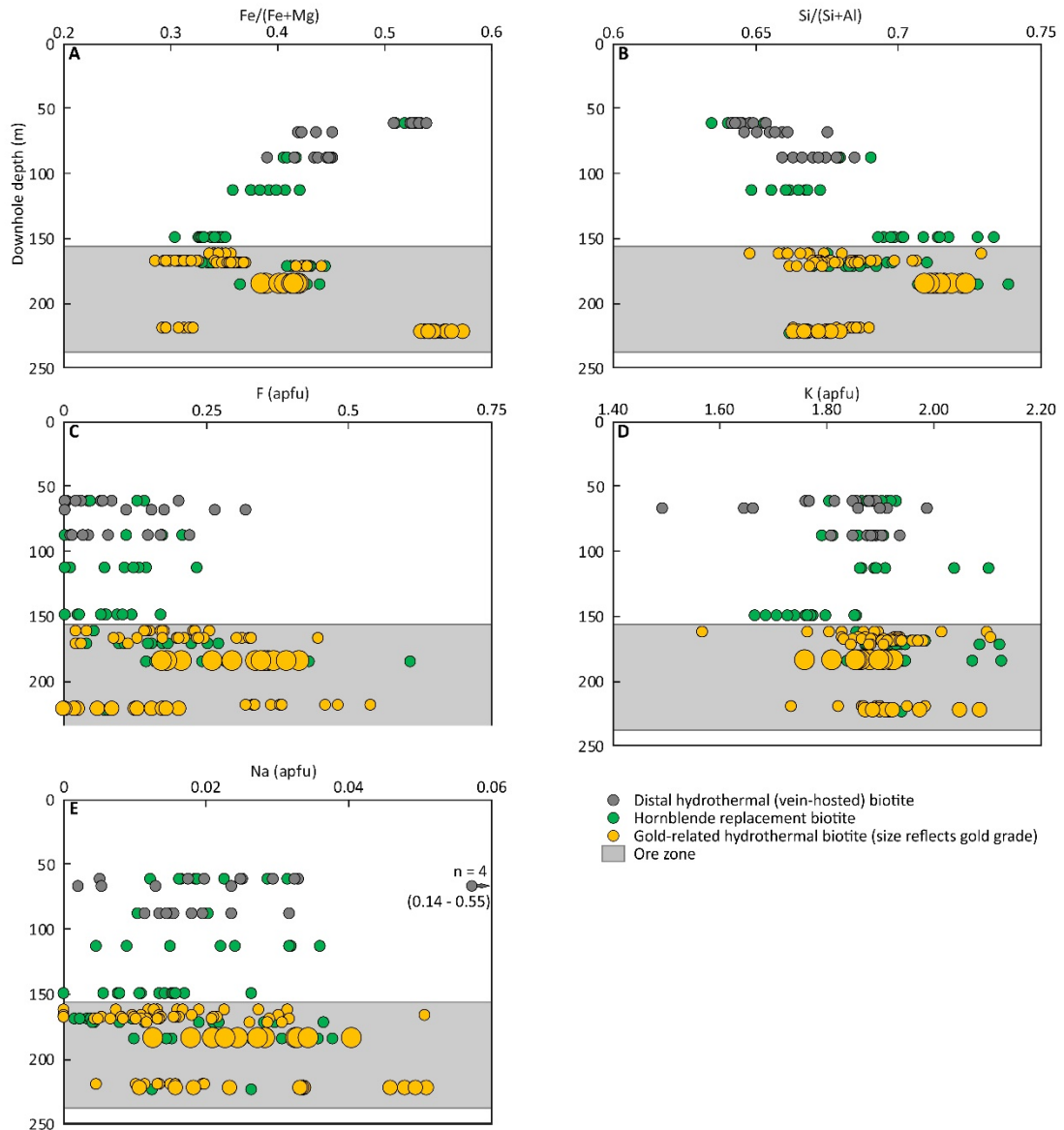


Figure 3.4. Major element geochemistry of biotite along a drill-hole intersecting the ore zone. Approaching the ore zone there is a progressive decrease in the $Fe/(Fe+Mg)$ ratio (A) and an increase in the $Si/(Si+Al)$ ratio (B). Fluorine content sharply increases at the ore zone boundary (C) whereas the K (D) and Na (E) content of biotite remains relatively constant.

Mg-bearing minerals (i.e. magnetite, pyrrhotite, biotite, actinolite), and it is likely that the interaction of the hydrothermal fluids with the biotite grains and the host rock minerals was more diverse, resulting in a wider compositional range. The level of silica enrichment is similar in grains from diorite and ironstone (Fig. 3.3c, d), but the Al^{vi} content is more variable in ironstone-hosted biotite due to the substitution of Fe^{3+} in the octahedral sites.

To understand how the biotite composition varies across the deposit, I will only compare biotite from rocks with a similar bulk composition. Only the plagioclase-rich diorite dykes are

suitable for this purpose, also considering their abundance across the deposit (Sanislav et al., 2016; Fig. 1.2). The fact that in the plagioclase-rich diorite, biotite grains in different textural positions have similar compositions (Fig. 3.3) makes this rock type ideal for comparing compositional variations at the deposit scale. Therefore, only biotite grains from plagioclase-rich diorite to discuss biotite will be used when assessing the compositional changes in biotite across the deposit.

The Fe/(Fe+Mg) ratio changes significantly with proximity to the ore zone (Fig. 3.4a). Distal to the ore zone the Fe/(Fe+Mg) ratio is between 0.50 and 0.55, and it decreases with to as low as 0.29 within the mineralised zone. That is, biotite becomes more Mg-rich with proximity to the ore zone. The biotite also becomes Si-rich and Al-poor with proximity to the ore zone (Fig. 3.4b). This change is illustrated by an increase in the Si/(Si+Al) ratio, and a corresponding decrease in Al_{total} towards the ore zone. Outside the ore zone, the Al_{total} content of biotite is consistently above 2.5 apfu, whereas in the ore zone it drops below this value and can be as low as 1.69 apfu. This relationship correlates with the observed silicification of the host rock within the ore zone where many biotite grains have no Al in the octahedral sites. Outside the ore zone the F content of biotite varies from values below detection limits to as high as 0.32 apfu (Fig. 3.4c). There is no systematic change of F content with proximity to the ore zone, however, within the ore zone, the F content of biotite shows an increase with some biotite grains recording more than 0.6 apfu F. There are no clear changes in the K and Na content of biotite with proximity to the mineralised zone (Fig. 3.4e, f).

3.4.5. *Biotite halogen chemistry*

3.4.5.1. *Log (X_{Cl}/X_{OH}) and log (X_F/X_{OH}) in biotite*

Zhu and Sverjensky (1992) showed that biotite phenocrysts which formed under similar temperature, pressure, and fluid composition conditions, display linear trends on log (X_{Cl}/X_{OH}) and log (X_F/X_{OH}) vs. X_{Mg} and X_{Fe} plots (Fig. 3.5) due to crystal chemical effects only (Munoz and Swenson, 1981; Munoz, 1990). The biotite grains from Geita Hill define linear trends on the log(X_{Cl}/X_{OH}) vs X_{Fe} and X_{Mg} plots (Fig. 3.5a, b), but with a broad scatter, whereas on log (X_F/X_{OH}) vs. X_{Mg} and X_{Fe} plots (Fig. 3.5c, d) they are widely scattered without any clear linear trends. Overall, mineralised and non-mineralised biotite display a similar variation in log (X_{Cl}/X_{OH}) and log (X_F/X_{OH}) values. Biotite grains from mineralised zones have log(X_{Cl}/X_{OH}) and log (X_F/X_{OH}) values that vary from -3.13 to -1.96, and

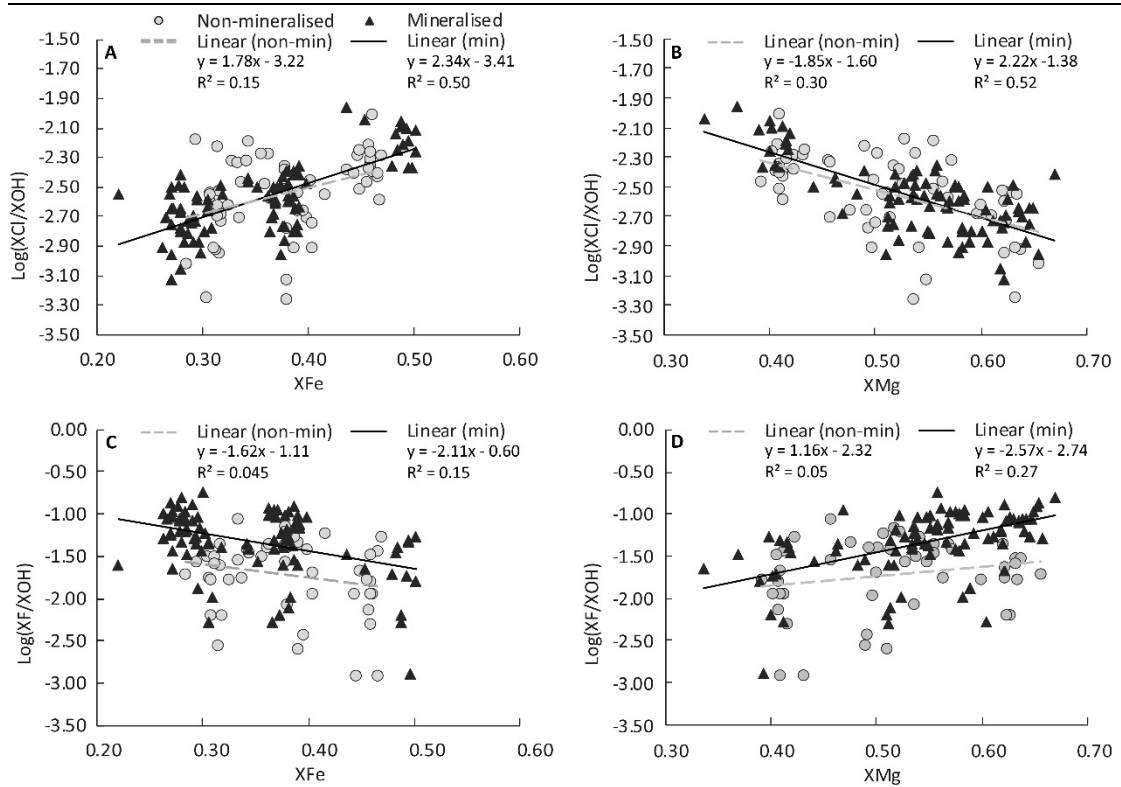


Figure 3.5. Biotite halogen chemistry following calculations by Zhu and Sverksky (1992). The values X_{Fe} and X_{Mg} are the relative proportion of Fe and Mg respectively in all octahedral sites. Both mineralised and non-mineralised biotite shows similar linear trends on $\text{Log}(XCl/XOH)$ vs X_{Fe} and X_{Mg} (A, B), but these linear trends break down when plotting $\text{Log}(XF/XOH)$ vs X_{Fe} and X_{Mg} (C, D).

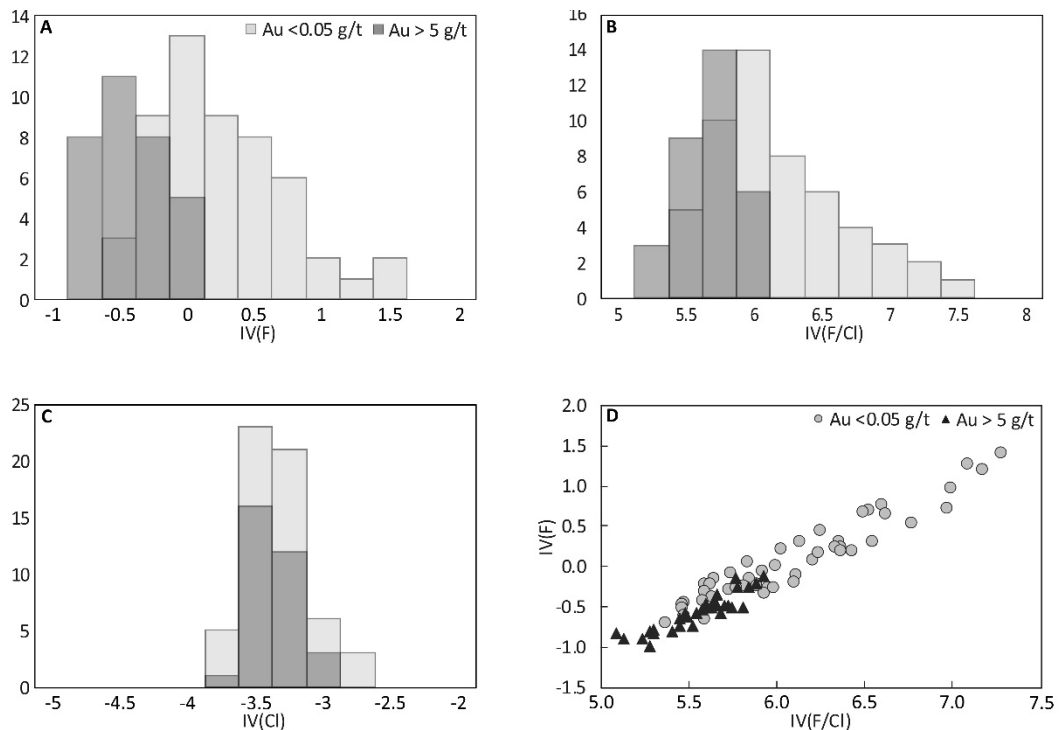


Figure 3.6. Calculated halogen intercept values for biotite grains hosted in mineralised ($>5.0 \text{ g/t Au}$) and non-mineralised ($<0.5 \text{ g/t Au}$) plagioclase-rich diorite. The calculated $IV(F)$ and $IV(F/Cl)$ intercepts (A and B respectively) for biotite within the ore zone (mineralised) are systematically lower than away from the ore zone (non-mineralised), whereas the $IV(Cl)$ intercepts do not change with proximity to the ore zone. This is consistent with biotite grains within the ore zone being enriched in F, irrespective of textural position.

-2.29 to -0.75 respectively, whereas biotite grains from non-mineralised zones yield $\log(X_{Cl}/X_{OH})$ and $\log(X_F/X_{OH})$ values that range from -3.26 to -2.01, and -2.91 to -1.06, respectively. These values indicate that for Cl, hydrothermal biotite precipitated in near-equilibrium with older metamorphic biotite grains, which suggests that the hydrothermal fluid had a similar Cl activity to the metamorphic assemblage. In contrast, the elevated (X_F/X_{OH}) values of mineralised biotite are significantly different from metamorphic grains, implying precipitation from a fluid with a higher F activity.

3.4.5.2. *The F and Cl intercept values*

The F content of biotite is partly influenced by the Fe/Mg ratio of biotite (Munoz, 1984; 1990; Zhu and Sverjensky, 1992), which in turn is controlled by the bulk rock composition, temperature and fluid. Experimental work (e.g., Munoz and Ludington, 1974; Munoz, 1984; Volfinger et al., 1985; Volfinger and Pascal, 1989) indicates that under similar conditions, Mg-rich biotite incorporate more F whereas Fe-rich biotite incorporate more Cl. These observations were described as the “Mg-Cl avoidance rule” and the “Fe-F” avoidance rule”. To account for the control of the Fe/Mg ratio on the incorporation of F and Cl into the biotite structure, Munoz (1984) developed the concepts of F and Cl intercept values. The F and Cl intercept values $IV(F)$ and $IV(Cl)$ and the F/Cl intercept value $IV(F/Cl)$ can be used to correct for the effect of the Fe/Mg ratio on the relative abundance of F or Cl in biotite (Munoz, 1984). Thus, the relative degree of F and Cl enrichment in biotite can be expressed with a single numerical value and biotite grains with different Mg/Fe ratios can be compared directly based on their intercept values. For example, increased enrichments in F correspond to decreased $IV(F)$. The $IV(F)$, $IV(Cl)$ and $IV(F/Cl)$ can be estimated with the following equations:

$$IV(F) = 1.52X_{Mg} + 0.42X_{An} + 0.20X_{Sid} - \log(X_F/X_{OH}) \quad (3.1)$$

$$IV(Cl) = -5.01 - 1.93X_{Mg} - \log(X_{Cl}/X_{OH}) \quad (3.2)$$

$$IV(F/Cl) = IV(F) - IV(Cl) = 3.45X_{Mg} + 0.41X_{An} + 0.20X_{Sid} - \log(X_F/X_{Cl}) + 5.01 \quad (3.3)$$

in which X_{An} and X_{Sid} are molar fractions of annite and siderophyllite. The biotite grains in the mineralised zone show limited variation in $IV(F)$, $IV(Cl)$ and $IV(F/Cl)$ values compared to biotite grains in non-mineralised rocks (Fig. 3.6). The $IV(F)$ values in the mineralised zone range from -0.11 to -0.99 (mean = -0.56), the $IV(Cl)$ values range from -3.15 to -3.88 (mean = -3.49), whereas the $IV(F/Cl)$ values range from 5.09 to 5.92 (mean = 5.56). Biotite grains in non-mineralised rocks have

IV(F) values between -0.69 and 1.43 (mean = 0.11), IV(Cl) values between -3.89 and -2.79 (mean = -3.45) and IV(F/Cl) values between 5.36 and 7.27 (mean = 6.10). Figure 3.5d shows biotite compositions in the mineralised and non-mineralised zones plotted with respect to IV(F) vs. IV(F/Cl). All biotite grains plot along the same trend line with little scatter and display a well-defined positive correlation with IV(F) and IV(F/Cl) values being lowest in mineralised biotite.

3.4.5.3. The fugacity ratios $\log(f_{\text{H}_2\text{O}}/f_{\text{HF}})$, $\log(f_{\text{H}_2\text{O}}/f_{\text{HCl}})$ and $\log(f_{\text{HF}}/f_{\text{HCl}})$

The F and Cl content of biotite can be used to estimate the $\log(f_{\text{H}_2\text{O}})/(f_{\text{HF}})$, $(f_{\text{H}_2\text{O}})/(f_{\text{HCl}})$, and $(f_{\text{HF}})/(f_{\text{HCl}})$ ratios (Munoz, 1992) using the following equations:

$$\text{Log}(f_{\text{H}_2\text{O}})/(f_{\text{HF}})^{\text{fluid}} = 1000/T(2.37 + 1.1(X_{\text{Mg}})^{\text{bio}}) + 0.43 - \log(X_{\text{F}}/X_{\text{OH}})^{\text{bio}} \quad (3.4)$$

$$\text{Log}(f_{\text{H}_2\text{O}})/(f_{\text{HCl}})^{\text{fluid}} = 1000/T(1.15 + 0.55(X_{\text{Mg}})^{\text{bio}}) + 0.68 - \log(X_{\text{Cl}}/X_{\text{OH}})^{\text{bio}} \quad (3.5)$$

$$\text{Log}(f_{\text{HF}})/(f_{\text{HCl}})^{\text{fluid}} = 1000/T(1.22 + 1.65(X_{\text{Mg}})^{\text{bio}}) + 0.25 - \log(X_{\text{F}}/X_{\text{Cl}})^{\text{bio}} \quad (3.6)$$

in which T is the temperature in Kelvin at which the halogen exchange takes place. Fugacity ratios for hydrothermal fluids associated with biotite in the mineralised zone and in non-mineralised rocks were calculated based on a temperature of 375 °C. This temperature is based on estimates by Borg (1994) and van Ryt et al. (2017) and from fluid inclusion studies (Chapter 5). Biotite grains in the mineralised zone yield $\log(f_{\text{H}_2\text{O}}/f_{\text{HF}})$ values that range between 5.8 and 6.4 (mean = 6.11), $\log(f_{\text{H}_2\text{O}}/f_{\text{HCl}})$ values between 5.2 and 6 (mean= 5.57) and $\log(f_{\text{HF}}/f_{\text{HCl}})$ values between 11.60 and

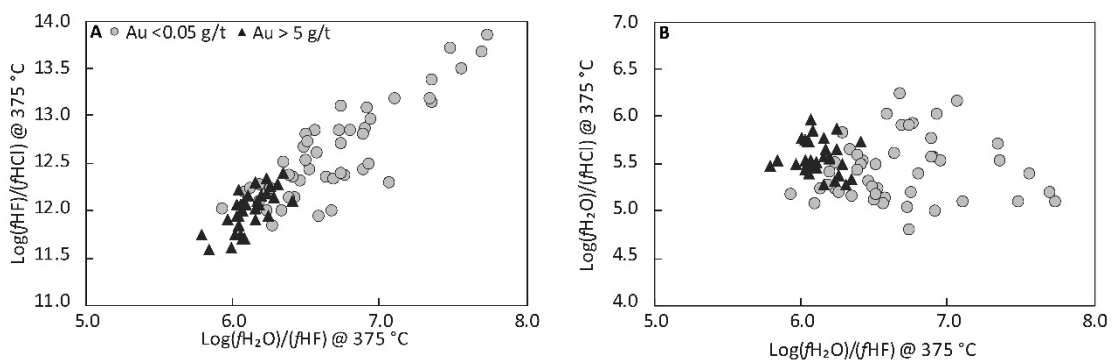


Figure 3.7. Calculated fugacity ratios for biotite grains hosted in mineralised (>5.0 g/t Au) and non-mineralised (<0.5 g/t Au) plagioclase-rich diorite. Plotting $\log(f_{\text{HF}}/f_{\text{HCl}})$ vs. $\log(f_{\text{H}_2\text{O}}/f_{\text{HF}})$ (A) reveals a high HF fugacity within the ore zone, whereas plotting $\log(f_{\text{H}_2\text{O}}/f_{\text{HCl}})$ vs. $\log(f_{\text{H}_2\text{O}}/f_{\text{HF}})$ (B) shows that the HCl fugacity does not change with proximity to the ore zone.

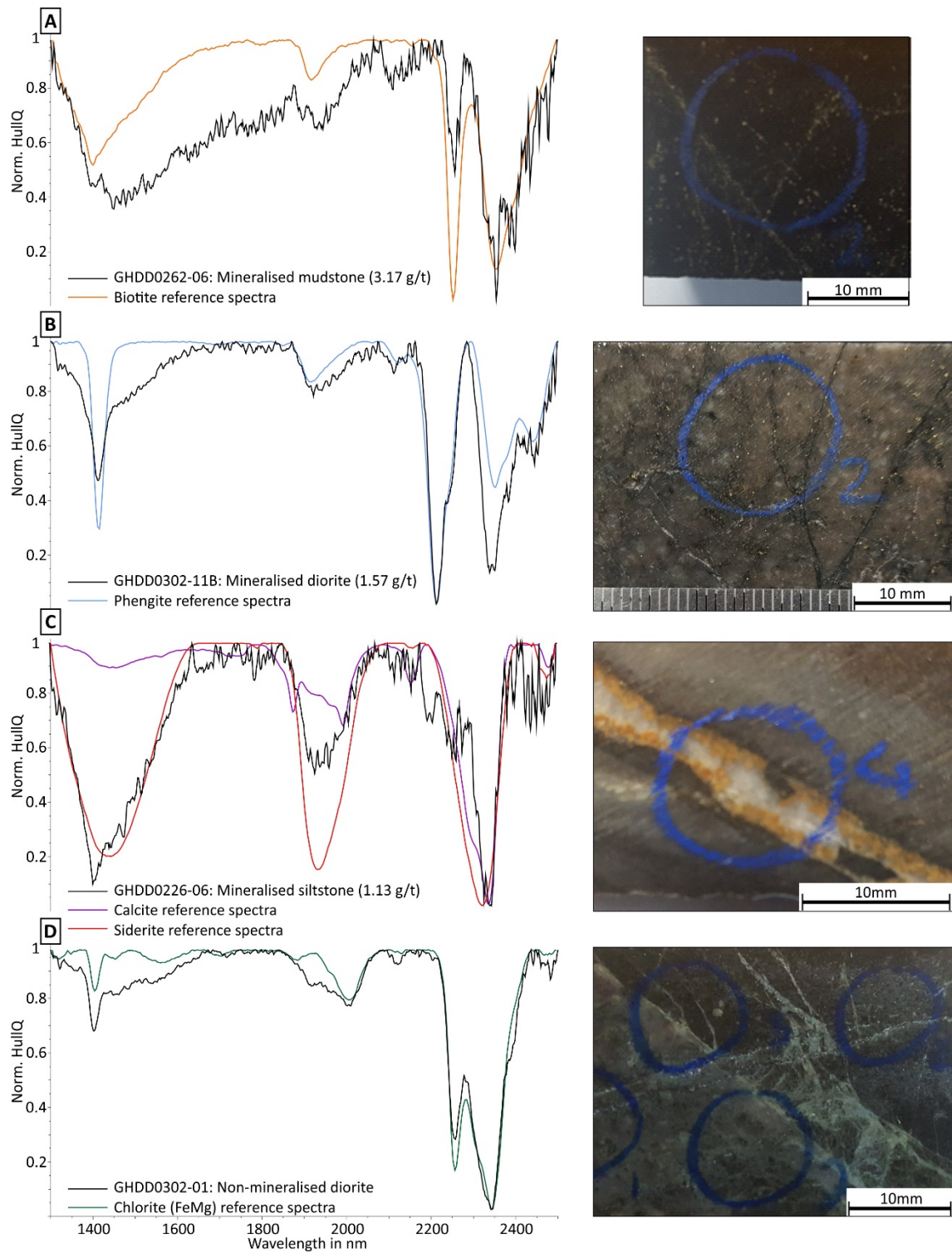


Figure 3.8. : Reflectance spectra with photos of analysed drill core reference spectra from TSG v7.1: A) mineralised micro-fracturing within mudstone; B) mineralised micro-fracturing within diorite; C) carbonate vein overprinting mineralised siltstone; D) Carbonate-chlorite vein overprinting non-mineralised diorite.

12.40 (mean = 12.02). Biotite grains in non-mineralised rocks yield $\log(f\text{H}_2\text{O}/f\text{Hf})$ values between 5.9 and 7.8 (mean = 6.68), $\log(f\text{H}_2\text{O}/f\text{HCl})$ values between 4.8 and 6.3 (mean = 5.43) and $\log(f\text{HF}/f\text{HCl})$ values between 11.85 and 13.85 (mean = 12.61). The $\log(f\text{H}_2\text{O}/f\text{Hf})$ and $\log(f\text{HF}/f\text{HCl})$ values are lowest in the mineralised zone and increase in the non-mineralised rocks (Fig. 3.7a) whereas the $\log(f\text{H}_2\text{O}/f\text{HCl})$ values are the same within error in the mineralised and non-mineralised zones (Fig. 3.7b).

3.5. Short-wavelength infrared spectroscopy (SWIR)

The main metamorphic and alteration minerals in the Geita Hill deposit that can be analysed using short-wavelength infrared spectroscopy (SWIR) are biotite, phengite, calcite, siderite and chlorite (Fig. 3.8). Biotite is the only mineral consistently associated with gold mineralisation, therefore its SWIR spectral variations were of interest for this study. Because chlorite and biotite spectra are similar, petrographic thin sections were prepared for all sites analysed by SWIR to confirm that the samples are free of chlorite and the measured spectra correspond to biotite absorption features. SWIR spectra were collected from the same drill holes and at the same location (i.e. same rock slab) for which biotite compositions were measured. SWIR measurements were performed on all rock types, but the ironstone has very low reflectance and the obtained spectra are of low quality. However, the SWIR spectra collected from all the other rock units are of good quality. I focused this study on the position of the Fe-OH absorption feature, because it is prominent and can be correlated with the chemical composition of biotite (e.g., Laakso et al., 2015; Lypaczewski and Rivard, 2018).

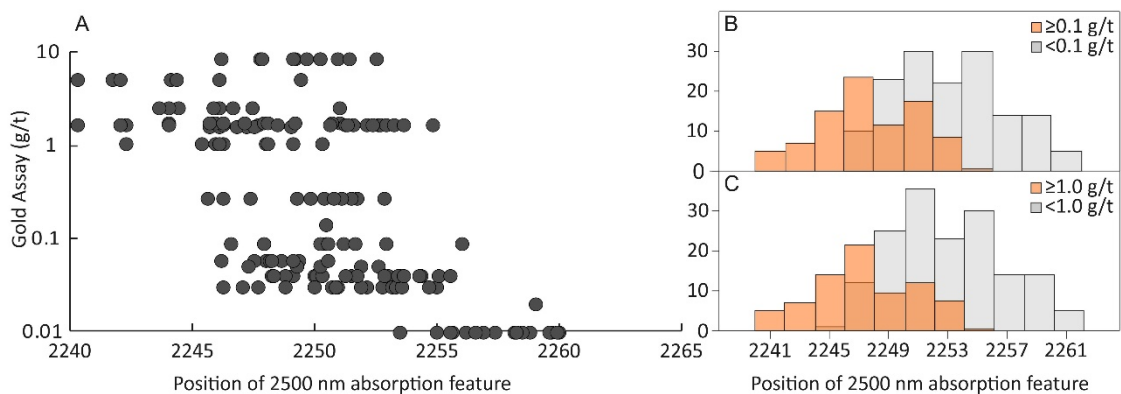


Figure 3.9. Assay grades against SWIR 2250 nm Fe-OH absorption feature position, data is from all diorite varieties at the deposit.

At the Geita Hill deposit, the Fe-OH absorption feature of biotite occupies a continuous range of wavelength positions between 2240 to 2265 nm and correlates well with the gold content of the host rock (Fig. 3.9a). The Fe-OH peak moves to shorter wavelengths in mineralised rocks, and this relationship is consistent for low grade (≥ 0.1 g/t Au; Fig. 3.9b) and high grade (≥ 1 g/t Au; Fig. 3.9c) mineralisation. This relationship is even better illustrated when comparing barren country rocks (< 0.01 g/t Au) with mineralised zones (≥ 1 g/t Au). In the former, the position of the Fe-OH peak varies from 2250 to 2265 nm while in the latter it varies from 2240 to 2255 nm. Figure 3.10. shows a down hole log from a drill hole passing through the middle of the mineralised zone. The measured gold grades are plotted on both side of the log. The right-hand side of the log shows the position of the 2250 nm absorption feature whereas the left-hand side shows the measured (Fe/Fe+Mg) ratio in

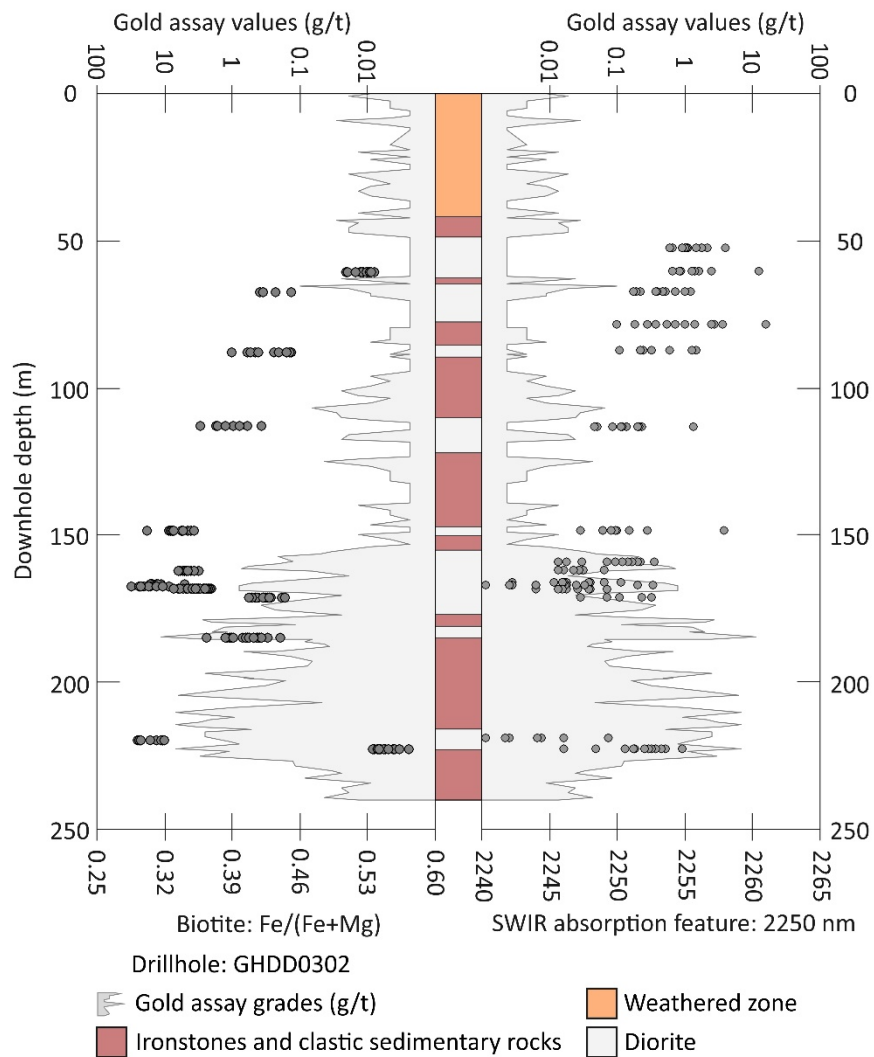


Figure 3.10. Summary diagram showing the relationship between the biotite Fe/(Fe+Mg) ratio and the 2250nm Fe-OH absorption feature plotted against downhole depth.

biotite grains from diorite. The position of the Fe-OH absorption peak shifts to lower values with proximity to the ore zone and reaches the lowest values within the ore zone. This shift is mirrored by a shift in the biotite composition, with biotite grains becoming more Mg rich towards the ore zone, and the lowest Fe/(Fe+Mg) values for biotite recorded in the ore zone.

3.6. Discussion

The data presented above suggests that the hydrothermal fluids responsible for the gold mineralisation at the Geita Hill deposit have interacted with igneous and metamorphic biotite, changed its chemistry and left a geochemical footprint that can be used to assess the nature of these fluids in the genesis of the Au mineralisation. Moreover, the wide distribution of biotite and its susceptibility to interact with the hydrothermal fluids can be used as a vectoring tool in exploration.

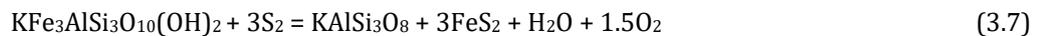
3.6.1. *Fluid control on biotite compositional variations*

3.6.1.1. *Fe/Fe+Mg ratio*

The Fe/Fe+Mg ratio of biotite appears to be decreasing with proximity to the ore zone with the minimum values observed within the ore zone (Fig. 3.4a). Similar trends have been observed in a number of porphyry (e.g., Munoz, 1984; Loferski and Ayuso, 1995; Selby and Nesbitt, 2000; Yavuz, 2003), lode gold (e.g., Bath et al., 2013) and intrusion-related deposits (e.g., Gaillard et al., 2018). Bulk chemistry, temperature and fluids are the main controls on biotite chemistry. To overcome the bulk chemistry effect, I used only biotite grains from plagioclase-rich diorite dykes and sills. These diorite bodies have almost identical mineralogy and geochemistry across the deposit so that I can assume that the changes in biotite chemistry, with proximity to the ore zone, reflect changes in temperature and/or fluids composition. Moreover, in diorite, the Fe/Fe+Mg ratio for all textural biotite types (Fig. 3.3) shifts in a similar manner. The host rocks of the Geita Hill deposit were metamorphosed at greenschist facies conditions with peak mineral assemblages being defined by biotite, actinolite and K-feldspar (Borg, 1994; Sanislav et al 2016; van Ryt et al., 2017). The alteration assemblage related to the gold mineralisation contains the same mineralogical association with the addition of sulfide minerals, Au, telurides and intense silicification. This indicates that the temperature of the

mineralising fluids during hydrothermal alteration was similar to the peak temperatures attained during regional metamorphism (Borg, 1994; Sanislav et al 2016; van Ryt et al., 2017).

This leaves the reaction of biotite with hydrothermal fluids as the only remaining variable to explain the change in biotite chemistry during hydrothermal alteration. The core of the mineralised zone is highly silicified and sulfidised, with the intensity of alteration decreasing away from the ore zone. The overlap in spatial distribution of silicification, sulfidation and changed biotite compositions suggests that the change in biotite chemistry is directly related to the processes that resulted in sulfidation and silicification of the host rocks during mineralisation. In the ironstones, sulfidation occurs by direct replacement of magnetite and pyrrhotite by pyrite (Sanislav et al., 2015; van Ryt et al., 2017). In diorite, pyrite is everywhere associated with biotite (Fig. 3.1e) indicating that the sulfidation of diorite occurred by the reaction of sulphur in hydrothermal fluid with the annite component of biotite, and Fe precipitated as FeS₂ close to the place where it was released from the biotite lattice. The reaction responsible for the sulfidation of plagioclase-rich diorite can be written as:



in which the annite end-member of biotite reacts with sulphur to form K-feldspar and pyrite. The net effect of this reaction is to decrease the Fe/Fe+Mg ratio of biotite within the mineralised zone. Since there is no evidence of a temperature gradient, the change in biotite chemistry with proximity to the ore zone is most likely related to the existence of a sulphur fugacity gradient that increases towards the ore body at constant temperature. Equation (3.7) above also indicates that with increasing sulphur activity, K-feldspar is produced at the expense of biotite, the stability field of pyrite is expanded, and the hydrothermal fluid becomes potentially more oxidised. This is confirmed by the mineralogy of the most altered diorite samples, from the core of the mineralised zone, which are dominated by quartz, K-feldspar and pyrite with only traces of biotite left. The lack of white micas and magnetite combined with the abundance of K-feldspar suggests that the hydrothermal fluid was mildly acidic to neutral (Gaillard et al., 2018), whereas the lack of hematite and sulphate minerals is consistent with a reduced fluid.

3.6.1.2. The halogen chemistry

Experimental data suggests that biotite grains that formed under the same T, P and fluid composition will delineate linear trends on the $\log(X_{\text{Cl}}/X_{\text{OH}})$ and $\log(X_{\text{F}}/X_{\text{OH}})$ vs. X_{Fe} or X_{Mg} diagrams due to crystal chemical effects (e.g., Munoz and Swenson, 1981; Munoz, 1990; Zhu and Sverjensky, 1992). If the P, T and fluid composition differ, the biotite composition will show scatter and depart significantly from the linear trends. The biotite grains from mineralised and non-mineralised zones in the Geita Hill deposit show linear trends on the $\log(X_{\text{Cl}}/X_{\text{OH}})$ vs. X_{Fe} and X_{Mg} plots (Fig. 3.5a, b), but with a large scatter, whereas on the $\log(X_{\text{F}}/X_{\text{OH}})$ vs. X_{Fe} or X_{Mg} plots (Fig. 3.5c, d) there are no linear trends. Since the overburden pressure is unlikely to have changed during ore formation processes and there is no evidence for a temperature gradient, I interpret the scatter in the dataset to indicate that biotite from mineralised and non-mineralised zones did not equilibrate with a fluid with a single chemistry, but rather records changing fluid conditions during mineralisation. This is consistent with the field observations that mineralisation at the Geita Hill deposit occurs mainly along discrete micro-fracture networks (Sanislav et al., 2015; van Ryt et al., 2017; Fig. 3.1), therefore, the mineralised fluid equilibrated only locally with the host rock. The IV(F) and IV(F/Cl) intercepts provide further constraints on the evolution of fluids during mineralisation. Both values display a much narrower range for the mineralised zone compared to the non-mineralised zone, and are consistent with a significant enrichment in F for biotite grains within the mineralised zone irrespective of their textural position. However, there is a significant overlap between mineralised and non-mineralised zones and biotite from both zones plot on a linear trend on a IV(F) vs. IV(F/Cl) diagram. This relationship can be interpreted as evidence for the existence of two fluids with different levels of F enrichment or as evidence of fluid rock interaction with decreasing F activity away from the ore zone. The linear trend on the $\log(f_{\text{HF}}/f_{\text{HCl}})$ vs. $\log(f_{\text{H}_2\text{O}}/f_{\text{HF}})$ diagram (Fig. 3.7a) can be interpreted in a similar way; i.e. the co-existence of two fluids, one with high HCl fugacity and one with high HF fugacity or as a decrease in HF fugacity away from the ore zone due to interaction with the host rock. The almost constant $\log(f_{\text{H}_2\text{O}}/f_{\text{HCl}})$ values for the mineralised and non-mineralised zones (Fig. 3.7b), but highly variable $\log(f_{\text{H}_2\text{O}}/f_{\text{HF}})$ values are consistent with the co-existence of two fluids. It suggests the pre-existence of a metamorphic fluid that was in equilibrium with biotite with $\log(f_{\text{H}_2\text{O}}/f_{\text{HCl}})$ values of 4.8-6.2, which was overprinted in the mineralised zone by an F-rich hydrothermal fluid that reacted

heterogeneously with the country rock. Within the mineralised zone, biotite grains in equilibrium with this F-rich hydrothermal fluid acquired a relatively homogenous halogen composition whereas in non-mineralised rocks heterogeneous fluid-rock interaction resulted in biotite grains with a more variable halogen composition.

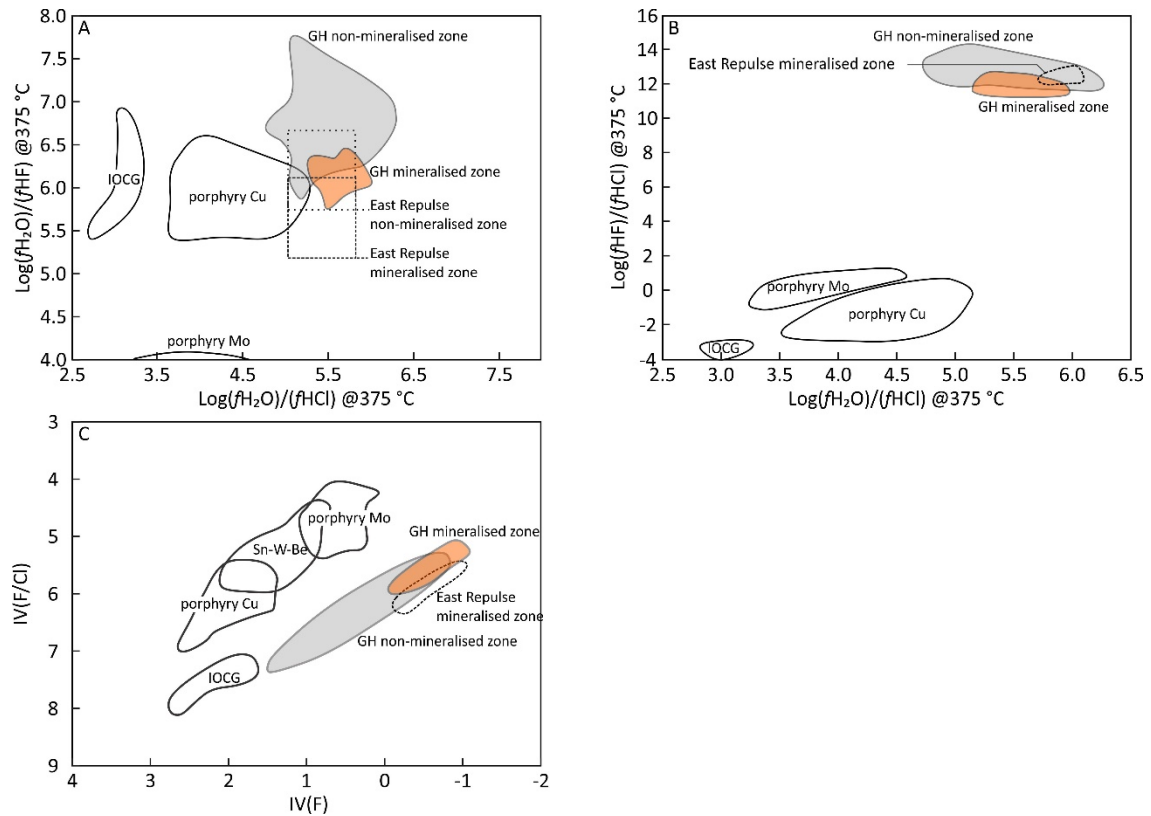


Figure 3.11. Biotite halogen chemistry showing the compositional fields of various deposit types including case studies IOCG (Monteiro et al., 2008), porphyry Mo (Jin et al., 2018), porphyry Cu (Selby and Nesbitt, 2000; Boomeri et al., 2010; Afshooni et al., 2013) and Sn-W-Ba (Munoz, 1984), GH: Geita Hill.

3.6.2. Comparison with other deposit types

A comparison of the biotite halogen geochemistry from the Geita Hill deposit with data from other Archean lode-Au deposits and data from porphyry and IOCG deposits (Fig. 3.11) reveals that the biotite halogen geochemistry is relatively consistent for similar deposit types. For example, IOCG, porphyry-Cu and lode-Au deposits appear to have similar $\text{log}(f\text{H}_2\text{O}/f\text{HF})$ values but different $\text{log}(f\text{H}_2\text{O}/f\text{HCl})$ values (Fig. 3.11a). This indicates that the hydrothermal fluids in equilibrium with biotite had similar $\text{log}(f\text{H}_2\text{O}/f\text{HF})$ values, but different $\text{log}(f\text{H}_2\text{O}/f\text{HCl})$ values. This also suggests that Cl-rich fluids are less common in lode-Au deposits compared to porphyry-Cu and IOCG deposits. Porphyry-Mo deposit (Munoz, 1984; Jin et al., 2018) have much lower $\text{log}(f\text{H}_2\text{O}/f\text{HF})$ values ranging from 3 to 4.5, indicating the presence of F-rich fluids or lowered aqueous fluid activity compared to

porphyry-Cu deposits. The distinction between these different deposit types is even more prominent when taking into account the $\log(f_{\text{HF}}/f_{\text{HCl}})$ values (Fig. 3.11b). These values are in general lower than 0 (negative values) for porphyry-Cu and IOCG deposits, somewhat bit higher (mostly between 0 and 1) for porphyry-Mo deposits, but above 10 for lode gold deposits for which data is available in the literature. Figure 3.11b clearly highlights the important contribution of F-rich hydrothermal fluids in lode-Au deposits compared to Cl-rich hydrothermal fluids in porphyry and IOCG deposits. On the $\text{IV}(\text{F})$ vs. $\text{IV}(\text{F}/\text{Cl})$ diagram (Fig. 3.11c) Archean lode-Au and IOCG deposits are positioned on a linear trend which is sub-parallel with a trend defined by porphyry-Cu, Sn-W-Be and porphyry-Mo deposits. These clear differences in halogen composition for biotite grains from different deposit types indicate that the hydrothermal fluids responsible for the formation of the Geita Hill deposit and possibly other Archean lode-Au deposits were significantly enriched in F and require a distinct source that can generate high-F fluids.

3.6.3. *Fluid source*

Biotite halogen chemistry is a sensitive indicator of hydrothermal and metamorphic processes (e.g., Munoz, 1984; Bath et al., 2013; Gaillard et al., 2018) and as shown in Figure 3.11 is also extremely sensitive to different ore genesis processes. The biotite grains in equilibrium with hydrothermal fluid at the Geita Hill deposit have very low $\text{IV}(\text{F})$ values (-0.11 to -0.99; mean = -0.56) which are consistent with a F-rich hydrothermal fluid. The source of fluids in Archean lode-Au deposits is in general attributed to metamorphic dehydration reactions (e.g., Goldfarb et al., 2005; Phillips and Powell, 2010) although an increasing number of studies point towards a magmatic source (e.g., Kendrick et al., 2011; Bath et al., 2013; Xue et al., 2013). However, it is unlikely that the F-rich hydrothermal fluid in equilibrium with hydrothermal biotite from the Geita Hill deposit was of metamorphic origin. First, the F concentration in fluids from metamorphic environments are low (e.g., Yardley, 1997; Svensen et al., 2001; Sallet et al., 2018). Second, the F-content of biotite increases significantly with metamorphic grade (e.g., Cesare et al., 2008; Finch and Tomkins, 2017) indicating a strong preference of F for the solid phase as opposed to the fluid phase (e.g., Zhu and Sverjensky, 1991; Kusebauch et al., 2015). Most importantly, this shows that dehydration reactions do not release halogens (e.g., Selverstone and Sharp, 2015; Siron et al., 2018) and therefore cannot be the source of the F-rich fluid recorded at the Geita Hill deposit. Moreover, the gold mineralisation post-dates peak metamorphism

and deformation (Sanislav et al., 2014b; Sanislav et al., 2018b). making it difficult to envisage fluids derived from metamorphic dehydration reactions.

The alternative is that the source of the hydrothermal fluid is igneous. The close temporal association between the emplacement of voluminous high-K granites with the timing of gold mineralisation suggests a genetic link (e.g. Sanislav et al., 2015; van Ryt et al., 2017). F-rich hydrothermal fluids from the Archean East Repulse gold deposit in Western Australia (Bath et al., 2013) and from the Canadian Malartic gold deposit (Gaillard et al., 2018) were interpreted to originate from coeval plutonic rocks. Fluorine-rich magmas are usually late or post-tectonic, evolved melts, generated in middle to lower crust (e.g., White et al., 1986; Sallet et al., 1997; Sallet, 2000). The high-K and high silica granites that are coeval with the gold mineralisation in Geita Greenstone Belt were emplaced late during tectonism as they overprint all ductile fabrics (Sanislav et al., 2014b; Sanislav et al., 2018b). They represent the last stage of a progressive crustal reworking process by successive partial melting events that lasted almost 150 Ma (Sanislav et al., 2018a). They are ferroan, alkali-calcic to calc-alkalic granites in the classification of Frost and Frost (2010) and formed mainly by partial melting of tonalite to granodiorite crust (Sanislav et al., 2018a). Thus, they have the right characteristics to generate the high-F fluids observed at the Geita Hill deposit. For example, Sallet (2000) measured IV(F) values between -1 and 1.5 from similar types of granite, which demonstrates their capacity to produce F enriched melts that can generate F-rich hydrothermal fluids.

3.6.4. *SWIR as a tool for vectoring towards mineralisation*

The decrease in Fe/Fe+Mg ratio in biotite grains from Geita Hill with proximity to the gold mineralisation is not unusual in mineral deposits. Similar changes have been observed in other deposits including volcanogenic massive sulfide deposits (e.g., McLeod et al., 1987; Herrmann et al., 2001; Jones et al., 2005; van Ruitenbeek et al., 2012; Laakso et al., 2016), porphyry deposits (e.g., Munoz, 1984; Selby and Nesbitt, 2000; Boomeri et al., 2010; Afshooni et al., 2013; Dalm et al., 2014; Dalm et al., 2017), lode-gold (e.g., Bath et al., 2013) and intrusion-related gold deposits (Gaillard et al., 2018). It has been shown that the change in the Fe/Fe+Mg ratio in biotite with proximity to gold mineralisation can be traced using SWIR (Fig. 3.10) by monitoring the position of the 2250 nm Fe-OH absorption feature. One problem may arise from the interference with chlorite, which has a strong absorption feature in the same spectral range (McLeod et al., 1987; Scott et al., 1998; Jones et al.,

2005) and may interfere with or mask the biotite signal. Another issue is the presence of biotite in different textural positions, however, as discussed, the Fe/Fe+Mg ratio of diorite hosted biotite shifts in a similar manner irrespective of the textural type. This makes the plagioclase-rich diorite ideal for using SWIR to track the change in biotite chemistry with proximity to mineralisation. For the Geita Hill deposit sulfidation is the main process that affects the Fe/Fe+Mg ratio of biotite, therefore the change in the 2250 nm SWIR peak to lower values also correlates with increased pyrite content and gold grade. Since in many deposits the hydrothermal alteration is related not only to a sulphur fugacity gradient, but also to a temperature gradient that may or may not correlate in space and time, a thorough petrological and alteration study is recommended before SWIR can be used to track mineralised zones.

3.7. Conclusions

The host rocks of the Geita Hill deposit contain different types of biotite that occur in different textural positions. These include: (a) metamorphic and hydrothermal biotite in ironstones; and (b) igneous, metamorphic and hydrothermal biotite in diorite. Biotite appears to be a sensitive tracer for hydrothermal fluids. However, data presented here indicates that the composition of biotite grains from ironstone, irrespective of their textural position, is heterogeneous and mainly influenced by local compositional variations in host rock chemistry rather than the interaction with hydrothermal fluids. Systematic changes in the chemistry of ironstone-hosted biotite with proximity to mineralisation were not observed. In this case, proximity to mineralisation is best indicated by the appearance of hydrothermal biotite, an increase in the pyrite content and silicification. In contrast, the chemistry of diorite-hosted biotite of all textural types is changing in a predictable manner with proximity to the ore zone, which suggests that the hydrothermal fluids exercised a strong control on the biotite composition. Thus, biotite becomes progressively enriched in Si, Mg and F with proximity to the ore zone. The systematic increase in Mg content of biotite towards the ore zone can be mapped with SWIR by recording the shift in the 2250 nm peak to lower values. Biotite associated with mineralisation records a high-F content, which indicates interaction with an F-rich hydrothermal fluid. The high-F content of the hydrothermal fluid and the late timing of mineralisation is not consistent with a metamorphic source, and suggest that the hydrothermal fluids at the Geita Hill

deposit are mainly of magmatic origin. Moreover, the halogen content of biotite grains from lode-Au deposits (Fig. 13) appears to be distinct from other deposit types (porphyry, IOCG) suggesting that the fluids involved in the formation of Geita Hill deposit and possibly other Archean lode gold-Au deposits require a source capable of producing high-F fluids.

Chapter 4

Trace element associations in magnetite and hydrothermal pyrite from the Geita Hill gold deposit, Tanzania.

Submitted to the Journal of Geochemical Exploration (in press)

Abstract

Gold mineralisation in the Geita Hill deposit is associated with pyrite formed along micro-fracture networks and sulfidation fronts together with K-feldspar and biotite. The sulfidation fronts are best developed in magnetite-bearing ironstone, while the micro-fractures are concentrated in silicified diorite and Fe-poor sediments. Gold mineralisation is concentrated around lithological contacts and ore-existing structures including sheers and fold hinges. The gold is present mainly as electrum and gold tellurides along grain boundaries, and as inclusions in pyrite, quartz, biotite and K-feldspar. Laser ablation inductively coupled plasma mass spectrometry (LA-ICP-MS) analyses of pyrite and magnetite grains reflect complex fluid-host rock interactions. Magnetite textures and chemistry change with alteration intensity, indicating the progression of the alteration front into the host rock. Pyrite textures are uniform across all rock types and reflect late-tectonic growth linked to multi-staged infiltration of hydrothermal fluids. Trace element distribution patterns in pyrite are locally complex and influenced by host rock chemistry.

Gold distribution patterns in pyrite correlate closely with Te, Ag, Bi and Pb, indicating that gold occurs in micro- and nano-inclusions of telluride minerals. This is especially so for gold in quartz veins, whereas gold in ironstone and diorite also occurs as electrum with an average Au/Ag ratio of 0.41. Arsenic, Co and Ni in pyrite are lattice bound and occur in high concentrations in ironstone and diorite where they show characteristic growth zoning patterns. Pyrite in quartz veins has As, Co and Ni concentrations that are low and variable. Cr, Cu, Mo, Mn and Zn are present in all rock types in isolated inclusions in pyrite grains, whilst Pb, Bi and Sb occur in more dispersed patches of fine clustered inclusions. The Se content in pyrite is typical for Archean gold deposits (~30 ppm), and reflects an average temperature of ~340°C for the mineralising fluid. The Co/Ni ratio of pyrite grains varies between 0 and 5.2 in ironstone and diorite, and most likely reflects the equilibration Co/Ni ratio of the host rock. The Co/Ni ratio of pyrite grains in quartz veins varies between 1 and 12, and is consistent with a magmatic-hydrothermal origin for the ore fluid. Trace element distribution patterns in magnetite and pyrite indicate that As, Ni, Co, Cr, Mn and Cu were mostly locally derived,

and remobilised into the pyrite during sulfidation of the host rock. The concentrations of these elements are strongly lithologically controlled, and they are not consistently incorporated into the pyrite after initial stages of growth. Au, Ag, Te, Bi and Pb were externally derived, and closely correlate in all varieties of pyrite as well as strongly altered magnetite. The alteration footprint of the Geita Hill deposit is limited in extent, and does not involve As and Sb that are typically enriched in Archaean lode-gold systems. Instead, Te and Bi are most characteristic for the deposit and could be of use as path finder elements together with altered magnetite grains.

4.1. Introduction

Pyrite and magnetite are some of the most common accessory minerals in many ore deposits. They form over a large spectrum of geological and hydrothermal conditions and incorporate various trace elements into their structure (e.g., Carew, 2004; Reich et al., 2005; Rusk et al., 2009; Large et al., 2009; Dupuis and Beaudoin, 2011; Ciobanu et al., 2012). Detailed laser ablation inductively coupled plasma mass spectrometry (LA-ICP-MS) studies indicate that the trace element composition of these minerals can be used as a petrogenetic indicator in discriminating ore types, ore fluid composition and determining the physicochemical conditions during mineralisation (e.g., Heimann et al., 2005; Leach et al., 2010; Large et al., 2009; Dupuis and Beaudoin, 2011; Dare et al., 2014; Grant et al., 2018). In most Archean gold deposits, magnetite is part of the host rock assemblage and an important constituent for ironstone-hosted deposits (e.g., Klein, 2005; Junqueira et al., 2007; Sanislav et al., 2015) where it reacts with the mineralising fluids to precipitate sulfides, causing gold to co-precipitate. Pyrite is the most common sulfide mineral in orogenic gold deposits (e.g., Goldfarb et al., 2005; Large et al., 2009; Reich et al., 2016) and can incorporate a wide range of trace metals (As, Co, Ni, Te, Se, Au, Ag, Pb, Bi, Cu, PGE etc.) in its structure, as solid solution and as nano- and micro-inclusions (e.g., Reich et al., 2005; Large et al., 2009; Ciobanu et al., 2012; Hough and Reich, 2011; Grant et al., 2018). Pyrite is stable over a wide range of physicochemical conditions, and resistant to post depositional modifications by metamorphism and fluids (e.g., Craig et al., 1998; Agangi et al., 2013; Román et al., 2019). Because of this, its trace metal composition has been used to trace ocean chemistry through time (e.g., Large et al., 2014), and to understand the chemistry of ore forming fluids in ancient and modern hydrothermal systems (e.g., Deditius et al., 2014; Steadman et al., 2014; Wohlgemuth-Ueberwasser et al., 2015; Reich et al., 2016; Grant et al., 2018; Román et al., 2019).

Some authors (e.g., Large et al., 2009; Winderbaum et al., 2012; Reich et al., 2013; Deditius et al., 2014; Keith et al., 2018) have pointed out that pyrite grains formed in different hydrothermal systems (epithermal, porphyry, Carlin-type, orogenic), record distinct trace metal compositions controlled by the source and host rock composition. As hydrothermal fluids evolve, they have an ability to mobilise, transport and deposit metals in pyrite in response to changing PTX conditions, thereby leaving a record of the hydrothermal history of the deposit (e.g., Tanner et al., 2016; Reich et al., 2016; Tardani et al., 2017).

In orogenic gold deposits, pyrite and arsenopyrite are the most common sulfide minerals that occur in close spatial and temporal association with Au mineralisation (e.g., Reich et al., 2005; Large et al., 2007; Cook et al., 2009; Large et al., 2009; Steadman et al., 2014). Fluid rock interaction and sulfidation of Fe-rich host rocks are the most important sulphide precipitation mechanism (Goldfarb et al., 2005). The mineralising fluids are generally low salinity, CO₂-bearing, with reduced to near neutral pH, and for most Archean deposits fluids range in temperature between 300-400 °C (e.g., Ridley and Diamond, 2000; Goldfarb et al., 2005; Large et al., 2011). Pyrite from orogenic deposits is characterised by complex growth zoning that reflects a multi-stage evolution linked to episodic influx of fluid along structural conduits (e.g., Goldfarb et al., 2005; Large et al., 2007; Cook et al., 2009; Thomas et al., 2011). Detailed studies have shown that pyrite preserves this complex hydrothermal history as different growth phases, highlighted by a heterogeneous distribution of Au and other trace elements (e.g., Large et al., 2007; 2009; Morey et al., 2008; Thomas et al., 2011). Au is commonly found incorporated into pyrite as inclusions of free Au and as Au in solid solution (Mumin et al., 1994; Reich et al., 2005; Large et al., 2009), but when tellurides are present most Au is found as Au-tellurides and free gold inclusions (e.g., Deditius et al., 2014; van Ryt et al., 2017; Keith et al., 2018).

The Geita Hill deposit is a late Archean, structurally controlled gold deposit located in the Geita Greenstone Belt of NW Tanzania (Borg, 1994; Cook et al., 2016). Detailed structural (Borg, 1994; Sanislav et al., 2017) and paragenetic studies (Borg, 1994; van Ryt et al., 2017) proposed that Au mineralisation occurred syn-tectonically, during the late-stage reactivation of pre-existing reverse faults as normal faults. Gold deposition occurred synchronously with the sulfidation of the

wall rock by the reaction of sulphur-rich fluids with magnetite in ironstone and biotite in diorite to form pyrite.

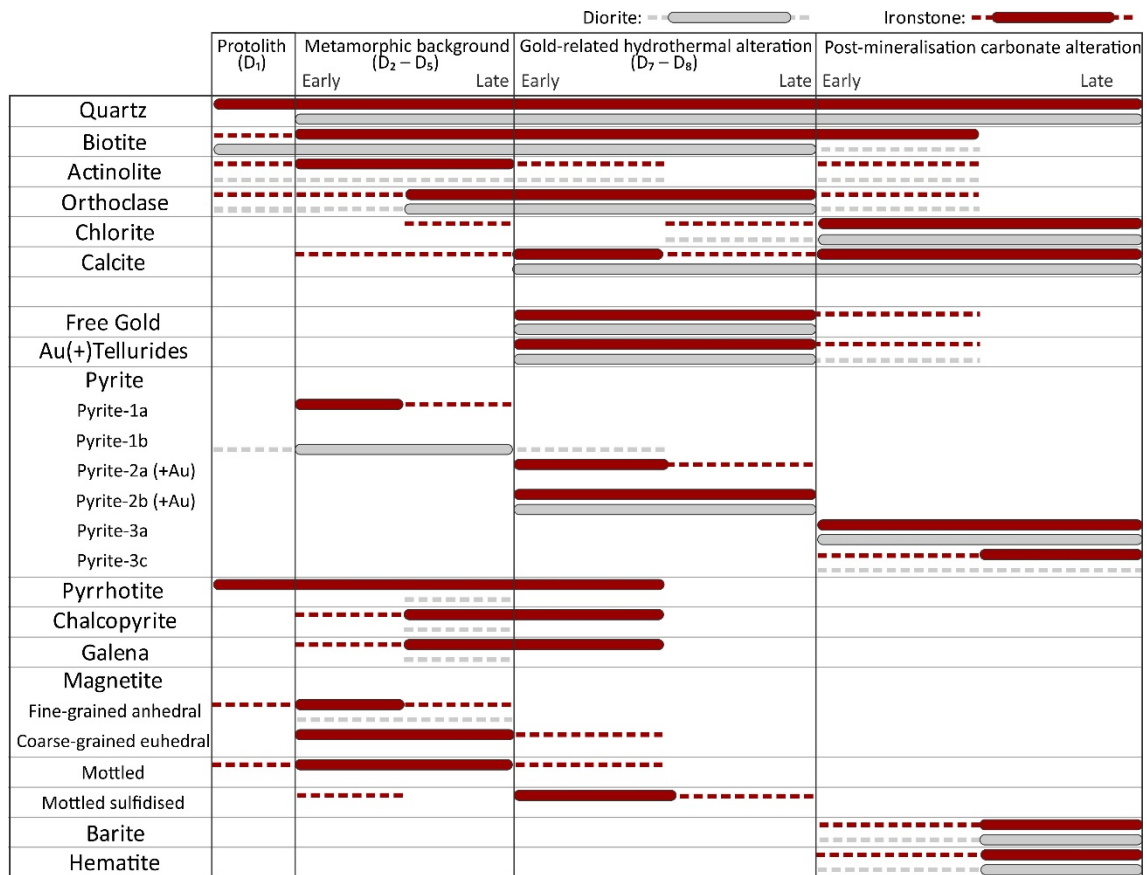


Figure 4.1. Schematic alteration paragenesis of the Geita Hill deposit, with specific reference to major alteration minerals, sulfides and oxides. The varieties of pyrite in this figure correspond to those described in Chapter 2.

In this chapter, I present new geochemical data for pyrite, magnetite and pyrrhotite from the Geita Hill deposit. I will investigate what elements were mobilised with gold and introduced from distal fluids and which elements were mobilised locally from the host rocks, with the aim of better constraining the nature of the mineralising fluids and providing new insights into the processes that lead to the formation of the Geita Hill deposit.

4.2. Alteration and mineral paragenesis

4.2.1. The metamorphic alteration assemblage

The alteration paragenesis for the Geita Hill deposit as presented in Van Ryt et al., (2017) is presented as Chapter 2 in this thesis. This paragenesis is summarised here with respect to the minerals of

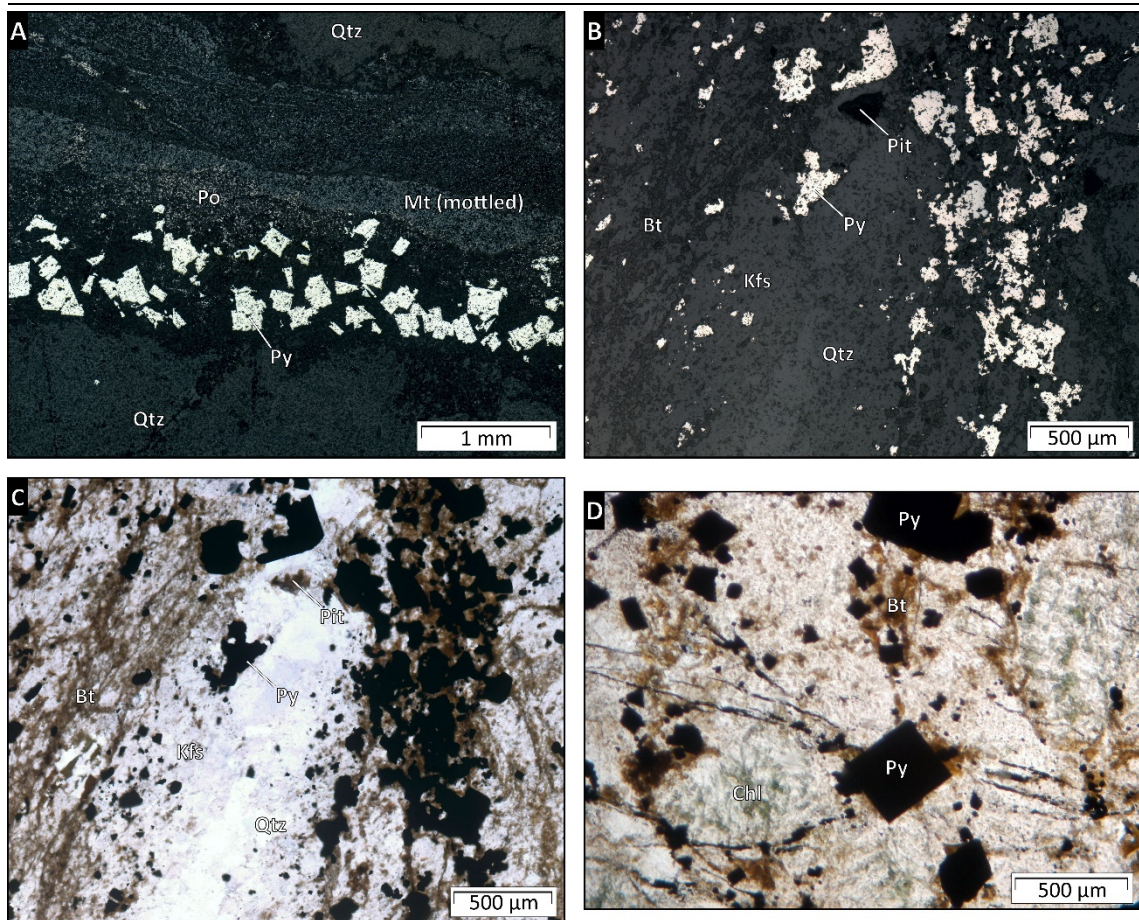


Figure 4.2. Microphotographs of gold-bearing assemblages at Geita Hill: (A) Reflected light (RL) microphotograph of a sulfidation front in ironstone; (B) RL and (C) transmitted light (TL) microphotograph of microfracturing in mudstone; (D) TL microphotograph of microfracturing in diorite.

relevance to this chapter. The peak metamorphic assemblage in the ironstones consists of biotite + K-feldspar + actinolite \pm chlorite \pm magnetite \pm pyrrhotite \pm pyrite \pm carbonates, and formed during the main D₂ – D₃ ductile deformation events synchronously with the emplacement of dioritic dykes and sills that are part of the Nyankanga Intrusive Complex. Magnetite is the primary oxide in the ironstone units. Some magnetite grains contain micron-scale inclusions of pyrite, chalcopyrite, sphalerite and galena. The dominant pre-mineralisation sulfide at Geita Hill is pyrrhotite, which occurs mainly along magnetite bands in ironstones. In diorite, primary hornblende and pyroxene are replaced by metamorphic biotite with accessory K-feldspar, calcite, chlorite, epidote, apatite, pyrite and Fe-oxides. Feldspar grains are selectively sericitised, with anorthite being more affected than albite. Orthoclase and primary biotite, are generally well preserved.

4.2.2. *The gold-related hydrothermal alteration assemblage*

The gold-related alteration is part of a multi-staged hydrothermal event (D_8) that overprinted all rock units and D_{1-7} structures (Fig. 4.1). Pre-mineralisation silicification and carbonatisation is present as veins, and as pervasive alteration around pre-existing shear zones. Mineralisation is associated with the development of silicic, potassic, carbonate and sulfide alteration, the distribution of which is structurally and lithologically controlled. This alteration presents as sulfidation fronts in ironstone (Fig. 4.2a), as disseminated replacement fronts in mudstone and diorite, and as sulfide-bearing micro-fracture networks in diorite, quartz veins and previously silicified units (Fig. 4.2b, c, d).

4.3. Magnetite, pyrrhotite and pyrite textures

Magnetite, pyrrhotite and pyrite are the most common oxide and sulfide phases within the mineralised zone in the Geita Hill deposit. Magnetite and texturally early varieties of pyrrhotite predate the gold mineralisation (Fig. 4.1) but their reaction rims indicate that these minerals interacted with the mineralising fluids and their geochemistry could provide some insights into the nature of these fluids. Pyrite is part of the mineralising assemblage and its chemistry can be used to track fluid-rock interaction and the composition of the hydrothermal fluids.

4.3.1. *Magnetite*

Three textural types of magnetite were observed in meta-ironstones that host the Geita Hill deposit (Fig. 4.1): (1) fine-grained, anhedral to subhedral magnetite (Fig. 4.3a); (2) mottled aggregates of sub-euhedral magnetite grains (Fig. 4.3b, c); and (3) coarse-grained euhedral magnetite (Fig. 4.3d). The fine-grained and mottled magnetite is mainly found in Fe-rich laminae, where magnetite comprises >50% of the rock volume (Fig. 4.3b), whereas coarse euhedral magnetite is restricted to silicate-dominated units (Fig. 4.3d). Mottled magnetite becomes progressively sulfidised with proximity to sulfidation fronts and microscopic inclusions of pyrite, minor pyrrhotite and galena are common (Fig. 4.3c). All magnetite varieties originally formed pre-mineralisation, but the mottled variety is locally strongly affected by hydrothermal overprints.

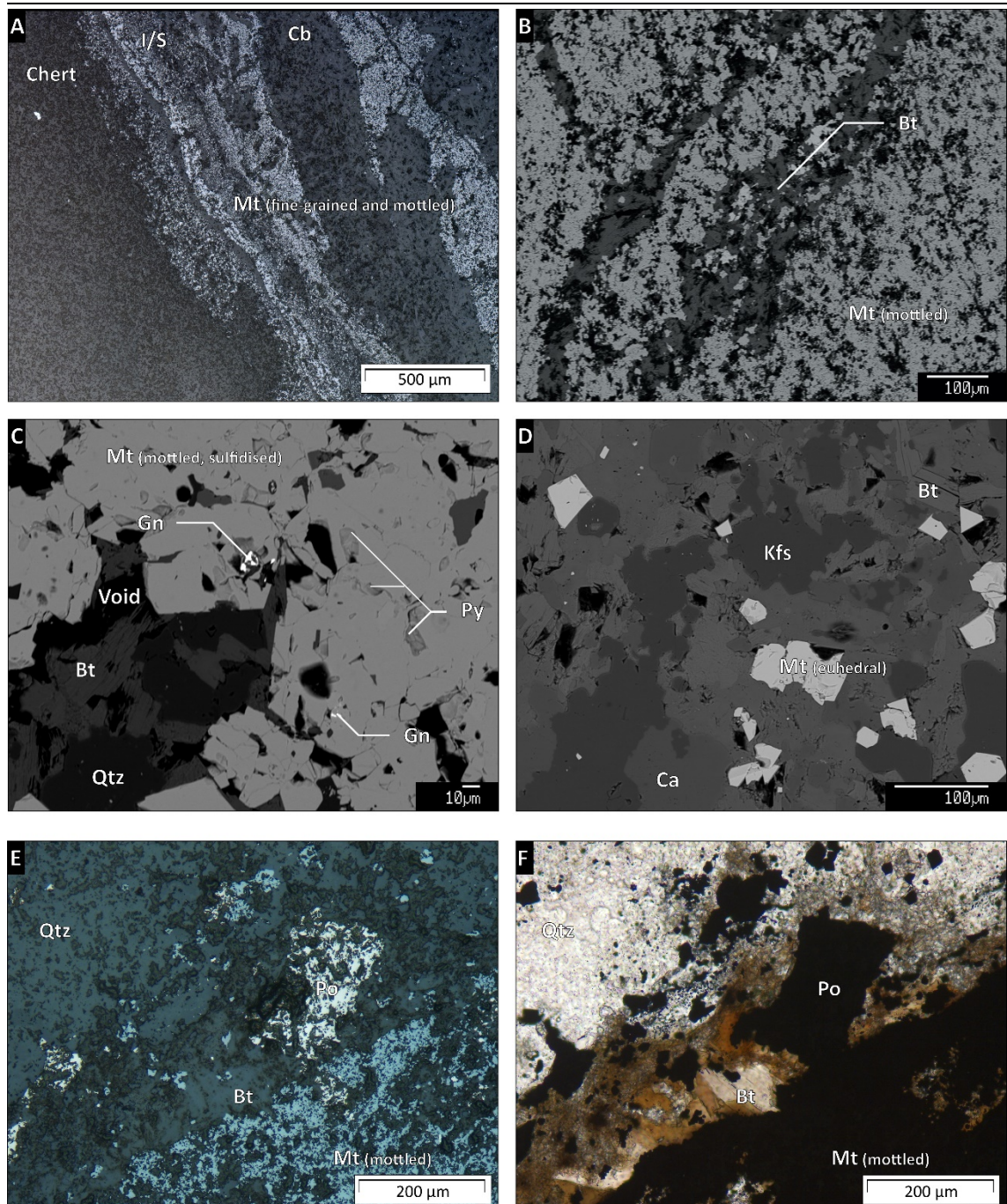


Figure 4.3. Varieties of magnetite and pyrrhotite at Geita Hill: (A) RL microphotograph of fine-grained and mottled magnetite; (B) backscattered electron (BSE) image of mottled magnetite; (C) BSE image of sulfidised mottled magnetite, image taken proximal to a gold-bearing sulfidation front; (D) BSE image of euhedral magnetite; (E) RL microphotograph of gold-bearing pyrrhotite replacing magnetite; (F) TL microphotograph of the same location.

4.3.2. Pyrrhotite

Early, pre-mineralisation pyrrhotite occurs throughout ironstones and magnetite-shale units, where it is concentrated in (and is likely synchronous with) D₁ layer parallel shearing (Sanislav et al., 2017).

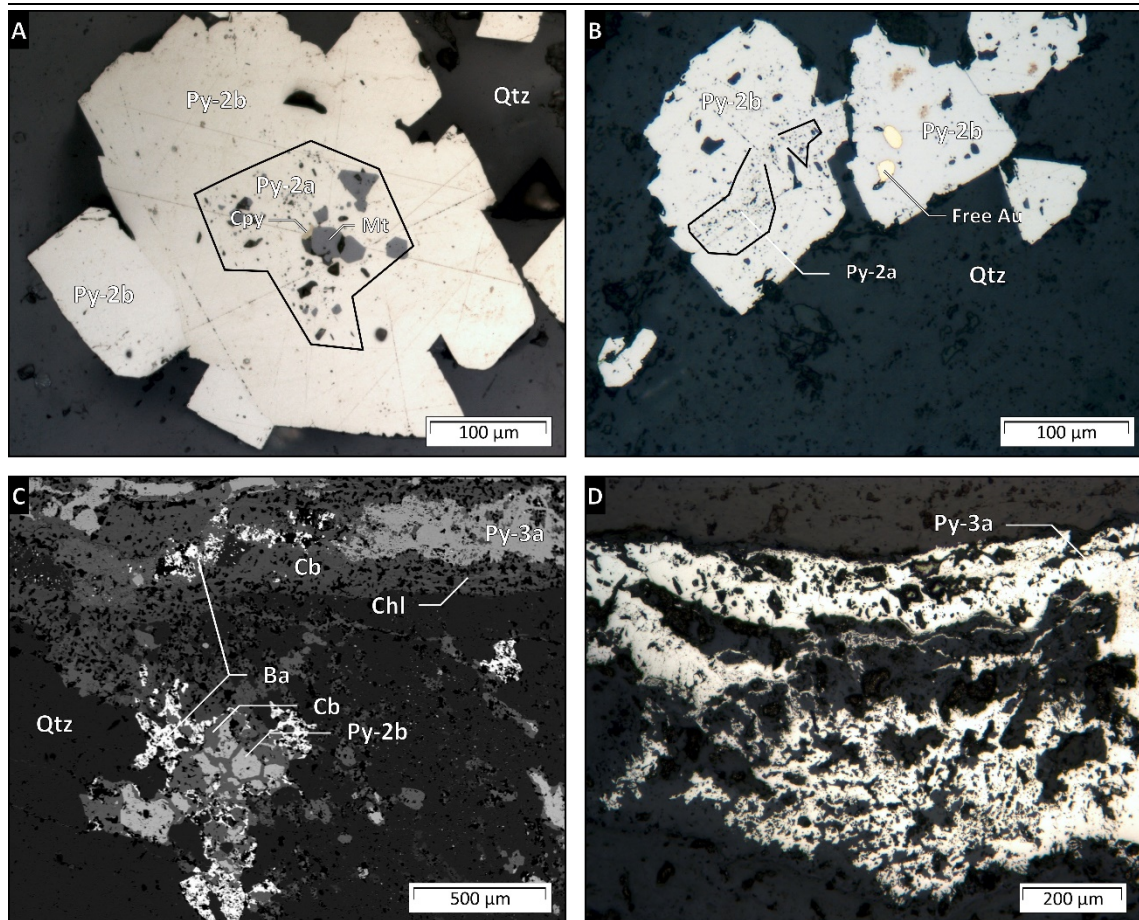


Figure 4.4. Varieties of pyrite at Geita Hill: (A) RL microphotograph of a texturally zoned grain with a core of inclusion rich Pyrite-2a and a rim of inclusion-poor Pyrite-2b; (B) RL microphotograph of Pyrite-2b with visible free-Au; (C) BSE image of a later Cb-Chl-Pyrite-3a vein overprinting and replacing mineralised pyrite-2b; (D) RL microphotograph of the pyrite-3a in the mentioned vein.

Gold-related pyrrhotite occurs as an accessory phase in quartz veins, either as isolated grains or as inclusions in pyrite grains. Pyrrhotite also occurs as anhedral grains along the contact between magnetite-rich laminae and quartz-rich laminae in ironstone (Fig. 4.2a), where it partly replaces and pseudomorphs magnetite (Fig. 4.3e, f), and is in turn locally replaced by hydrothermal pyrite.

4.3.3. Pyrite

Van Ryt et al. (2017) described six textural types of pyrite in the Geita Hill deposit (Fig. 4.1), of which two pre-date mineralisation (Pyrite-1a, b), two formed during mineralisation and are gold-bearing (Pyrite-2a, b) and two post-date mineralisation (Pyrite-3a, b). Pyrite-1a is found in ironstone as small grains, less than 20 µm in diameter, and are included in magnetite grains. Pyrite-1b is found in diorite within relics of mafic phenocrysts replaced by biotite, and varies in size between 10-40 µm.

Mineralised pyrite-2a is found only in ironstones and ironstone-hosted quartz veins, and consists of euhedral to anhedral pyrite grains that contain micron-scale mineral inclusions. These mineral inclusions mainly consist of magnetite, pyrrhotite, quartz and biotite with minor amounts of chalcopyrite, galena, sphalerite and tellurides. No visible gold inclusions were found in pyrite-2a. Pyrite-2b is the most common type of mineralised pyrite in the Geita Hill deposit, is found in all textural settings and consists of inclusion-poor, anhedral to euhedral shaped pyrite grains (Fig. 4.4a). In general, the only visible inclusions found in pyrite-2b are gold grains and tellurides (Fig. 4.4b). It is common for the inclusion-rich, pyrite-2a, to occur as cores, surrounded by an inclusion-poor, pyrite-2b rim, suggesting that the growth of pyrite-2b postdates pyrite-2a.

Pyrite-3a and 3b are associated with late carbonate veins that overprint and post-date the gold-related assemblage. Pyrite-3a is associated with carbonate-chlorite veins, is fine-grained and lacks internal textures visible under the microscope (Fig. 4.4c, d). Pyrite-3b is associated with quartz-carbonate veins, is coarser grained and euhedral in shape. Pyrite-3b appears to preferentially form where quartz-carbonate veins intersect magnetite-rich laminae in ironstone. Neither type of pyrite is systematically mineralised, but Pyrite-3b can locally remobilise gold if it overprints a gold-bearing unit.

4.4. Analytical methods

4.4.1. *Sampling Strategy*

All samples used in this study were collected from the Geita Hill pit and from newly drilled core through the Geita ore zone (Table 4.1). The aim was to sample mineralised pyrite grains with a composition that most likely reflects the composition of the hydrothermal fluid (i.e. pyrite from quartz veins), and compare the composition of these grains with that of gold-bearing pyrite grains from the host rocks (ironstone and diorite). Variably altered magnetite grains found in association with pyrite were compared to provide additional constraints on the mobility of host-rock derived elements. Two samples (GQ-01 and GQ-02) were collected from > 10 m long mineralised quartz veins in the pit, which trend ~ N-S and formed during D₈ extensional deformation (van Ryt et al., 2017). Along the contact between the veins and the host rock a well-developed, sulfide-rich alteration halo

formed. Gold assays for the alteration halo returned 20 g/t Au, suggesting that the veins acted as feeder veins. Two mineralised ironstone samples were used in this study. One sample (GQ-03) was collected from the alteration halo that formed around the quartz feeder veins and one sample (262-11-291.5) was collected from a drill core intersecting the mineralisation. Three samples were collected from drill holes intersecting mineralised diorite dykes.

Table 4.1.

List of samples used for LA-ICP-MS analysis

Sample ID	Drillhole	Depth	Lithology	Alteration
226-02	GHDD-0226	293.0	Diorite	N/A
226-14	"	444.0	Ironstone	N/A
262-06	GHDD-0262	247.3	Mudstone	Silicification, potassification and minor sulfidation
262-07	"	252.3	Diorite	Silicification, carbonatisation and potassification
262-11	"	291.5	Ironstone	Sulfidation, minor silicification and potassification
302-11A	GHDD-0302	159.0	Diorite	Silicification, potassification and post-Au carbonatisation
302-13A	"	168.3	Diorite	Silicification, potassification and carbonatization
GQ-01	Pit sourced (Geita West)		Quartz vein	Silicification, potassification, minor carbonatisation
GQ-01a	"		"	"
GQ-02	Pit Sourced		"	Silicification, potassification and post-Au carbonatisation
GQ-03	"		Ironstone	Sulfidation, silicification and minor potassification

4.4.2. *LA-ICP-MS trace element analysis*

Trace element analysis of magnetite, pyrite and pyrrhotite was conducted following the methodology described by Steadman et al. (2013; 2014). Laser ablation of magnetite and sulfides was conducted using a Coherent GeoPro 193 nm ArF laser, connected to a Varian 820 series ICP-MS housed at the Advanced Analytical Centre, James Cook University. Analyses were performed in a He atmosphere (0.8 l/min), with vaporised material mixed with Ar (0.95 l/min) before entering the detector. Spot analyses were conducted with a beam size of 32 μm , operating at 10 hz for 60 seconds (600 hits per spot). Total analysis time per measurement was 110 s, which included a 30 s background measurement with the detector open before ablation, and 20 ss afterwards. Analyses were run in time-resolved mode with element acquisition times of 10 ms per element and a sweep time of 0.33 s. Data reduction for spot analysis was completed according to standard procedures (Longerich et al., 1996), using Fe as the internal standard. External standards used were MASS-1 (Wilson et al., 2002), NIST-610 (Jochum et al., 2011) and GSD-1 (Jochum et al., 2005). Standards were measured at the start and end of each analytical session, as well as every 2 hours during analyses to correct for

instrument drift. Pyrite and pyrrhotite spot analyses were processed with the MASS-1 standard for transition, basic, semi- and non-metals.

Sulfide transects were conducted in two steps. The first step was run with a beam size of 32 μm for an initial pass to ensure a clean surface. The second step consisted of a measurement pass, with a beam size of 24 μm , operating at 10 Hz and moving laterally at 24 μms^{-1} . A single point along the centre-line of the transect would be ablated 10 times, while points towards the edge of a transect would be less represented. Elements and acquisition times for transect data are identical to spot analysis. Transect data comprises pixels $\sim 24 \times \sim 8 \mu\text{m}$ in size (24 μm beam size, moving at 24 μms^{-1} for 0.33 s), with each pixel effectively showing an average composition, weighted towards the centreline of the transect, resulting in semi-quantitative data. In total, 33 transects were completed for this study.

The average elemental concentration (in ppm) was calculated from transect CPS data. The conversion followed a similar method to that described by (Steadman et al., 2013; 2014), with the exception that concentrations were averaged over each transect instead of the conversion being applied pixel by pixel. Averaged transect data is included in bivariate plot (Fig. 4.14), but is not included in average trace element abundancies (Table 4.2).

Acquiring trace element images involved ablating a sequence of parallel transects, offset to give full coverage of a sample area. Element acquisition times were 10 ms per element, with a total sweep time of 0.33 seconds. The transects used a beam size of 16 μm , operating at 10 Hz and moving laterally at 16 μms^{-1} . A small beam size was used because of the generally small size of the analysed grains. Each run was completed individually, with 30 seconds of background measurement before ablation, and 20 seconds afterwards. The mapped area was planned around a total area of $\sim 1 \times 1 \text{mm}$, with a measurement time of around 2 hours. Images are comprised of pixels measuring $\sim 5.3 \mu\text{m} \times 16 \mu\text{m}$ (16 μm beam size, moving at 16 μms^{-1} for 0.33 s). In total, 28 elements were mapped. Element acquisition and sweep times were identical to spot analysis. In total, nine trace element images were acquired. As imaged sites contained different mineralogy (some with excessive quartz), automatic selection of signal intervals based on single elements returned generally poorly matched transects. Raw counts of Al, Fe, Mg, Ca, Mn, K and Ba were used to manually select signal intervals in database software. Visual basic was used to compile transect data into 28 element maps. Statistical software

Rx64v3.4.3 (available at <https://www.r-project.org>) was used to combine the element maps into stacked rasters for import into ArcGIS geographic software. The combination of R-statistical software and ArcGIS provided a range of processing tools, including point averaging and elemental association mapping that proved useful for data interpretation. Due to the wide variety in mineralogy covered by the element images, the data is qualitative, and presented as raw CPS values.

4.5. Results

4.5.1. *LA-ICP-MS Images*

LA-ICP-MS trace element maps of a mineralised quartz vein (Fig. 4.4), mineralised mudstone (Fig. 4.5), mineralised ironstone (Fig. 4.6) and mineralised diorite (Fig. 4.7) are presented to compare trace element distribution patterns between different host rock types.

4.5.2. *Mineralised quartz vein*

This sample (Fig. 4.5) was taken from a ~30 cm thick quartz vein that cuts across intercalated ironstone and mudstone. Where the quartz vein intersects the ironstone a wide sulfidation front developed. The quartz vein contains pyrite + biotite + K-feldspar and gold. The pyrite in the vein mainly consists of pyrite-2a, but some grains contain a well-developed inclusion free rim interpreted as pyrite-2b. These type of veins were interpreted as feeder veins and contain ~ 3 ppm Au on average (van Ryt et al., 2017). Quartz feeder veins similar to the ones sampled here were targeted during past underground mining, but currently comprise only a small percentage of total gold reserves at Geita Hill. The area mapped by LA-ICP-MS contains a string of pyrite grains located in the middle of the vein and surrounded by quartz, K-feldspar and biotite. No systematic zoning of elements typically found in pyrite (As, Co, Ni etc.) was observed. Trace element mapping shows that the majority of Au and Ag occurs as high intensity spots inside pyrite grains. These spots are interpreted to represent inclusions. There is a good correlation between zones high in Au and Ag and zones high in Te suggesting that most likely these metals occur as tellurides. Cu, Mo and Sb also occur as high intensity spots inside pyrite grains and in the surrounding matrix, suggesting that they represent micron-size sulfide grains. Co, Ni and As have low count rates and display a patchy distribution that correlates

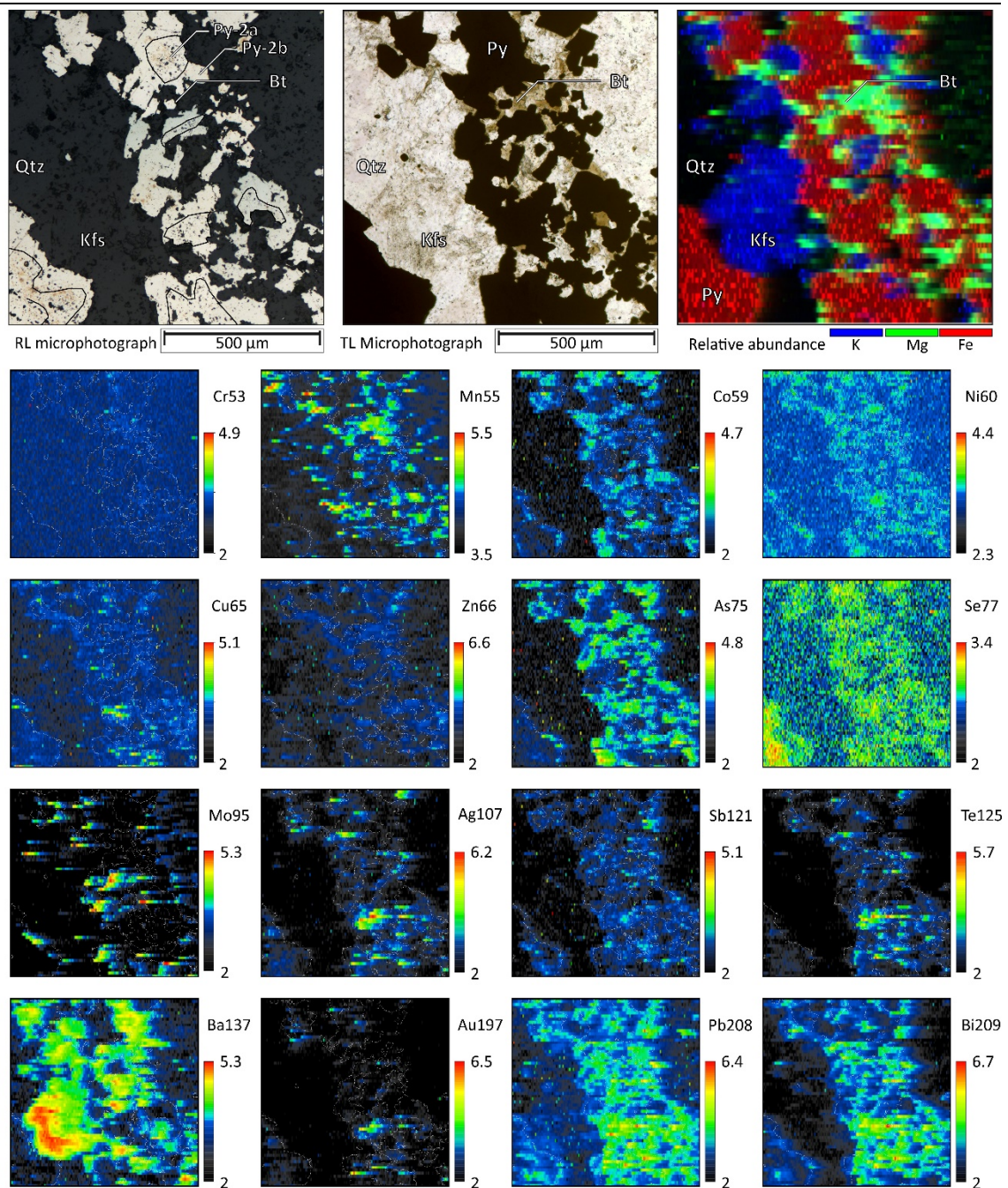


Figure 4.5. GQ-01 LA-ICP-MS image: Mineralised quartz vein microfracturing, colour scales are expressed as \log_{10} units.

with pyrite rims. Pb and Bi have a similar distribution and in general correlate well with the pyrite-2a cores, where they occur as sulfide and telluride inclusions as well as in the pyrite lattice. Se is homogeneously distributed inside the pyrite grains but yields low count rates suggesting that it is present in low quantities. Cr and Zn are below detection limits, Mn occurs mainly in biotite and the Ba distribution correlates with K-feldspar.

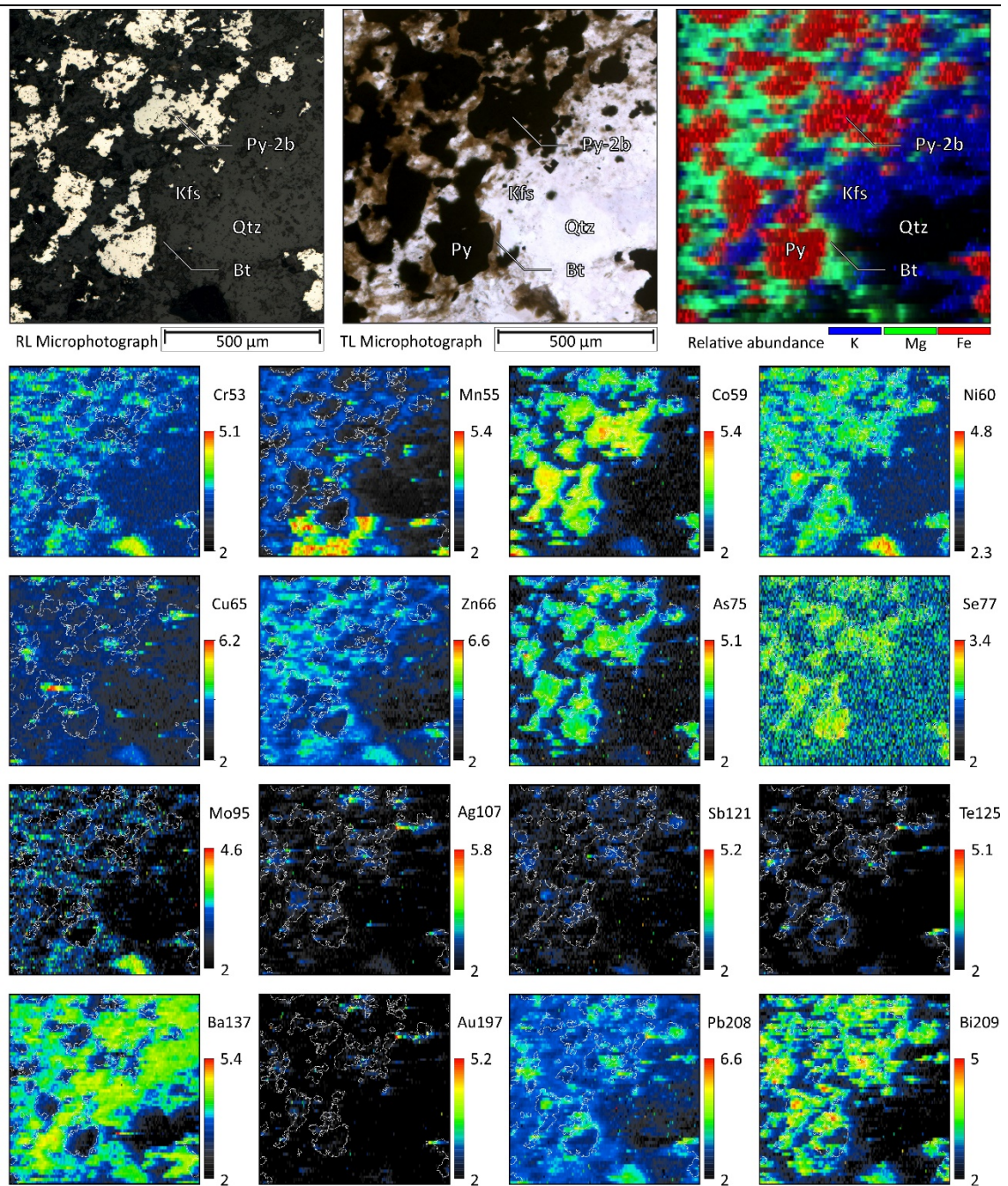


Figure 4.6. 262-06-247.3 LA-ICP-MS image: Mineralised mudstone in the halo of a quartz feeder vein.

4.5.3. Mineralised mudstone layer in ironstone

This sample (Fig. 4.6) is from a mineralised mudstone layer and contains anhedral pyrite grains (pyrite-2b) that occur together with biotite, K-feldspar, quartz and minor carbonate. The pyrite grains formed in the alteration halo of a quartz feeder vein, which intersects the lower right corner of the ablated area in Figure 4.6. Au and Ag occur as high intensity isolated spots in pyrite and in the matrix and their distribution closely correlates with that of Te, suggesting that these elements occur

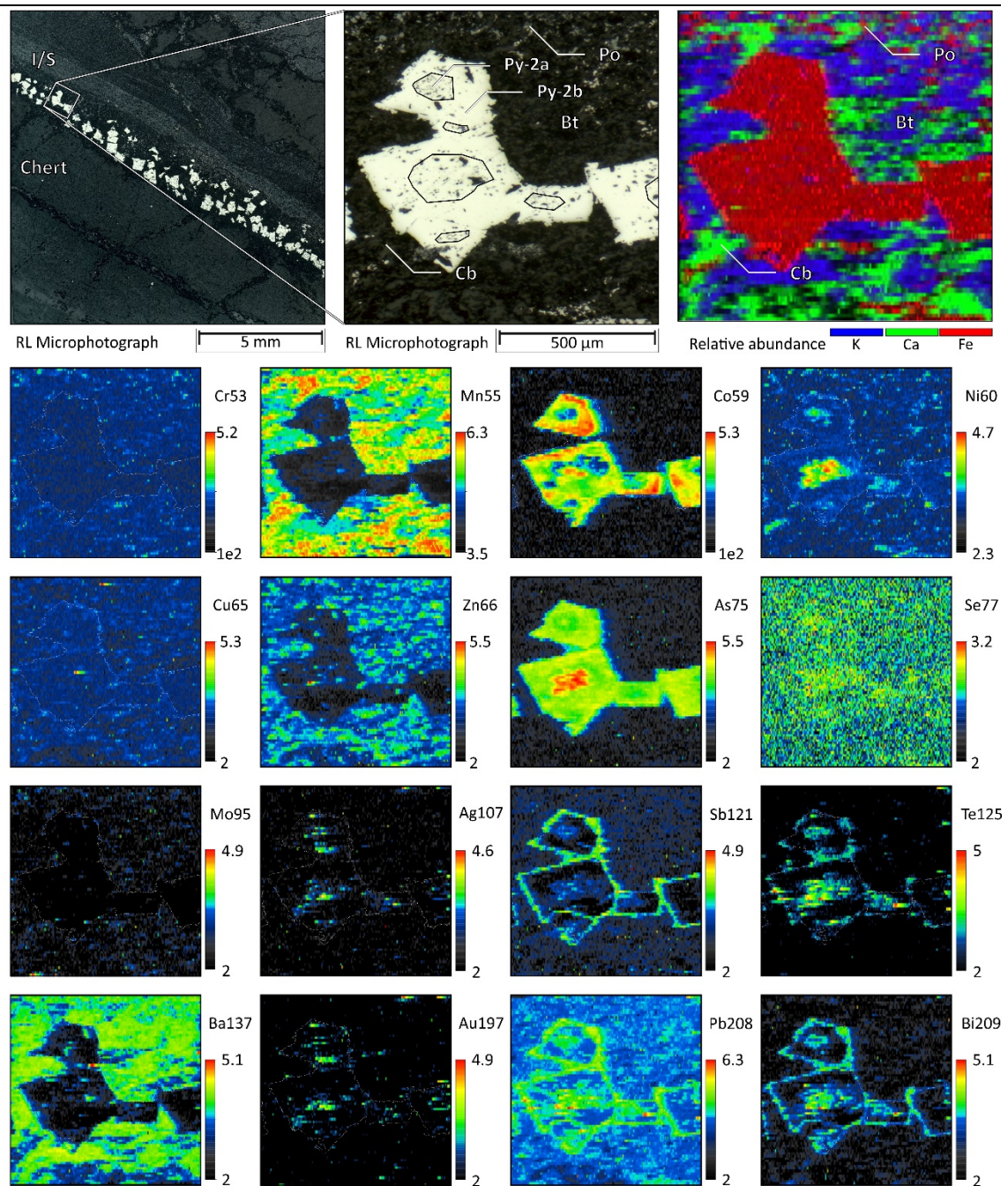


Figure 4.7. 262-11-291.5 LA-ICP-MS image: Mineralised sulfidation front in ironstone

as micron scale telluride mineral grains. Co, Ni, As and Se are relatively uniformly distributed in the pyrite grains and most likely are lattice bound. However, all pyrite grains display a thin outer rim, which is depleted in these elements. Bi shows an inhomogeneous distribution pattern; some pyrite grains have a uniform Bi concentration whereas other pyrite grains show Bi enrichment only in cores or small portions of their rims. In areas of uniform concentration, Bi may be lattice bound whereas high intensity areas may represent zones with abundant Bi sulfosalt or telluride micro-inclusions.

Some of the areas showing high Bi counts correspond with the location of biotite grains. Cr, Mo and Zn correlate best with biotite and are generally below detection limits in pyrite. Sb is in general below detection limits and occurs only as small sulfide inclusions in pyrite. Mn is below with detection limits in the pyrite grains, but is concentrated in carbonates. The Ba distribution correlates with K-Feldspar.

4.5.4. *Mineralised magnetite layer in ironstone*

This sample (Fig. 4.7) is from a mineralised sulfidation front in ironstone. The pyrite grains formed along the boundary between chert-rich laminae and magnetite rich-laminae. The pyrite grains occur together with biotite, K-feldspar, and carbonates. Pyrite-2b is the dominant pyrite type, with only a few pyrite grains containing a core of pyrite-2a. Trace element mapping shows that Au and Ag occur as high intensity spots located in the pyrite core, pyrite rims and in the matrix. The distribution of Au and Ag overlaps with that of Te, Bi and Pb suggesting that these elements may occur as telluride inclusions. Pb appears relatively uniformly distributed in the core and around the rims of the pyrite grains. Because of the large ionic potential of Pb^{2+} , it is unlikely for Pb to be incorporated into the pyrite lattice, therefore, most likely Pb is present as a combination of micro-inclusions of galena, Pb-sulfosalts and Pb-tellurides. Sb is concentrated mainly in a continuous, thin layer along the pyrite outer rim. Since Sb^{3+} can participate in coupled substitutions with two Fe^{2+} cations (e.g., Huston et al., 1995), it is possible to be lattice bound. Co is homogeneously distributed across the pyrite grains, but is below detection limit along a thin portion around the outer rim. Ni is found only in the pyrite inner core and is below detection limits for the remainder of the pyrite grain. Ni also occurs in high quantities in disseminated magnetite grains found in the matrix. As is highly concentrated in the pyrite inner core, is high in a wide mantle surrounding the inner core and is below detection limits around a thin outer rim. Se, Cr, Cu and Mo are below detection limits. The presence of a few hot spots of Cr, Cu and Mo suggests that these elements are found as micron-scale sulfide grains mostly external to the pyrite grains. Mn is below detection limits in pyrite, but it shows high-count rates in the surrounding matrix where it correlates with carbonates, biotite and magnetite. Zn is concentrated in biotite whereas Ba is concentrated in K-feldspar.

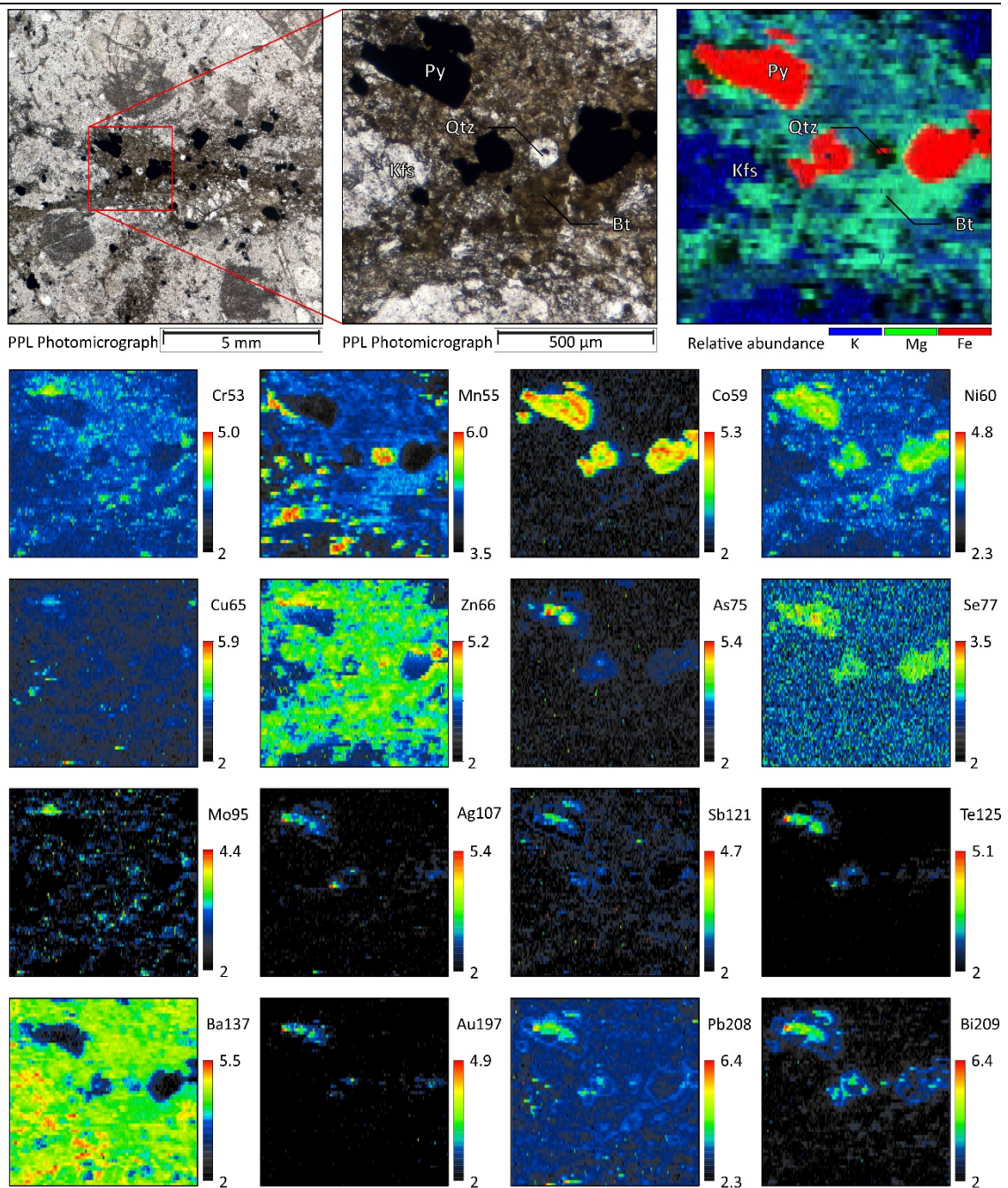


Figure 4.8. 302-13A-168.3 LA-ICP-MS image: Mineralised micro-fracture network in porphyritic diorite

4.5.5. Mineralised Diorite

This sample (Fig. 4.8) is from a mineralised diorite dyke and contains pyrite grains deposited along biotite- and K-feldspar-rich micro-fracture networks. Minor amounts of carbonate are also found along the micro-fractures. All pyrite in this sample is pyrite-2b, is euhedral in shape and is free of inclusions. The elements Au, Ag, Sb, Pb, Bi and Te have a similar distribution, suggesting that these

elements may occur as tellurides or as micro-inclusions of sulfosalts. They appear to be concentrated primarily in the pyrite core, although Bi and to a lesser degree Pb also occur concentrated along the outer rims of the pyrite grains. As concentrations are high in the core of some of the pyrite grains, but in general As is below detection limits. The elements Co, Ni and Se are uniformly distributed across the pyrite grains and are likely lattice bound. Mn is primarily concentrated in the calcite grains with minor amounts found in biotite. Zones high in Cr, Mo and Zn correlate with biotite grains rich in opaque minerals. A few Cu hot spots are interpreted to indicate the presence of small chalcopyrite grains in the matrix. Ba is high in K-feldspar, biotite and carbonate, but is below detection limits in pyrite.

4.5.6. *LA-ICP-MS Transects*

Thirty-three LA-ICP-MS transects were measured on various mineralised and non-mineralised pyrite grains. Four representative transects are discussed here. The first transect (Fig. 4.9) was run across a pyrite-2b grain from mineralised ironstone. This pyrite grain is euhedral and contains scattered inclusions of pyrrhotite and minor magnetite that do not define a clear core-rim texture (Fig. 4.9a). Two distinct Au peaks occur along the transect (Fig. 4.9b), one in the core of the grains and one towards the rim. The gold peaks are directly correlated with peaks in Ag and Te suggesting that most likely gold is found as Au-Ag tellurides inclusions. Bi and Pb correlate well with the location of the Au-Ag tellurides, suggesting that they occur together, but retain a higher baseline across the rest of the grain, implying that these two elements also occur in the pyrite lattice. Cu is present at low levels in the pyrite lattice and as chalcopyrite inclusions, Zn and Sb are present as inclusions of sphalerite and stibnite whereas Sn and Mo are below detection limits (Fig. 4.9c). The distribution of Co, As and Se (Fig. 4.9d) have elevated base line counts and display symmetrical distribution patterns across the central point of the grain, which suggests that these elements are lattice bound and indicative of concentric internal zoning in the pyrite grains.

The second transect (Fig. 4.10) was measured across a pyrite grain in a mineralised quartz vein with a well-defined inclusion-rich core of pyrite-2a, surrounded by an inclusion-poor rim of pyrite-2b (Fig. 4.10a). Gold is distributed throughout the grain, but the most elevated values of gold (Fig. 4.10b) are found within the inclusion-rich core (pyrite-2a). A small peak in Au in the left rim, correlates with small peaks in Te, Ag, Bi and Pb, suggesting the presence of these elements as tellurides. In the

inclusion-rich core of the grain, Au values are strongly elevated, but still show similar trends to Te suggesting that Au may be present in the pyrite core as distributed fine-grained electrum particles as well as tellurides. Te and Pb correlate very well across the core and rims of this pyrite grain suggesting the occurrence of these elements as Pb-tellurides. Cu counts (Fig. 4.10c) are particularly high within the inclusion-rich pyrite core and low in the inclusion-poor pyrite rims. Zn, Mo and Sn occur mainly as peaks within the pyrite core or at the core-rim boundary. Se (Fig. 4.10d) returned low counts across the pyrite grains, whereas Cr displays a high peak within the pyrite core, which could be related to the presence of fine magnetite inclusions. The Ni, Co and As (Fig. 4.10d) distribution suggests the presence of complex growth zoning. Co displays high counts within the pyrite core and low counts within the pyrite rims. As displays two peaks marking the transition from the inclusion rich core to the inclusion poor rim.

The third transect was measured diagonally across a grain of quartz vein-hosted pyrite-2b grain with visible inclusions of gold (Fig. 4.11a). Au, Ag, Te, Bi and Pb closely correlated in three locations within the transect, likely corresponding to ablated telluride mineral inclusions (Fig. 4.11b). There is a slight offset between the Au-Ag and Bi-Pb peaks, implying these elements were hosted in distinct tellurides. Appreciable Mo was detected in the transect, which during this study was observed only in pyrite grains hosted in the quartz veins. The distribution of the Mo as sharp peaks suggests this element is inclusion-hosted rather than lattice-bound in the pyrite grains, and does not correlate with any other element measured. The distribution of Co, Ni and As implies growth zoning in the pyrite grain that was otherwise invisible optically. The core of the grain is relatively enriched in Co, while Ni and As are only enriched in the rims of the pyrite grain. This distribution is in sharp contrast to both diorite and ironstone-hosted pyrite grains, which contain return elevated Cu and As in the pyrite cores.

The last two transects were measured across an aggregate of inclusion-poor pyrite-2b hosted in a large quartz vein (Fig. 4.12a). The distribution of gold is highly variable, averaged Au concentration across the first transect is ~930 ppm, whereas the second transect, 100 μm below the first one, averages ~40 ppm Au. The correlation between Au and Ag is very good, as is the correlation between Bi and Pb (Fig. 4.12b), but the two sets of elements do not perfectly correlate with each other. Base metal content in the transect is very low (Fig. 4.12c), with Cu and Zn implying intersection

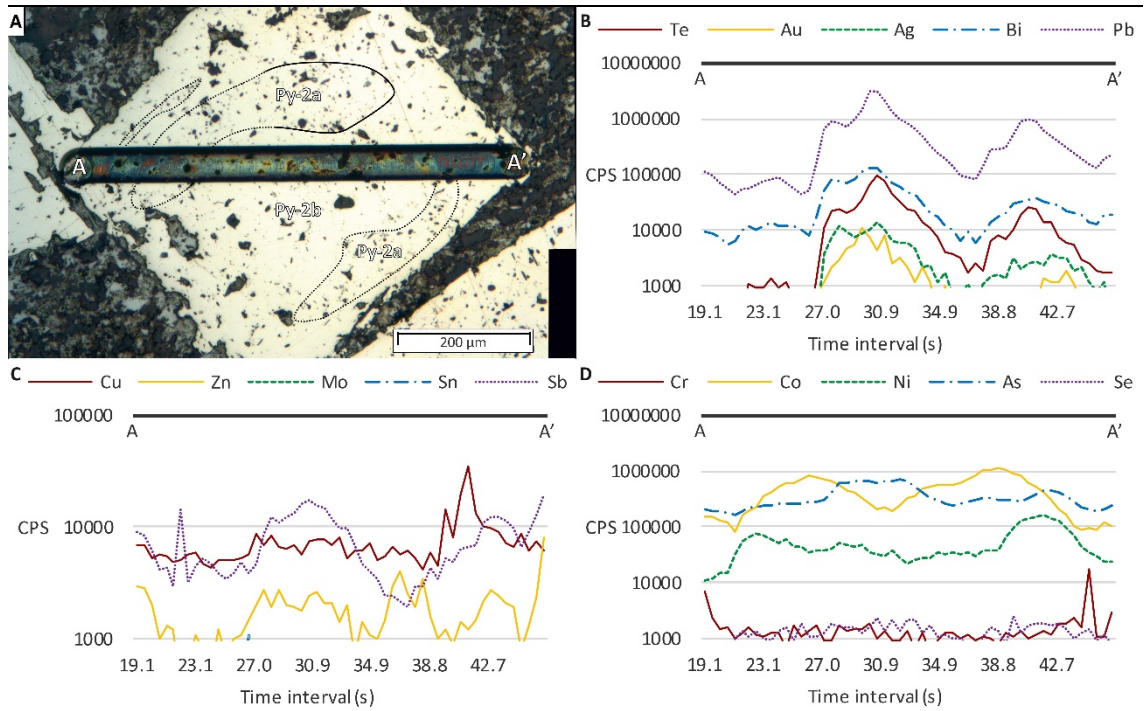


Figure 4.9. 262-11-01 Ironstone transect and time-resolved signal data across a grain of pyrite-2b

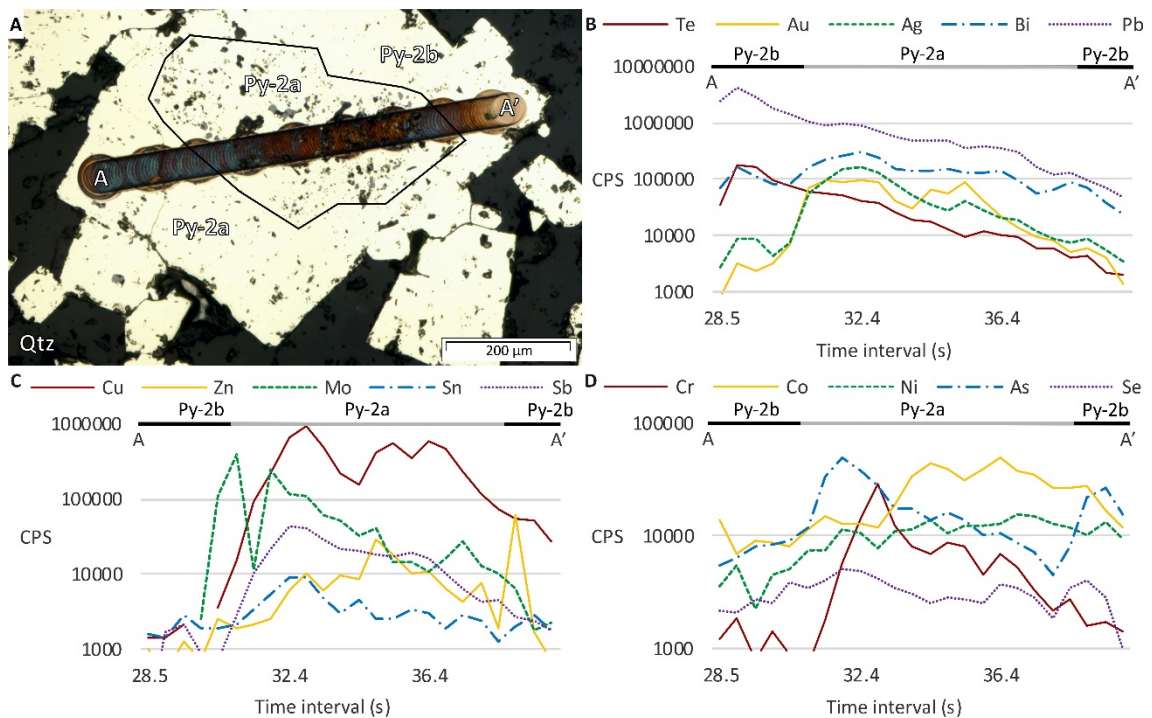


Figure 4.10. GQ-01-06 Quartz vein transect and time-resolved signal data across a grain with pyrite-2a and pyrite-2b textural zonation.

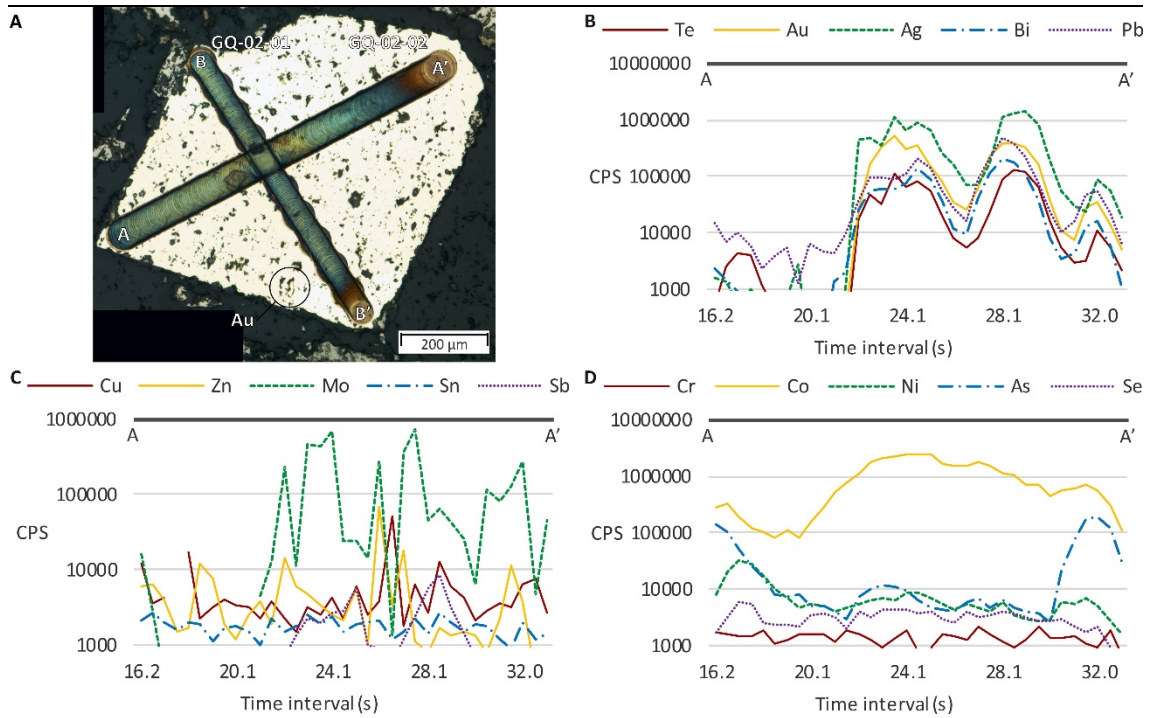


Figure 4.11. GQ-02-01 Quartz vein transect and time-resolved signal data, a visible gold grain is circled in the RL microphotograph. The second transect (GQ-02-02) shown in the microphotograph is presented in appendix 6.3.

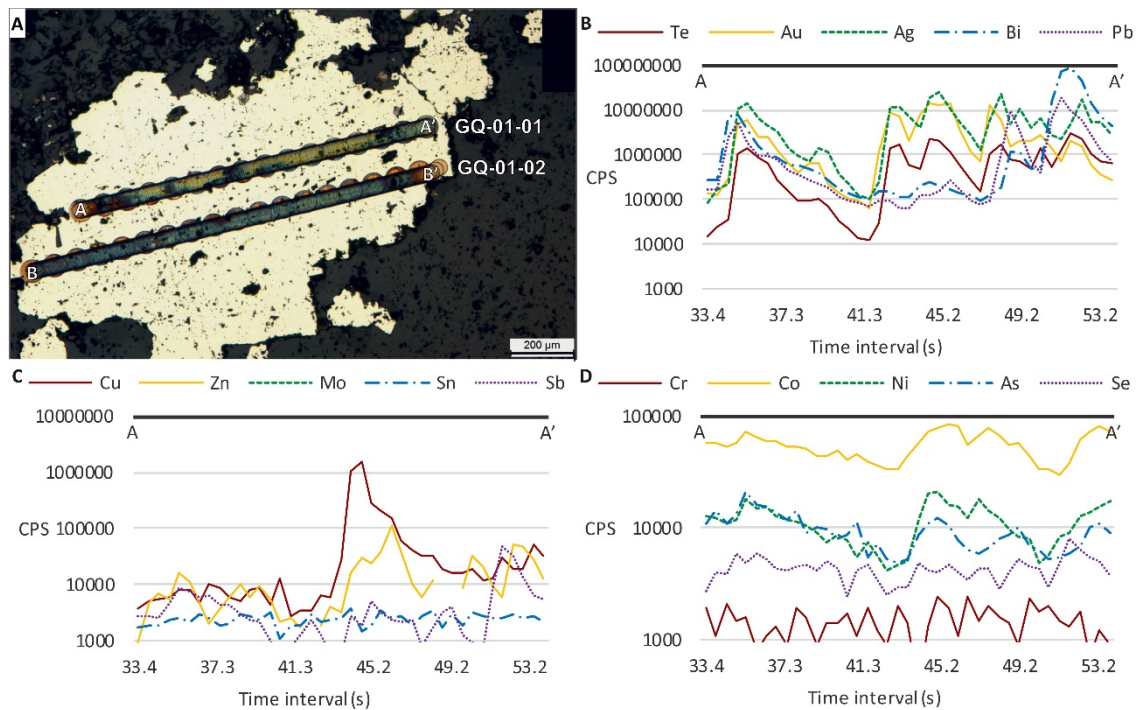


Figure 4.12. GQ-01-01 Quartz vein transect and time-resolved signal data. The second transect (GQ-02-01) shown in the microphotograph is presented in appendix 6.3.

of a single inclusion in the centre of the aggregate grain. Counts of typically lattice bound elements Co, Ni and As do not describe any consistent growth zoning in this pyrite grain.

4.5.7. *LA-ICP-MS spot analyses*

4.5.7.1. *Magnetite*

Of the three types of magnetite observed at Geita Hill (fine-grained anhedral magnetite; coarse-grained mottled magnetite; coarse-grained euhedral magnetite, (Fig. 4.3). The fine-grained anhedral magnetite was too small to be reliably analysed by LA-ICP-MS.

The other two textural varieties of magnetite are chemically distinct (Table. 4.2). The composition of euhedral magnetite is homogenous across grains. This magnetite is relatively enriched in V and Cr, and depleted in Ti, Cu, Zn, Pb and As when compared to mottled magnetite (Table 4.2; Fig. 4.13a). The chemistry of mottled magnetite shows more variability between grains; e.g. Ti ranges from 561 to 3600 ppm with two outliers recording 10,120 ppm (1.1 wt.%) and 36,480 ppm (3.6 wt.%) respectively. Additionally, several mottled magnetite grains have elevated values of Au, Ag, Te, Pb and Bi (Fig. 4.13d, e, f).

Partly sulfidised, mottled magnetite is enriched in Ti, Co, Cu, Zn, As, Mo, Ag, Sn, Sb, Te, W, Au, Pb and Bi compared to non-sulfidised, mottled or euhedral magnetite (Table 4.2). The concentrations of Co, Ni, Cu, W, Te, Au, Ag and Bi increase with proximity to gold-bearing pyrrhotite and pyrite, Cr drops and Zn, As and Pb show no systematic change.

4.5.7.2. *Pyrrhotite*

A minor amount of hydrothermal pyrrhotite was observed in the sulfidation fronts in ironstone and in quartz veins. In all occurrences, the pyrrhotite has been overprinted by mineralised pyrite. The average trace element composition of pyrrhotite from ironstone and from the quartz veins is presented in Table 4.2. The Au content of pyrrhotite is low with an average of 0.06 ppm Au in ironstone and an average of 0.01 ppm Au in quartz veins. The Ag content is almost an order of magnitude higher with averages of 0.3 and 0.7 ppm in ironstone and quartz veins respectively. Te values are on average 2.6 ppm in ironstone and 0.8 ppm in quartz veins whereas the As content of pyrrhotite for both rock types is ~1 ppm. The Cr, Sn, Sb and Bi content of pyrrhotite from ironstone

Table 4.2.

Average trace element abundances in magnetite, pyrrhotite and pyrite (ppm). Trace element data is presented as Appendix 6.2.

	Texture	Ti	V	Cr	Mn	Co	Ni	Cu	Zn	As	Mo	Ag	Sn	Sb	Te	W	Au	Pb	Bi
Magnetite																			
GQ-03-PIT																			
Non-mineralised	Euhedral	64	2196	116	373	0.5	66	8.2	100	3.2	0.1	0.3	1.1	1.1	bdl	3.2	0.04	3.7	0.03
Mineralised	Sulfidised mottled	391	2326	25	971	30	513	425	1356	50	2.9	4.9	1.2	12	12	130	2.4	611	6.0
0262-11-291.5	Mottled	1639	927	75	1462	0.6	21	80	1322	46	0.9	1.5	2.4	19	0.6	5.1	0.05	774	0.9
		V	Cr	Mn	Co	Ni	Cu	Zn	As	Se	Mo	Ag	Sn	Sb	Te	W	Au	Pb	Bi
Pyrrhotite																			
262-11-291.5	Ironstone	31	12	201	1.0	116	97	30	1.0	22	0.3	0.3	1.1	2.5	2.6	0.5	0.06	49	1.7
GQ-02	Qtz vein	1.4	10	102	0.2	64	2.8	17	1.1	43	118	0.7	1.3	2.3	0.8	57	0.01	19	2.2
	Lithology	V	Cr	Mn	Co	Ni	Cu	Zn	As	Se	Mo	Ag	Sn	Sb	Te	W	Au	Pb	Bi
Pyrite																			
226-02-256.3	Diorite	1.4	bdl	4.6	2874	576	84	2.5	124	17	bdl	2.7	0.1	1.7	1.9	0.1	0.1	76	17
302-13A-168.3	Diorite	3.7	8.2	2.9	254	336	14	2.6	36	63	0.4	7.0	0.2	2.0	57	5.1	3.3	18	8.9
262-07-252.3	Quartz Diorite	12	5.6	13	1271	243	354	33	497	12	1.8	3.4	0.4	7.3	7.4	1.5	0.5	270	26
262-11-291.5	Ironstone	15	2.1	32	254	56	4.9	575	599	13	0.0	0.5	0.4	3.5	11	0.1	0.2	29	1.8
GQ-03-PIT	Ironstone	3.2	bdl	69	82	100	37	18	296	35	0.08	0.8	8.4	1.1	3.9	0.3	0.3	33	1.8
GQ-01-PIT	Quartz vein																		
Core		18	7.5	14	14	18	221	19	50	34	0.1	30	0.3	3.9	102	1.8	7.4	66	46
Rim		0.5	0.6	8.7	17	19	2.8	2.9	70	45	21	3.0	0.2	1.0	12	0.0	1.0	10	6.8
GQ-02-PIT	Quartz vein																		
Mineralised		6.6	4.5	66	284	24	3.3	7.9	370	29	86	30	0.3	1.1	67	0.7	18	36	10
Post-mineralisation		bdl	bdl	160	0.2	6.4	6.6	18	0.2	36	0.2	0.3	0.3	6.0	bdl	0.5	0.08	3.9	0.07

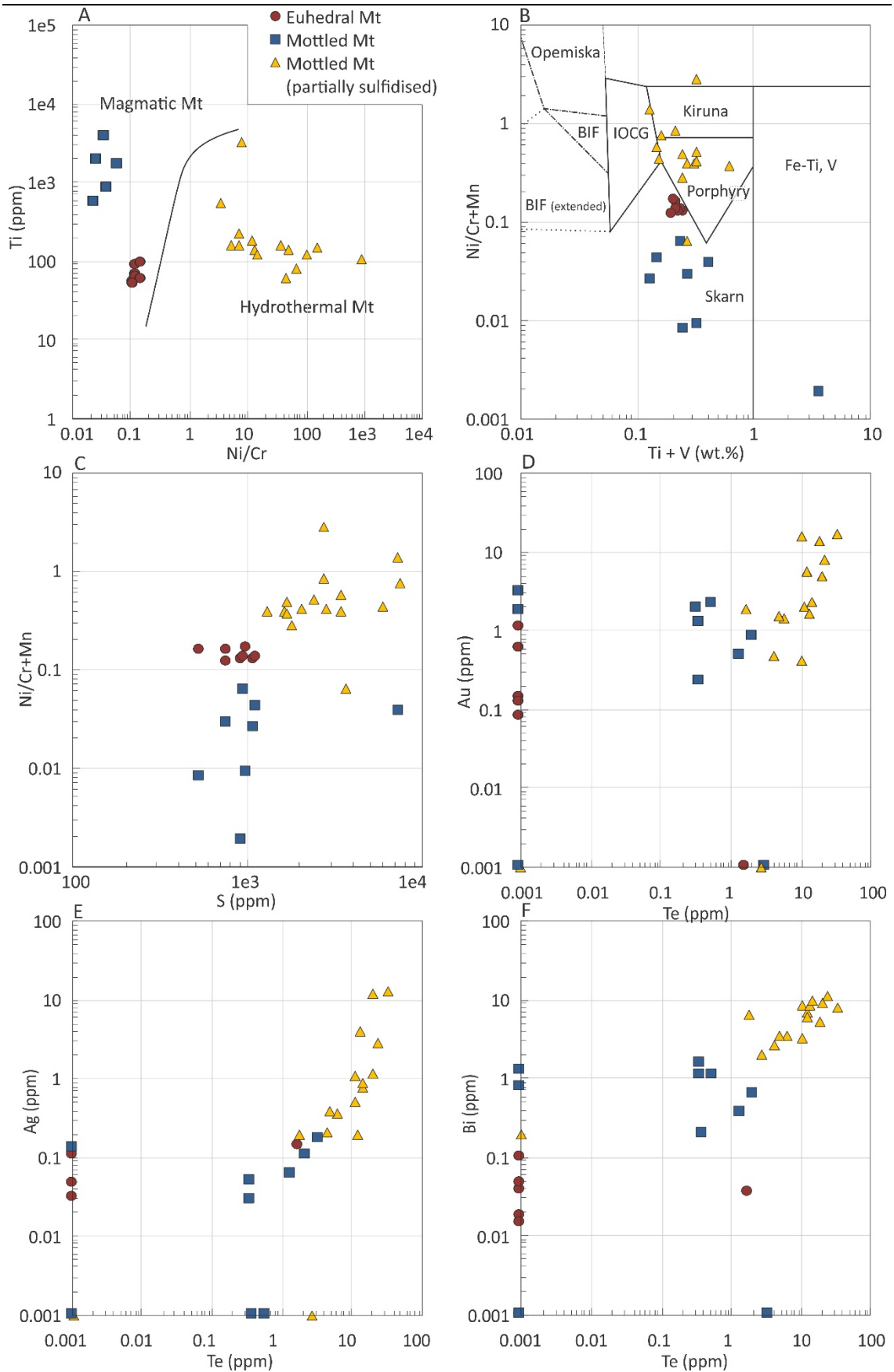


Figure 4.13. Magnetite discrimination diagrams and binary plots: (A) Ni/(Cr+Mn) vs (Ti+V) discrimination diagram, modified after Dupuis and Beaudoin, (2011); Ti vs Ni/Cr discrimination diagram, modified after Dare et al., (2014), extended BIF region after Gourcerol et al., (2016).

and quartz veins is almost identical whereas the Se and Mo content is higher for quartz veins. The concentration of V, Mn, Co, Ni, Cu, Zn and Pb is higher in pyrrhotite grains from ironstone.

4.5.7.3. *Pyrite*

The average composition of pyrite grains from mineralised diorite, ironstone and quartz veins and from post-mineralisation veins is presented in Table 4.2. In general, the trace element composition of the pyrite grains is dependent on the host rock and grains from similar rock types cluster in distinct domains on binary plots (Fig. 4.14). The measured Au content of pyrite grains varies between 0.02-21.3 ppm in mineralised diorite, 0-21.9 ppm in mineralised ironstone and 0-170 ppm in mineralised quartz veins. The gold content of the inclusion rich pyrite cores (pyrite-2a) is consistently around 5-10 ppm, while analysis of the surrounding inclusion-poor rim (pyrite-2b) can vary from below detection limit to >100 ppm. The gold content of post-mineralisation pyrite is low (avg. 0.08 ppm).

The measured Ag content varies between 0.02-37.0 ppm in diorite, 0.04-83.1 ppm in ironstone and 0.02-257 ppm in quartz veins. Pyrite grains from post mineralisation veins have in average of 0.3 ppm Ag. There is a positive linear relationship between the Au and Ag content in mineralised pyrite grains from all rock types (types 2a and 2b; Fig. 4.13b), but this relationship is absent in post-mineralisation pyrite. The average Au/Ag ratio of pyrite grains for all analyses conducted in this study is 0.41 (Table 4.3), and when restricting analysis to those grains that lack appreciable Te (i.e., ablation of a free-Au inclusion) the Au/Ag ratio remains <1. The measured Te content in mineralised pyrite 2a and 2b varies between 0-371 ppm in pyrite grains from diorite, 0-100 ppm in pyrite grains from ironstone and 0-375 ppm in quartz veins. The Te content of type 3 pyrite grains from post-mineralisation veins is in general below detection limits. The Co concentration in pyrite grains is highly variable across different rock types and pyrite generations; e.g., in diorite it varies between 34-3259 ppm (average: 809 ppm), in ironstone between <1-755 ppm (average: 155 ppm), in quartz veins between <1-1402 ppm (average: 124 ppm), whereas values in post-mineralisation pyrite are always below 1ppm.

Average trace element ratios and correlation coefficients for various metals in mineralised pyrite are presented in Table 3. Gold concentrations in pyrite show strong positive correlations with Ag, Te, Bi, Pb and to a lesser degree Zn, whereas Au is weakly to poorly correlated with all the other

Table 4.3.

Summary of trace element ratios and element correlation coefficients of mineralised pyrite. Trace element data is presented as Appendix 6.2.

Pyrite trace element ratios across all lithologies					Pyrite Co/Ni ratios									
	Average	σ	Max	n		Average	σ	Max	n					
Au/Ag	0.4	0.5	5.1	114	Quartz vein hosted pyrite	7.0	12.3	46.9	34					
Au/Te	0.2	0.4	2.7	110	Ironstone hosted pyrite	4.0	5.6	21.6	31					
Ag/Te	1.1	3.6	35.2	111	Diorite hosted pyrite	4.7	4.9	17.6	37					
Au/As	0.8	6.6	71.2	114										
Correlation coefficients between selected elements														
Element		Co	Ni	Cu	Zn	As	Se	Mo	Ag	Sb	Te	Au	Pb	Bi
Quartz vein hosted pyrite	Au	-0.07	-0.03	0.11	0.38	-0.08	0.15	-0.01	1.00	-0.02	0.99		0.64	0.97
	Te	-0.08	0.00	0.13	0.43	-0.09	0.17	-0.04	1.00	0.03		0.99	0.72	0.99
	As	0.77	0.18	-0.20	-0.25		-0.21	-0.09	-0.09	-0.29	-0.09	-0.08	-0.15	-0.11
Ironstone hosted pyrite	Au	-0.13	0.20	0.01	-0.04	-0.18	0.03	-0.06	1.00	-0.14	0.55		0.52	0.05
	Te	0.03	0.36	0.17	0.10	0.07	-0.06	0.25	0.57	0.19		0.55	0.83	0.55
	As	0.46	0.07	0.04	0.04		-0.10	-0.05	-0.18	0.27	0.07	-0.18	0.05	0.02
Diorite hosted pyrite	Au	-0.29	0.01	-0.21	-0.16	-0.20	0.68	-0.08	0.97	-0.08	0.76		-0.23	0.13
	Te	-0.30	-0.11	-0.23	-0.19	-0.17	0.79	-0.07	0.74	-0.08		0.76	-0.22	0.12
	As	0.60	0.04	0.82	0.83		-0.46	0.16	-0.13	0.38	-0.17	-0.20	0.55	0.21

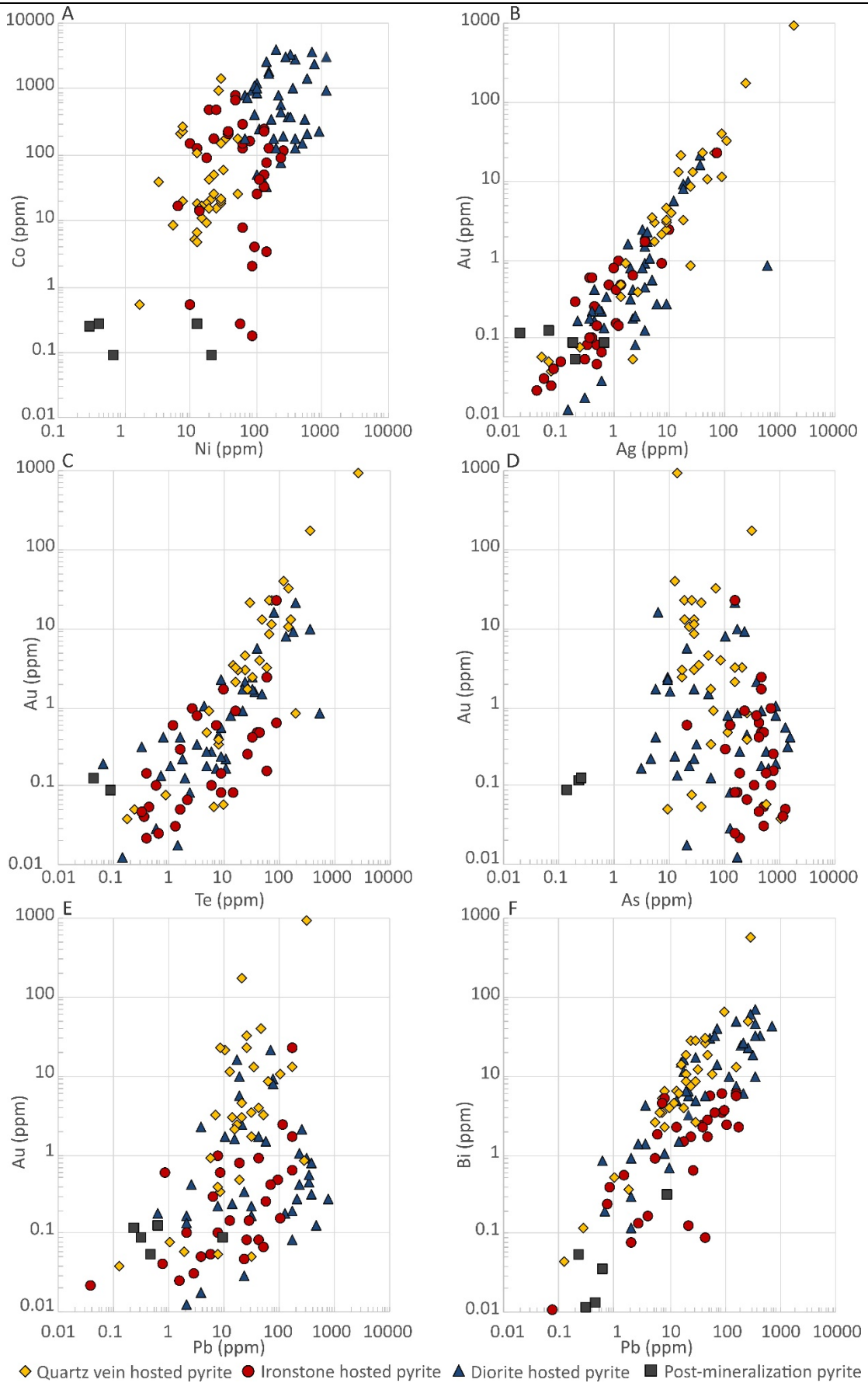


Figure 4.14. Binary plots summarising pyrite LA-ICP-MS spot analysis.

elements. There is an almost perfect positive correlation between Au and Ag (Fig. 4.14b) in type 2 pyrite grains from all rock types suggesting an identical evolution of these two elements during mineralisation. The correlation coefficient between Au and Te is 0.99 in pyrite grains from quartz veins, 0.55 in pyrite grains from ironstone and 0.76 in pyrite grains from diorite. This suggests that, in the quartz veins, all gold precipitated as tellurides and was incorporated in pyrite as gold telluride particles and nanoparticles. However, in ironstone and diorite some of the gold precipitated as free gold and was incorporated in pyrite grains as free gold and gold-tellurides. Au and Pb show a moderate positive correlation (Table 4.3) in pyrite grains from quartz veins ($r=0.64$) and ironstones ($r=0.52$) suggesting that some of the gold is present as the Pb-rich endmember of nagyagite ($\text{Au,Pb}[\text{Sb,Bi}]\text{Te}_2$). Figure 14e illustrates that at Au concentrations above 1 ppm the correlation between Au and Pb breaks down and gold concentrations can increase significantly without a corresponding change in Pb concentrations, possibly as a result of the nucleation and growth of Pb- and Pb-Bi-tellurites. In pyrite grains from diorite, Au and Pb display a weak negative correlation ($r=0.23$). Au and Bi concentrations show a strong positive correlation ($r=0.97$) in pyrite grains from quartz veins, no correlation in pyrite grains from ironstone ($r=0.05$) and a very weak correlation in pyrite grains from diorite ($r=0.13$). This indicates that Bi was introduced with gold in the system and, the evolution of Au and Bi in the hydrothermal fluid during mineralisation are intimately linked, whereas the reaction between the hydrothermal fluid and the host rock affected Au and Bi differently.

4.6. Discussion

Magnetite and pyrite are abundant throughout the mineralised zone in Geita Hill, and their geochemistry provides insights into the characteristics of the mineralising fluids (e.g., McQueen and Cross, 1998; Reich et al., 2005; Large et al., 2007; Kamvong et al., 2007; Cook et al., 2009). The effect of the hydrothermal fluids on magnetite manifests itself as textural changes and direct replacement by pyrite (Borg, 1994; van Ryt et al., 2017), with consequent changes in the composition of magnetite in host lithologies that are otherwise similar. In contrast, the majority of pyrite in the mineralised zone is of hydrothermal origin, and similarities in pyrite composition across different host rock types may reflect the original composition of the mineralising fluid. Constraints on the composition

of the hydrothermal fluid and conditions of formation of mineralisation are discussed in detail for magnetite and pyrite.

4.6.1. *Constraining the effects of hydrothermal alteration with magnetite*

Magnetite is the dominant oxide in the Geita Hill deposit. Borg (1994) distinguished three types; fine-grained anhedral to subhedral grains (Type I), large euhedral grains or irregular aggregates (Type II) and magnetite pseudomorphs after hematite (Type III). There were no magnetite pseudomorphs after hematite observed, and as such the large euhedral grains and the irregular aggregates (Type II of Borg, 1994) were treated as two different types of magnetite. The irregular magnetite aggregates (mottled magnetite in our classification) occur only in magnetite-rich layers in proximity to the ore zone (< 2m) becomes variably sulfidised. The euhedral magnetite is common in quartz-dominated layers. All magnetite types occur along layers or laminae parallel to the sedimentary layering, which experienced all folding events (Sanislav et al., 2017), and magnetite in D₃ fold hinges is aligned with the fold axis and a weak axial planar cleavage. These observations suggest that magnetite formed part of the peak-metamorphic assemblage (e.g., van Ryt et al. 2017), predates mineralisation and most likely formed or recrystallised during metamorphism from precursor iron-rich oxyhydroxides (e.g., Klein, 2005). Mineralising hydrothermal fluids later affected the magnetite to cause the mottled texture. Thus, the different textural types of magnetite seen now reflect different degrees of hydrothermal alteration; i.e. the euhedral magnetite is the least affected by the hydrothermal fluids, the mottled magnetite is only partly affected and the sulfidised magnetite is the most affected by the hydrothermal fluids.

Compared to magnetite from other BIF-hosted Au deposits (Dupuis and Beaudoin, 2011), the chemical composition of magnetite at Geita Hill (i.e. enriched in Ti, V, Mn, Zn; and depleted in Cr, Cu, Ni) resembles magmatic and hydrothermal magnetite (Fig. 4.13a, b) with a clear compositional difference between euhedral magnetite, mottled magnetite and partly-sulfidised mottled magnetite. The Ni/Cr ratios of euhedral and mottled magnetite are similar to magnetite derived from magmatic fluids, whereas the Ni/Cr ratio of partly sulfidised magnetite is similar to that of hydrothermal magnetite (Dare et al., 2014). On the Ti+V vs Ni/(Cr+Mn) discrimination diagram of Dupuis and Beaudoin (2011), the euhedral and mottled magnetite plot in the hydrothermal skarn field whereas the sulfidised magnetite grains plot mostly in the field of magnetite in porphyry systems, along the

boundary with IOCG and Kiruna type magnetite. None of the textural types of magnetite plot in the field of banded iron formations (BIF, Fig. 4.13b) suggesting either that they did not form as a BIF, their chemistry was modified by fluids, or that the chemistry of ironstone hosted magnetite is much more variable than shown in existing discrimination diagrams. Given that many of the magnetite-rich ironstone layers preserve sedimentary structures such as graded bedding, crossbedding and fluidisation structures (e.g., Kwelwa et al., 2018b), they originated as Fe-rich sandstone and siltstone layers rather than chemical BIF's. Peak-metamorphism was synchronous with the intrusion of numerous diorite dykes (~30% by volume at Geita Hill deposit) originating from the Nyankanga Intrusive Complex (Fig. 1.1, 1.2). Therefore, that the magmatic signature preserved in many of the magnetite grains (Fig. 4.13a) could be a consequence of the interaction with fluids derived from the intrusion of the diorite dykes during peak metamorphism. Alternatively, the magmatic signature could have a sedimentary origin considering that the ironstones at Geita Hill are intercalated with immature sediments with an andesitic to dioritic composition (Sanislav et al., 2017); i.e. the magnetite itself is of magnetic origin or the magmatic signature could have resulted from fluids released by the enveloping volcanoclastic sediments during metamorphism. There is little variation in the immobile trace element composition of the euhedral magnetite and all analyses cluster tightly when plotted on selected discrimination diagrams (Fig. 4.13a and b). This clustering is consistent with the euhedral magnetite achieving equilibrium with the ambient metamorphic fluid during peak metamorphism, whereas the more variable concentration of trace elements in the mottled and the sulfidised magnetite reflect the different stages of alteration during interaction with the overprinting mineralising fluids.

The changes in trace element composition during alteration from euhedral to mottled to sulfidised magnetite are not necessarily linear, but reflect complex mineral interactions at grain boundary scale as alteration proceeds, e.g. the Ti content in magnetite grains increases by an order of magnitude from euhedral magnetite to mottled magnetite than decreases again in sulfidised magnetite (Fig. 4.12a). These changes reflect a staged dissolution-precipitation process (e.g., Rickard and Luther, 2007; Qian et al., 2010), during which, in first instance (and in parts of the rock where alteration is less evolved), euhedral magnetite is partly dissolved by hydrothermal fluids to form the mottled magnetite, which becomes enriched in Ti. as interaction with the hydrothermal fluid continues and sulfidation of the mottled magnetite occurs, pyrrhotite + pyrite + biotite + K-feldspar

start to form, at which time Ti is released from the mottled magnetite (now sulfidised) to move into biotite. Mn follows similar trends except that it preferentially moves into alteration carbonate. During the same process, highly chalcophile Ni is initially released from euhedral magnetite, and then becomes concentrated in newly formed pyrite inclusions within the sulfidised magnetite grains, thereby also affecting the Ni content in adjacent magnetite grains (Table 4.2). Cr shows far less variability than Ni, but becomes gradually more depleted as alteration proceeds. As a consequence, Ni/Cr ratio's show variations with textural type as well; i.e. compared to the euhedral magnetite the Ni/Cr ratio of sulfidised magnetite has shifted to higher values whereas the Ni/Cr ratio of mottled magnetite has shifted to lower values (Fig. 4.12a and b). Euhedral and mottled magnetite have similar sulphur content (Fig. 4.12c), which suggests that the higher sulphur content in the sulfidised magnetite is externally derived. Other elements that display a clear increase in concentration that changes as a function of textural variation in magnetite include Au, Ag, Te and Bi (Fig. 4.12d-f); e.g. Te is below detection limits in euhedral magnetite, reaches an average of 0.6 ppm in mottled magnetite and increases to an average of 12 ppm in the sulfidised magnetite (Table 1). The systematic increase in these elements with intensity of alteration strongly suggests that they were externally derived and introduced into the magnetite together with S. Note, however, that many seemingly unaltered, euhedral magnetite grains that were analysed also yielded Au (Fig. 12d), which indicates that the precipitation of free gold along microfracture networks occurs inside all magnetite types away from visible alteration fronts.

4.6.2. *Constraining the effects of hydrothermal alteration with pyrite*

All mineralised pyrite grains in the Geita Hill deposit formed late tectonically along similar structures and are part of the same alteration assemblage (van Ryt et al., 2017; Sanislav et al., 2017). Although two textural types of pyrite (pyrite-2a and pyrite-2b) were identified in ironstone-related assemblages (van Ryt et al., 2017), the chemical zonation that characterises them is present in texturally uniform (pyrite-2b), diorite-hosted pyrite as well. This zonation is characterised by changing concentrations of elements that are typically lattice bound (Co, Ni, As), together with differences in the abundance of elements that are typically inclusion hosted (Au, Ag, Sb, Te, Pb, Bi). Images of trace element distribution patterns (Figs 4.7, 4.8) and transects (Fig. 4.9) of ironstone- and diorite-hosted pyrite grains show complex, core-mantle-rim, chemical zonation. Pyrite cores are

typically enriched in As, Co, Ni, Cu and Zn, and have an increased abundance of (small) inclusions. These inclusions are too small to be visible under the microscope and in BSE imaging, but their presence is evident in the cores of pyrite in all lithological units, where overlapping concentrations of Au, Ag, Te, Pb and Bi can be measured (e.g. Fig. 4.9b). Ni, Co and As show similar distribution patterns in pyrite, but Ni and As tend to be more concentrated in the core of pyrite grains with a drop in the concentration of Ni and As defining the core-mantle transition, whilst Co is typically more enriched in pyrite mantles (Fig. 4.7). The outermost rims of zoned pyrite grains may be severely depleted in Ni, Co and As, but can be enriched in Sb, Pb, Bi and Te (e.g. Fig. 4.7). The zonation patterns are also reflected in the size and abundance of Au and Au-telluride inclusions. The abundance of such inclusions decreases in pyrite mantles, but their size increases significantly and the average gold concentration of pyrite mantles increases as well. The chemical zonation patterns are consistent with the textural observation that pyrite-2a and pyrite-2b do not represent two distinct pyrite generations, but rather reflect changes in composition in response to an evolving hydrothermal fluid or varying fluid pulses. The elemental variations could reflect the mixing of local host-rock derived fluids enriched in Ni, Co and As, with externally derived fluids enriched in Bi, Te, Au, Ag and Sb.

Chemical variation plots (Fig. 4.14) show that pyrite grains from the same rock type plot in distinct groups. Assuming that all rock types interacted with the same hydrothermal fluid, it is likely that the trace element geochemistry of pyrite grains in diorite and ironstone is more strongly influenced by the host rock chemistry and fluid-rock interaction, whereas the trace element geochemistry of pyrite grains in quartz veins most closely reflects the hydrothermal fluid composition. This is particularly obvious for elements such as Co and Ni, which have high values in pyrite grains hosted in diorite compared to pyrite grains in quartz veins with ironstone plotting in between (Fig. 4.14a). In contrast, pyrite grains in ironstone have elevated concentrations of Zn, As and Sn (Table 4.2), whereas pyrite grains in quartz veins have elevated values of Te, Bi and Mo (Table 4.2). The As, Co and Ni distribution in pyrite grains from quartz veins is patchy, with the highest concentrations occurring in inclusion free pyrite rims (Fig. 4.5). By comparison, pyrite grains in ironstone and diorite show a uniform distribution for As, Co and Ni (Fig. 4.7) or more complex growth zoning (Figs. 4.7 and 4.8). The patchy distribution of As, Co and Ni observed in quartz vein hosted pyrite grains is interpreted to reflect poor availability of these elements in the hydrothermal fluid, even though ironstone and diorite were originally enriched in these elements. This pattern is

particularly obvious for Co, which has an average concentration of 809 ppm ($n = 37$) in pyrite grains in diorite, compared to an average concentration of 155 ppm ($n = 31$) in pyrite grains in quartz veins.

The Co/Ni ratio of pyrite can be used to determine the environment of formation. For example, sedimentary pyrite grains record Co/Ni ratios that generally fall between 0.01-2 (Gregory et al., 2015); volcanogenic ores have Co/Ni ratios >10 (e.g., Bajwah et al., 1987; Meyer et al., 1990; Large et al., 2009; Koglin et al., 2010); low temperature hydrothermal pyrite has Co/Ni ratios between 5-10 (Bralia et al., 1979; Mookherjee and Philip, 1979); pyrite from magmatic-hydrothermal deposits yield Co/Ni ratios between 1-10 (Bajwah et al., 1987); and pyrite from orthomagmatic segregations record Co/Ni ratios of <1 (Piña et al., 2013). For the Geita Hill deposit, pyrite grains from diorite and ironstone yield average Co/Ni ratios of 4.7 and 4.0 respectively (Table 4.3). The Co/Ni ratio is broadly similar across these mineralised pyrite grains, suggesting that equilibrium was reached between the mineralising fluid and the host rock. However, Co/Ni ratios do vary locally across a single pyrite grain. Pyrite cores enriched in Co and Ni, in both ironstone and diorite (Fig. 4.7, 4.8; Table 4.2), yield systematically higher Co/Ni ratios than adjacent rims. This trend is particularly clear in diorite-hosted pyrite, for which Co/Ni ratios cluster around ~ 10 in pyrite cores and ~ 1 in rims (Table 4.3). We interpret this type of zonation to be due to the local scavenging of Co and Ni from the surrounding rock during the early stages of sulfidation. The Co/Ni ratio of pyrite hosted in the quartz veins is more erratic. Co/Ni ratios are systematically higher in the cores of these pyrite grains (Fig. 4.9d, 4.10d), with several grains returning Co/Ni ratios that exceed 20 (Table 4.3). Such high ratios are due to the combined effects of low Ni and high Co, and suggests that the mineralising fluid may have had a high Co/Ni ratio as well. High Co/Ni ratios have been described for magmatic-hydrothermal fluids (Bajwah et al., 1987), suggesting that the mineralising fluids at Geita Hill had an igneous origin. This is consistent with the high fluorine content of hydrothermal biotite grains associated with the gold mineralisation (van Ryt et al., 2019), and the temporal and spatial association between gold deposition and potassic magmatism in and around the GGB. For example, multiple studies (e.g., Borg, 1994; Sanislav et al., 2015; 2017; van Ryt et al., 2017; Kwelwa et al., 2018b) have pointed out that gold is texturally late and coeval with the emplacement of lamprophyre dykes at ~ 2644 Ma (Borg and Krogh, 1999) and voluminous high-K granites between 2660 and 2620 Ma (Sanislav et al., 2014b).

Trace element mapping (Figs. 4.5-4.8) shows that the Te content of pyrite is below detection limits and most Te is found as micro-inclusions of telluride minerals. Our petrographic observations indicate that most Au in quartz veins is found in Au-tellurides, whereas ironstone contains a large proportion of free Au as well as Au-tellurides. The close association of gold with tellurides (e.g. Table 4.3, Figs 4.5-4.8, 4.14c) suggests that Te and Au were transported together in the mineralising hydrothermal fluid. Te is highly soluble in neutral to alkaline fluids with low salinity and high oxygen fugacity at high temperatures (e.g., Phillips and Groves, 1983; Cook et al., 2009; Grundler et al., 2013). Te precipitation is controlled by redox changes independent of the pH (e.g., Grundler et al., 2013; Keith et al., 2018). In the Geita Hill deposit, the main ore precipitation mechanism involved sulfidation of the wall rock due to the reaction of the hydrothermal fluids with magnetite in ironstone and biotite in diorite (van Ryt et al., 2017). The precipitation of pyrite due to fluid-rock interactions causes loss of sulphur from the ore fluids, destabilisation of the Au complexes and deposition of Au (e.g., Cline et al., 2005; Muntean et al., 2011) as free gold and Au-tellurides. The sulfidation of magnetite involved initial magnetite dissolution followed by oxidative precipitation of pyrite (e.g., Rickard and Luther, 2007; Qian et al., 2010). This process resulted in a fO_2 decrease in the fluid phase, which may have driven Te precipitation to explain the abundance of tellurides in the ore zones.

4.6.3. *Constraints on the temperature of the mineralising fluid*

The gold-related alteration assemblage at Geita Hill is relatively simple, comprising pyrite + tellurides + biotite + K-feldspar ± quartz ± carbonate (van Ryt et al., 2017; Borg, 1994). Gold has been observed as free-Au and gold-telluride inclusions in pyrite, biotite and along grain boundaries. The main gold bearing telluride minerals in the Geita Hill deposit are sylvanite [(Au,Ag)₂Te₄], nagyagite [Pb₃(Pb,Sb)₂S₆(Au,Te)₂] and calaverite [AuTe₂] (van Ryt et al., 2017)

Borg (1994) and Van Ryt et al. (2017) estimated maximum metamorphic conditions of 480 °C at no more than 3 kbar, based on the upper stability limit of actinolite, and suggested that mineralisation occurred at temperatures between 350-400°C. Telluride stability can place additional constraints on ore-fluid temperatures at Geita Hill. Experimental work by Cabri (1965) constrained the melting points of sylvanite and calaverite to ~354 °C and ~464 °C respectively, and also devised an Au-Ag-Te ternary geothermometer. A maximum temperature of 290 °C was calculated for sylvanite-calaverite assemblages by Kelly and Goddard (1969). Hotter temperatures favour

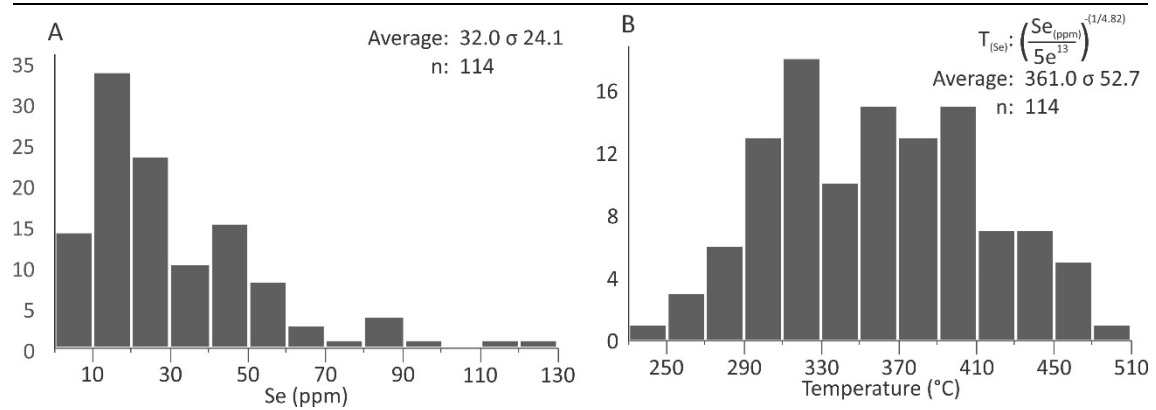


Figure 4.15. *Se*-based temperature constraints at Geita Hill; A) summary histogram of *Se* concentrations from gold-bearing pyrite-2a and 2b LA-ICP-MS spot analysis; B) temperature range based on regression coefficient by (Keith et al., 2018).

precipitation of krennerite [Au_{0.8-1}Ag_{0.2}Te₂], which is stable up to ~382 °C (Cabri, 1965). Thus, the abundance of tellurides in the Geita Hill deposit is consistent with the temperature estimates for mineralising fluids of <400 °C. The incorporation of Te in pyrite is temperature independent, but the Se content of pyrite is fluid temperature dependent (Large et al., 2009; Revan et al., 2014) and increases with decreasing temperature as follows (Keith et al., 2018):

$$Se_{pyrite} = 5 \cdot 10^{13} \cdot T^{-4.82} \quad (4.1)$$

The distribution of Se throughout most gold-bearing pyrite grains is uniform (e.g., Fig. 4.5-4.8), which implies that Se is lattice bound and not hosted in discrete inclusions. Se concentrations in pyrite are similar in all lithological units and appear to have a slight positive correlation with gold grades, especially in diorite (Table 4.3). The average Se content across mineralised pyrite in the Geita Hill deposit varies between 5.5-139 ppm (Fig. 4.15a). These concentrations correspond to a temperature range of 250 to 500 °C (Fig. 4.15b), with an average of 350 ± 40 °C. The Se content in pyrite from quartz veins is least variable, resulting in better-constrained temperature estimates between 300-383 °C (average 340 °C). The average Se content of post-mineralisation pyrite is 36 ppm, which yields a temperature estimate of 330 °C. These values are similar to temperature estimates based on the alteration mineralogy (Borg, 1994; van Ryt et al., 2017), and fall within the typical temperature range for Archean gold deposits (Goldfarb and Groves, 2015). Considering that the trace element composition of pyrite grains from quartz veins is least likely to be influenced by host rock chemistry and, therefore, most likely reflects the composition of the hydrothermal fluids, I

propose that the average temperature (340°C) determined from Se in mineralised pyrite grains provides the best estimate for the temperature of the hydrothermal fluid.

4.6.4. *Implications for exploration*

The data presented here demonstrate that mineralised pyrite and magnetite at Geita Hill are geochemically and texturally distinct and have the potential to be useful in exploration. Certain chemical elements, such as As, Sb, Bi, Te, Mo, Se (McCuaig and Kerrich, 1998), are commonly used as pathfinders for lode-gold deposits. Our study indicates that in the Geita Hill deposit the most useful pathfinder elements for mineralisation are Te and Bi. The concentration of various trace metals in pyrite and strongly altered magnetite indicate that Ag, Bi, Te, to a lesser extent Pb and possibly Mo were introduced into the system during the gold mineralisation event. The concentration of Au in mineralised pyrite grains from quartz veins shows an almost perfect positive correlation (Table 4.3) with Ag ($r = 1$), Te ($r=0.99$) and Bi ($r=0.97$) suggesting a co-genetic relationship. The oxidation of mineralised pyrite in the supergene environment will release and redistribute these metals in saprolite and soils. The behaviour of Ag in these environments is similar to that of Au (e.g., Webster, 1986) and unlikely to form a wide dispersion halo. Te, on the other hand, is preferentially enriched in soils (Diehl et al., 2012; Parnell et al., 2015) and has the potential to form a relatively wide Te anomaly around the mineralised quartz vein system. Bi shows the highest degree of mobility during supergene breakdown of pyrite (e.g., Nesbitt and Muir, 1994; Lu et al., 2005), and has a tendency to co-precipitate with hydrous Fe and Mn oxides. Therefore, it is likely to form a wide Bi anomaly around the mineralised vein system. As and Sb are commonly used as gold pathfinder elements (e.g., Boyle, 1974; McCuaig and Kerrich, 1998), but there is no correlation between Au and As or Sb in mineralised pyrite grains from Geita Hill. Moreover, there are no As- or Sb-bearing minerals found in the deposit, and it is, therefore, unlikely that these elements can be used as pathfinders for Geita Hill style mineralisation in the region. The mineralised pyrite is texturally different from earlier or later generations of pyrite, but the fact that its occurrence is limited to the mineralised zone makes it difficult to use in exploration. However, pyrite textures in conjunction with the occurrence of silica, K-feldspar and biotite alteration can be successfully used in identifying mineralised zones in drill core and open pit and, therefore, useful during mining operations. Altered magnetite grains that link to mineralisation are chemically distinct for a range of elements (Table 4.2; Co, Ni, Cu, W, Te, Au, Ag,

Bi increase with proximity to gold-bearing pyrite), and may be of use in regional exploration using heavy mineral separates.

4.7. Conclusions

Constraints on the composition of the hydrothermal fluid and conditions of formation of mineralisation have been discussed in detail for magnetite and pyrite. With increased alteration, peak-metamorphic, euhedral magnetite textures changed to mottled magnetite due to grain-scale dissolution and sulphidised magnetite as sulphidation progressed. These textural changes were accompanied by allied changes in magnetite chemistry; e.g. concentrations of Ni, Cr and Ti in non-altered magnetite are typical for igneous magnetite, whereas in sulphidised mottled magnetite their concentrations reflect hydrothermal processes. The compositional changes in hydrothermal magnetite involved the redistribution of elements that originated from the host ironstone (e.g. Ni, Cr, Ti, Pb, Mn and Cu), as well as enrichment of elements by an external fluid (Au, Ag, Bi, Te, Mo).

The majority of pyrite in the mineralised zone is of hydrothermal origin. Gold mineralisation at Geita Hill is associated with sulfidation of metamorphosed ironstone and diorite host rocks. Sulfidation reactions commenced with the precipitation of pyrrhotite, progressively overprinted by texturally distinct phases of pyrite. Similarities in texture, structural setting and elemental enrichment in Au, Ag, Te, Bi and Pb for alteration pyrite in different host rock types implies a single generation of mineralising fluids. However, significant variations across different host rock types occur as reflected in the distribution of inclusions, and lattice-bound elements like As, Ni and Co, which vary due to complex fluid-rock interactions at the grain-scale.

Trace element distribution patterns in pyrite grains highlight complex core-mantle-rim growth zoning. Pyrite cores, especially in ironstone and diorite are enriched in As, Co, Ni and base metals including Cu and Zn. Co is re-mobilised into the pyrite mantles as growth continues, but Ni and As are not, whilst the outermost rim of pyrite grains may be severely depleted in As, Co and Ni, but enriched in Sb, Pb and Bi. Gold is hosted throughout these pyrite grains as free-Au and Au±Ag-telluride inclusions. These inclusions are smaller and more numerous within the cores of pyrite grains, and larger though less numerous in the mantles and rims. For pyrite grains in ironstones and

ironstone-hosted quartz veins, the core-mantle structure of pyrite grains is highlighted by the distribution of inclusions of pyrrhotite, magnetite and minor base metal sulphides, which are largely concentrated in the cores of the pyrite grains. Pyrite grains in mudstones and diorite lack inclusions, but still display similar growth zoning patterns as pyrite in ironstone, as illustrated by LA-ICP-MS mapping.

Elements like As, Ni, Co and Cu appear to be largely locally derived, and remobilised into pyrite during sulfidization. The concentrations and distribution patterns of these elements are variable depending on host lithology, textural position and temperature of formation. Au, Ag, Te, Bi and to a lesser degree Pb are strongly correlated and show a spatial association with electrum and tellurites in or near pyrite. These elements appear to be externally derived, and precipitate together. Se concentrations in pyrite from quartz veins indicate some temperature variability and an average temperature for the mineralising fluids of $\sim 340^{\circ}\text{C}$. Gold ore is significantly enriched in Ag, with an average Au/Ag ratio of 0.41, and gold grades do not correlate with As, but are almost perfectly correlated with Te and Bi in pyrite in mineralised veins, which also yields high Co/Ni ratios of >20 typical for magmatic-hydrothermal fluids. These trace element associations together with the high fluorine content of hydrothermal biotite grains (van Ryt et al., 2019), and the temporal and spatial association between gold deposition and potassic magmatism in and around the GGB, are consistent with a magmatic-hydrothermal origin for the ore-forming fluid at Geita Hill.

The alteration footprint of the Geita Hill deposit is limited in extent, and does not involve elements like As and Sb which are typically enriched in Archaean lode-gold systems. Instead, Te and Bi are most characteristic for the deposit and could be of use as path finder elements together with altered magnetite grains.

Chapter 5

Evolution of fluids associated with Archean gold
mineralisation at Geita Hill (Tanzania): a fluid inclusion study

Abstract

The Geita Hill deposit is a structurally controlled, lode gold system associated with the influx of late-tectonic hydrothermal fluids into the diorite and ironstones of the Geita Greenstone Belt in Tanzania. Three stages of gold-related hydrothermal alteration are preserved in the alteration zone, representing a developing fluid system. Alteration commenced with silicification of the host rocks, which in can be recognised extending several metres from narrow quartz feeder veins. Silicification is followed by the development of gold-bearing micro-fractures and later multi-phased, crack-seal tension veins. Detailed microthermometry and raman microspectroscopy have identified three principle fluids synchronous with gold precipitation: (1) A low salinity, carbonic-rich ($X_{CO_2} > 0.8$) fluid with minor N_2 ($X_{N_2}/(X_{CO_2} + X_{N_2}) < 0.15$) that was interpreted to be metamorphic in origin; (2) A high salinity ($NaCl+CaCl_2 > 20$ wt.%; $NaCl/(NaCl+CaCl_2)$ mass ratio > 0.45), aqueous brine that was interpreted to be magmatic in origin; and (3) A low salinity ($NaCl < 5$ wt.%) aqueous fluid that was interpreted to be meteoric in origin. These preserved fluid assemblages imply mineralisation occurred at pressures of less than 2 kbar, likely from 1.4 to 1.7 kbar, at temperatures of approximately 350 °C. C-O-H fluid modelling of the carbonic-rich fluid has constrained $f_{O_2}^{fluid}$ to 1.5-1.8 \log_{10} units above $f_{O_2}^{FMQ}$ corresponding to absolute values of $10^{-30.5}$ bar. Our calculations also show that a typical, H_2O -rich orogenic-style metamorphic fluid interacting with graphitic sediments at these conditions would become enriched in CO_2 and N_2 . The gold was likely transported in the high salinity brine as Au-bisulfide complexes with tellurium, potentially introduced as a vapour. Deposition of Au was triggered via interaction of gold-bearing fluids with the relatively reduced Fe-rich host rocks and the low salinity CO_2 -rich fluid.

5.1. Introduction

Archean greenstone-hosted lode gold deposits comprise a significant proportion of global gold production and reserves. Reviews by Mikucki (1998), Ridley and Diamond (2000), and Goldfarb and Groves (2015) have summarised the nature of fluids responsible for the formation of orogenic gold systems. Ore fluids in orogenic deposits are low to moderate salinity aqueous-carbonic fluids ($0.05 < X_{CO_2} < 0.2$; $\pm CH_4 \pm N_2$), with a neutral to slightly alkaline pH and significant H₂S (Goldfarb and Groves, 2015). Fluids with these properties have a high solubility for Au as hydrosulfide complexes, along with Ag, As and Sb (Phillips and Evans, 2004), but are less effective at transporting base metals (Ridley and Diamond, 2000), which explains the “gold-only” nature of these deposits.

The origin of gold-bearing fluids in Archean lode old deposits is generally linked to either a metamorphic or felsic magmatic source, or a combination thereof (Goldfarb and Groves, 2015). Metamorphic fluids form as a result of prograde devolatilisation reactions during greenschist- to amphibolite-facies metamorphism (e.g., Phillips and Powell, 2009; Tomkins, 2010), to produce fluids that can focus into regional fault systems. The ultimate source for gold in this model are greenstone belt rocks from which gold is dissolved and transported in metamorphic fluids (Phillips and Powell, 2010). In the magmatic model, gold is concentrated in progressively fractionating magmatic fluids due to its incompatibility in the melt, and exsolved during crystallisation (Cline and Bodnar, 1991). The intrusive systems held responsible for gold mineralisation are usually highly evolved, oxidised-alkaline and calc-alkaline granites (e.g., Helt et al., 2014; Fayol et al., 2016). Mesothermal intrusion-related systems are typically characterised by an early phase of low-salinity carbonic-aqueous fluid inclusions similar to those observed in metamorphic systems, followed by a later phase of moderate- to high-salinity brines (Baker, 2002). The timing relationship of these evolving fluids has been linked to complex interactions of volatiles in intrusive melts at different crustal levels; i.e. carbon dioxide has a low solubility in felsic melt and is exsolved early during magma ascent, whereas later fluids become increasingly water-rich and more saline (Baker, 2002).

Archean greenstone-hosted gold systems in the Geita Greenstone Belt (GGB) include eight operating deposits that produce ca. 0.5 Moz of gold per year. The largest deposits, Nyankanga, Geita Hill, Kukulama and Matandani have been the focus of a series of studies investigating the structures

(e.g., Sanislav et al., 2015; 2017; 2018b; Kwelwa et al., 2018b) and alteration assemblages (e.g., Sanislav et al., 2015; van Ryt et al., 2017; van Ryt et al., in press; Kwelwa et al., 2018a) associated with gold mineralisation, and suggest a complex fluid history. In this contribution we present results of a detailed fluid inclusion study from the Geita Hill deposit. We aim to constrain the physico-chemical conditions during gold mineralisation and discuss the source of mineralising fluids.

5.2. The paragenetic framework

Host rocks to the mineralising fluids in the Geita Hill deposit contain mineral assemblages that can be subdivided into three principle groupings: (1) the metamorphic background assemblage; (2) a hydrothermal alteration assemblage associated with gold mineralisation; and (3) a post-mineralisation alteration assemblage (van Ryt et al., 2017). The principle characteristics of each of these groupings is summarised below.

5.2.1. *The metamorphic background assemblage*

The regional biotite + actinolite + sericite (phengite) ± K-feldspar ± carbonate ± chlorite assemblage observed in meta-diorite and meta-ironstone formed during upper greenschist facies metamorphism, at estimated temperatures of 375 – 480 °C and pressures of < 3 kbar (van Ryt et al., 2017). Primary igneous hornblende and pyroxene grains in meta-diorite were replaced by biotite with accessory K-feldspar, chlorite, calcite, apatite and iron oxides. Primary igneous plagioclase was partially altered to sericite. Sedimentary units including ironstone, black (graphitic) shale and mudstone, contain biotite and actinolite with accessory graphite, chlorite, calcite and K-feldspar. Magnetite is the dominant oxide in the ironstone units, and sulfides present during peak metamorphism include pyrite and pyrrhotite. Early quartz veins are folded and consist of white, milky quartz without significant alteration halos or accessory hydrothermal minerals.

5.2.2. *Alteration associated with gold mineralisation*

The gold mineralising event is characterised by the assemblage quartz + biotite + K-feldspar + pyrite + Au (free-Au and gold-tellurides). This alteration assemblage occurs in sulfidation fronts affecting iron-rich sediments, along micro-fracture networks in silicified diorite and Fe-poor sediments, and

as disseminated sulfide alteration. Alteration associated with gold mineralisation is tectonically late and overprints the primary bedding and all structural foliations, and is generally concentrated along lithological contacts with high competency contrasts and along pre-existing structures (Sanislav et al., 2017). High-grade mineralisation (>5 g/t) and associated alteration is commonly accompanied by (and overprints) quartz feeder veins, with silicification halos that extend out for several metres. The alteration assemblage formed at pressure-temperature conditions that are similar to peak metamorphic conditions (van Ryt et al., 2017).

5.2.3. *Post-mineralisation alteration*

Late-stage veining is characterised by the assemblage calcite ± ankerite ± siderite ± quartz ± chlorite ± barite ± pyrite ± hematite, and locally overprints and replaces the gold-related alteration assemblage. The composition of late-stage carbonate veins, especially with respect to their accessory minerals, are strongly dependent on the host lithology. Two of the most common vein types are quartz-carbonate (in ironstone and mudstone units) and carbonate-chlorite (in diorite units). Pyrite occurs where the veins intersect magnetite-bearing shale units and zones with pre-existing sulfides. Chlorite replaces biotite and actinolite in the halo of late-stage veins, and occurs as a primary vein mineral in Mg-rich units such as hornblende-diorite. Carbonate species transition from calcite to ankerite-siderite in proximity to magnetite-shale laminae and mafic phenocrysts within ironstone and diorite, respectively. The composition of the post-mineralisation mineral assemblage is consistent with lower greenschist facies conditions.

5.3. Methodology

5.3.1. *Sample selection for fluid inclusion studies*

Five 180 µm, double polished sections were made of representative, mineralised (samples GQ-DBL, GQ-01a, GHDD0302-13A, GHDD0302-15) and non-mineralised (sample GHDD0302-01), hydrothermally altered rocks from the Geita Hill deposit (Fig. 1.2). The selected samples include plagioclase-diorite, ironstone and quartz feeder veins. Samples GHDD0302-15 (Fig. 3.1a) and GHDD0302-13A (Fig. 5.1b) represent moderately altered mudstone, and highly altered porphyritic

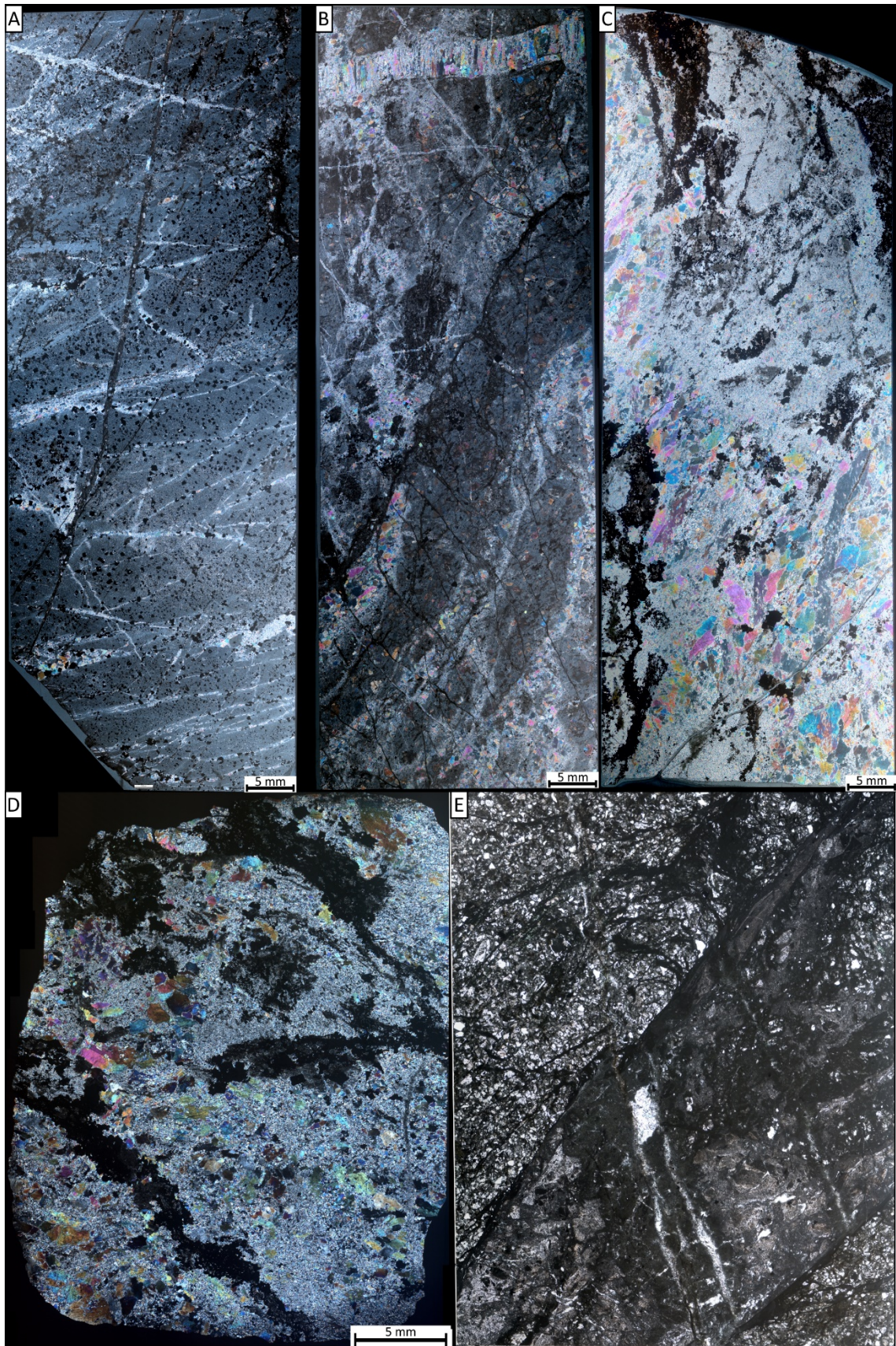


Figure 5.1. Cross polarised light (XPL) microphotographs of the double polished sections: A) silicified mudstone (GHDD0302-15); B) silicified and highly altered diorite (GHDD0302-13A); C) quartz feeder vein (GQ-01); D) Quartz feeder vein GQ-DBL); E) non-mineralised carbonate-chlorite vein in diorite (GHDD0302-01).

diorite, respectively. Both the mudstone and diorite samples experienced pervasive silicification, and gold-bearing micro fracturing is common. Samples GQ-01a (Fig. 5.1c) and GQ-DBL (Fig. 5.1d) were collected from mineralised quartz feeder veins, and sample GHDD0302-01 (Fig. 5.1e) was collected from a post-mineralisation quartz-carbonate-chlorite vein cutting porphyritic diorite away from the ore zone. Mineral assemblages and textural relationships were mapped in thin section to determine overprinting relationships, and to place hydrothermal alteration phases into the paragenesis framework for the deposit (van Ryt et al. 2017). Following this work, one sample (GHDD0302-13A, Fig. 5.1b) of a gold-bearing altered diorite was selected for a detailed fluid inclusion study as it contains a sufficient number of suitable inclusions in quartz grains.

5.3.2. *Fluid inclusion microthermometry*

A combination of detailed optical microscopy, microthermometry and Raman spectroscopy was used to identify and characterise the fluid inclusion assemblages. Fluid inclusion microthermometry was conducted using an OLYMPUS BX51 microscope with 40x and 50x objectives. A Linkham MDS600 heating-freezing stage is attached to the microscope and is operated using Linksys 32 software. Samples to be measured were placed within the insulated stage on a 10 mm diameter quartz lens, itself affixed to perpendicular threaded axels and resting on a thick silver block. Temperature within the stage is controlled through interaction between a heating element inside the silver block, and liquid nitrogen pumped through the block. The temperature range for this setup is from -190 °C to 600 °C, with heating and cooling rates that range from 0.1 °C/min to 90 °C/min. The stage was calibrated daily using a standard CO₂-H₂O fluid inclusion, by measuring the triple points of CO₂ (-56.6 °C) and H₂O (0.0 °C). The following phase transitions were measured upon heating:

1. Final melting of CO₂: ($T_m^{CO_2}$): solid + vap = liq + vap.
2. Initial melting (T_i) in H₂O-NaCl-CaCl₂ and H₂O-NaCl fluid inclusions in which either antarcticite (antarcticite + hydrohalite [hh] + ice + vap = liq + hh + ice + vap), or hydrohalite (hh + ice + vap = liq + ice + vap) is the first solid phase to disappear.
3. Final melting of ice in H₂O-NaCl-CaCl₂ and H₂O-NaCl fluid inclusions (T_m^{ice}): ice + liq + vap = liq + vap.

-
4. Homogenisation of CO₂-rich carbonic inclusions by disappearance of the vapour bubble into the liquid phase ($T_h^{CO_2}$): liq + vap = liq.
 5. Homogenisation of aqueous fluid inclusions by disappearance of the vapour bubble into the liquid phase (T_h^{aq}): liq + vap = liq

Phase transitions were recorded using a Point Grey Research Grasshopper3 GS3-U3-28S5C video camera, creating 2560×1440p, 12 fps video files. Video files were created allowing the measurement of multiple fluid inclusions within a field of view and enhancing the reliability of temperature measurements. Three or four video files were created for a given inclusion site, covering heating from -100 °C to 280 °C.

Molar volume calculations of all fluid inclusion types were performed using the BULK software by Bakker, (2003). Equations of state by Span and Wagner (1996) were used to calculate the bulk fluid properties for CO₂ and CO₂-H₂O fluid inclusions, with additional equations by Krumgalz et al. (1996) for CO₂-H₂O-NaCl-CaCl₂ fluid inclusions. Bulk fluid properties of CO₂-N₂, CO₂-N₂-H₂O, and CO₂-N₂-H₂O-NaCl-CaCl₂ fluid inclusions were modelled following equations by Bowers and Helgeson (1983) and Bakker (1999). The molar volume and composition of carbonic phases in the fluid inclusions were determined using molar volume vs composition diagrams from Thiéry et al., (1994). The NaCl + CaCl₂ salinities (wt.%) and minimum NaCl/(NaCl+CaCl₂) mass ratio of H₂O-NaCl-CaCl₂ fluid inclusions were calculated on the basis of final melting (T_m^{ice}) following Williams-Jones and Samson (1990).

ISOC software (Bakker, (2003) was used for the calculation of isochores, with equations of state as follows: CO₂, CO₂-N₂, CO₂-H₂O and CO₂-N₂-H₂O after Duan et al. (1992; 1996); CO₂-H₂O-NaCl after Anderko and Pitzer (1993a; 1993b) and Duan et al. (1995); H₂O-NaCl after Knight and Bodnar (1989) and Bodnar and Vityk, (1994).

5.3.3. *Laser Raman spectroscopy*

Laser Raman spectroscopy is a valuable tool for the identification of gaseous, liquid and solid phases in fluid inclusions, and can detect substances otherwise invisible to microthermometry. Raman analyses were conducted with a WITec Alpha Access 300 at the Advanced Analytical Centre at James Cook University. The Raman is equipped with a UHTS 300 SMFC VIS-NIR laser with an excitation

wavelength of 532 nm. Data processing was done with WITec Project Data Analysis Software 4.1. Raman vibrations were compared to known signatures (Frezzotti et al., 2012). Laser Raman spectroscopy was conducted on 122 fluid inclusions.

5.4. Results

5.4.1. *Sample description*

Sample GHDD0302-13A is a gold-bearing altered diorite (Fig. 5.2). No late carbonate overprint is present in this sample, i.e. the gold-bearing assemblages have not been affected by post-mineralisation overprints. The sample has been affected by three stages of hydrothermal alteration, which collectively have largely destroyed the original igneous texture. These stages include: (1) pre-mineralisation silicification; (2) gold-related micro-fracturing; and (3) late-mineralisation quartz veins. Each alteration stage is characterised by a suite of distinct fluid inclusions types (Table 5.1), which will be described below.

5.4.2. *Pre-mineralisation silicification*

The earliest hydrothermal alteration stage linked to gold mineralisation involves silicification, characterised by fine-grained hydrothermal quartz (Fig. 5.2). Silicification overprints the primary mineralogy, and partially follows the pre-existing foliation. Fine-grained (<5 μm), disseminated graphite is present where silicification overprints graphite-bearing ironstone and shale units, but was not observed where silicification overprints porphyritic diorite. The areas of rock affected by silicification are only locally auriferous, and silicification served to prime the rock for the development of gold-bearing Pyrite + Biotite + K-feldspar micro-fractures (van Ryt et al., 2017), i.e., not all silicified rocks in the deposit are mineralised, but all mineralised rocks are silicified.

Only one fluid inclusion type (Type 1 in Table 5.1) was observed in quartz grains that define with silicification. These carbonic fluid inclusions are hosted in clusters and rarely as trails (Fig. 5.3). No aqueous phase is visible in the fluid inclusions, but Raman microspectroscopy (Fig. 5.4a) indicates the presence of H_2O and N_2 in some. Fluid inclusions are, therefore, either pure carbonic ($\text{CO}_2 \pm \text{N}_2$) or carbonic-aqueous ($\text{CO}_2\text{-H}_2\text{O} \pm \text{N}_2$) with less than 10 vol.% (invisible) H_2O and well-defined negative crystal shapes (Table 5.1).

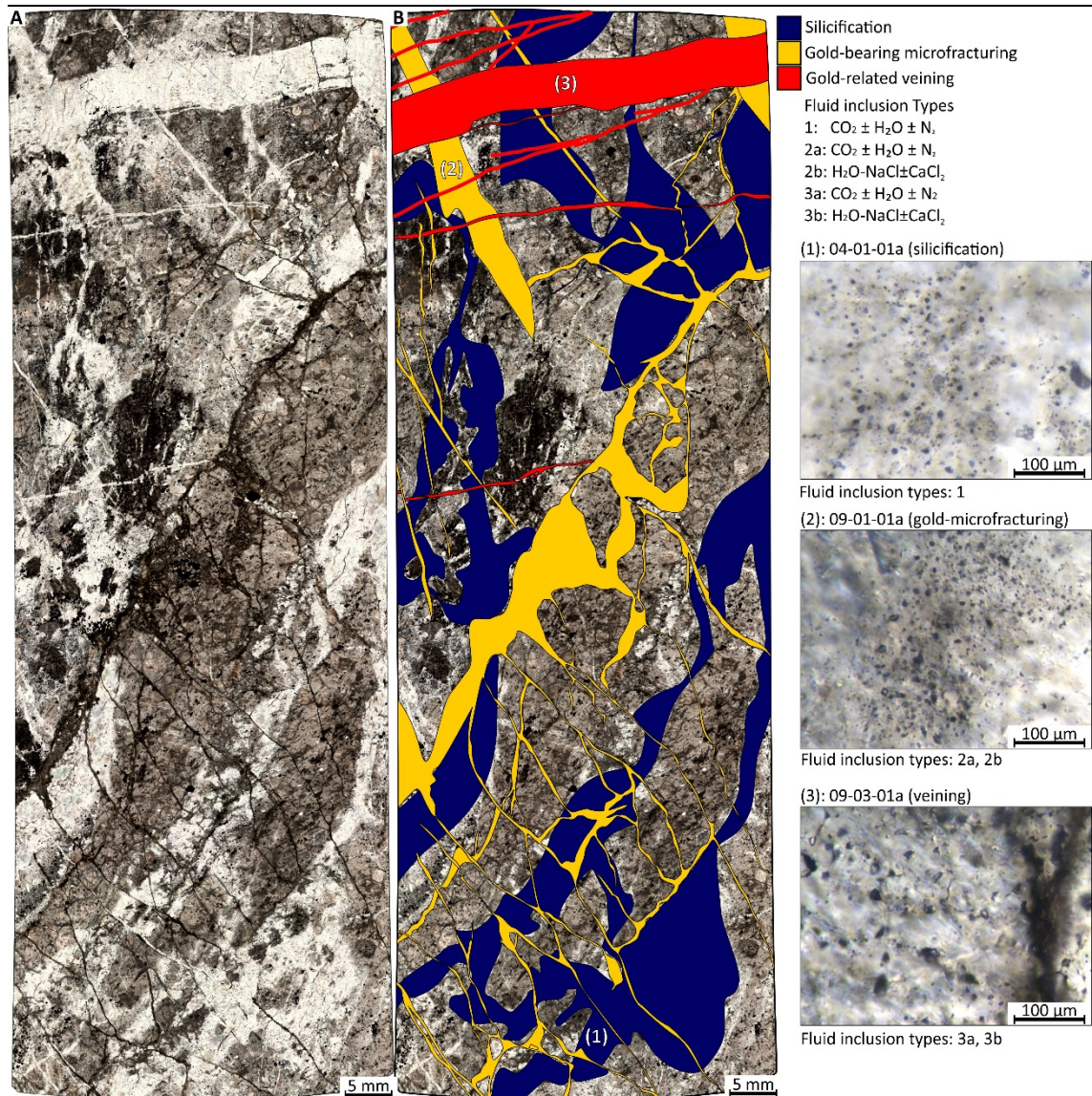


Figure 5.2. High resolution transmitted light (TL) microphotograph (A) of section GHDD0302-13A. Overlain is a schematic alteration paragenesis (B) comprising silicification (1), gold-bearing micro-fracturing (2) and gold-related veins (3). Silicification follows the pre-existing foliation in the section, and is overprinted by micro-fractures that opened along a broadly consistent orientation of 45° from the sections long axis. Veining overprints both silicification and microfracturing, and is roughly parallel ($\pm 20^\circ$) from the short axis of the section. The TL microphotographs (right) are examples fluid inclusions from each of these assemblages, their exact position in the section is also marked.

5.4.3. Gold-related microfracturing

Gold-bearing micro-fractures generally cross-cut silicification (Fig. 5.2). The micro-fractures occur as an interconnected network of fine, mm-scale fractures that opened along a broadly consistent orientation (van Ryt et al., 2017). Most micro-fractures contain biotite, K-feldspar and pyrite with quartz as a minor component. Graphite was not observed in these micro-fractures. The prevalence of quartz increases where multiple fractures intersect, or within the cores of larger fractures. Wider

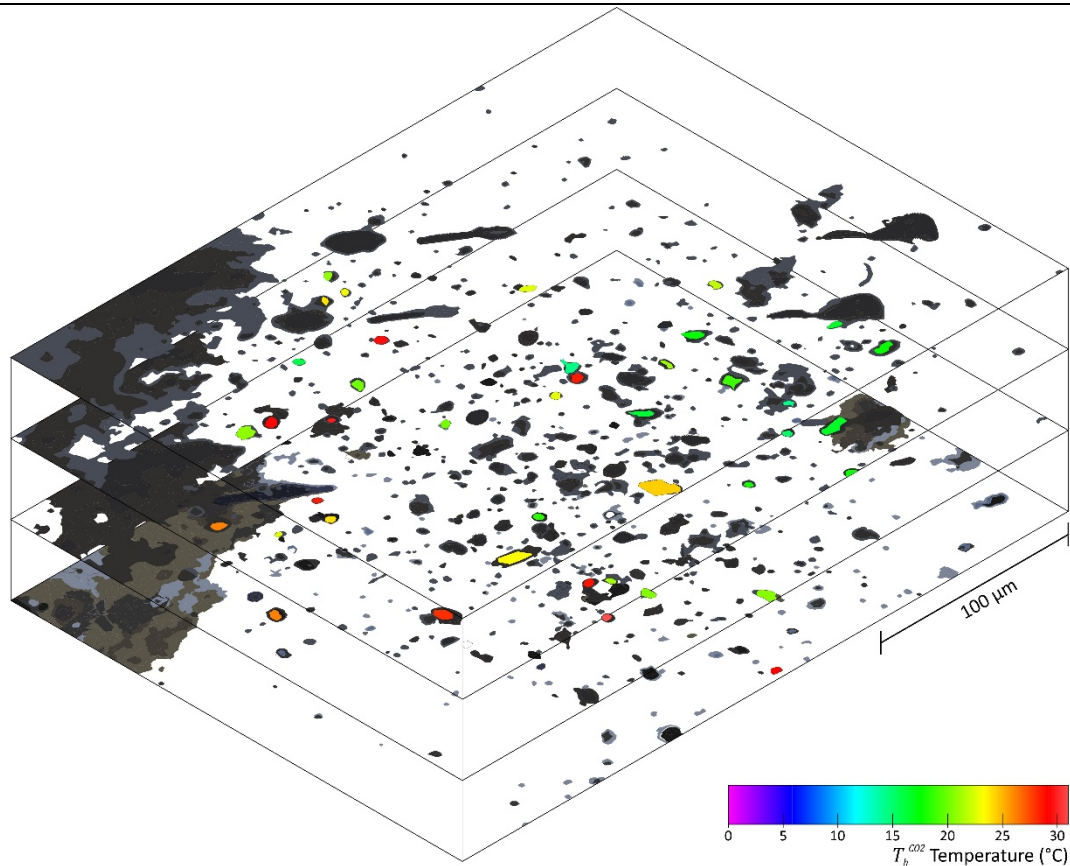


Figure 5.3. Isometric three-dimensional projection illustrating the clustered nature of the primary Type 1 $CO_2 \pm N_2 \pm H_2O$ fluid inclusions hosted in silicification-related quartz. Measured fluid inclusions are colour coded according to $T_h^{CO_2}$ in °C, non-measured fluid inclusions are left black in the projection.

bands of disseminated, replacement-style alteration in equilibrium with gold and comprising pyrite + biotite + K-feldspar can be seen along fractures near the contact between silicified zones and the host diorite. Locally, the micro-fractures blend into and merge with zones of silicification. Larger micro-fracture networks in less altered rocks develop a silicification halo; i.e. micro-fracturing and silicification are related processes.

Quartz grains that formed along gold-bearing micro-fractures contain clusters of at least 50 fluid inclusions of both carbonic ($CO_2 \pm N_2$), carbonic-aqueous ($CO_2-H_2O \pm N_2$; < 10 vol.% H_2O) fluid inclusions (collectively grouped as Type 2a in Table 5.1), as well as aqueous ($H_2O-NaCl \pm CaCl_2$) fluid inclusions (Type 2b in Table 5.1). Type 2a fluid inclusions represent 75-85% of all fluid inclusions in these clusters.

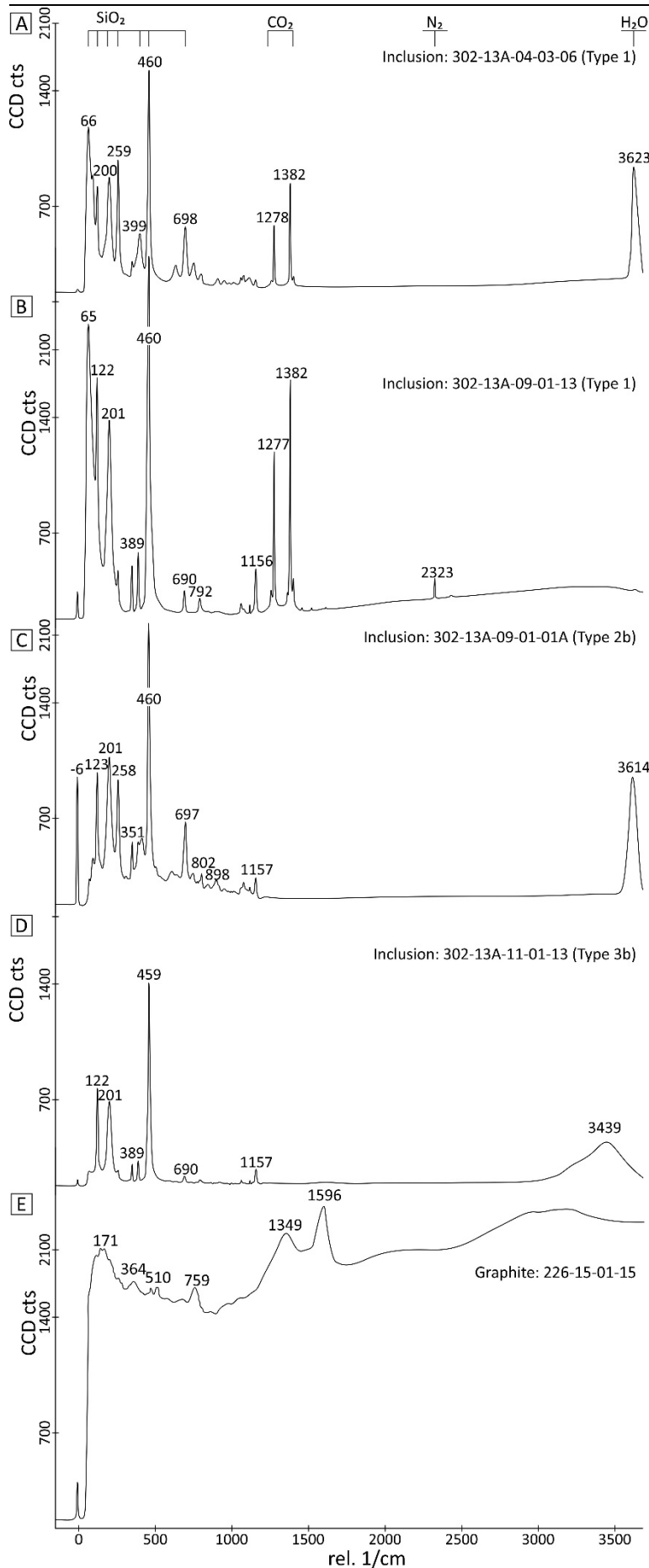


Figure 5.4. Raman spectra of representative inclusions; (A) Type 1 $\text{CO}_2\pm\text{N}_2\pm\text{H}_2\text{O}$ fluid inclusion associated with pre- to syn-mineralisation silicification; (B) Type 2a $\text{CO}_2\pm\text{N}_2\pm\text{H}_2\text{O}$ fluid inclusion associated with gold-bearing microfracturing, fluid inclusion has a $T_m(\text{CO}_2)$ of $-57.1\text{ }^\circ\text{C}$; (C) Type 2b $\text{H}_2\text{O-NaCl}\pm\text{CaCl}_2$ inclusion associated with gold-bearing microfracturing; (D) Type 3b $\text{H}_2\text{O-NaCl}\pm\text{CaCl}_2$ inclusion associated with gold-bearing quartz veins; (E) Graphite hosted in the sedimentary pile.

5.4.4. *Late-mineralisation quartz veins*

Most of the gold-bearing micro-fractures are cross-cut by quartz veins that contain minor gold-bearing pyrite, biotite and K-feldspar. No graphite was observed in these veins. The quartz textures within the veins include (partly recrystallised) quartz that formed at right angles to the vein wall consistent with antitaxial growth (i.e. vein opening along the vein margins, with crack-seal textures visible as regular trails of fine inclusions parallel to the vein margin (Fig. 5.5; e.g., Fossen, 2016). This indicates that the quartz veins are multi-phased tension veins, i.e. they opened over a period of time in response to multiple events. The veins comprise quartz and some incorporate selvages of host diorite. Quartz textures and vein geometries indicate three distinct stages of growth: The initial stage is characterised by fine-grained, equidimensional, anhedral-subhedral quartz grains along the edges of the vein that are interpreted to represent the first stages of vein opening. Fluid inclusions in this type of quartz occur isolated or in clusters of up to several hundred individual fluid inclusions. Most (>90%) fluid inclusions in these clusters are carbonic ($\text{CO}_2 \pm \text{N}_2$) or carbonic-aqueous ($\text{CO}_2\text{-H}_2\text{O} \pm \text{N}_2$; <10 vol.% H_2O), collectively grouped as Type 3a in Table 5.1. The remainder are aqueous ($\text{H}_2\text{O-NaCl} \pm \text{CaCl}_2$) fluid inclusions (Type 3b in Table 5.1).

The intermediate growth stage is characterised by elongated quartz grains that are distributed throughout the core of the vein. The crystallographic c-axis of these grains is oriented at a high angle (> 60 °) to the vein walls, and up to 80 fine intragranular inclusion trails interpreted as healed cracks (as in crack-seal textures) can be observed in each grain, with trails orientated parallel to vein walls (Fig. 5.5c, d). These features are consistent with crack-seal tension veining, with each crack representing another phase of vein widening allowing quartz growth (Fossen, 2016). The continuation of the elongated grains across the centre of the veins implies the veins widened along the vein margins rather than the vein centre. Fluid inclusions in these elongated quartz grains are aqueous ($\text{H}_2\text{O-NaCl} \pm \text{CaCl}_2$), hosted in the intragranular inclusion trails and rarely as isolated fluid inclusions (Type 3b in Table 5.1).

The final growth stage is characterised by fine-grained quartz grains associated with irregular, healed fractures that cut the vein. Limited fluid inclusions were observed in these healed fractures.

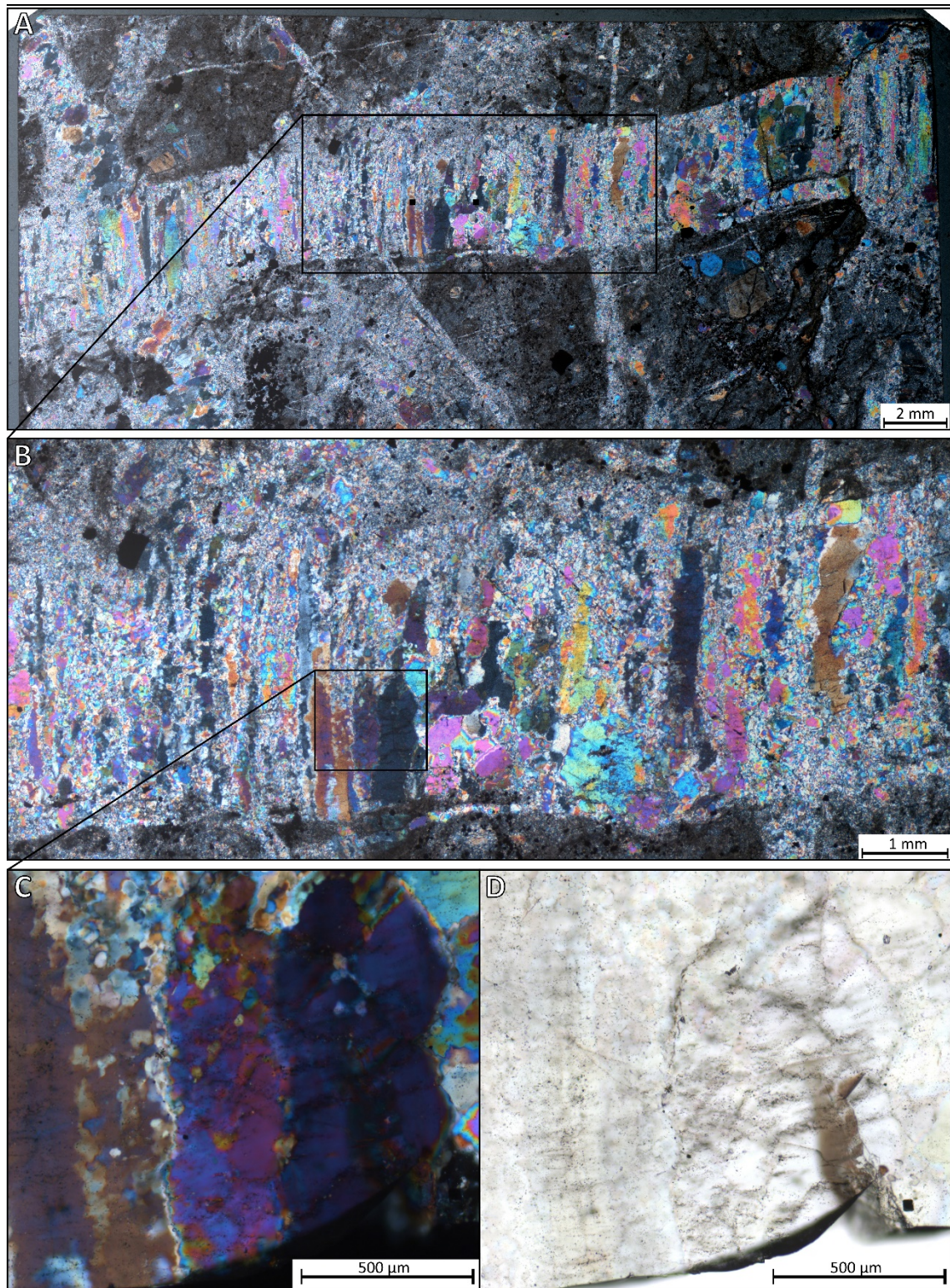


Figure 5.5. Photomicrographs of fluid inclusions from section GHDD0302-13A, centred within a multi-phase quartz crack-seal tension vein (e.g., Fossen, 2016). A), B) and C) show crossed polarised photomicrographs of the vein at increasing magnification, D) Transmitted light photomicrograph of the same region as C) showing inclusion trails that define the crack-seal textures.

5.4.5. Fluid inclusions descriptions

5.4.5.1. Inclusion Type 1 ($CO_2 \pm N_2 \pm H_2O$)

Type 1 fluid inclusions are restricted to areas of rock affected by pre-mineralisation silicification (Fig. 5.2). These clustered fluid inclusions show negative crystal shape, ranging in size from sub-microscopic, up to 15 μm . Some larger fluid inclusions appear decrepitated and now exist as wreckage. $T_m^{CO_2}$ occurred across a range from -56.6 to -59.0 $^{\circ}C$ (Fig. 5.6a), temperatures below -56.6 $^{\circ}C$ indicate the presence of N_2 which was confirmed by Raman spectroscopy (Fig. 5.4b). $T_h^{CO_2}$ was observed between +6.0 and +31 $^{\circ}C$, with most (>80%) fluid inclusions homogenising between +14 and +27 $^{\circ}C$ (Fig. 5.6b). The molar volume of the carbonic phase determined from $T_h^{CO_2}$ and $T_m^{CO_2}$, (Thiery et al., 1994) ranges from 50 to 88 cc/mol, with 80% ranging from 53 to 65 cc/mol (Fig. 5.6c). The $T_h^{CO_2}$ and $T_m^{CO_2}$ values indicate a $X_{N_2}/(X_{CO_2} + X_{N_2})$ ratio of < 0.15 (Fig. 5.6d, 5.7a). Clathrate

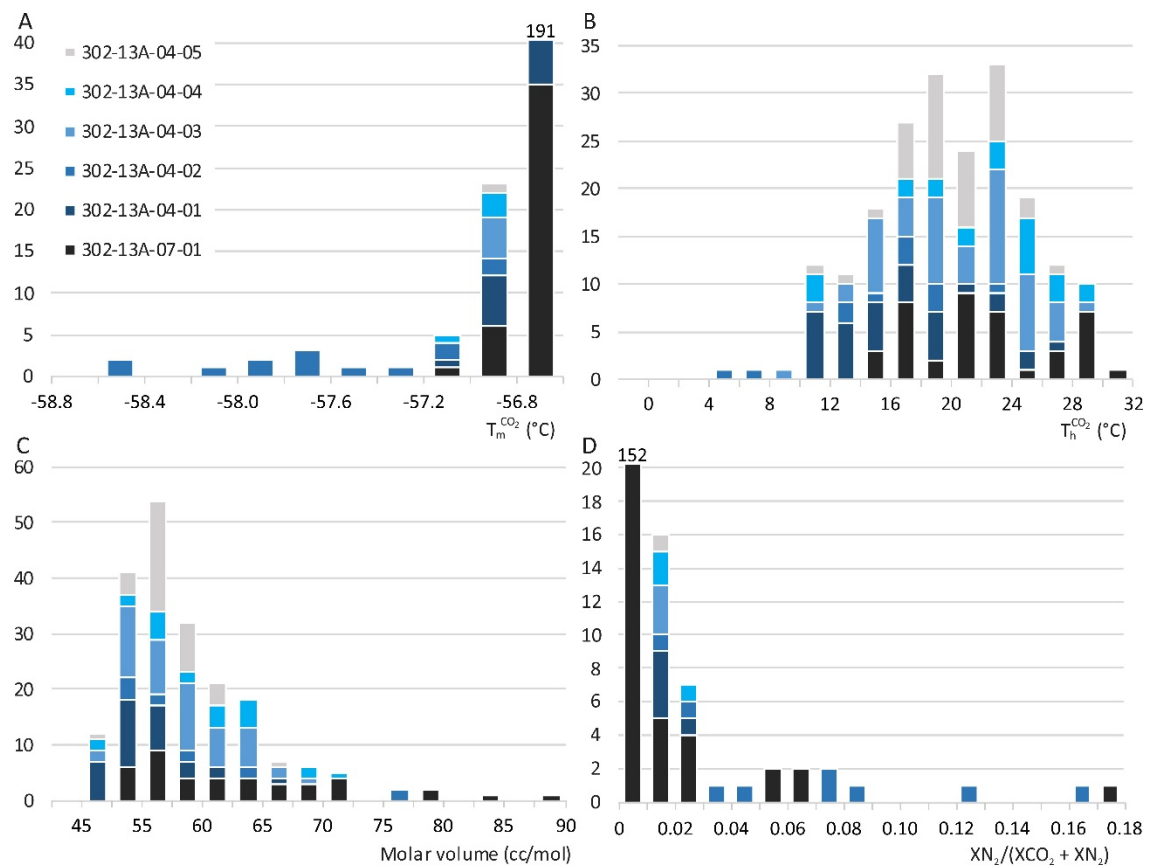


Figure 5.6. Type 1 $CO_2 \pm N_2 \pm H_2O$ fluid inclusions in quartz associated with silicification: A) $T_m^{CO_2}$; B) $T_h^{CO_2}$; C) Calculated molar volumes (including N_2); D) $X_{N_2}/(X_{CO_2} + X_{N_2})$ determined from $T_m^{CO_2}$ and $T_h^{CO_2}$ following Thiery et al., (1994). Histogram data is colour coded according fluid inclusion to measurement sites.

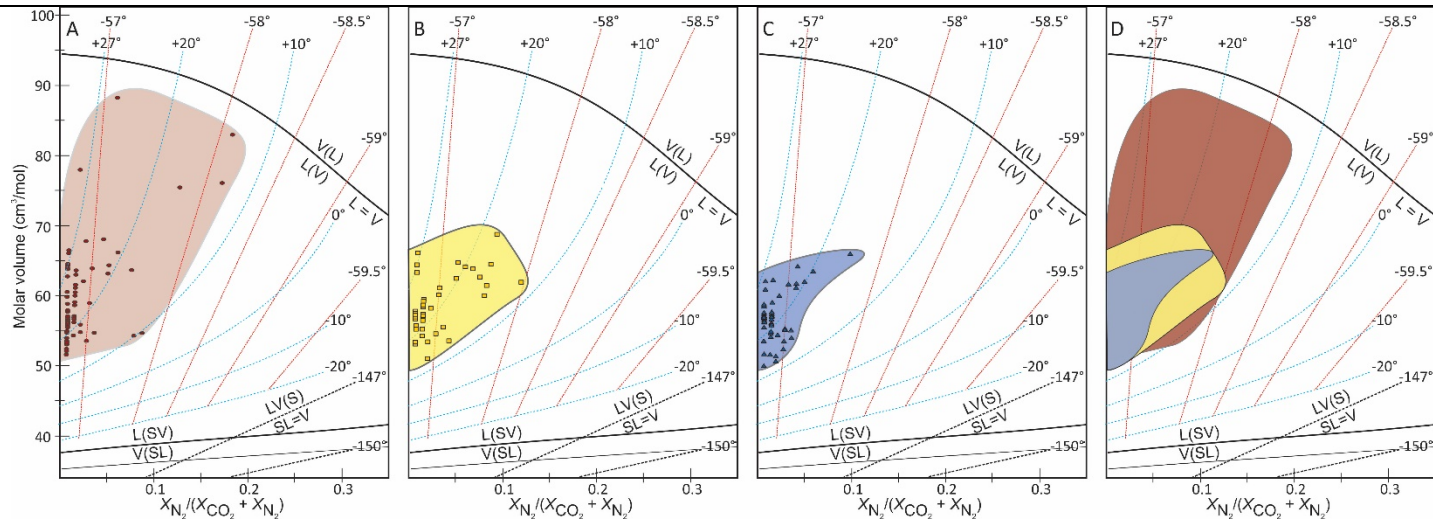


Figure 5.7. Molar volume vs $X_{N_2}/(X_{CO_2} + X_{N_2})$ for the $CO_2 \pm N_2 \pm H_2O$ fluid inclusions (Type 1, 2a, 3a) (modified from (Thiéry et al., 1994): A) Type 1 fluid inclusions associated with silicification; B) Type 2a fluid inclusions associated with microfracturing; C) Type 3a fluid inclusions associated with crack-seal tension veining, and D) Fields of Type 1, 2a and 3a fluid inclusions overlain. Note that $X_{N_2}/(X_{CO_2} + X_{N_2})$ and molar volume decreases as the system progresses from silicification to veining.

Table 5.1. Summary of fluid inclusion properties. Fluid inclusion data is presented as Appendix 7.1.

Alteration style	Silicification	Microfracturing		Veining	
Fluid Type	Type 1	Type 2a	Type 2b	Type 3a	Type 3b
Fluid inclusion size and shape	< 15 μm	< 15 μm	< 10 μm	< 20 μm	< 30 μm
Occurrence	Isolated and clustered	Clustered	Clustered	Clustered	Clustered and trail hosted
Composition	$CO_2 \pm H_2O \pm N_2$	$CO_2 \pm H_2O \pm N_2$	$H_2O - NaCl \pm CaCl_2$	$CO_2 \pm H_2O \pm N_2$	$H_2O - NaCl \pm CaCl_2$
	$(CO_2/(CO_2 + N_2)): 0.83 - 1$ $X_{H_2O}: < 0.1$	$(CO_2/(CO_2 + N_2)): 0.88 - 1$ $X_{H_2O}: < 0.1$	2.9 – 25.3 wt.% NaCl equiv. NaCl wt fr. = 0.55 – 1	$(CO_2/(CO_2 + N_2)): 0.9 - 1$ $X_{H_2O}: < 0.1$	0 – 29.0 wt.% NaCl equiv. NaCl wt fr. = 0.45 – 1
Carbonic phase molar volume (cc/mol)	50.4 – 88.0 (>80%: 53 – 65)	52.0 – 68.5 (>95%: 53 – 65)	n/a	49.9 – 73.0 (>89%: 53 – 65)	n/a
Bulk inclusion density (g/cc)	0.53 – 0.86	0.66 – 0.84	0.83 – 0.97 g/cc (2.9 wt.% NaCl)	0.62 – 0.87	0.72 – 0.96 g/cc (0 wt.% NaCl)
	>80%: 0.69 – 0.82 0	>95%: 0.69 – 0.82	1.03 – 1.13 g/cc (25.3 wt.% NaCl)	>89%: 0.69 – 0.82	1.02 – 1.17 g/cc (29 wt.% NaCl)

melting could not be observed in the fluid inclusions, but Raman microspectroscopy implies a low salinity (Fig. 5.4a; Frezzotti et al., 2012) of the aqueous phase.

5.4.5.2. Inclusion Type 2a ($CO_2 \pm N_2 \pm H_2O$)

Type 2a fluid inclusions occur in quartz associated with mineralised micro-fracture networks (Fig. 5.2). Type 2a CO_2 -rich fluid inclusions show a subhedral to negative crystal shape, and range in size from sub-microscopic to 20 μm , although, fluid inclusions larger than 15 μm are rare. No aqueous phase was observed, but H_2O was detected with Raman microspectroscopy, indicating the presence of <10 vol. % H_2O . $T_m^{CO_2}$ varies from -56.6 to -60 °C (Fig. 5.8a). These depressed melting points are consistent with the presence of N_2 as confirmed by Raman spectroscopy (Fig. 5.4b). $T_h^{CO_2}$ values range from +7.5 °C to +27.0 °C, with most fluid inclusions (>80%) homogenising between +15 and +24 °C (Fig. 5.8c). Molar volumes for the carbonic phase based on $T_h^{CO_2}$ and $T_m^{CO_2}$ range from 52.0 to 68.5 cc/mol (Fig. 5.8c), with >90% of fluid inclusions between 54 and 64 cc/mol. The $T_h^{CO_2}$ and $T_m^{CO_2}$ indicate an $X_{N_2}/(X_{CO_2} + X_{N_2})$ ratio of < 0.1 (Fig. 5.7b, 5.8d). Similar to Type 1 fluid inclusions, clathrate melting was not observed in these fluid inclusions, but Raman analysis of the aqueous component indicates a low salinity of the aqueous phase.

5.4.5.3. Inclusion Type 2b ($H_2O-NaCl \pm CaCl_2$)

Type 2b fluid inclusions are restricted to quartz grains that formed within mineralised micro-fracture networks (Fig. 5.2). Clustered aqueous Type 2b fluid inclusions are rounded and usually less than 10 μm in diameter. Initial melting of ice could only be observed in a dozen of the larger fluid inclusions and varied between -30 and -16 °C. However, these initial melting temperatures are probably significantly lower due to observational difficulties regarding initial melting in the small fluid inclusions. Final melting of ice ranges from -24.6 to -1.7 °C (Fig. 5.8e). Fluid inclusions with a relatively low T_i show T_m^{ice} below -21 °C (i.e., the eutectic temperature of the $H_2O-NaCl$ system), indicating that they comprise another salt in addition to NaCl. The most likely candidate for the additional salt is $CaCl_2$, which has been reported in numerous orogenic gold deposits (e.g., Bodnar et al., 2014). Fluid inclusions with NaCl and $CaCl_2$, inferred by T_i values below -21.2 °C, all had T_m^{ice} values of less than -13 °C, whereas fluid inclusions interpreted to comprise only NaCl returned T_m^{ice} values that were higher than -13 °C. The lowest and highest T_m^{ice} values correspond to salinities

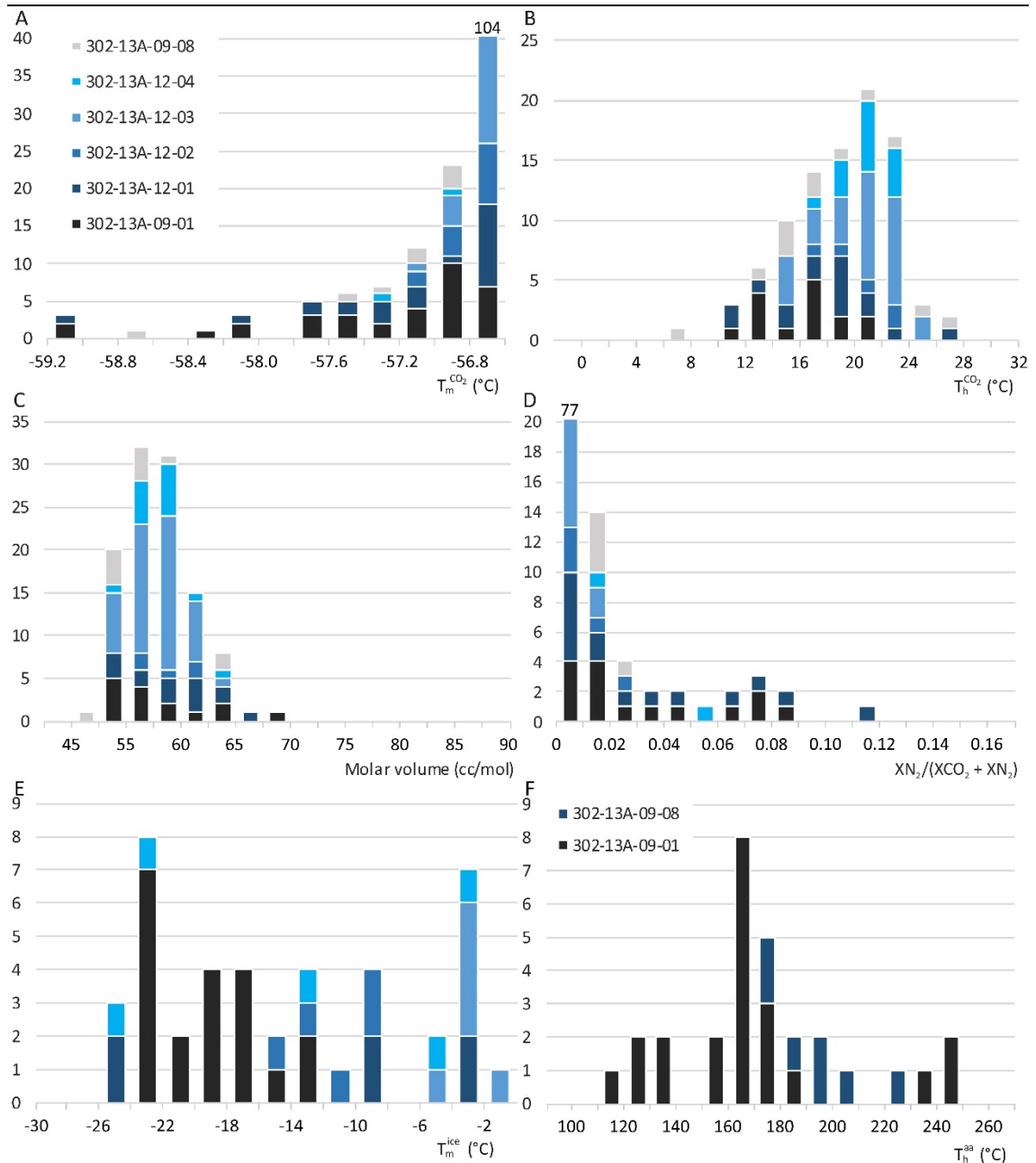


Figure 5.8. Microthermometry and compositional data of fluid inclusions associated with gold-bearing microfracturing. A to D: Type 2a $CO_2 \pm N_2 \pm H_2O$ fluid inclusions, E-F: Type 2b $H_2O-NaCl \pm CaCl_2$ fluid inclusions. A) $T_m^{CO_2}$; B) $T_h^{CO_2}$; C) Molar volume determined from $T_m^{CO_2}$ and $T_h^{CO_2}$ following Thiery et al., (1994); D) $X_{N_2}/(X_{CO_2} + X_{N_2})$ determined from $T_m^{CO_2}$ and $T_h^{CO_2}$ following Thiery et al., (1994); E) T_m^{ice} ; F) T_h^{aa} . Histogram data is colour coded according fluid inclusion to measurement sites.

ranging from 25.3 wt.% NaCl+CaCl₂ to 2.9 wt.% NaCl, respectively (Fig. 5.9a). The high salinity fluid inclusions require a NaCl/(NaCl+CaCl₂) mass ratio of less than 0.45 (Fig. 5.9). Homogenisation into the liquid phase occurred at temperatures between 120 and 244 °C, which indicate a density range of 0.83 to 1.13 g/cc for the given salinities. There is no correlation between T_m^{ice} and T_h^{aa} (Fig. 5.10), and Raman analysis of the vapour phase of these fluid inclusions did not show any evidence of CO₂.

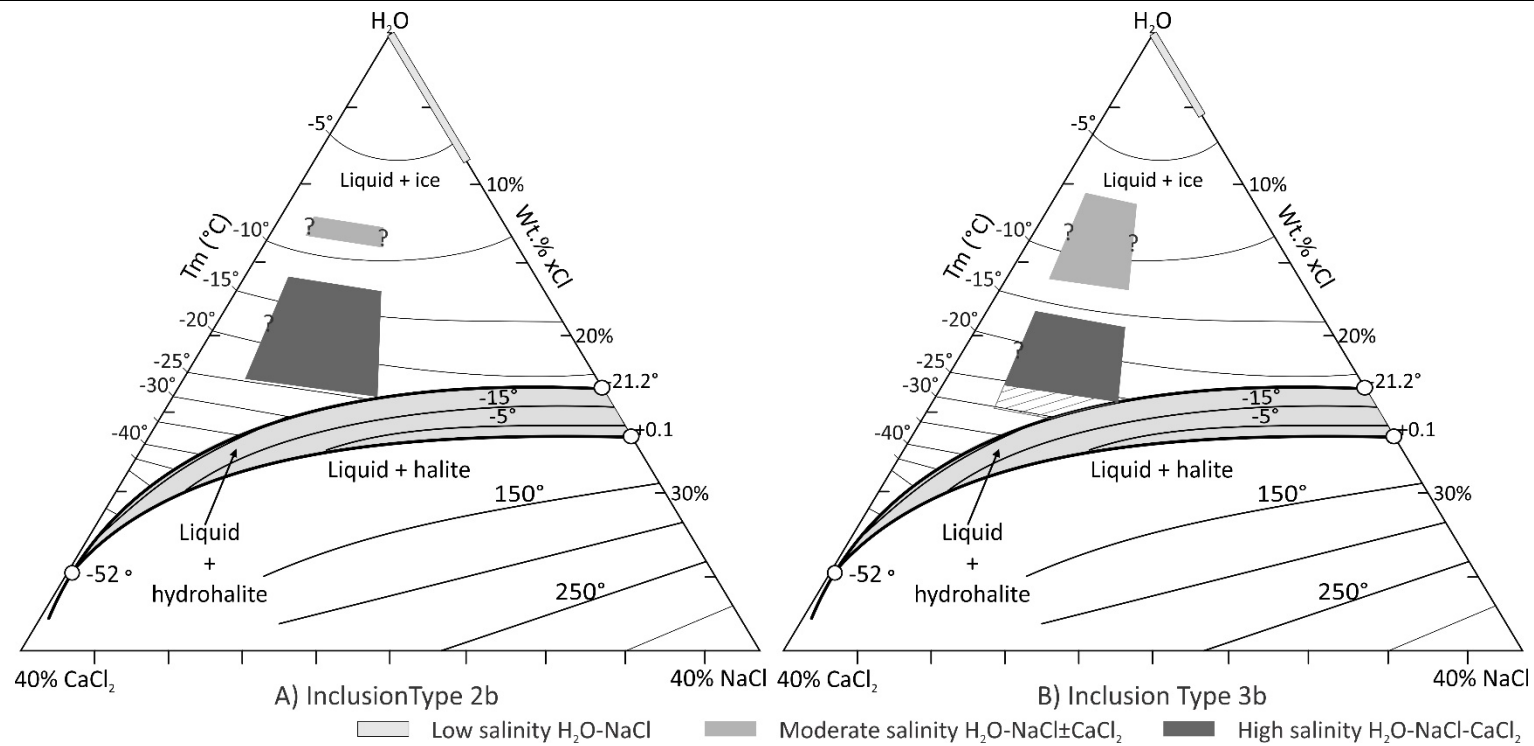


Figure 5.9. Ternary H₂O-CaCl₂-NaCl diagrams presenting measured salinities for A) micro-fracture hosted Type 2b aqueous fluid inclusions and B) vein hosted Type 3b aqueous fluid inclusions. Types 2b and 2b aqueous fluid inclusions can be grouped into three populations on the basis of $\langle T_m^{ice} \rangle$ values and corresponding salinity; Low salinity H₂O-NaCl fluid inclusions with $T_m^{ice} > -7$ °C (Type 2b) or > -4 °C (Type 3b); High salinity H₂O-NaCl-CaCl₂ fluid inclusions with $\langle T_m^{ice} \rangle$ between -25 and -13 °C (Type 2b) or between -26 and -16 °C (Type 3b); and Moderate salinity H₂O-NaCl±CaCl₂ aqueous fluid inclusions with variable $\langle T_m^{ice} \rangle$ values. Fluid inclusions of which $T_i < -21.2$ °C contain a minimum amount of CaCl₂, which is defined by the intersecting of T_m^{ice} isotherms with the upper boundary of the liquid+hydrohalite stability field. With the assumption that salinity values of a parent fluid are consistent, this can constrain the maximum NaCl/(NaCl+CaCl₂) mass ratio of the high salinity hydrothermal fluid to 47 (Type 2b) and 42 % (Type 3b) respectively. Figure modified from Williams-Jones and Samson (1990).

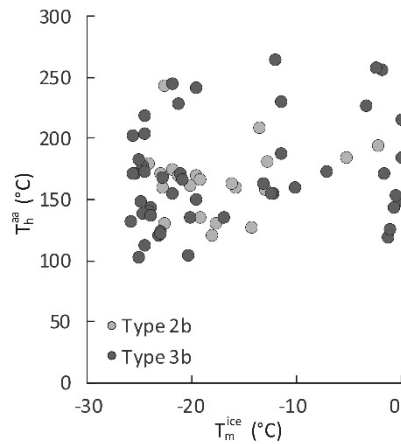


Figure 5.10. T_h^{aa} versus T_m^{ice} of $H_2O-NaCl\pm CaCl_2$ fluid inclusions associated with microfracturing (Type 2b) and crack-seal tension veins (Type 3b). Note that no clear groupings can be identified for the two different types. This distribution is consistent with non-isobaric fluid mixing during partial heat exchange (e.g., Dubessy et al., 2003).

5.4.5.4. Inclusion Type 3a ($CO_2\pm N_2\pm H_2O$)

These fluid inclusions are hosted in quartz grains corresponding to the initial stages of vein growth. They occur as isolated and clustered fluid inclusions and in short, crack-seal trails. They show a subrounded to negative crystal shape and are usually less than 20 μm across. $T_m^{CO_2}$ values vary between -56.6 $^{\circ}C$ and -58 $^{\circ}C$ (Fig. 5.11a) and are associated with the presence of N_2 confirmed by Raman microspectroscopy. Clathrate melting could not be determined for these fluid inclusions as the minor aqueous phase is again invisible and could only be detected by Raman microspectroscopy, indicating that H_2O occupies <10 vol.%. $T_h^{CO_2}$ homogenisation temperatures of the carbonic phase range from +7.5 to +27 $^{\circ}C$, with most values (>80%) between +15 and +24 $^{\circ}C$ (Fig. 5.11b). Molar volumes for the carbonic phase based on $T_h^{CO_2}$ and $T_m^{CO_2}$ range from 49.9 to 73.4 cc/mol (Fig. 5.11c), with more than 80% of fluid inclusions having molar volumes between 54.0 and 64.0 cc/mol. The $T_h^{CO_2}$ and $T_m^{CO_2}$ indicate a $X_{N_2}/(X_{CO_2} + X_{N_2})$ ratio of < 0.1 (Fig. 5.6c, 13d). Similar to Type 1 and 2b fluid inclusions, clathrate melting could not be observed in these fluid inclusions, but Raman analysis of the aqueous component indicates a low salinity of the aqueous phase.

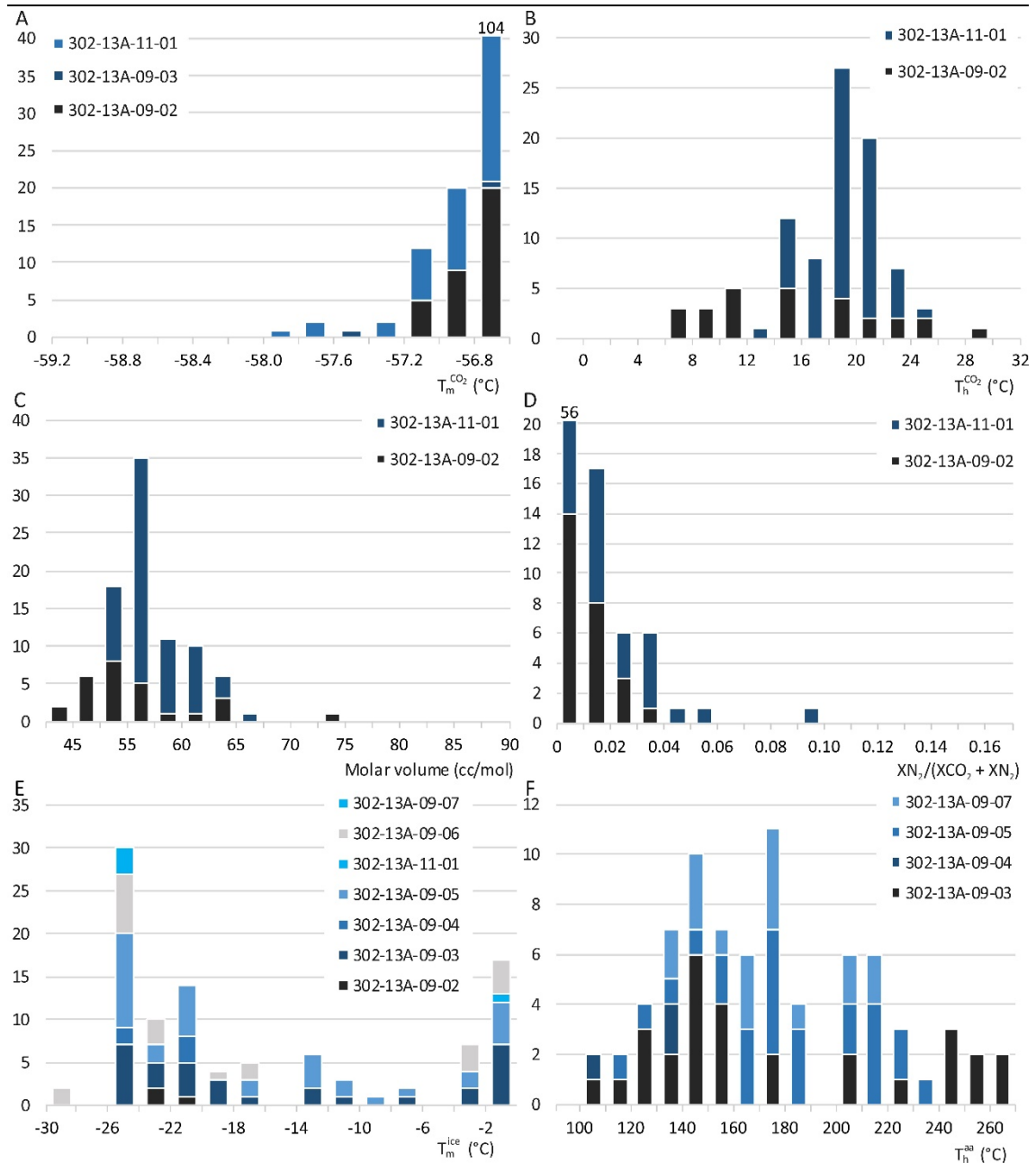


Figure 5.11. Microthermometry and compositional data of fluid inclusions in quartz associated with crack-seal tension veining. A to D: Type 3a $CO_2 \pm N_2 \pm H_2O$ fluid inclusions, E-F: Type 3b $H_2O-NaCl \pm CaCl_2$ fluid inclusions. A) $T_m^{CO_2}$; B) $T_h^{CO_2}$; C) Molar volume determined from $T_m^{CO_2}$ and $T_h^{CO_2}$ following Thiery et al., (1994); D) $X_{N_2}/(X_{CO_2} + X_{N_2})$ determined from $T_m^{CO_2}$ and $T_h^{CO_2}$ following Thiery et al., (1994); E) T_m^{ice} ; F) T_h^{aq} . Histogram data is colour coded according fluid inclusion to measurement sites.

5.4.5.5. Inclusion Type 3b ($H_2O-NaCl \pm CaCl_2$)

H_2O -rich fluid inclusions (Type 3b) occur in clusters and in trails in the late-stage veins (Fig. 5.2). Clustered aqueous fluid inclusions are either irregular or rounded and smaller than the Type 3a CO_2 -

rich fluid inclusions (< 10 μm). They are present in the quartz grains associated with the initial stages of veining together with Type 3a fluid inclusions. Trail-bound aqueous fluid inclusions occur in crack-seal fractures within intermediate-stage quartz grains and do not cross grain boundaries (Fig. 5.5d, e). These fluid inclusions are larger on average than those hosted in clusters (10 to > 20 μm), and they are generally rounded in shape.

Initial melting was observed in 31 fluid inclusions between -36 and -3 $^{\circ}\text{C}$, with 29 fluid inclusions showing initial melting below -23 $^{\circ}\text{C}$. Similar to Type 2b fluid inclusions, it is noted that the initial melting temperatures are probably much lower due to observational difficulties of initial melting in small fluid inclusions. Final melting of ice occurs between -30.5 to 0 $^{\circ}\text{C}$, corresponding to salinities of 29 and 0 wt.% NaCl equivalent, respectively. Most Type 3b fluid inclusions show final ice melting between -25.8 and -1.0 $^{\circ}\text{C}$ (Fig. 5.11e), which corresponds to a salinity range from ca. 26 wt.% NaCl+CaCl₂ to ca. 2 wt.% NaCl (Fig. 5.8b). The high salinity fluid inclusions require a NaCl/(NaCl+CaCl₂) mass ratio of less than 0.45 (Fig. 5.8). Homogenisation temperatures for aqueous inclusions occupy a wide range from 110 to 280 $^{\circ}\text{C}$ indicating a density range of 0.72 to 1.17 g/cc. The T_m^{ice} and T_h^{aq} show no correlation (Fig. 5.10). Raman analysis of the vapour phase of these inclusions showed no evidence for the presence of CO₂ (Fig. 5.4d).

5.5. Interpretation and discussion

5.5.1. Fluid evolution during gold mineralisation

Based on the nature and distribution of the various fluid inclusion types in the sample, three principle constraints can be placed on the evolution of the fluids involved in gold mineralisation.

Firstly, the presence of similar fluid inclusion types (i.e. carbonic dominated Type 1, 2a, and 3a, and H₂O-NaCl±CaCl₂ Type 2b and 3b fluid inclusions) in early silicified zones, micro-fractures and later veins (Fig. 5.2), indicate that three principal fluids were trapped during the various stages of mineralisation. These are: (1) a carbonic (CO₂±N₂±H₂O) fluid; (2) a high salinity (H₂O-NaCl-CaCl₂) fluid; and (3) a low salinity (H₂O-NaCl) fluid. The carbonic fluid was the dominant fluid type during

the initial silicification stage, whereas all three fluids were present during the subsequent microfracturing and quartz veining stages.

Secondly, the fluid inclusions show evidence of mixing of the low-salinity and high-salinity aqueous fluids (Fig. 5.9, 10). This is exemplified by the wide salinity range of the aqueous Type 2b and Type 3b fluid inclusions, which varies from 2 wt.% NaCl (low salinity H₂O-NaCl fluid) to 29 wt.% NaCl equiv. (high salinity H₂O-NaCl-CaCl₂ fluid). There is no fluid inclusion evidence of mixing between the carbonic fluid and the low- and high-salinity aqueous fluids. This is demonstrated by the fact that the aqueous fluid inclusions do not contain CO₂ in the liquid or vapour phase, which would be expected if the fluids were mixing. Dubessy et al. (2003) provides a framework through which to interpret the type of fluid mixing via the relationship between $T_h^{H_2O}$ and T_m^{ice} . Plotting these values for aqueous Type 2b and Type 3b fluid inclusions (Fig. 5.10) indicates partial heat exchange during non-isobaric mixing (Dubessy et al., 2003).

Thirdly, there is no textural evidence for fluid-fluid immiscibility. In the case of fluid-fluid immiscibility, one would expect to find both CO₂±N₂-rich (with minor H₂O) and H₂O-rich (with minor CO₂±N₂) fluid inclusions (e.g., Ramboz et al., 1982; Hurai, 2010). However, only CO₂±N₂-rich (Type 1, 2a, 3a) fluid inclusions were found whereas H₂O-rich, CO₂±N₂-bearing fluid inclusions are absent, which excludes fluid-fluid immiscibility as a possibility.

5.5.2. *P-T conditions of fluid trapping and gold mineralisation*

5.5.2.1. *Constraints on isochore calculations*

Isochores were calculated for each fluid assemblage to model variations in density and composition. The similarity in composition and molar volumes of CO₂±N₂±H₂O fluid inclusions (Type 1, 2a, 3a) allows them to be combined together. Type 2b and Type 3b, H₂O-NaCl-CaCl₂ fluid inclusions can be, on the basis of salinity, subdivided into a high salinity H₂O-NaCl-CaCl₂ fluid assemblage and a low salinity H₂O-NaCl assemblage for the purposes of isochore calculations (Fig. 5.8).

The molar volume of the carbonic fluid inclusions has a measured range of 53 to 65 cc/mol (> 80% measured inclusions, see Table 5.1.), which serves as the lower and upper bound of calculated isochores. Approximately half of measured carbonic rich fluid inclusions contain N₂. In most

instances (i.e. in > 98% of measured inclusions; Figs 7, 8, 12), this N₂ component comprises < 10 mol.% of the fluid inclusions' carbonic phase. Relative to a pure CO₂ fluid inclusions, 10 mol.% N₂ produces only slightly steeper isochores, i.e. N₂ can be ignored in the isochore calculations.

Raman analysis (Fig. 5.4) identified H₂O as a minor component in approximately half of the carbonic inclusions. As this phase was optically invisible it was assumed to represent <10 vol. %, and a value of 10 vol. % was used for calculating the isochores. Raman analysis indicates that the H₂O component has a low salinity (Fig. 5.4a), i.e. isochores were calculated assuming the aqueous phase to be pure H₂O. Increasing the proportion of the minor H₂O component in these models lowers molar volumes and results in slightly steeper isochores.

High salinity H₂O-NaCl-CaCl₂ fluid inclusions show final melting temperatures clustering around -22 °C, equating to ca. 24 wt.% NaCl equiv. For simplicity, the salt is considered to consist of NaCl only, as including CaCl₂ results in negligible changes in the calculated isochores. Low salinity H₂O-NaCl-CaCl₂ fluid inclusions show final melting temperatures that cluster around -2 °C, corresponding to ca. 3 wt.% NaCl. Both high and low salinity aqueous fluids homogenised into the liquid phase over a wide temperature range of 110-250 °C, which has been used as the lower and upper bounds of the calculated isochores (Fig. 5.12).

5.5.2.2. *P-T estimates for gold mineralisation*

Isochores describe a univariant line in P-T space, requiring either the temperature to be independently constrained to calculate the pressure or vice-versa. At Geita Hill, the mineral assemblages imply the gold bearing hydrothermal alteration to have occurred between 300 and 375 °C (van Ryt et al., 2017). The 300 °C lower temperature limit is constrained by the stability of biotite + K-feldspar in the gold-bearing samples. The upper temperature limit is constrained by (1) the presence of localised hydrothermal actinolite and ferro-actinolite in some gold-bearing microfractures (van Ryt et al., 2017; in press), indicating a temperature of at least 350 °C (Jenkins and Bozhilov, 2003), and (2) the presence of a variety of telluride phases (Au, Au-Ag, Ag, Au-Pb-Bi, Pb, and Pb-Bi tellurides) hosted in pyrite (van Ryt et al., 2017; Chapter 4 of this thesis) indicating a maximum temperature of ca. 380 °C based on the melting point of sylvanite (ca. 350 °C) and krennerite (ca. 380 °C; Cabri, 1965).

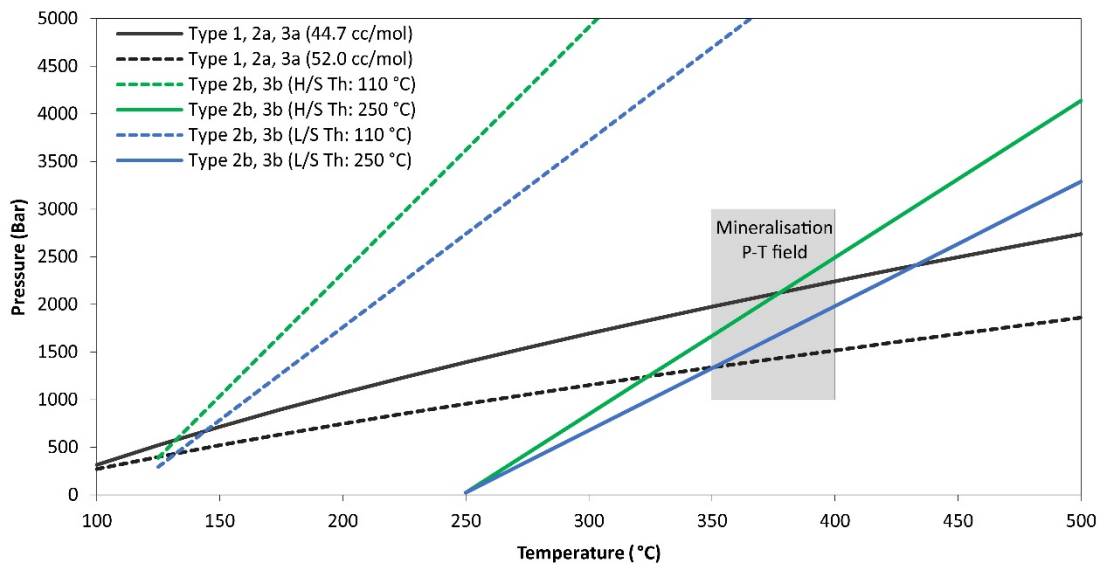


Figure 5.12. Intersection isochores of the three fluid assemblages at Geita Hill. The isochores representing Type 1a, 2a and 3a $\text{CO}_2 \pm \text{H}_2\text{O} \pm \text{N}_2$ fluid inclusions contain 10 vol.% H_2O with 0 mol.% N_2 in the carbonic phase, and have total molar volumes of 44.7 and 52.0 cc/mol (0.85 and 0.71 g/cc) respectively. Type 2b and 3b aqueous $\text{H}_2\text{O}-\text{NaCl} \pm \text{CaCl}_2$ fluid inclusions are split into high salinity (24 wt.% NaCl equiv.) and low salinity (3 wt.% NaCl) fluid assemblages. The isochores mark the upper and low bounds of fluid inclusion molar volumes/densities. At the temperatures assumed for mineralisation at Geita Hill (350-380 °C; van Ryt et al., 2017; Chapter 4 of this thesis), maximum pressures for Type 1, 2a and 3a fluid inclusions are 2.1-2.0 kbar respectively, and minimum pressures are 1.4-1.3 kbar.

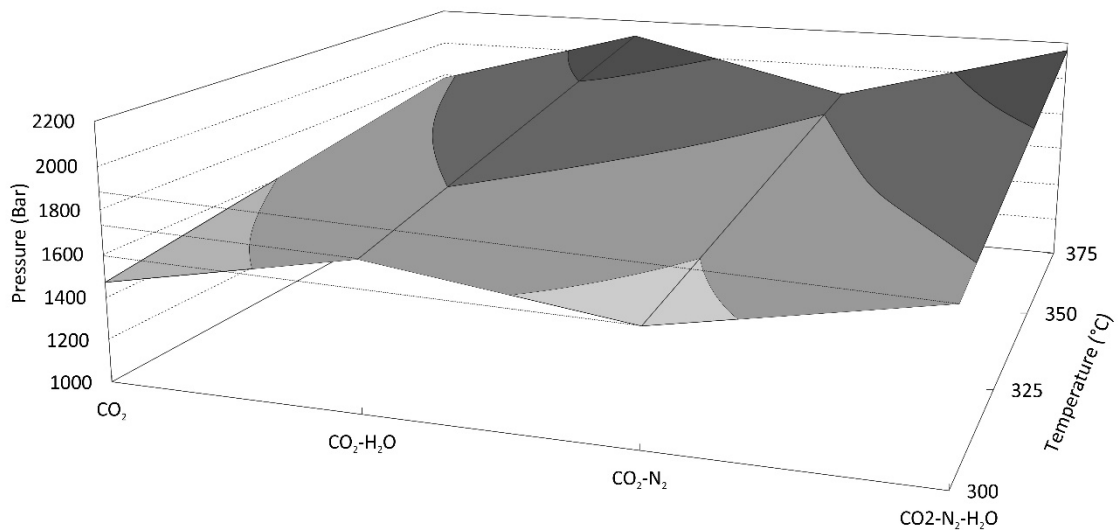


Figure 5.13. Surface plot of the maximum pressures implied by various fluid compositions at Geita Hill.

At these temperatures the maximum and minimum mineralisation pressures are determined from the isochores of the carbonic-aqueous (Type 1, 2a, 3a) fluid inclusions. The maximum and minimum pressure measured at for 380 °C and 350 °C, are 2.1-2.0 kbar and 1.4-1.3 kbar, respectively (Fig. 5.12, 5.13). The pressure range drops to 1.7-1.2 kbar at 300 °C. It is worth

noting that the intersection of the isochores for the carbonic fluid inclusions with the highest density aqueous fluid inclusions occurs at a temperature and pressure range of 350-380 °C and 1.4-2.2 kbar (Fig. 5.12).

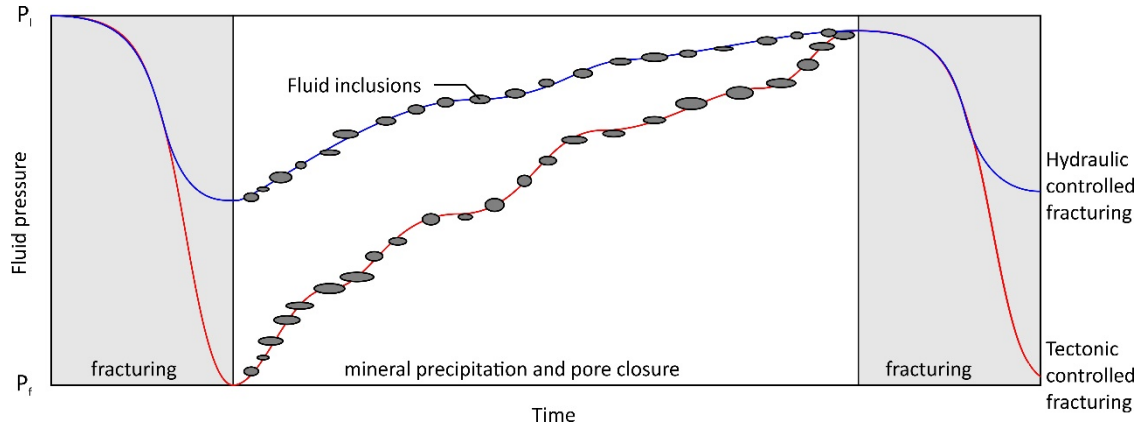


Figure 5.14. Schematic diagram illustrating variation in pore fluid pressures (P_f) during entrapment of a fluid inclusion assemblage. Fluids are entrapped in equilibrium with pore fluid pressures. In a tectonic controlled system, pressures will show more variation (down to hydrostatic pressures) than in a hydraulic controlled system.

5.5.3. Hydraulic vs tectonic microfracturing

Pore fluid pressures (P_{fluid}) are estimated to be approximately lithostatic ($P_{lithostatic}$) when they are in equilibrium with the surrounding rock (Ridley, 1993). The opening of a crack or micro-fracture will result in a rapid drop of the local pore fluid pressures (Fig. 5.14). In tectonic-controlled brecciation, pressures can drop to hydrostatic pressures ($P_{fluid} = 0.4P_{lithostatic}$) and even lower (Ridley, 1993), but where brecciation is hydraulically controlled, fluid pressures will drop to values between hydrostatic and lithostatic. Fluid pressures will normalise again over time with the ingress of surrounding fluids and precipitation of hydrothermal minerals. Consequently, fluid inclusions trapped in such an environment will preserve a range of densities. The upper bound of these densities can be assumed to correspond with lithostatic pressure, and the lower bound is representative of minimum pore fluid pressures (Fig. 5.12) reached during the fracturing process. The pore-pressure factor (λ_f) is the ratio of $P_{fluid}/P_{lithostatic}$ (Ridley, 1993). In a purely tectonically controlled regime, where fluid pressures can drop to hydrostatic, λ_f can be as low as 0.4. In fluid systems dominated by hydraulic, fluid pressure-induced fracturing, fluid pressures should drop by less (i.e., λ_f values approaching 0.8) (Ridley, 1993). Calculating this ratio for Geita Hill returns values

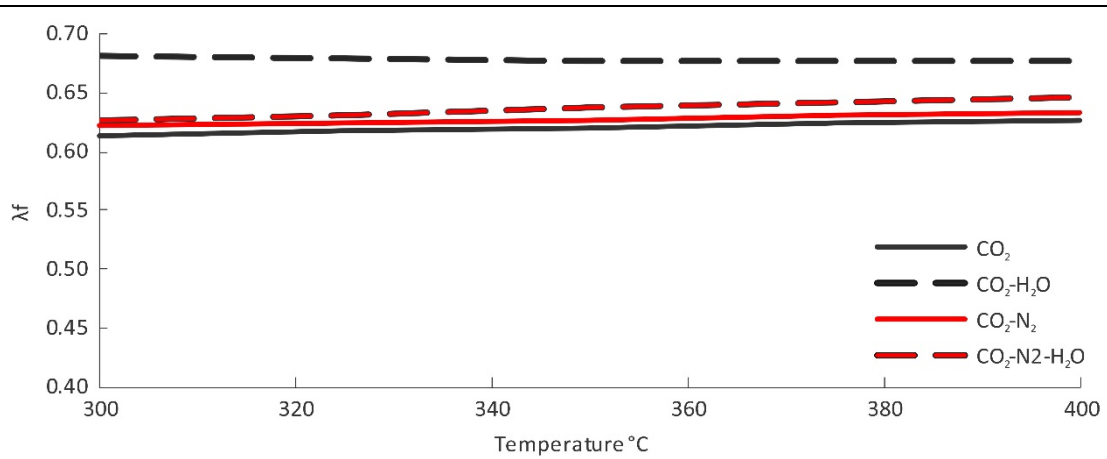


Figure 5.15. Ratio of lithostatic pressures to minimum fluid pressures (λ_f) of carbonic and carbonic-aqueous (Type 1, 2a, 3a) fluid inclusions over the range of inferred trapping conditions. Ratios vary with fluid composition but occupy a narrow range from 0.61 to 0.68 at 300 °C, and 0.63 to 0.68 at 375 °C.

of between 0.6 and 0.7 (Fig. 5.15), indicating that the gold-bearing micro-fractures were formed as a result of hydraulic fracturing.

5.5.4. C-O-H fluid modelling

The redox state of the hydrothermal fluids can be constrained by C-O-H model calculations (e.g., Huizenga, 2001; 2011). These calculations can be used to test if the fluid inclusion data is consistent with the observed mineral assemblages and hydrothermal reactions at Geita Hill. Calculations were completed using an updated version of the Excel spreadsheet COH (Huizenga, 2005). Thermodynamic data for the fluid species and graphite for calculation equilibrium constants for the reactions in the fluid phase were sourced from Holland and Powell, (1998). Fugacity coefficients for the fluid species were calculated from the equations of state by (Zhang and Duan, 2009). At a fixed pressure and temperature, a C-O-H fluid system has seven unknowns including $X_{\text{H}_2\text{O}}, X_{\text{CO}_2}, X_{\text{CH}_4}, X_{\text{H}_2}, X_{\text{CO}}, f_{\text{O}_2}^{\text{fluid}}$ and $a_{\text{carbon}}^{\text{fluid}}$ i.e., the mole fractions of H₂O, CO₂, CH₄, H₂ and CO₂, the fluid oxygen fugacity and the fluid carbon activity, respectively. Four independent equilibria can be written for the C-O-H system (e.g., French, 1966; Ohmoto and Kerrick, 1977): $\text{CO} + \frac{1}{2} \text{O}_2 \rightleftharpoons \text{CO}_2$, $\text{H}_2 + \frac{1}{2} \text{O}_2 \rightleftharpoons \text{H}_2\text{O}$, $\text{CH}_4 + 2 \text{O}_2 \rightleftharpoons \text{CO}_2 + 2\text{H}_2\text{O}$, and $\text{C} + \text{O}_2 \rightleftharpoons \text{CO}_2$. If the minute quantities of X_{O_2} are ignored, the mass balance constraint can be expressed as $X_{\text{H}_2\text{O}} + X_{\text{CO}_2} + X_{\text{CH}_4} + X_{\text{H}_2} + X_{\text{CO}} = 1$. There are seven compositional parameters and five the defined equations for the C-O-H system, requiring two parameters to be specified in order to model system.

The following constraints were used to calculate the oxygen fugacity: (1) pressure and temperature conditions were set at 1.8-1.3 kbar, and 350-300 °C; (2) carbon saturation was assumed for the fluid ($a_{\text{carbon}}^{\text{fluid}} = 1$); and (3) the $X_{\text{CH}_4}/(X_{\text{CO}_2} + X_{\text{CH}_4})$ ratio is less than 0.01. The first constraint is based on the isochores for Type 1, 2a and 3a carbonic fluid inclusions (Fig. 5.12). The second constraint is based on the presence of graphite in the system (Fig. 5.4e, French, 1966). Graphite is an accessory mineral in the black shales and turbiditic sediments that host the Geita Hill deposit, and in the quartz feeder veins hosted in these units. The last constraint is in accordance with the absence of CH_4 in the $\text{CO}_2 \pm \text{H}_2\text{O} \pm \text{N}_2$ fluid inclusions (Type 1, 2a, 3a). Methane has a stronger inelastic scattering effect on photos than CO_2 (e.g., Burke, 2001), and is thus more sensitive to Raman. Fluid inclusions that were used for CH_4 by Raman spectroscopy were close to the surface and had $T_h^{\text{CO}_2}$ of +12 to +25 °C, i.e. any significant amount of CH_4 should have been detected. The absence of a CH_4 peak in the Raman spectrum indicates that $X_{\text{CH}_4}/(X_{\text{CO}_2} + X_{\text{CH}_4})$ was much less than 0.01. These three constraints allow C-O-H system to be treated invariant, allowing the calculation of $f_{\text{O}_2}^{\text{fluid}}$ and $X_{\text{H}_2\text{O}}/(X_{\text{CO}_2} + X_{\text{H}_2\text{O}})$.

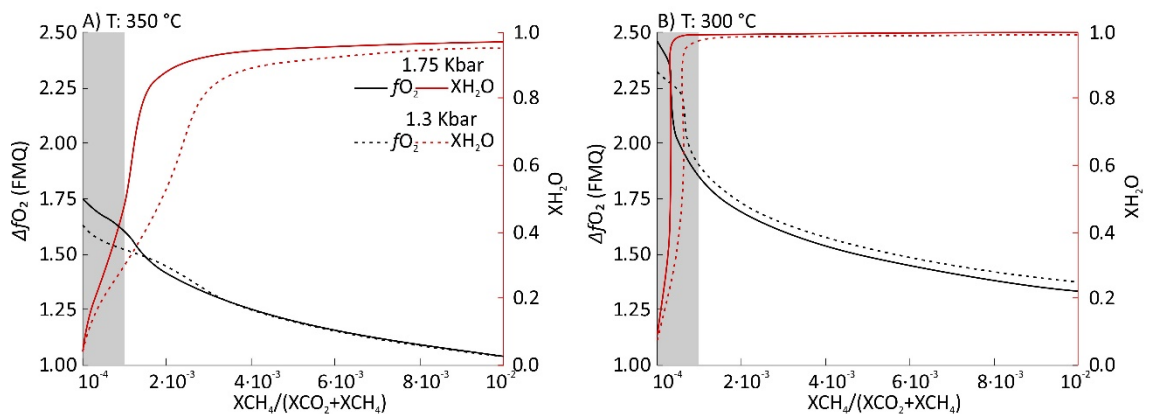


Figure 5.16. Modelled Δf_{O_2} and $X_{\text{H}_2\text{O}}$ vs $X_{\text{CH}_4}/(X_{\text{CO}_2} + X_{\text{CH}_4})$ for the infiltrating fluids (Type 1, 2a, 3a) at Geita Hill. Values of Δf_{O_2} are relative to the FMQ redox buffer (O'Neill and Wall, 1987; Ballhaus et al., 1991), values for X_{CH_4} , X_{CO_2} and $X_{\text{H}_2\text{O}}$ are in mol.%. The system is modelled at 1.75 and 1.3 kbar, and at 350 and 300 °C. The proportion of CH_4 within the carbonic phase is estimated to be less than $1 \cdot 10^{-3}$ (shaded area), which is an order of magnitude more than the detection limit of methane shown by Caumon et al., (2014).

The calculations demonstrate that $f_{O_2}^{\text{fluid}}$ values are 1.5 to 1.8 \log_{10} units higher than $f_{O_2}^{\text{FMQ}}$ (defined by (O'Neill and Wall, 1987; Ballhaus et al., 1991) at 350 °C and 1.3 to 1.8 kbar (Fig. 5.16a), corresponding to absolute $f_{O_2}^{\text{fluid}}$ values of $10^{-30.5}$ bar. The redox state increases at lower temperatures, ranging from 1.9 to 2.5 \log_{10} units above $f_{O_2}^{\text{FMQ}}$ at 300 °C and 1.3 to 1.8 kbar (Fig. 5.16b). The modelling also shows that X_{H_2O} decreases sharply at low X_{CH_4} values, with X_{H_2O} approaching 5 mol.% whereas $X_{CH_4}/(X_{CO_2} + X_{CH_4})$ approaches 0, confirming the low H₂O-content in the fluid inclusions. These temperatures and redox values lie within the stability field of magnetite (Frost, 1991). The calculation results demonstrate that a typical greenstone belt metamorphic H₂O-rich aqueous-carbonic fluid (e.g., Goldfarb and Groves, 2015) evolves to become a CO₂-rich carbonic-aqueous fluid if it moves into a graphite-bearing host rock of which f_{O_2} is +1.5 to +2.5 \log_{10} units higher than $f_{O_2}^{\text{FMQ}}$.

5.5.5. *Fluid evolution during gold mineralisation*

The gold-related hydrothermal mineralisation styles (silicification, microfracturing and crack-seal tension veining) and fluid inclusion assemblages described in this study interpreted to a progressing hydrothermal system. Carbonic fluid inclusions (Type 1, 2a and 3a) are associated with all alteration stages, whereas low and high salinity aqueous fluid inclusions (Type 2b and 3b) were only measured in quartz that formed along micro-fractures and in crack-seal tension veins. Type 1 CO₂±N₂±H₂O fluid inclusions occupy a wide range of molar volumes (50-90 cc/mol) and $X_{N_2}/(X_{CO_2} + X_{N_2})$ ratios (0-0.18; Fig. 5.6a). The ranges for Type 3a CO₂±N₂±H₂O fluid inclusions are 50-73 cc/mol and 0-0.1 for $X_{N_2}/(X_{CO_2} + X_{N_2})$, respectively (Fig. 5.6c). This evolution towards a more consistent fluid chemistry and fluid density can be explained in terms of host rock interaction as will be discussed below.

Structural mapping has linked the development of the gold-related hydrothermal alteration at Geita Hill to fluid conduits (van Ryt et al., 2017), including early thrusts that were reactivated as normal faults, later faults and joint sets, fold hinges and lithological contacts (Sanislav et al., 2017). In this context, the pre-mineralisation silicification stage probably represents the initial reaction front between fluids and the wall rock (Fig. 5.17a). In such an environment, the interaction between hydrothermal fluids and wall rock is expected to be heterogeneous, as the system will have a lower

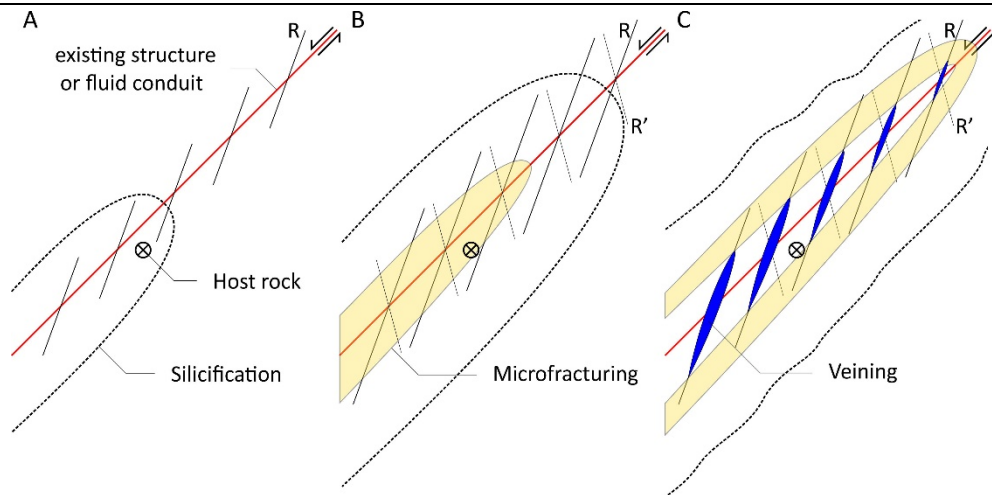


Figure 5.17. Idealised schematic of the progression of the hydrothermal alteration at Geita Hill. Gold-related hydrothermal fluids show strong structural controlled, permeating host rocks along fluid conduits such as pre-existing shears, faults and joint sets, as well as along lithological contacts and the hinges of folds.

fluid rock ratio. Wide swings in fluid pressure (and trapped fluid inclusion densities) may occur because of episodic fracturing of the host rocks. This explains why fluid inclusions associated with silicification are limited to Type 1 $\text{CO}_2 \pm \text{N}_2 \pm \text{H}_2\text{O}$ and describe the large range of molar volumes (Fig. 5.6d).

As fluids continue to pulse through the system, the silicification front moves further out (Fig. 5.17b). Hydraulic microfracturing develops in and overprints the now more competent, silicified host rocks. In the newly formed fractures, gold-bearing hydrothermal pyrite, biotite and K-feldspar precipitated. These fractures also mark the earliest textural evidence of high salinity ($\text{H}_2\text{O}-\text{NaCl}-\text{CaCl}_2$) fluids in the deposit. As the system continues to develop and the silicification front continues to progress outward, the core of the fluid system characterised by an increased presence of high salinity fluids permeates the micro-fracture network (Fig. 5.17c). The system is now largely externally buffered, i.e. the infiltrating fluids are in equilibrium with the altered host rock, gold complexes are stable and gold precipitation slows. Hydrothermal fluids continue to pulse through the system, developing the multi-phase tension veins.

5.5.6. Implications for the fluid source

Fluid assemblages linked to Archean gold systems have as much variability as the systems themselves. Strong structural control, different host lithologies and frequent post-mineralisation alteration can severely complicate microthermometry. Geita Hill has historically been described as

an orogenic gold system (e.g., Goldfarb et al., 2001; Bierlein et al., 2006), but recent research has interpreted the deposit as intrusion-related and linked to the possible emplacement of High-K granites into the greenstone pile (van Ryt et al., 2017; Chapters 3 and 4 of this thesis; Dirks et al., in press). Three principle fluids have been described in this study: 1) A low salinity, carbonic-rich ($X_{CO_2} > 0.8$) fluid with minor N_2 ($X_{N_2}/(X_{CO_2} + X_{N_2}) < 0.15$), 2) A high salinity ($NaCl+CaCl_2 > 20$ wt.%; $NaCl/(NaCl+CaCl_2)$ mass ratio > 0.45), aqueous brine, and 3) A low salinity ($NaCl < 5$ wt.%) aqueous fluid. Each principle fluid had a different origin. The low salinity aqueous fluid can be ascribed to the influx of meteoric water (e.g., Yardley, 2009; Bodnar et al., 2014), and is not related to gold mineralisation. The pressures ascribed to mineralisation in this study are low (Fig. 5.12, 13) and the system was relatively close to surface; whereas the deformation during mineralisation is extensional (van Ryt et al., 2017; Sanislav et al., 2017). These conditions are conducive to meteoric water being drawn downward. Additionally, post-mineralisation veining in the deposit contains barite and hematite (e.g., van Ryt et al., 2017), which is consistent with the influx of oxidised meteoric fluids.

Possible sources for the carbonic-rich fluid and high salinity brines will be discussed below, with implications for the wider gold mineralisation model.

5.5.6.1. Carbonic-rich (Type 1, 2a, 3a: $CO_2 \pm H_2O \pm N_2$) fluids

Goldfarb and Groves (2015) outline some general properties of fluids associated with orogenic gold deposits. Parent fluids are usually carbonic-aqueous in composition, with less than 20 mol.% CO_2 , minor amounts of CH_4 and less N_2 , 2 to 7 wt.% $NaCl$ and a near neutral pH. The orogenic model assigns a metamorphic source to these fluids, which were transported from depth along crustal-scale structures (Groves et al., 1998).

The lack of H_2O in the carbonic-aqueous fluid described from Geita Hill could imply immiscibility of a more H_2O -rich parent fluid at greater depths (Ramboz et al., 1982; Spear, 1993). However, there is no evidence in the sample studied of the proposed immiscible H_2O -rich fluid, and fluid-fluid immiscibility is therefore ruled out as a mechanism to form more than one of the three fluid types. The amount of CO_2 in the carbonic-aqueous fluid at Geita Hill is better explained through interaction with the metamorphic host rocks. Our calculations show that a typical, orogenic-style

carbonic-aqueous fluid that interacted with graphitic shales would become CO₂-rich as it approached equilibrium.

The presence of N₂ is also unusual for fluids associated with orogenic gold deposits, but could be explained via devolatilisation of N₂-bearing metamorphic source rocks. NH₄⁺ substitutes for K⁺ in potassic minerals such as biotite and K-feldspar (Honma and Itihara, 1981; Dubessy and Ramboz, 1986), and biotite in metamorphic black shales (as described at Geita Hill) is a known reservoir for N (Dubessy and Ramboz, 1986, Nieto, 2002). N₂ is produced through the reactions (Moin et al., 1994):



and



Higher NH₄⁺ concentrations in biotite push the equilibria towards higher N₂/CO₂ ratios in the fluid. Temperature is a strong control on the reactions, with higher temperatures requiring exponentially higher NH₄⁺ concentrations for a constant N₂/CO₂ ratio. At the peak metamorphic conditions assumed for most greenstone belts, (550 °C, Powell et al., 1991) source rocks would require either significant enrichment in N₂ or a high $a_{\text{K}^+}/a_{\text{H}^+}$ ratio, which also favours the production of N₂-rich fluids. Our C-O-H calculations show that such a fluid interacting with the graphite-bearing host rocks at Geita Hill under the pressure, temperature and relatively high $f\text{O}_2$ conditions of mineralisation described here would become almost purely composed of CO₂-N₂, with minimal H₂O.

Instead of assuming a metamorphic source for the carbonic-aqueous fluids described at Geita Hill, these fluids could be magmatically derived. CO₂-rich fluids are ubiquitously associated with intrusion-related gold systems (e.g., Baker, 2002; Fornadel et al., 2011), specifically those formed at higher pressures (e.g., Vikent'eva et al., 2018). CO₂ is one tenth as soluble as H₂O in felsic melts (Fogel and Rutherford, 1990) and exsolves at greater crustal depths, resulting in the production of early, low salinity carbonic-aqueous fluids followed by higher salinity aqueous brines (Baker, 2002). The presence of N₂ in magmatic fluids is usually attributed to the interaction with metasediments (e.g., Lang and Baker, 2001), through reactions similar to those described above. Ultimately the data is equivocal. The bulk of literature (e.g., Goldfarb and Groves, 2015 and references therein.) favours a

metamorphic source for carbonic-aqueous fluids, and we have no definitive reason to argue otherwise for the N-bearing low salinity carbonic fluids at Geita Hill.

5.5.6.2. *High salinity aqueous (H₂O-NaCl-CaCl₂) fluids*

High-salinity brines have been described in many Archean lode gold deposits and have been linked variously to saline groundwater (e.g., Robert et al., 1995), phase separation and immiscibility reactions (e.g., Neumayr and Hagemann, 2002), and interaction with felsic intrusives (e.g., Rezeau et al., 2017). In orogenic systems, high salinity brines are usually interpreted to be unrelated to ore formation (e.g., Goldfarb and Groves, 2015), but in magmatic-hydrothermal systems, they are repeatedly shown to be the primary mineralising fluid (Fan et al., 2011; Kontak and Kyser, 2011; Nikolaev et al., 2013). Based on its textural association (Fig. 5.2) and salinity range (Fig. 5.9), I interpret the high salinity brine at Geita Hill to be of magmatic-hydrothermal origin, and directly linked to gold precipitation.

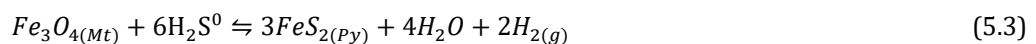
Though historically classified as an orogenic BIF-hosted gold deposit (e.g., Borg, 1994; Goldfarb et al., 2001), the Geita Hill deposit bears many similarities to a magmatic epithermal system. Gold deposition post-dates the main compressional events by at least 50 Ma (Sanislav et al., 2014b), and is associated with extensional reactivation of collisional orogenic structures (Sanislav et al., 2017; van Ryt et al., 2017). Bulk elements introduced during gold mineralisation are dominated by K₂O and SiO₂. The deposit is also rich in silver, with laser ablation of gold inclusions in pyrite returning Au/Ag mass ratios of ca 0.4 (Chapter 4 of this thesis). Trace element analyses of gold-bearing pyrite shows Au, Ag, Te, Bi, Pb, Se and Sb to be hydrothermally derived during mineralisation, while Fe, As, Ni and Co are locally remobilised by surrounding host rock (Chapter 4 of this thesis). Mineral geochemistry of gold-related hydrothermal biotite shows it to be enriched in fluorine, relative to the fluorine content of background metamorphic biotite, which is ubiquitously low, i.e. fluorine is unlikely to be scavenged during hydrothermal recrystallisation of these minerals and must have been introduced with the mineralising fluids. Thus, the high silver content, the Au-Ag-Te-Bi-Sb-Pb metal association, elevated fluorine and potassic alteration are all consistent with a link between mineralisation and felsic magmatism. In this context it is interesting to note that Borg (1994) linked mineralisation to the emplacement of late-stage lamprophyre dykes around 2644 Ma.

5.5.7. *Gold transport and precipitation*

The low salinity CO₂-rich fluid, while spatially associated with mineralisation and the silicification that precedes it, is not texturally restricted to gold-bearing hydrothermal assemblages. Non-mineralised silicified rocks are present throughout the deposit. This leaves the high salinity H₂O-NaCl-CaCl₂ brine as the most likely candidate for the gold transporting fluid, with the implication that Geita Hill is a magmatic epithermal gold system. The fluids associated with intrusion-related Archean systems are frequently oxidised alkaline to sub-alkaline, with the gold transported as a bisulfide complex (e.g., Helt et al., 2014). At the temperatures assumed for mineralisation at Geita Hill (~350 °C), the most important gold ligand is HS⁻ (Seward, 1973; Shenberger and Barnes, 1989), and in near neutral pH conditions $Au(HS)_2^-$ is the dominant bisulfide complex (Stefánsson and Seward, 2004).

Petrographic and trace element studies have shown a strong positive correlation between Au(+Ag) and Te (van Ryt et al., 2017; Chapter 4 of this thesis), with much of the gold occurring in Au-tellurides, which themselves occur in spatial association with pyrite. The source of the Te is not immediately clear, but its spatial association with Au suggests it may have been brought in with the mineralising fluids. Grundler et al. (2013) have shown that Te is soluble in oxidised fluids as Te(IV) complexes, and in reduced alkaline fluids as Te_2^- complexes. Either of these Te species will react with Au-bisulfide at the measured conditions, through fluid mixing or fluid-rock interaction to form gold tellurides, and it is therefore unlikely that Te moved with $Au(HS)_2^-$ in the same fluid (e.g., Cooke and McPhail, 2001). However, Te, may have been introduced as a vapour phase, as there is a strong preference of Te for the vapour phase under moderately reducing conditions (i.e., $f_{H_2S(g)} > f_{SO_2(g)}$) for acidic to moderately basic pH's; i.e. the conditions over which $Au(HS)_2^-$ solubility is highest (McPhail, 1995; Cooke and McPhail, 2001; Grundler et al., 2013), and the conditions consistent with the fluid inclusions from Geita Hill. Thus, the Au-tellurides may have formed through condensation of magmatically derived Te, which interacted with the aqueous brines that carried the gold as $Au(HS)_2^-$ (Cooke and McPhail, 2001).

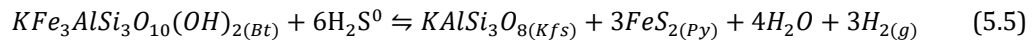
In ironstones, the breakdown of Au-bisulfide complexes in the presence of magnetite precipitates Au following the coupled reaction (e.g., Mikucki, 1998):



and



which also results in the formation of pyrite. On the periphery of sulfidation fronts, pyrrhotite rather than pyrite is observed to be the dominant sulfide (Chapter 4 of this thesis), confirming the host rock to be reducing. In diorite and other intrusive units, Fe-rich metamorphic biotite rather than magnetite is involved in the coupled reactions:



and



in which the annite end-member of biotite reacts with gold-sulphur complexes to form K-feldspar and pyrite while precipitating Au. This also results in the replacement of metamorphic biotite by Mg-enriched hydrothermal biotite in proximity to gold (van Ryt et al., 2017; in press).

5.6. Conclusions

Three stages of gold-related hydrothermal alteration are preserved in the Geita Hill ore zone, representing a developing fluid system. Alteration commenced with silicification of the host rocks, followed by development of gold-bearing micro-fractures, and later multi-phased, crack-seal tension veins. The fluid assemblages preserved in the Geita Hill ore zone imply gold mineralisation occurred in the range of 1.4 to 1.7 kbar (5.2 to 6.3km), at temperatures of approximately 350 °C. The densities calculated from the carbonic aqueous fluid assemblage imply gold-bearing micro-fractures were generated by fluid pressure, rather than tectonic brecciation, as was the crack-seal tension veining.

This detailed fluid inclusion study demonstrates that three different fluids were present during gold precipitation: (1) A low salinity, carbonic-rich ($X_{CO_2} > 0.8$) fluid with minor N_2 ($X_{N_2}/(X_{CO_2} + X_{N_2}) < 0.15$); (2) A high salinity ($NaCl+CaCl_2 > 20$ wt.%; $NaCl/(NaCl+CaCl_2)$ mass ratio > 0.45), aqueous brine; and (3) A low salinity ($NaCl < 5$ wt.%) aqueous fluid. The low salinity carbonic-rich fluid is likely metamorphic in origin, becoming N_2 and CO_2 -rich through interaction

with the sedimentary pile that included graphitic shale. The high salinity brine is interpreted to be of magmatic origin, exsolved from an oxidised, alkaline- to calc-alkaline felsic intrusive. The low salinity aqueous fluid is interpreted to represent meteoric water, which mixed with the high salinity brine. The gold was likely transported within the high salinity brine as $Au(HS)_2^-$ complexes with Te potentially introduced as a vapour. Deposition of Au was triggered via the interaction of gold-bearing fluids with the relatively reduced, Fe-rich host rocks and the low salinity CO₂-rich fluid.

Chapter 6

Thesis Conclusions

The aim of this thesis is to improve our understanding of gold mineralisation in Archean greenstone belts, based on a comprehensive case study of the Geita Hill deposit in northwestern Tanzania. The work presented in this thesis builds on recently conducted detailed structural mapping of the deposit, and is primarily focused on the role of fluids and associated hydrothermal alterations. Towards this end the research objectives were; to construct a detailed mineral and alteration paragenesis for the deposit, teasing apart the various hydrothermal assemblages and placing them into a structural context; to investigate changes in silicate and sulfide mineral chemistry associated with the gold-related hydrothermal alteration and identify new exploration techniques that can detect these changes; identify which elements were hydrothermally derived in addition to gold and which were locally remobilised during mineralisation; and to characterise the hydrothermal fluids active in the deposit during gold mineralisation, constraining the physiochemical conditions of mineralisation and the source of gold-bearing fluids. The research progressed from a foundation of detailed core logging, structural mapping, optical microscopy and textural studies, into mineral geochemistry, and finally a direct study of the hydrothermal fluids. This thesis is comprised of four independent studies that are each focused on a component of this common theme.

The alteration and mineral paragenesis presented in Chapter 2 constrained peak metamorphic conditions at the deposit to less than 480 °C and 3 kbar, and described metamorphic mineral assemblages for the various host rock types at the deposit. Gold mineralisation was related to the development of a pyrite + biotite + K-Feldspar alteration, with the gold hosted as sub-microscopic inclusions in pyrite and on grain boundaries. Of particular interest was the discovery of multiple species gold-bearing telluride minerals, along with various other silver, lead and bismuth tellurides. Six types of pyrite were recognised on the basis of textures, with two related to gold mineralisation. The textures of gold-related pyrite imply a timing relationship. In ironstones, subhedral pyrite that is rich in inclusions of magnetite, pyrrhotite and base metals is overgrown by a euhedral and inclusion free type of pyrite. In diorite, gold bearing assemblages contain only the euhedral, inclusion free pyrite. The gold-related alteration was linked to the development of steeply dipping quartz feeder veins which overprint all structures at the deposit. The orientation of these feeder veins implies they formed during late tectonic reactivation of earlier thrusts, placing gold mineralisation very late in the tectonic history of the greenstone belt and confirming the findings of earlier structural mapping.

Silicate mineral geochemistry presented in Chapter 3 focused on the chemistry of biotite, which was identified to be a critical mineral in both the metamorphic and gold-bearing hydrothermal assemblages. The composition of biotite hosted in ironstones and other sedimentary units was heterogeneous and influenced primarily by bulk rock geochemistry, without a clear systematic relationship to any auriferous alteration. In contrast, the chemistry diorite-hosted biotite becomes progressively enriched in Si, Mg and F with proximity to the ore zone. The systematic increase in the Mg content of biotite can be detected and mapped using short wavelength infrared (SWIR) as a shift in the 2250 nm absorption feature to shorter wavelengths. The change in mineral chemistry detectable through SWIR has larger footprint than gold-grades returned via assay, which combined with the low costs associated with spectral reflectance makes this technique a possibly valuable exploration tool. The technique has since been tested successfully in the nearby Nyankanga deposit. Halogen chemistry conducted on the biotite implied the presence of multiple hydrothermal fluids during mineralisation, suggesting that within the ore zone a metamorphic fluid in equilibrium with the host rock was overprinted by and mixed with an infiltrating fluid that was enriched in fluorine.

Chapter 4 presents the results of trace element geochemistry conducted on the magnetite and sulfides at the deposit. LA-ICP-MS trace element images revealed complex chemical zonation within the gold-bearing pyrite grains. Moreover, the chemical zonation patterns are not limited to grains with the textural zonation described in Chapter 2, but also occurs in optically uniform diorite-hosted pyrite grains. Elements including As, Ni, Co, Cu and Zn appear to be dominantly locally derived, and remobilised into the pyrite during sulfidation. The concentrations of these elements are highly lithological controlled, and they are not consistently incorporated into the pyrite after initial stages of growth. Au, Ag, Te, Sn, Bi and Pb appear to be dominantly externally derived, and closely correlate in all varieties of pyrite. The gold ore was found to be significantly Ag rich, with an average Au/Ag ratio of 0.41, and gold grades do not correlate at all with As, which is unusual for Archean greenstone-hosted gold systems.

Direct study of the hydrothermal fluids active in the deposit was conducted through microthermometry and raman microspectrometry, presented in Chapter 5. Three principle hydrothermal fluids were present during gold precipitation; a CO₂-rich fluid with minor H₂O and N₂; a high salinity aqueous brine with significant CaCl₂; and a low salinity aqueous fluid which was

interpreted to be meteoric water. The fluid assemblages preserved in the ore zone imply gold mineralisation occurred at pressures of less than 2 kbar, probably in the range of 1.4 to 1.7 kbar, and at temperatures of approximately 350 °C. The densities calculated from the carbonic-rich fluid imply fluid pressure was the controlling the development of gold-bearing micro-fractures, rather than tectonic brecciation. The carbonic-rich fluid was determined to be metamorphic in origin and in equilibrium with the host rocks at the deposit. COH modelling of this fluid showed it's unusually low H₂O and high N₂ content could be the result of interaction with the graphite bearing sediments, and also constrained the oxidation state to just above the FMQ buffer. The high salinity aqueous brine was interpreted to be of magmatic origin, and likely exsolved from an alkaline- or calc-alkaline felsic intrusive. Gold precipitation is linked to the mixing of these two principle fluids and interaction with the Fe-rich host rocks at the deposit. The high salinity aqueous brine was determined the likely gold carrying fluid, with the gold transported as bisulfide complexes.

The results of this study make a compelling case for the mineralising fluids at the Geita Hill gold deposit to be of magmatic origin, and related to the late-tectonic intrusion of high-k, alkaline- to calc-alkaline felsic intrusive units into the Geita Greenstone Belt.

References

- Afshooni, S. Z., Mirnejad, H., Esmaily, D. and Asadi Haroni, H. A. (2013) 'Mineral chemistry of hydrothermal biotite from the Kahang porphyry copper deposit (NE Isfahan), Central Province of Iran', *Ore Geology Reviews*, 54, pp. 214-232.
- Agangi, A., Hofmann, A. and Wohlgemuth-Ueberwasser, C. C. (2013) 'Pyrite zoning as a record of mineralization in the Ventersdorp Contact Reef, Witwatersrand Basin, South Africa', *Economic Geology*, 108(6), pp. 1243-1272.
- Allmendinger, R. 2001. FaultKinWin, Version 1.1: a program for analyzing fault slip data for Windows™. (www.geo.cornell.edu/geology/faculty/RWA/programs.html).
- Anderko, A. and Pitzer, K. S. (1993a) 'Equation-of-state representation of phase equilibria and volumetric properties of the system NaCl-H₂O above 573 K', *Geochimica et Cosmochimica Acta*, 57(8), pp. 1657-1680.
- Anderko, A. and Pitzer, K. S. (1993b) 'Phase equilibria and volumetric properties of the systems KCl-H₂O and NaCl-KCl-H₂O above 573 K: Equation of state representation', *Geochimica et Cosmochimica Acta*, 57(20), pp. 4885-4897.
- Angelier, J. (1994) 'Fault slip analysis and paleostress reconstruction', *Continental deformation*, 4, pp. 101-120.
- Angelier, J. t. and Mechler, P. (1977) 'Sur une methode graphique de recherche des contraintes principales egalement utilisables en tectonique et en seismologie: la methode des diedres droits', *Bulletin de la Société géologique de France*, 7(6), pp. 1309-1318.
- Anhaeusser, C. R. (2014) 'Archaean greenstone belts and associated granitic rocks – A review', *Journal of African Earth Sciences*, 100(0), pp. 684-732.
- Arlegui-Crespo, L. and Simon-Gomez, J. (1998) 'Reliability of palaeostress analysis from fault striations in near multidirectional extension stress fields. Example from the Ebro Basin, Spain', *Journal of Structural Geology*, 20(7), pp. 827-840.
- Bajwah, Z., Seccombe, P. and Offler, R. (1987) 'Trace element distribution, Co: Ni ratios and genesis of the Big Cadia iron-copper deposit, New South Wales, Australia', *Mineralium Deposita*, 22(4), pp. 292-300.
- Baker, T. (2002) 'Emplacement depth and carbon dioxide-rich fluid inclusions in intrusion-related gold deposits', *Economic Geology*, 97(5), pp. 1111-1117.

-
- Baker, T., Bertelli, M., Blenkinsop, T., Cleverley, J., McLellan, J., Nugus, M. and Gillen, D. (2010) 'PTX conditions of fluids in the Sunrise Dam gold deposit, Western Australia, and implications for the interplay between deformation and fluids', *Economic Geology*, 105(5), pp. 873-894.
- Bakker, R. J. (1999) 'Adaptation of the Bowers and Helgeson (1983) equation of state to the H₂O-CO₂-CH₄-N₂-NaCl system', *Chemical Geology*, 154(1-4), pp. 225-236.
- Bakker, R. J. (2003) 'Package FLUIDS 1. Computer programs for analysis of fluid inclusion data and for modelling bulk fluid properties', *Chemical Geology*, 194(1-3), pp. 3-23.
- Ballhaus, C., Berry, R. and Green, D. (1991) 'High pressure experimental calibration of the olivine-orthopyroxene-spinel oxygen geobarometer: implications for the oxidation state of the upper mantle', *Contributions to Mineralogy and Petrology*, 107(1), pp. 27-40.
- Bateman, R. and Hagemann, S. (2004) 'Gold mineralisation throughout about 45 Ma of Archaean orogenesis: protracted flux of gold in the Golden Mile, Yilgarn craton, Western Australia', *Mineralium Deposita*, 39(5-6), pp. 536-559.
- Bateman, R., Hagemann, S., McCuaig, T. and Swager, C. (2001) 'Protracted gold mineralization throughout Archaean orogenesis in the Kalgoorlie camp, Yilgarn Craton, Western Australia: structural, mineralogical, and geochemical evolution', *Geological Survey of Western Australia, Record*, 17, pp. 63-98.
- Bath, A. B., Walshe, J. L., Cloutier, J., Verrall, M., Cleverley, J. S., Pownceby, M. I., Macrae, C. M., Wilson, N. C., Tunjic, J., Nortje, G. S. and Robinson, P. (2013) 'Biotite and apatite as tools for tracking pathways of oxidized fluids in the archaean east repulse gold deposit, Australia', *Economic Geology*, 108(4), pp. 667-690.
- Bath, H. (1990) 'Provisional geological map of Lake Victoria Gold Fields, Tanzania 1: 500000', *Geologisches Jahrbuch Reihe B. Schweizerbart'sche, Hannover*.
- Beane, R. E. (1974) 'Biotite stability in porphyry copper environment', *Economic Geology*, 69, pp. 241-256.
- Bédard, J. H. (2006) 'A catalytic delamination-driven model for coupled genesis of Archaean crust and sub-continental lithospheric mantle', *Geochimica et Cosmochimica Acta*, 70(5), pp. 1188-1214.
- Bédard, J. H., Brouillette, P., Madore, L. and Berclaz, A. (2003) 'Archaean cratonization and deformation in the northern Superior Province, Canada: an evaluation of plate tectonic versus vertical tectonic models', *Precambrian Research*, 127(1-3), pp. 61-87.
-

-
- Bierlein, F. P., Groves, D. I., Goldfarb, R. J. and Dubé, B. (2006) 'Lithospheric controls on the formation of provinces hosting giant orogenic gold deposits', *Mineralium Deposita*, 40(8), pp. 874.
- Bleeker, W. (2002) 'Archaean tectonics: a review, with illustrations from the Slave craton', *Geological Society, London, Special Publications*, 199(1), pp. 151-181.
- Blewett, R., Czarnota, K. and Henson, P. (2010) 'Structural-event framework for the eastern Yilgarn Craton, Western Australia, and its implications for orogenic gold', *Precambrian Research*, 183(2), pp. 203-229.
- Bodnar, R., Lecumberri-Sanchez, P., Moncada, D. and Steele-MacInnis, M. (2014) '13.5—Fluid inclusions in hydrothermal ore deposits', *Treatise on Geochemistry, Second Edition* 10th edn. Elsevier, Oxford, pp. 119-142.
- Bodnar, R. J. and Vityk, M. O. (1994) 'Interpretation of microthermometric data for H₂O–NaCl fluid inclusions', *Fluid Inclusions in Minerals: Methods and Applications. Short Course IMA (1994)*, pp. pp. 117-130.
- Boomeri, M., Nakashima, K. and Lentz, D. R. (2009) 'The Miduk porphyry Cu deposit, Kerman, Iran: A geochemical analysis of the potassic zone including halogen element systematics related to Cu mineralization processes', *Journal of Geochemical Exploration*, 103(1), pp. 17-29.
- Boomeri, M., Nakashima, K. and Lentz, D. R. (2010) 'The Sarcheshmeh porphyry copper deposit, Kerman, Iran: A mineralogical analysis of the igneous rocks and alteration zones including halogen element systematics related to Cu mineralization processes', *Ore Geology Reviews*, 38(4), pp. 367-381.
- Borg, G. (1992) 'New aspects of the lithostratigraphy and evolution of the Siga Hills, an Archaean granite-greenstone terrain in NW Tanzania', *Zeitschrift Angewandte Geologie*, 38, pp. 89-93.
- Borg, G. (1994) 'The Geita gold deposit in NW Tanzania—geology, ore petrology, geochemistry and timing of events', *Geologisches Jahrbuch D*, 100, pp. 545-595.
- Borg, G. and Krogh, T. (1999) 'Isotopic age data of single zircons from the Archean Sukumaland Greenstone Belt, Tanzania', *Journal of African Earth Sciences*, 29(2), pp. 301-312.
- Borg, G., Lyatuu, D. R. and Rammlmair, D. (1990) 'Genetic aspects of the Geita and Jubilee Reef Archean BIF-hosted gold deposits, Tanzania', *Geologische Rundschau*, 79(2), pp. 355-371.
- Borg, G. and Rittenauer, A. (2000) 'Syn - and epigenetic sulphides in Archean BIFs of NW - Tanzania and their significance to gold mineralisation', In: *Rammlmair et al. (eds) Applied Mineralogy, Balkema, Rotterdam*, (263 - 266).
-

-
- Borg, G. and Shackleton, R. (1997) 'The Tanzania and NE-Zaire Cratons', in De Wit, M.J. & Ashwal, L.D. (eds.) *Greenstone belts: Vol. Book, Whole*. Oxford; New York: Clarendon Press.
- Bowers, T. S. and Helgeson, H. C. (1983) 'Calculation of the thermodynamic and geochemical consequences of nonideal mixing in the system H₂O-CO₂-NaCl on phase relations in geologic systems: Equation of state for H₂O-CO₂-NaCl fluids at high pressures and temperatures', *Geochimica et Cosmochimica Acta*, 47(7), pp. 1247-1275.
- Boyle, R. W. (1974) *Elemental Associations in Mineral Deposits and Indicator Elements of Interest in Geochemical Prospecting: Rev.* La Commission.
- Bralia, A., Sabatini, G. and Troja, F. (1979) 'A reevaluation of the Co/Ni ratio in pyrite as geochemical tool in ore genesis problems', *Mineralium Deposita*, 14(3), pp. 353-374.
- Burke, E. A. J. (2001) 'Raman microspectrometry of fluid inclusions', *Lithos*, 55(1-4), pp. 139-158.
- Cabri, L. J. (1965) 'Phase relations in the Au-Ag-Te systems and their mineralogical significance', *Economic Geology*, 60(8), pp. 1569-1606.
- Carew, M. J. (2004) *Controls on Cu-Au mineralisation and Fe oxide metasomatism in the Eastern Fold Belt, NW Queensland, Australia*. James Cook University.
- Carter, G. S. (1959) *Exploration at Geita and NE. extension mines*, (unpub. rep.): Geological Survey of Tanganyika.
- Cassidy, K. F., Groves, D. I. and McNaughton, N. J. (1998) 'Late-Archean granitoid-hosted lode-gold deposits, Yilgarn Craton, Western Australia: Deposit characteristics, crustal architecture and implications for ore genesis', *Ore Geology Reviews*, 13(1-5), pp. 65-102.
- Caumon, M.-C., Robert, P., Laverret, E., Tarantola, A., Randi, A., Pironon, J., Dubessy, J. and Girard, J.-P. (2014) 'Determination of methane content in NaCl-H₂O fluid inclusions by Raman spectroscopy. Calibration and application to the external part of the Central Alps (Switzerland)', *Chemical Geology*, 378, pp. 52-61.
- Cesare, B., Satish-Kumar, M., Cruciani, G., Pocker, S. and Nodari, L. (2008) 'Mineral chemistry of Ti-rich biotite from pegmatite and metapelitic granulites of the Kerala Khondalite Belt (southeast India): Petrology and further insight into titanium substitutions', *American Mineralogist*, 93(2-3), pp. 327-338.
- Chamberlain, C. and Tosdal, R. (2007) 'U-Pb geochronology of the Lake Victoria Greenstone Terranes. Confidential report to project sponsors', *Mineral Deposits Research Unit, University of British Columbia, Vancouver, BC 81p*.
-

-
- Chamberlain, C. M. (2003) *Geology and genesis of the Bulyanhulu gold deposit, Sukumaland greenstone belt, Tanzania*. Imperial College London (University of London).
- Ciobanu, C. L., Cook, N. J., Utsunomiya, S., Kogagwa, M., Green, L., Gilbert, S. and Wade, B. (2012) 'Gold-telluride nanoparticles revealed in arsenic-free pyrite', *American Mineralogist*, 97(8-9), pp. 1515-1518.
- Clark, R. N. (1999) 'Spectroscopy of rocks and minerals, and principles of spectroscopy', *Manual of remote sensing*, 3, pp. 3-58.
- Cleverley, J. S. 'Using the chemistry of apatite to track fluids in Feoxide Cu-Au systems [abs]', *Annual V.M. Goldschmidt Conference*, Melbourne, 2006, Abstracts, p. A105.
- Cline, J. S. and Bodnar, R. J. (1991) 'Can economic porphyry copper mineralization be generated by a typical calc - alkaline melt?', *Journal of Geophysical Research: Solid Earth*, 96(B5), pp. 8113-8126.
- Cline, J. S., Hofstra, A. H., Muntean, J. L., Tosdal, R. M. and Hickey, K. A. (2005) 'Carlin-type gold deposits in Nevada: Critical geologic characteristics and viable models', *Economic Geology 100th anniversary volume*, 451, pp. 484.
- Collins, W., Van Kranendonk, MJ and Teyssier, C. (1998) 'Partial convective overturn of Archaean crust in the east Pilbara Craton, Western Australia: driving mechanisms and tectonic implications', *Journal of Structural Geology*, 20(9-10), pp. 1405-1424.
- Condie, K. (2007) 'The distribution of Paleoproterozoic crust', *Developments in Precambrian Geology*, 15, pp. 9-18.
- Condie, K. C. (1981) *Archean greenstone belts*. Elsevier.
- Cook, N., Ciobanu, C., Spry, P., Voudouris, P. and participants of the Igcp, t. (2009) *Understanding gold-(silver)-telluride-(selenide) mineral deposits*.
- Cook, Y. A., Sanislav, I. V., Hammerli, J., Blenkinsop, T. G. and Dirks, P. H. G. M. (2016) 'A primitive mantle source for the Neoproterozoic mafic rocks from the Tanzania Craton', *Geoscience Frontiers*, 7(6), pp. 911-926.
- Cooke, D. R. and McPhail, D. (2001) 'Epithermal Au-Ag-Te mineralization, Acupan, Baguio district, Philippines: numerical simulations of mineral deposition', *Economic Geology*, 96(1), pp. 109-131.
- Craig, R. J., Vokes, M. F. and Solberg, N. T. (1998) 'Pyrite: physical and chemical textures', *Mineralium Deposita*, 34(1), pp. 82-101.
-

-
- Dalm, M., Buxton, M. W., van Ruitenbeek, F. J. and Voncken, J. H. (2014) 'Application of near-infrared spectroscopy to sensor based sorting of a porphyry copper ore', *Minerals Engineering*, 58, pp. 7-16.
- Dalm, M., Buxton, M. W. N. and van Ruitenbeek, F. J. A. (2017) 'Discriminating ore and waste in a porphyry copper deposit using short-wavelength infrared (SWIR) hyperspectral imagery', *Minerals Engineering*, 105, pp. 10-18.
- Dare, S. A., Barnes, S.-J., Beaudoin, G., Méric, J., Boutroy, E. and Potvin-Doucet, C. (2014) 'Trace elements in magnetite as petrogenetic indicators', *Mineralium Deposita*, 49(7), pp. 785-796.
- Davis, B. K. and Maidens, E. (2003) 'Archaean orogen-parallel extension: evidence from the northern Eastern Goldfields Province, Yilgarn Craton', *Precambrian Research*, 127(1), pp. 229-248.
- de Souza Martins, B., Lobato, L. M., Rosière, C. A., Hagemann, S. G., Santos, J. O. S., Villanova, F. L. d. S. P., Figueiredo e Silva, R. C. and de Ávila Lemos, L. H. (2016) 'The Archean BIF-hosted Lamego gold deposit, Rio das Velhas greenstone belt, Quadrilátero Ferrífero: Evidence for Cambrian structural modification of an Archean orogenic gold deposit', *Ore Geology Reviews*, 72, pp. 963-988.
- de Wit, M. J. (1998) 'On Archean granites, greenstones, cratons and tectonics: does the evidence demand a verdict?', *Precambrian Research*, 91(1-2), pp. 181-226.
- de Wit, M. J. and Ashwal, L. D. (1995) 'Greenstone belts: what are they?', *South African Journal of Geology*, 98(4), pp. 505-520.
- de Wit, M. J. and Ashwal, L. D. (1997) *Greenstone belts*. Oxford; New York: Clarendon Press.
- Deblond, A., Punzalan, L. E., Boven, A. and Tack, L. (2001) 'The Malagarazi supergroup of southeast Burundi and its correlative Bukoba supergroup of northwest Tanzania: neo- and mesoproterozoic chronostratigraphic constraints from Ar-Ar ages on mafic intrusive rocks', *Journal of African Earth Sciences*, 32(3), pp. 435-449.
- Deditius, A. P., Reich, M., Kesler, S. E., Utsunomiya, S., Chryssoulis, S. L., Walshe, J. and Ewing, R. C. (2014) 'The coupled geochemistry of Au and As in pyrite from hydrothermal ore deposits', *Geochimica et Cosmochimica Acta*, 140, pp. 644-670.
- Delvaux, D. (1993) 'The TENSOR program for paleostress reconstruction: examples from the east African and the Baikal rift zones', *Terra Nova*, 5(1), pp. 216.
- Delvaux, D. 2012. Win-Tensor for palaeostress reconstruction: version 3.4, available at: <http://users.skynet.be/damien.delvaux/Tensor/tensor-index.html>.
-

-
- Delvaux, D. and Sperner, B. (2003) 'New aspects of tectonic stress inversion with reference to the TENSOR program', *Geological Society, London, Special Publications*, 212(1), pp. 75-100.
- Diehl, S., Goldhaber, M., Koenig, A., Lowers, H. and Ruppert, L. (2012) 'Distribution of arsenic, selenium, and other trace elements in high pyrite Appalachian coals: evidence for multiple episodes of pyrite formation', *International Journal of Coal Geology*, 94, pp. 238-249.
- Dirks, P. H., Charlesworth, E. G., Munyai, M. R. and Wormald, R. (2013) 'Stress analysis, post-orogenic extension and 3.01 Ga gold mineralisation in the Barberton Greenstone Belt, South Africa', *Precambrian Research*, 226, pp. 157-184.
- Dirks, P. H. G. M., Sanislav, I. V., Van Ryt, M. R., Huizenga, J., Blenkinsop, T., Kolling, S. L. and Kwelwa, S. D. (in press) 'The Geita Gold deposit, Tanzania: a late Archaean, Te-enriched, intrusion related gold system', *Economic Geology, special issue on world class gold deposits*.
- Doublier, M. P., Thébaud, N., Wingate, M. T., Romano, S. S., Kirkland, C. L., Gessner, K., Mole, D. R. and Evans, N. (2014) 'Structure and timing of Neoproterozoic gold mineralization in the Southern Cross district (Yilgarn Craton, Western Australia) suggest leading role of late Low-Ca I-type granite intrusions', *Journal of Structural Geology*, 67, pp. 205-221.
- Duan, Z., Møller, N. and Weare, J. H. (1992) 'An equation of state for the CH₄-CO₂-H₂O system: II. Mixtures from 50 to 1000°C and 0 to 1000 bar', *Geochimica et Cosmochimica Acta*, 56(7), pp. 2619-2631.
- Duan, Z., Møller, N. and Weare, J. H. (1995) 'Equation of state for the NaCl-H₂O-CO₂ system: prediction of phase equilibria and volumetric properties', *Geochimica et Cosmochimica Acta*, 59(14), pp. 2869-2882.
- Duan, Z., Møller, N. and Weare, J. H. (1996) 'A general equation of state for supercritical fluid mixtures and molecular dynamics simulation of mixture PVTX properties', *Geochimica et Cosmochimica Acta*, 60(7), pp. 1209-1216.
- Dubessy, J., Derome, D. and Sausse, J. (2003) 'Numerical modelling of fluid mixings in the H₂O-NaCl system application to the North Caramal U prospect (Australia)', *Chemical Geology*, 194(1-3), pp. 25-39.
- Dubessy, J. and Ramboz, C. (1986) 'The history of organic nitrogen from early diagenesis to amphibolite facies: mineralogical, chemical, mechanical and isotopic implications', *Extended Abstracts, Water-Rock Interaction 5, Reykjavik*, pp. 171-174.
- Dupuis, C. and Beaudoin, G. (2011) 'Discriminant diagrams for iron oxide trace element fingerprinting of mineral deposit types', *Mineralium Deposita*, 46(4), pp. 319-335.
-

-
- Ernst, W. (1966) 'Synthesis and stability relations of ferrotremolite', *American Journal of Science*, 264(1), pp. 37-65.
- Etchecopar, A., Vasseur, G. and Daignieres, M. (1981) 'An inverse problem in microtectonics for the determination of stress tensors from fault striation analysis', *Journal of Structural Geology*, 3(1), pp. 51-65.
- Fan, H.-R., Hu, F.-F., Wilde, S. A., Yang, K.-F. and Jin, C.-W. (2011) 'The Qiyugou gold-bearing breccia pipes, Xiong'er shan region, central China: fluid-inclusion and stable-isotope evidence for an origin from magmatic fluids', *International Geology Review*, 53(1), pp. 25-45.
- Fayol, N., Jébrak, M. and Harris, L. B. (2016) 'The magnetic signature of Neoproterozoic alkaline intrusions and their related gold deposits: Significance and exploration implications', *Precambrian Research*, 283, pp. 13-23.
- Finch, E. G. and Tomkins, A. G. (2017) 'Pyrite-Pyrrhotite Stability in a Metamorphic Aureole: Implications for Orogenic Gold Genesis', *Economic Geology*, 112(3), pp. 661-674.
- Fogel, R. A. and Rutherford, M. J. (1990) 'The solubility of carbon dioxide in rhyolitic melts; a quantitative FTIR study', *American Mineralogist*, 75(11-12), pp. 1311-1326.
- Fornadel, A. P., Spry, P. G., Melfos, V., Vavelidis, M. and Voudouris, P. C. (2011) 'Is the Palea Kavala Bi-Te-Pb-Sb±Au district, northeastern Greece, an intrusion-related system?', *Ore Geology Reviews*, 39(3), pp. 119-133.
- Fossen, H. (2016) *Structural geology*. Cambridge University Press.
- French, B. M. (1966) 'Some geological implications of equilibrium between graphite and a C - H - O gas phase at high temperatures and pressures', *Reviews of Geophysics*, 4(2), pp. 223-253.
- Frezzotti, M. L., Tecce, F. and Casagli, A. (2012) 'Raman spectroscopy for fluid inclusion analysis', *Journal of Geochemical Exploration*, 112, pp. 1-20.
- Frost, B. R. (1991) 'Introduction to oxygen fugacity and its petrologic importance', *Reviews in Mineralogy and Geochemistry*, 25(1), pp. 1-9.
- Frost, C. D. and Frost, B. R. (2010) 'On ferroan (A-type) granitoids: their compositional variability and modes of origin', *Journal of Petrology*, 52(1), pp. 39-53.
- Gabert, G. (1990) 'Precambrian Ore Deposits Related to Tectonics Lithostratigraphic and tectonic setting of gold mineralization in the Archean cratons of Tanzania and Uganda, East Africa', *Precambrian Research*, 46(1), pp. 59-69.
-

-
- Gaillard, N., Williams-Jones, A. E., Clark, J. R., Lypaczewski, P., Salvi, S., Perrouy, S., Piette-Lauzière, N., Guilmette, C. and Linnen, R. L. (2018) 'Mica composition as a vector to gold mineralization: Deciphering hydrothermal and metamorphic effects in the Malartic district, Quebec', *Ore Geology Reviews*, 95, pp. 789-820.
- Geusebroek, P. and Duke, N. (2004) 'An update on the geology of the Lupin Gold Mine, Nunavut, Canada', *Exploration and Mining Geology*, 13(1-4), pp. 1-13.
- Goldfarb, R. J., Baker, T., Dube, B., Groves, D. I., Hart, C. J. and Gosselin, P. (2005) 'Distribution, character, and genesis of gold deposits in metamorphic terranes', *Economic Geology 100th anniversary volume*, 40.
- Goldfarb, R. J. and Groves, D. I. (2015) 'Orogenic gold: Common or evolving fluid and metal sources through time', *Lithos*, 233, pp. 2-26.
- Goldfarb, R. J., Groves, D. I. and Gardoll, S. (2001) 'Orogenic gold and geologic time: a global synthesis', *Ore Geology Reviews*, 18(1-2), pp. 1-75.
- Grant, H. L., Hannington, M. D., Petersen, S., Frische, M. and Fuchs, S. H. (2018) 'Constraints on the behavior of trace elements in the actively-forming TAG deposit, Mid-Atlantic Ridge, based on LA-ICP-MS analyses of pyrite', *Chemical Geology*, 498, pp. 45-71.
- Gregory, D. D., Large, R. R., Halpin, J. A., Baturina, E. L., Lyons, T. W., Wu, S., Danyushevsky, L., Sack, P. J., Chappaz, A., Maslennikov, V. V. and Bull, S. W. (2015) 'Trace element content of sedimentary pyrite in black shales', *Economic Geology*, 110(6), pp. 1389-1410.
- Groves, D. and Foster, R. (1991) 'Archaean lode gold deposits', *Gold metallogeny and exploration: Springer*, pp. 63-103.
- Groves, D., Ridley, J., Bloem, E., Gebre-Mariam, M., Hagemann, S., Hronsky, J., Knight, J., McNaughton, N., Ojala, J. and Vielreicher, R. (1995) 'Lode-gold deposits of the Yilgarn block: products of Late Archaean crustal-scale overpressured hydrothermal systems', *Geological Society, London, Special Publications*, 95(1), pp. 155-172.
- Groves, D. I., Goldfarb, R. J., Gebre-Mariam, M., Hagemann, S. G. and Robert, F. (1998) 'Orogenic gold deposits: A proposed classification in the context of their crustal distribution and relationship to other gold deposit types', *Ore Geology Reviews*, 13(1-5), pp. 7-27.
- Groves, D. I., Goldfarb, R. J., Robert, F. and Hart, C. J. R. (2003) 'Gold Deposits in Metamorphic Belts: Overview of Current Understanding, Outstanding Problems, Future Research, and Exploration Significance', *Economic Geology*, 98(1), pp. 1-29.
-

-
- Groves, D. I. and Santosh, M. (2016) 'The giant Jiaodong gold province: The key to a unified model for orogenic gold deposits?', *Geoscience Frontiers*, 7(3), pp. 409-417.
- Groves, D. I., Santosh, M., Goldfarb, R. J. and Zhang, L. (2018) 'Structural geometry of orogenic gold deposits: implications for exploration of world-class and giant deposits', *Geoscience Frontiers*.
- Grundler, P. V., Brugger, J., Etschmann, B. E., Helm, L., Liu, W., Spry, P. G., Tian, Y., Testemale, D. and Pring, A. (2013) 'Speciation of aqueous tellurium(IV) in hydrothermal solutions and vapors, and the role of oxidized tellurium species in Te transport and gold deposition', *Geochimica et Cosmochimica Acta*, 120, pp. 298-325.
- Hamilton, W. B. (2011) 'Plate tectonics began in Neoproterozoic time, and plumes from deep mantle have never operated', *Lithos*, 123(1-4), pp. 1-20.
- Heimann, A., Spry, P. G. and Teale, G. S. (2005) 'Zincian spinel associated with metamorphosed Proterozoic base-metal sulfide occurrences, Colorado: a re-evaluation of gahnite composition as a guide in exploration', *The Canadian Mineralogist*, 43(2), pp. 601-622.
- Hellner, E. and Schürmann, K. (1966) 'Stability of Metamorphic Amphiboles: The Tremolite-Ferroactinolite Series', *The Journal of Geology*, 74(3), pp. 322-331.
- Helt, K. M., Williams-Jones, A. E., Clark, J. R., Wing, B. A. and Wares, R. P. (2014) 'Constraints on the Genesis of the Archean Oxidized, Intrusion-Related Canadian Malartic Gold Deposit, Quebec, Canada', *ECONOMIC GEOLOGY*, 109(3), pp. 713-735.
- Henckel, J., Poulsen, K., Sharp, T. and Spora, P. (2016) 'Lake Victoria Goldfields', *Episodes*, 39(2), pp. 135-154.
- Herrmann, W., Blake, M., Doyle, M., Huston, D., Kamprad, J., Merry, N. and Pontual, S. (2001) 'Short wavelength infrared (SWIR) spectral analysis of hydrothermal alteration zones associated with base metal sulfide deposits at Rosebery and Western Tharsis, Tasmania, and Highway-Reward, Queensland', *Economic Geology*, 96(5), pp. 939-955.
- Hickman, A. (2004) 'Two contrasting granite– greenstone terranes in the Pilbara Craton, Australia: evidence for vertical and horizontal tectonic regimes prior to 2900 Ma', *Precambrian Research*, 131(3-4), pp. 153-172.
- Hickman, A. (2009) 'Pilbara Supergroup of the East Pilbara Terrane, Pilbara Craton: Updated lithostratigraphy and comments on the influence of vertical tectonics', *GSWA Annual Review*, 10, pp. 50-59.
-

-
- Hickman, A. H. (2012) 'Review of the Pilbara Craton and Fortescue Basin, Western Australia: crustal evolution providing environments for early life', *Island Arc*, 21(1), pp. 1-31.
- Holland, T. and Powell, R. (1998) 'An internally consistent thermodynamic data set for phases of petrological interest', *Journal of metamorphic Geology*, 16(3), pp. 309-343.
- Holwell, D. A., Jenkin, G. R. T., Butterworth, K. G., Abraham-James, T. and Boyce, A. J. (2013) 'Orogenic gold mineralisation hosted by Archaean basement rocks at Sortekap, Kangerlussuaq area, East Greenland', *Mineralium Deposita*, 48(4), pp. 453-466.
- Honma, H. and Itihara, Y. (1981) 'Distribution of ammonium in minerals of metamorphic and granitic rocks', *Geochimica et Cosmochimica Acta*, 45(6), pp. 983-988.
- Horne, R. G. (1959) *Notes on the structure of Geita Mine*.
- Hough, R. and Reich, M. (2011) 'Noble metal nanoparticles in ore systems', *Ore Geology Reviews*, 42, pp. 55-61.
- Huizenga, J.-M. (2001) 'Thermodynamic modelling of C-O-H fluids', *Lithos*, 55(1-4), pp. 101-114.
- Huizenga, J.-M. (2011) 'Thermodynamic modelling of a cooling C-O-H fluid-graphite system: implications for hydrothermal graphite precipitation', *Mineralium Deposita*, 46(1), pp. 23-33.
- Huizenga, J. M. (2005) 'COH, an Excel spreadsheet for composition calculations in the COH fluid system', *Computers & Geosciences*, 31(6), pp. 797-800.
- Hurai, V. (2010) 'Fluid inclusion geobarometry: Pressure corrections for immiscible H₂O-CH₄ and H₂O-CO₂ fluids', *Chemical Geology*, 278(3-4), pp. 201-211.
- Huston, D. L., Sie, S. H., Suter, G. F., Cooke, D. R. and Both, R. A. (1995) 'Trace elements in sulfide minerals from eastern Australian volcanic-hosted massive sulfide deposits; Part I, Proton microprobe analyses of pyrite, chalcopyrite, and sphalerite, and Part II, Selenium levels in pyrite; comparison with delta 34 S values and implications for the source of sulfur in volcanogenic hydrothermal systems', *Economic Geology*, 90(5), pp. 1167-1196.
- Hynes, A. (2013) 'How feasible was subduction in the Archean?', *Canadian Journal of Earth Sciences*, 51(3), pp. 286-296.
- Ikingura, J. R., Reynolds, P. H., Watkinson, D. H. and Bell, K. (1992) '⁴⁰Ar/³⁹Ar dating of micas from granites of NE Kibaran Belt (Karagwe-Ankolean), NW Tanzania', *Journal of African Earth Sciences (and the Middle East)*, 15(3), pp. 501-511.
-

-
- Jelsma, H. A. and Dirks, P. H. (2002) 'Neoproterozoic tectonic evolution of the Zimbabwe Craton', *Geological Society, London, Special Publications*, 199(1), pp. 183-211.
- Jenkins, D. M. and Bozhilov, K. N. (2003) 'Stability and thermodynamic properties of ferro-actinolite: a re-investigation', *American Journal of science*, 303(8), pp. 723-752.
- Jin, C., Gao, X.-Y., Chen, W. T. and Zhao, T.-P. (2018) 'Magmatic-hydrothermal evolution of the Donggou porphyry Mo deposit at the southern margin of the North China Craton: evidence from chemistry of biotite', *Ore Geology Reviews*, 92, pp. 84-96.
- Jochum, K. P., Weis, U., Stoll, B., Kuzmin, D., Yang, Q., Raczek, I., Jacob, D. E., Stracke, A., Birbaum, K. and Frick, D. A. (2011) 'Determination of reference values for NIST SRM 610–617 glasses following ISO guidelines', *Geostandards and Geoanalytical Research*, 35(4), pp. 397-429.
- Jochum, K. P., Willbold, M., Raczek, I., Stoll, B. and Herwig, K. (2005) 'Chemical Characterisation of the USGS Reference Glasses GSA - 1G, GSC - 1G, GSD - 1G, GSE - 1G, BCR - 2G, BHVO - 2G and BIR - 1G Using EPMA, ID - TIMS, ID - ICP - MS and LA - ICP - MS', *Geostandards and Geoanalytical Research*, 29(3), pp. 285-302.
- Jones, S., Herrmann, W. and Gemmill, J. B. (2005) 'Short wavelength infrared spectral characteristics of the HW horizon: implications for exploration in the Myra Falls volcanic-hosted massive sulfide camp, Vancouver Island, British Columbia, Canada', *Economic Geology*, 100(2), pp. 273-294.
- Junqueira, P. A., Lobato, L. M., Ladeira, E. A. and Simões, E. J. M. (2007) 'Structural control and hydrothermal alteration at the BIF-hosted Raposos lode-gold deposit, Quadrilátero Ferrífero, Brazil', *Ore Geology Reviews*, 32(3–4), pp. 629-650.
- Kabete, J. M., Groves, D. I., McNaughton, N. J. and Mruma, A. H. (2012a) 'A new tectonic and temporal framework for the Tanzanian Shield: Implications for gold metallogeny and undiscovered endowment', *Ore Geology Reviews*, 48(0), pp. 88-124.
- Kabete, J. M., McNaughton, N. J., Groves, D. I. and Mruma, A. H. (2012b) 'Reconnaissance SHRIMP U–Pb zircon geochronology of the Tanzania Craton: Evidence for Neoproterozoic granitoid–greenstone belts in the Central Tanzania Region and the Southern East African Orogen', *Precambrian Research*, 216–219, pp. 232-266.
- Kamvong, T., Zaw, K. and Siegele, R. (2007) 'PIXE/PIGE microanalysis of trace elements in hydrothermal magnetite and exploration significance: a pilot study 15th Australian Conference on Nuclear and Complementary Techniques of Analysis and 9th Vacuum Society of Australia Congress', *University of Melbourne, Melbourne*.
-

-
- Keith, M., Smith, D. J., Jenkin, G. R., Holwell, D. A. and Dye, M. D. (2018) 'A review of Te and Se systematics in hydrothermal pyrite from precious metal deposits: Insights into ore-forming processes', *Ore Geology Reviews*, 96, pp. 269-282.
- Kelly, W. C. and Goddard, E. N. (1969) *Telluride ores of Boulder County, Colorado*. Geological Society of America.
- Kendrick, M., Honda, M., Walshe, J. and Petersen, K. (2011) 'Fluid sources and the role of abiogenic-CH₄ in Archean gold mineralization: Constraints from noble gases and halogens', *Precambrian Research*, 189(3-4), pp. 313-327.
- Kitney, K. E., Olivo, G. R., Davis, D. W., Desrochers, J.-P. and Tessier, A. (2011) 'The Barry gold deposit, Abitibi Subprovince, Canada: A greenstone belt-hosted gold deposit coeval with late Archean deformation and magmatism', *Economic Geology*, 106(7), pp. 1129-1154.
- Klein, C. (2005) 'Some Precambrian banded iron-formations (BIFs) from around the world: Their age, geologic setting, mineralogy, metamorphism, geochemistry, and origins', *American Mineralogist*, 90(10), pp. 1473-1499.
- Knight, C. L. and Bodnar, R. J. (1989) 'Synthetic fluid inclusions: IX. Critical PVTX properties of NaCl-H₂O solutions', *Geochimica et Cosmochimica Acta*, 53(1), pp. 3-8.
- Koglin, N., Frimmel, H. E., Lawrie Minter, W. E. and Brätz, H. (2010) 'Trace-element characteristics of different pyrite types in Mesoarchaeon to Palaeoproterozoic placer deposits', *Mineralium Deposita*, 45(3), pp. 259-280.
- Kontak, D. J. and Kyser, K. (2011) 'A fluid inclusion and isotopic study of an intrusion-related gold deposit (IRGD) setting in the 380 Ma South Mountain Batholith, Nova Scotia, Canada: evidence for multiple fluid reservoirs', *Mineralium Deposita*, 46(4), pp. 337-363.
- Krapez, B. 2008. Stratigraphic analysis of the Geita Mine Sequence. Geita Gold Mine internal Report - unpublished
- Krumgalz, B. S., Pogorelsky, R. and Pitzer, K. S. (1996) 'Volumetric Properties of Single Aqueous Electrolytes from Zero to Saturation Concentration at 298.15° K Represented by Pitzer's Ion - Interaction Equations', *Journal of Physical and Chemical Reference Data*, 25(2), pp. 663-689.
- Kuehn, S., Ogola, J. and Sango, P. (1990) 'Precambrian Ore Deposits Related to Tectonics Regional setting and nature of gold mineralization in Tanzania and southwest Kenya', *Precambrian Research*, 46(1), pp. 71-82.
-

-
- Kusebauch, C., John, T., Whitehouse, M. J., Klemme, S. and Putnis, A. (2015) 'Distribution of halogens between fluid and apatite during fluid-mediated replacement processes', *Geochimica et Cosmochimica Acta*, 170, pp. 225-246.
- Kwelwa, S., Sanislav, I., Dirks, P., Blenkinsop, T. and Kolling, S. (2018a) 'The petrogenesis of the neoproterozoic Kukuluma intrusive complex, NW Tanzania', *Precambrian Research*, 305, pp. 64-78.
- Kwelwa, S. D., Dirks, P. H., Sanislav, I. V., Blenkinsop, T. and Kolling, S. L. (2018b) 'Archaean Gold Mineralization in an Extensional Setting: The Structural History of the Kukuluma and Matandani Deposits, Geita Greenstone Belt, Tanzania', *Minerals*, 8(4), pp. 171.
- Kwelwa, S. D., Sanislav, I. V., Dirks, P. H. G. M., Blenkinsop, T. and Kolling, S. L. (2018c) 'Zircon U-Pb ages and Hf isotope data from the Kukuluma Terrain of the Geita Greenstone Belt, Tanzania Craton: Implications for stratigraphy, crustal growth and timing of gold mineralization', *Journal of African Earth Sciences*, 139, pp. 38-54.
- Laakso, K., Peter, J., Rivard, B. and White, H. (2016) 'Short-wave infrared spectral and geochemical characteristics of hydrothermal alteration at the Archean Izok Lake Zn-Cu-Pb-Ag volcanogenic massive sulfide deposit, Nunavut, Canada: application in exploration target vectoring', *Economic Geology*, 111(5), pp. 1223-1239.
- Laakso, K., Rivard, B., Peter, J., White, H., Maloley, M., Harris, J. and Rogge, D. (2015) 'Application of airborne, laboratory, and field hyperspectral methods to mineral exploration in the Canadian Arctic: recognition and characterization of volcanogenic massive sulfide-associated hydrothermal alteration in the Izok Lake deposit area, Nunavut, Canada', *Economic Geology*, 110(4), pp. 925-941.
- Lang, J. R. and Baker, T. (2001) 'Intrusion-related gold systems: the present level of understanding', *Mineralium Deposita*, 36(6), pp. 477-489.
- Large, R. R., Bull, S. W. and Maslennikov, V. V. (2011) 'A carbonaceous sedimentary source-rock model for Carlin-type and orogenic gold deposits', *Economic Geology*, 106(3), pp. 331-358.
- Large, R. R., Danyushevsky, L., Hollit, C., Maslennikov, V., Meffre, S., Gilbert, S., Bull, S., Scott, R., Emsbo, P. and Thomas, H. (2009) 'Gold and trace element zonation in pyrite using a laser imaging technique: implications for the timing of gold in orogenic and Carlin-style sediment-hosted deposits', *Economic Geology*, 104(5), pp. 635-668.
- Large, R. R., Halpin, J. A., Danyushevsky, L. V., Maslennikov, V. V., Bull, S. W., Long, J. A., Gregory, D. D., Lounejeva, E., Lyons, T. W., Sack, P. J., McGoldrick, P. J. and Calver, C. R. (2014) 'Trace element content of sedimentary pyrite as a new proxy for deep-time ocean-atmosphere evolution', *Earth and Planetary Science Letters*, 389, pp. 209-220.
-

-
- Large, R. R., Maslennikov, V. V., Robert, F., Danyushevsky, L. V. and Chang, Z. (2007) 'Multistage sedimentary and metamorphic origin of pyrite and gold in the giant Sukhoi Log deposit, Lena gold province, Russia', *Economic Geology*, 102(7), pp. 1233-1267.
- Leach, D. L., Bradley, D. C., Huston, D., Pisarevsky, S. A., Taylor, R. D. and Gardoll, S. J. (2010) 'Sediment-hosted lead-zinc deposits in Earth history', *Economic Geology*, 105(3), pp. 593-625.
- Lenoir, J. L., Liégeois, J. P., Theunissen, K. and Klerkx, J. (1994) 'The Palaeoproterozoic Ubendian shear belt in Tanzania: geochronology and structure', *Journal of African Earth Sciences*, 19(3), pp. 169-184.
- Lisle, R. J. (1987) 'Principal stress orientations from faults: an additional constraint', *Annales Tectonicae-International Journal of Structural Geology and Tectonics*, 1, pp. 155-158.
- Loferski, P. J. and Ayuso, R. A. (1995) 'Petrography and mineral chemistry of the composite Deboullie pluton, northern Maine, USA: Implications for the genesis of Cu \square Mo mineralization', *Chemical Geology*, 123(1-4), pp. 89-105.
- Longerich, H. P., Jackson, S. E. and Günther, D. (1996) 'Inter-laboratory note. Laser ablation inductively coupled plasma mass spectrometric transient signal data acquisition and analyte concentration calculation', *Journal of Analytical Atomic Spectrometry*, 11(9), pp. 899-904.
- Lu, L., Wang, R., Chen, F., Xue, J., Zhang, P. and Lu, J. (2005) 'Element mobility during pyrite weathering: implications for acid and heavy metal pollution at mining-impacted sites', *Environmental geology*, 49(1), pp. 82-89.
- Lypaczewski, P. and Rivard, B. (2018) 'Estimating the Mg# and AlVI content of biotite and chlorite from shortwave infrared reflectance spectroscopy: Predictive equations and recommendations for their use', *International journal of applied earth observation and geoinformation*, 68, pp. 116-126.
- Manya, S. and Maboko, M. A. H. (2003) 'Dating basaltic volcanism in the Neoproterozoic Sukumaland Greenstone Belt of the Tanzania Craton using the Sm-Nd method: implications for the geological evolution of the Tanzania Craton', *Precambrian Research*, 121(1-2), pp. 35-45.
- Manya, S. and Maboko, M. A. H. (2008) 'Geochemistry of the Neoproterozoic mafic volcanic rocks of the Geita area, NW Tanzania: Implications for stratigraphical relationships in the Sukumaland greenstone belt', *Journal of African Earth Sciences*, 52(4-5), pp. 152-160.
- Marrett, R. and Allmendinger, R. W. (1990) 'Kinematic analysis of fault-slip data', *Journal of structural geology*, 12(8), pp. 973-986.
-

-
- McCuaig, T. C. and Kerrich, R. (1998) 'P—T—t—deformation—fluid characteristics of lode gold deposits: evidence from alteration systematics', *Ore Geology Reviews*, 12(6), pp. 381-453.
- McLeod, R., Gabell, A., Green, A. and Gardavsky, V. 'Chlorite infrared spectral data as proximity indicators of volcanogenic massive sulphide mineralization'. *Pacific Rim Congress*, 26-29.
- McPhail, D. (1995) 'Thermodynamic properties of aqueous tellurium species between 25 and 350', *Geochimica et Cosmochimica Acta*, 59(5), pp. 851-866.
- McQueen, K. and Cross, A. (1998) 'Magnetite as a geochemical sampling medium: application to skarn deposits', *Brisbane, Geological Society of Australia*, pp. 194-199.
- Meffre, S., Large, R. R., Steadman, J. A., Gregory, D. D., Stepanov, A. S., Kamenetsky, V. S., Ehrig, K. and Scott, R. J. (2015) 'Multi-stage enrichment processes for large gold-bearing ore deposits', *Ore Geology Reviews*.
- Meyer, F. M., OberthLir, H. D., Saager, R. and Stupp, H. D. (1990) 'Cobalt, nickel, and gold in pyrite from primary gold deposits and Witwatersrand reefs', *South African Journal of Geology*, 93(1), pp. 70-82.
- Michel, D., Giuliani, G., Olivo, G. R. and Marini, O. J. (1994) 'As growth banding and the presence of Au in pyrites from the Santa Rita gold vein deposit hosted in Proterozoic metasediments, Goias State, Brazil', *Economic Geology*, 89(1), pp. 193-200.
- Mikucki, E. and Ridley, J. (1993) 'The hydrothermal fluid of Archaean lode-gold deposits at different metamorphic grades: compositional constraints from ore and wallrock alteration assemblages', *Mineralium Deposita*, 28(6), pp. 469-481.
- Mikucki, E. J. (1998) 'Hydrothermal transport and depositional processes in Archean lode-gold systems: A review', *Ore Geology Reviews*, 13(1-5), pp. 307-321.
- Mishra, B., Pruseth, K. L., Hazarika, P. and Chinnasamy, S. S. (2018) 'Nature and source of the ore-forming fluids associated with orogenic gold deposits in the Dharwar Craton', *Geoscience Frontiers*, 9(3), pp. 715-726.
- Moin, B., Guillot, C. and Gibert, F. (1994) 'Controls of the composition of nitrogen-rich fluids originating from reaction with graphite and ammonium-bearing biotite', *Geochimica et Cosmochimica Acta*, 58(24), pp. 5503-5523.
- Möller, A., Appel, P., Mezger, K. and Schenk, V. (1995) 'Evidence for a 2 Ga subduction zone: eclogites in the Usagaran belt of Tanzania', *Geology*, 23(12), pp. 1067-1070.
-

-
- Monteiro, L. V. S., Xavier, R. P., Hitzman, M. W., Juliani, C., de Souza Filho, C. R. and Carvalho, E. d. R. (2008) 'Mineral chemistry of ore and hydrothermal alteration at the Sossego iron oxide–copper–gold deposit, Carajás Mineral Province, Brazil', *Ore Geology Reviews*, 34(3), pp. 317-336.
- Mookherjee, A. and Philip, R. (1979) 'Distribution of copper, cobalt and nickel in ores and host-rocks, Ingladhal, Karnataka, India', *Mineralium Deposita*, 14(1), pp. 33-55.
- Morey, A. A., Tomkins, A. G., Bierlein, F. P., Weinberg, R. F. and Davidson, G. J. (2008) 'Bimodal distribution of gold in pyrite and arsenopyrite: Examples from the Archean Boorara and Bardoc shear systems, Yilgarn craton, Western Australia', *Economic Geology*, 103(3), pp. 599-614.
- Morey, A. A., Weinberg, R. F., Bierlein, F. P. and Davidson, G. J. (2007) 'Gold deposits of the Bardoc Tectonic Zone: a distinct style of orogenic gold in the Archaean Eastern Goldfields Province, Yilgarn Craton, Western Australia', *Australian Journal of Earth Sciences*, 54(6), pp. 783-800.
- Mumin, A., Fleet, M. and Chryssoulis, S. (1994) 'Gold mineralization in As-rich mesothermal gold ores of the Bogosu-Prestea mining district of the Ashanti gold belt, Ghana: Remobilization of "invisible" gold', *Mineralium Deposita*, 29(6), pp. 445-460.
- Munoz, J. (1984) 'F-OH and Cl-OH exchange in micas with applications to hydrothermal ore deposits', *Reviews in Mineralogy and Geochemistry*, 13(1), pp. 469-493.
- Munoz, J. (1990) 'F and Cl contents of hydrothermal biotites: A reevaluation', *GSA Abst. Prog.*, 22.
- Munoz, J. 'Calculation of HF and HCl fugacities from biotite compositions: revised equations'. *Geol. Soc. Am., Abstract Programs*, A221.
- Munoz, J. and Swenson, A. (1981) 'Chloride-hydroxyl exchange in biotite and estimation of relative HCl/HF activities in hydrothermal fluids', *Economic Geology*, 76(8), pp. 2212-2221.
- Munoz, J. L. and Ludington, S. D. (1974) 'Fluorine-hydroxyl exchange in biotite.', *American Journal of Science*, 274, pp. 396-413.
- Muntean, J. L., Cline, J. S., Simon, A. C. and Longo, A. A. (2011) 'Magmatic–hydrothermal origin of Nevada's Carlin-type gold deposits', *Nature Geoscience*, 4(2), pp. 122.
- Nesbitt, H. and Muir, I. (1994) 'X-ray photoelectron spectroscopic study of a pristine pyrite surface reacted with water vapour and air', *Geochimica et Cosmochimica Acta*, 58(21), pp. 4667-4679.
-

-
- Neumayr, P. and Hagemann, S. G. (2002) 'Hydrothermal fluid evolution within the Cadillac tectonic zone, Abitibi greenstone belt, Canada: relationship to auriferous fluids in adjacent second- and third-order shear zones', *Economic Geology*, 97(6), pp. 1203-1225.
- Nikolaev, Y. N., Prokof'ev, V. Y., Apletalin, A. V., Vlasov, E. A., Baksheev, I. A., Kal'ko, I. A. and Komarova, Y. S. (2013) 'Gold-telluride mineralization of the Western Chukchi Peninsula, Russia: Mineralogy, geochemistry, and formation conditions', *Geology of Ore Deposits*, 55(2), pp. 96-124.
- O'Neill, H. S. C. and Wall, V. (1987) 'The Olivine—Orthopyroxene—Spinel oxygen geobarometer, the nickel precipitation curve, and the oxygen fugacity of the Earth's Upper Mantle', *Journal of Petrology*, 28(6), pp. 1169-1191.
- Ohmoto, H. and Kerrick, D. (1977) 'Devolatilization equilibria in graphitic systems', *American Journal of Science*, 277(8), pp. 1013-1044.
- Parnell, J., Bellis, D., Feldmann, J. and Bata, T. (2015) 'Selenium and tellurium enrichment in palaeo-oil reservoirs', *Journal of Geochemical Exploration*, 148, pp. 169-173.
- Phillips, G. and Evans, K. (2004) 'Role of CO₂ in the formation of gold deposits', *Nature*, 429(6994), pp. 860.
- Phillips, G. N. and Groves, D. I. (1983) 'The nature of Archaean gold - bearing fluids as deduced from gold deposits of Western Australia', *Journal of the Geological Society of Australia*, 30(1-2), pp. 25-39.
- Phillips, G. N. and Powell, R. (2009) 'Formation of gold deposits: Review and evaluation of the continuum model', *Earth-Science Reviews*, 94(1-4), pp. 1-21.
- Phillips, G. N. and Powell, R. (2010) 'Formation of gold deposits: a metamorphic devolatilization model', *Journal of Metamorphic Geology*, 28(6), pp. 689-718.
- Piña, R., Gervilla, F., Barnes, S.-J., Ortega, L. and Lunar, R. (2013) 'Platinum-group elements-bearing pyrite from the Aguablanca Ni-Cu sulphide deposit (SW Spain): a LA-ICP-MS study', *European Journal of Mineralogy*, 25(2), pp. 241-252.
- Pitcairn, I. K., Teagle, D. A., Craw, D., Olivo, G. R., Kerrich, R. and Brewer, T. S. (2006) 'Sources of metals and fluids in orogenic gold deposits: insights from the Otago and Alpine Schists, New Zealand', *Economic Geology*, 101(8), pp. 1525-1546.
- Powell, R., Will, T. and Phillips, G. (1991) 'Metamorphism in Archaean greenstone belts: calculated fluid compositions and implications for gold mineralization', *Journal of Metamorphic Geology*, 9(2), pp. 141-150.
-

-
- Qian, G., Brugger, J., Skinner, W. M., Chen, G. and Pring, A. (2010) 'An experimental study of the mechanism of the replacement of magnetite by pyrite up to 300 C', *Geochimica et Cosmochimica Acta*, 74(19), pp. 5610-5630.
- Quenell, A. M., Mckinlay, A. C. and Aitken, W. G. (1956) 'Summary of the geology of Tanganyika, part 1.', *Geological Survey of Tanganyika Memoirs*, pp. 1-26.
- Ramboz, C., Pichavant, M. and Weisbrod, A. (1982) 'Fluid immiscibility in natural processes: Use and misuse of fluid inclusion data: II. Interpretation of fluid inclusion data in terms of immiscibility', *Chemical Geology*, 37(1-2), pp. 29-48.
- Rasmussen, K. L. and Mortensen, J. K. (2013) 'Magmatic petrogenesis and the evolution of (F:Cl:OH) fluid composition in barren and tungsten skarn-associated plutons using apatite and biotite compositions: Case studies from the northern Canadian Cordillera', *Ore Geology Reviews*, 50, pp. 118-142.
- Reich, M., Deditius, A., Chryssoulis, S., Li, J.-W., Ma, C.-Q., Parada, M. A., Barra, F. and Mittermayr, F. (2013) 'Pyrite as a record of hydrothermal fluid evolution in a porphyry copper system: A SIMS/EMPA trace element study', *Geochimica et Cosmochimica Acta*, 104, pp. 42-62.
- Reich, M., Kesler, S. E., Utsunomiya, S., Palenik, C. S., Chryssoulis, S. L. and Ewing, R. C. (2005) 'Solubility of gold in arsenian pyrite', *Geochimica et Cosmochimica Acta*, 69(11), pp. 2781-2796.
- Reich, M., Simon, A. C., Deditius, A., Barra, F., Chryssoulis, S., Lagas, G., Tardani, D., Knipping, J., Bilenker, L. and Sánchez-Alfaro, P. (2016) 'Trace element signature of pyrite from the Los Colorados iron oxide-apatite (IOA) deposit, Chile: A missing link between Andean IOA and iron oxide copper-gold systems?', *Economic Geology*, 111(3), pp. 743-761.
- Revan, M. K., Genç, Y., Maslennikov, V. V., Maslennikova, S. P., Large, R. R. and Danyushevsky, L. V. (2014) 'Mineralogy and trace-element geochemistry of sulfide minerals in hydrothermal chimneys from the Upper-Cretaceous VMS deposits of the eastern Pontide orogenic belt (NE Turkey)', *Ore Geology Reviews*, 63, pp. 129-149.
- Rezeau, H., Moritz, R. and Beaudoin, G. (2017) 'Formation of Archean batholith-hosted gold veins at the Lac Herbin deposit, Val-d'Or district, Canada: Mineralogical and fluid inclusion constraints', *Mineralium Deposita*, 52(3), pp. 421-442.
- Ribeiro-Rodrigues, L. C., de Oliveira, C. G. and Friedrich, G. (2007) 'The Archean BIF-hosted Cuiabá Gold deposit, Quadrilátero Ferrífero, Minas Gerais, Brazil', *Ore Geology Reviews*, 32(3-4), pp. 543-570.
-

-
- Rickard, D. and Luther, G. W. (2007) 'Chemistry of iron sulfides', *Chemical reviews*, 107(2), pp. 514-562.
- Ridley, J. (1993) 'The relations between mean rock stress and fluid flow in the crust: with reference to vein-and lode-style gold deposits', *Ore Geology Reviews*, 8(1-2), pp. 23-37.
- Ridley, J. and Mengler, F. (2000) 'Lithological and structural controls on the form and setting of vein stockwork orebodies at the Mount Charlotte gold deposit, Kalgoorlie', *Economic Geology*, 95(1), pp. 85-98.
- Ridley, J., Vearncombe, J. and Jelsma, H. (1997) 'Relations between greenstone belts and associated granitoids', *OXFORD MONOGRAPHS ON GEOLOGY AND GEOPHYSICS*, 35(1), pp. 376-397.
- Ridley, J. R. and Diamond, L. W. (2000) 'Fluid chemistry of orogenic lode gold deposits and implications for genetic models', *Reviews in Economic Geology. Society of Economic Geologists*, 13, pp. 141-162.
- Robert, F., Boullier, A. M. and Firdaus, K. (1995) 'Gold - quartz veins in metamorphic terranes and their bearing on the role of fluids in faulting', *Journal of Geophysical Research: Solid Earth*, 100(B7), pp. 12861-12879.
- Robert, F. and Brown, A. C. (1986a) 'Archean gold-bearing quartz veins at the Sigma Mine, Abitibi greenstone belt, Quebec; Part I, Geologic relations and formation of the vein system', *Economic Geology*, 81(3), pp. 578-592.
- Robert, F. and Brown, A. C. (1986b) 'Archean gold-bearing quartz veins at the Sigma Mine, Abitibi greenstone belt, Quebec; Part II, Vein paragenesis and hydrothermal alteration', *Economic Geology*, 81(3), pp. 593-616.
- Robert, F., Poulsen, K. H., Cassidy, K. F. and Hodgson, C. J. (2005) 'Gold metallogeny of the Superior and Yilgarn cratons', *Economic Geology 100th anniversary volume*, 1001, pp. 1034.
- Román, N., Reich, M., Leisen, M., Morata, D., Barra, F. and Deditius, A. P. (2019) 'Geochemical and micro-textural fingerprints of boiling in pyrite', *Geochimica et Cosmochimica Acta*, 246, pp. 60-85.
- Rusk, B., Oliver, N., Brown, A., Lilly, R. and Jungmann, D. (2009) 'Barren magnetite breccias in the Cloncurry region, Australia: comparisons to IOCG deposits'.
- Sallet, R. (2000) 'Fluorine as a tool in the petrogenesis of quartz-bearing magmatic associations: applications of an improved F-OH biotite-apatite thermometer grid', *Lithos*, 50(1), pp. 241-253.
-

-
- Sallet, R., Moritz, R. and Sabatier, H. (1997) 'Geochemistry of the Tabuleiro high-silica fluorite granites: Pelotas Batholith, southern Brazil. Potential for Sn–Mo Mineralizations', *Mineral Deposits: Research and Exploration — Where do they meet?* Balkema, Rotterdam: Papunen, H. Ed., pp. 667–670.
- Sallet, R., Price, J. D. and Moritz, R. (2018) 'Natural and experimental fluorine substitution in biotite: Implications for fluid-rock thermochronometry and application to the Seridó Belt, northeastern Brazil', *Chemical Geology*, 482, pp. 32-45.
- Sanislav, I., Brayshaw, M., Kolling, S., Dirks, P., Cook, Y. and Blenkinsop, T. (2017) 'The structural history and mineralization controls of the world-class Geita Hill gold deposit, Geita Greenstone Belt, Tanzania', *Mineralium Deposita*, 52(2), pp. 257-279.
- Sanislav, I., Dirks, P., Cook, Y., Blenkinsop, T. and Kolling, S. (2014a) 'A Giant Gold System, Geita Greenstone Belt, Tanzania', *Acta Geologica Sinica (English Edition)*, 88(s2), pp. 110-111.
- Sanislav, I., Wormald, R., Dirks, P., Blenkinsop, T. G., Salamba, L. and Joseph, D. (2014b) 'Zircon U–Pb ages and Lu–Hf isotope systematics from late-tectonic granites, Geita Greenstone Belt: Implications for crustal growth of the Tanzania Craton', *Precambrian Research*, 242, pp. 187-204.
- Sanislav, I. V., Blenkinsop, T. G. and Dirks, P. H. (2018a) 'Archaean crustal growth through successive partial melting events in an oceanic plateau - like setting in the Tanzania Craton', *Terra Nova*, 30(3), pp. 169-178.
- Sanislav, I. V., Dirks, P. H. G. M., Blenkinsop, T. and Kolling, S. L. (2018b) 'The tectonic history of a crustal-scale shear zone in the Tanzania Craton from the Geita Greenstone Belt, NW-Tanzania Craton', *Precambrian Research*, 310, pp. 1-16.
- Sanislav, I. V., Kolling, S. L., Brayshaw, M., Cook, Y. A., Dirks, P. H. G. M., Blenkinsop, T. G., Mturi, M. I. and Ruhega, R. (2015) 'The geology of the giant Nyankanga gold deposit, Geita Greenstone Belt, Tanzania', *Ore Geology Reviews*, 69(0), pp. 1-16.
- Scott, K., Yang, K. and Huntington, J. (1998) 'The application of spectral reflectance studies chlorites in exploration', *Australia: CSIRO Exploration & Mining Report*, 545, pp. 1998.
- Selby, D. and Nesbitt, B. E. (2000) 'Chemical composition of biotite from the Casino porphyry Cu–Au–Mo mineralization, Yukon, Canada: evaluation of magmatic and hydrothermal fluid chemistry', *Chemical Geology*, 171(1), pp. 77-93.
- Silverstone, J. and Sharp, Z. D. (2015) 'Chlorine isotope behavior during prograde metamorphism of sedimentary rocks', *Earth and Planetary Science Letters*, 417, pp. 120-131.
-

-
- Seward, T. M. (1973) 'Thio complexes of gold and the transport of gold in hydrothermal ore solutions', *Geochimica et Cosmochimica Acta*, 37(3), pp. 379-399.
- Shenberger, D. and Barnes, H. (1989) 'Solubility of gold in aqueous sulfide solutions from 150 to 350 °C', *Geochimica et Cosmochimica Acta*, 53(2), pp. 269-278.
- Siron, G., Baumgartner, L. and Bouvier, A.-S. (2018) 'Significance of OH, F and Cl content in biotite during metamorphism of the Western Adamello contact aureole', *Contributions to Mineralogy and Petrology*, 173(8), pp. 63.
- Sizova, E., Gerya, T., Brown, M. and Stüwe, K. (2018) 'What drives metamorphism in early Archean greenstone belts? Insights from numerical modeling', *Tectonophysics*, 746, pp. 587-601.
- Span, R. and Wagner, W. (1996) 'A new equation of state for carbon dioxide covering the fluid region from the triple - point temperature to 1100 K at pressures up to 800 MPa', *Journal of physical and chemical reference data*, 25(6), pp. 1509-1596.
- Spear, F. S. (1993) *Metamorphic phase equilibria and pressure-temperature-time paths*. Washington, D.C: Mineralogical Society of America.
- Sperner, B., Müller, B., Heidbach, O., Delvaux, D., Reinecker, J. and Fuchs, K. (2003) 'Tectonic stress in the Earth's crust: Advances in the World Stress Map project', *Geological Society, London, Special Publications*, 212(1), pp. 101-116.
- Steadman, J. A., Large, R. R., Davidson, G. J., Bull, S. W., Thompson, J., Ireland, T. R. and Holden, P. (2014) 'Paragenesis and composition of ore minerals in the Randalls BIF-hosted gold deposits, Yilgarn Craton, Western Australia: Implications for the timing of deposit formation and constraints on gold sources', *Precambrian Research*, 243, pp. 110-132.
- Steadman, J. A., Large, R. R., Meffre, S. and Bull, S. W. (2013) 'Age, origin and significance of nodular sulfides in 2680Ma carbonaceous black shale of the Eastern Goldfields Superterrane, Yilgarn Craton, Western Australia', *Precambrian Research*, 230, pp. 227-247.
- Stefánsson, A. and Seward, T. M. (2004) 'Gold(I) complexing in aqueous sulphide solutions to 500°C at 500 bar', *Geochimica et Cosmochimica Acta*, 68(20), pp. 4121-4143.
- Sung, Y.-H., Brugger, J., Ciobanu, C., Pring, A., Skinner, W. and Nugus, M. (2009) 'Invisible gold in arsenian pyrite and arsenopyrite from a multistage Archean gold deposit: Sunrise Dam, Eastern Goldfields Province, Western Australia', *Mineralium Deposita*, 44(7), pp. 765-791.
- Svensen, H., Jamtveit, B., Banks, D. and Karlsen, D. (2001) 'Fluids and halogens at the diagenetic-metamorphic boundary: evidence from veins in continental basins, western Norway', *Geofluids*, 1(1), pp. 53-70.
-

-
- Tanner, D., Henley, R. W., Mavrogenes, J. A. and Holden, P. (2016) 'Sulfur isotope and trace element systematics of zoned pyrite crystals from the El Indio Au-Cu-Ag deposit, Chile', *Contributions to Mineralogy and Petrology*, 171(4), pp. 33.
- Tardani, D., Reich, M., Deditius, A. P., Chryssoulis, S., Sánchez-Alfaro, P., Wrage, J. and Roberts, M. P. (2017) 'Copper-arsenic decoupling in an active geothermal system: A link between pyrite and fluid composition', *Geochimica et Cosmochimica Acta*, 204, pp. 179-204.
- Thiéry, R., Van Den Kerkhof, A. M. and Dubessy, J. (1994) 'vX properties of CH₄-CO₂ and CO₂-N₂ fluid inclusions: modelling for T < 31 C and P < 400 bars', *European Journal of Mineralogy*, 6(6), pp. 753-771.
- Thomas, H. V., Large, R. R., Bull, S. W., Maslennikov, V., Berry, R. F., Fraser, R., Froud, S. and Moye, R. (2011) 'Pyrite and pyrrhotite textures and composition in sediments, laminated quartz veins, and reefs at Bendigo gold mine, Australia: insights for ore genesis', *Economic Geology*, 106(1), pp. 1-31.
- Tomkins, A. G. (2010) 'Windows of metamorphic sulfur liberation in the crust: implications for gold deposit genesis', *Geochimica et Cosmochimica Acta*, 74(11), pp. 3246-3259.
- van Hunen, J. and Moyen, J.-F. (2012) 'Archean subduction: fact or fiction?', *Annual Review of Earth and Planetary Sciences*, 40, pp. 195-219.
- van Kranendonk, M. J. (2011) 'Onset of plate tectonics', *Science*, 333(6041), pp. 413-414.
- van Ruitenbeek, F. J., Cudahy, T. J., van der Meer, F. D. and Hale, M. (2012) 'Characterization of the hydrothermal systems associated with Archean VMS-mineralization at Panorama, Western Australia, using hyperspectral, geochemical and geothermometric data', *Ore geology reviews*, 45, pp. 33-46.
- van Ryt, M. R., Sanislav, I. V., Dirks, P. H. G. M., Huizenga, J., Mturi, M. I. and Kolling, S. L. (in press) 'Biotite chemistry and the role of halogens in Archean greenstone hosted gold deposits: a case study from Geita Gold Mine, Tanzania', *Ore Geology Reviews*, Under Review.
- van Ryt, M. R., Sanislav, I. V., Dirks, P. H. G. M., Huizenga, J. M., Mturi, M. I. and Kolling, S. L. (2017) 'Alteration paragenesis and the timing of mineralised quartz veins at the world-class Geita Hill gold deposit, Geita Greenstone Belt, Tanzania', *Ore Geology Reviews*, 91, pp. 765-779.
- van Ryt, M. R., Sanislav, I. V., Dirks, P. H. G. M., Huizenga, J. M., Mturi, M. I. and Kolling, S. L. (2019) 'Biotite chemistry and the role of halogens in Archean greenstone hosted gold deposits: A case study from Geita Gold Mine, Tanzania', *Ore Geology Reviews*, 111, pp. 102982.
-

-
- Vielreicher, N., Groves, D., McNaughton, N. and Fletcher, I. (2015) 'The timing of gold mineralization across the eastern Yilgarn craton using U-Pb geochronology of hydrothermal phosphate minerals', *Mineralium Deposita*, 50(4), pp. 391-428.
- Vielreicher, R., Groves, D., Ridley, J. and McNaughton, N. (1994) 'A replacement origin for the BIF-hosted gold deposit at Mt. Morgans, Yilgarn Block, WA', *Ore Geology Reviews*, 9(4), pp. 325-347.
- Vikent'eva, O. V., Prokofiev, V. Y., Gamyandin, G. N., Goryachev, N. A. and Bortnikov, N. S. (2018) 'Intrusion-related gold-bismuth deposits of North-East Russia: PTX parameters and sources of hydrothermal fluids', *Ore Geology Reviews*, 102, pp. 240-259.
- Volfinger, M. and Pascal, M.-L. (1989) 'Partitioning of chlorine between muscovite and HCl-buffered solutions from 400 to 600 C at 2 kbar', *European Journal of Mineralogy*, pp. 791-800.
- Volfinger, M., Robert, J.-L., Vielzeuf, D. and Neiva, A. (1985) 'Structural control of the chlorine content of OH-bearing silicates (micas and amphiboles)', *Geochimica et Cosmochimica Acta*, 49(1), pp. 37-48.
- Webster, J. (1986) 'The solubility of gold and silver in the system Au-Ag-O₂-H₂O at 25° C and 1 atm', *Geochimica et Cosmochimica Acta*, 50(9), pp. 1837-1845.
- Weinberg, R. F., Hodkiewicz, P. F. and Groves, D. I. (2004) 'What controls gold distribution in Archean terranes?', *Geology*, 32(7), pp. 545-548.
- Weinberg, R. F. and Van Der Borgh, P. (2008) 'Extension and gold mineralization in the Archean Kalgoorlie Terrane, Yilgarn Craton', *Precambrian Research*, 161(1), pp. 77-88.
- White, A., Clemens, J., Holloway, J., Silver, L., Chappell, B. W. and Wall, V. (1986) 'S-type granites and their probable absence in southwestern North America', *Geology*, 14(2), pp. 115-118.
- Williams-Jones, A. E. and Samson, I. M. (1990) 'Theoretical estimation of halite solubility in the system NaCl-CaCl₂-H₂O; applications to fluid inclusions', *The Canadian Mineralogist*, 28(2), pp. 299-304.
- Wilson, S., Ridley, W. and Koenig, A. (2002) 'Development of sulfide calibration standards for the laser ablation inductively-coupled plasma mass spectrometry technique', *Journal of Analytical Atomic Spectrometry*, 17(4), pp. 406-409.
- Winderbaum, L., Ciobanu, C. L., Cook, N. J., Paul, M., Metcalfe, A. and Gilbert, S. (2012) 'Multivariate analysis of an LA-ICP-MS trace element dataset for pyrite', *Mathematical Geosciences*, 44(7), pp. 823-842.
-

-
- Witt, W. K. and Vanderhor, F. (1998) 'Diversity within a unified model for Archaean gold mineralization in the Yilgarn Craton of Western Australia: An overview of the late-orogenic, structurally-controlled gold deposits', *Ore Geology Reviews*, 13(1-5), pp. 29-64.
- Wohlgemuth-Ueberwasser, C. C., Viljoen, F., Petersen, S. and Vorster, C. (2015) 'Distribution and solubility limits of trace elements in hydrothermal black smoker sulfides: An in-situ LA-ICP-MS study', *Geochimica et Cosmochimica Acta*, 159, pp. 16-41.
- Xue, Y., Campbell, I., Ireland, T. R., Holden, P. and Armstrong, R. (2013) 'No mass-independent sulfur isotope fractionation in auriferous fluids supports a magmatic origin for Archean gold deposits', *Geology*, 41(7), pp. 791-794.
- Yardley, B. W. (1997) 'The evolution of fluids through the metamorphic cycle', *Fluid flow and transport in rocks*: Springer, pp. 99-121.
- Yardley, B. W. (2009) 'The role of water in the evolution of the continental crust', *Journal of the Geological Society*, 166(4), pp. 585-600.
- Yavuz, F. (2003) 'Evaluating micas in petrologic and metallogenic aspect: I-definitions and structure of the computer program MICA+', *Computers & Geosciences*, 29(10), pp. 1203-1213.
- Zhang, C. and Duan, Z. (2009) 'A model for C-O-H fluid in the Earth's mantle', *Geochimica et Cosmochimica Acta*, 73(7), pp. 2089-2102.
- Zhu, C. and Sverjensky, D. A. (1991) 'Partitioning of F-Cl-OH between minerals and hydrothermal fluids', *Geochimica et Cosmochimica Acta*, 55(7), pp. 1837-1858.
- Zhu, C. and Sverjensky, D. A. (1992) 'F-Cl-OH partitioning between biotite and apatite', *Geochimica et Cosmochimica Acta*, 56(9), pp. 3435-3467.

Appendix 1

Alteration paragenesis and the timing of mineralised quartz
veins at the world-class Geita Hill gold deposit, Geita
Greenstone Belt, Tanzania

Ore Geology Reviews (2017)

M. R. van Ryt, I. V. Sanislav, P. H. G. M. Dirks, J. M. Huizenga, M. I. Mturi @ S. L. Kolling

Appendix 2

The Geita Gold deposit, Tanzania: a late Archaean, Te-enriched, intrusion related gold system

Journal (in press)

P. H. G. M. Dirks, I. V. Sanislav, M. R. van Ryt, J-M Huizenga, T. Blenkinsop, S. L. Kolling,

S. D. Kwelwa

